STUDIA UNIVERSITATIS
BABEŞ-BOLYAI

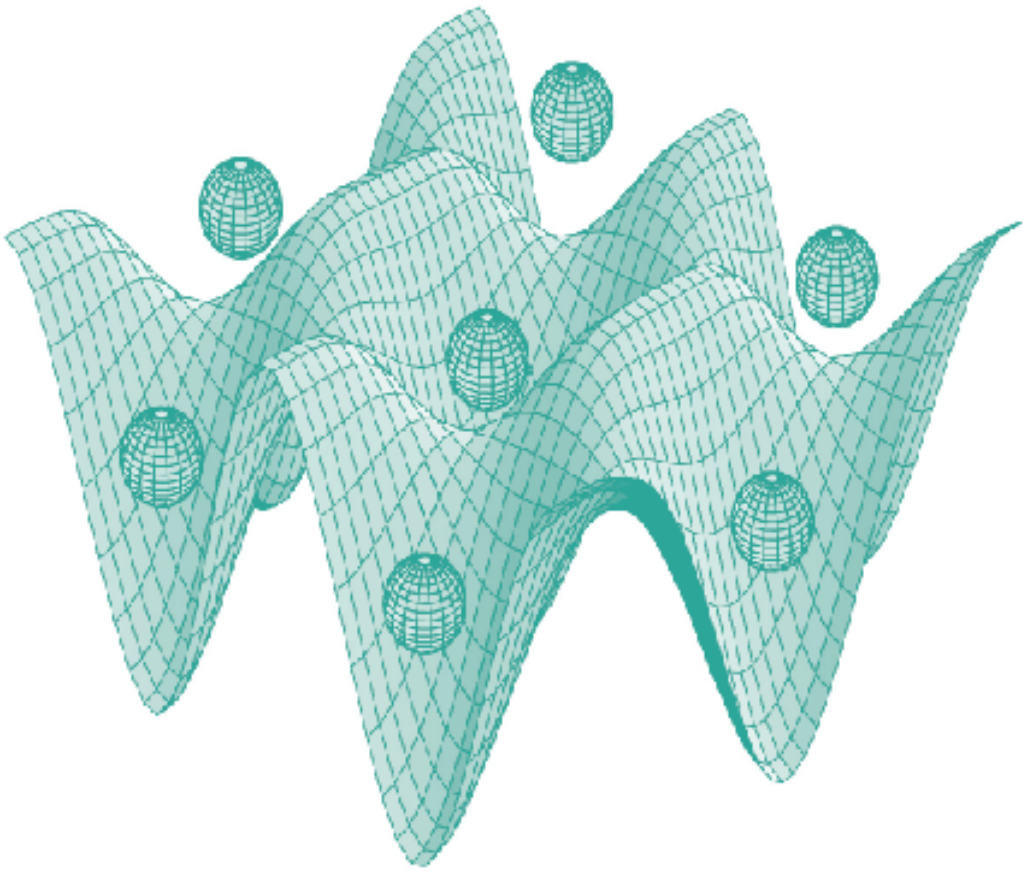

PHYSICA

1/2010

ANUL LV **2010**

S T U D I A

UNIVERSITATIS BABEŞ–BOLYAI

PHYSICA

1

– Dedicated to Professor MARIN COLDEA on his 65th anniversary –

Desktop Editing Office: 51ST B.P. Hasdeu, Cluj-Napoca, Romania, Phone + 40 264-40.53.52

CUPRINS – CONTENT – SOMMAIRE – INHALT

FOREWORD

Professor Marin Coldea was born in 1944, Mănăstireni, Cluj county. He graduated from Babes-Bolyai University Cluj-Napoca in 1967. Prof. Marin Coldea in 1967-1968 teached Physics in Bistrita High School and since 1968 he worked at Babes-Bolyai University as researcher, assistant (1975-1978), lecturer (1978-1990) and professor (1990-present). Prof. Marin Coldea was the Head of Mechanics, Molecular Physics and Solid State Physics. Department at the Physics Faculty (1990-2000). Prof. Marin Coldea earned his Ph D in Physics with thesis "Nuclear Magnetic Resonance and Magnetic Susceptibility of RCu_6 intermetallic compounds under the guidance" of Prof. I. Pop, in 1974.

Professor Marin Coldea presented courses and lectures in Mechanics and Acoustics, Solid State Physics, Physics of Low Temperatures, Physics of Metalls and Alloys, Electronics of Solids and Magnetic and Electrical Properties of Solid State for students in Physics and Chemistry Physics. In the framework of Master of Science Program he has been involved in teaching advanced courses in Physics of Thin Films, Advanced Solid State Physics and Transport Phenomena in Solids. At doctoral school presented lectures on Bidimensional Systems and Interfaces.

The teaching activities performed by Prof. Marin Coldea are much appreciated by the students. The courses are very clearly presented and at high scientific level. As a result, he has been classified by students as one of the best professors in teaching Physics at Babes-Bolyai University.

The scientific activities of Prof. M. Coldea were directed particularly on Physics of Metallic Systems. He used many methods in characterizing new type of materials by XRD, magnetic measurements, NMR, EPR and photoelectron spectroscopy. Prof. M. Coldea obtained significant scientific results concerning the function of magnetic moments, the nature and intensities of magnetic interactions, the degree of localization of magnetic moments, local environment effects, the connection between crystalline structure and magnetic properties, spin and ordered structures. The scientific results of Prof. M. Coldea were published in 166 papers, 84 being in ISI quoted journals. Around 55 papers were published in Proceeding of International Conferences. The scientific results of Prof. M. Coldea are frequently cited in literature, particularly for their rigorous presentation of new magnetic phenomena.

Professor Marin Coldea published also four books, frequently used by the students in area of their courses. These are remarkable for their accuracy and clarity as well as scientific level.

Professor Marin Coldea has been awarded by Alexander von Humboldt foundation and presented lectures in many universities, particularly at Technical University Darmstadt and University of Osnabrück. He was involved in "co-tutelle" programs for PhD students with University J. Fourier Grenoble and University of Osnabrück.

Today, at sixty five years old, Prof. Marin Coldea is surrounded by young students and researchers which continue their researchable scientific activity and also very much appreciated for their human and scientific results by all colleges.

Prof. dr. EMIL BURZO
Member of Romanian Academy

STUDIA UNIVERSITATIS BABEŞ-BOLYAI, PHYSICA, LV, 1, 2010

THE FIELD DISTRIBUTION AT THE MUON SITE FOR INCOMMENSURATE MAGNETIC STRUCTURES

DANIEL ANDREICA[a]

ABSTRACT. The dipolar magnetic field distribution at the muon site was calculated for a single ***k*** incommensurate magnetic structure using Monte Carlo simulation. It is shown that the generated dipolar magnetic field vectors lie on a plane, their ends defining an ellipse. With this information, a simple analytical formula for the field distribution at the muon site was computed.

Keywords: *incommensurate magnetic structure, field distribution, μSR*

INTRODUCTION

The knowledge of the field distribution at a particular crystallographic site in a magnetic sample is important for μSR experiments if one wants to extract quantitative information about the magnetic properties of the sample. Calculating the local dipolar magnetic field at the muon site is quite straightforward using Monte-Carlo simulation on modern computers if the muon site and the magnetic structure are known. Information about the magnetic structure (amplitude and orientation of the local magnetic moments) is usually provided by neutron scattering experiments. The position of the muon stopping site in the crystallographic unit cell is not easy to identify but symmetry analysis combined with electric potential calculations and μSR techniques might give some insights about the possible places.

In the following, we will calculate the field distribution at the muon site created by an incommensurate magnetic structure (IMS).

μSR basics: in a μSR experiment, polarized muons (elementary particles with spin 1/2) are stopped in the sample of interest, in an interstitial position, where their spin precesses around the local magnetic field. The muons decay by emitting a positron *preferentially* along their spin direction in the moment of the decay. By recording the number of emitted positrons in a certain direction function of time, one monitors the time dependence of the muon spin polarization and obtain information about the local field at the muon site, field distribution and field dynamics. The recorded μSR histogram is usually fitted to ([1,2], and references therein]):

[a] *Babes-Bolyai University, Physics Department, Kogalniceanu Str. 1, 400084 Cluj-Napoca, Romania, daniel.andreica@phys.ubbcluj.ro*

$$N_{e^+}(t) = B + \frac{N_0}{\tau_\mu}\exp\left(-t/\tau_\mu\right)\left[1 + AP_r(t)\right] \quad (1)$$

where B is a time independent background, N_0 is a normalization constant and the exponential accounts for the μ^+ decay. A is the so called *asymmetry* of the decay and equals 1/3 when all positron energies are sampled with equal probability. In practice, values of A of about 0.25 are found (due to the possible reduction of polarization of the muon beam, geometry of the positron counters, non-uniform energy sensitivity of the detectors, …). $P_r(t)$ reflects the time dependence of the μ^+ polarization and contains the information about the magnetic properties of the sample, see below. $P_r(t)$ is in fact the projection of the muon polarization on the direction of observation (r indicates the direction of observation, with unit vector $\boldsymbol{n} \parallel P(0)$ in our case):

$$P_r(t) = \boldsymbol{n} \cdot \boldsymbol{P}(t)/P(0) \quad (2)$$

We now assume that the sample of interest is paramagnetic above a certain temperature T_m and magnetic below T_m. Moreover, we assume that the magnetic ordering is static (for the time window of a μSR experiment i.e. 10 μs) and that the muon diffusion can be neglected. In the paramagnetic state the time averaged local field at the muon site is zero because of the thermal fluctuations of the surrounding magnetic moments.

At temperatures below T_m the amplitude of the static magnetic moments at different crystallographic sites can be computed using the general formula:

$$\boldsymbol{m}_i = \boldsymbol{M}\cos(2\pi\boldsymbol{k}\boldsymbol{r}_i + \varphi) \quad (3)$$

where $\boldsymbol{M}$ is the magnetic moment that is modulated, $\boldsymbol{r}_i$ is the coordinate of the site of the magnetic moment, φ is a phase factor and $\boldsymbol{k}$ is a vector in the reciprocal space that describes the magnetic modulation (simple ferromagnetic (F) and antiferromagnetic (AF) types of magnetic ordering are particular cases of the above formula). The dipolar field at the muon site can then be calculated from:

$$\boldsymbol{B}_{\text{dip}} = \sum_i \frac{1}{r_i^3}\left(\frac{3(\boldsymbol{m}_i \cdot \boldsymbol{r}_i)\boldsymbol{r}_i}{r_i^2} - \boldsymbol{m}_i\right) \quad (4)$$

where $\boldsymbol{r}_i$ is a vector from the muon to the i^{th} magnetic moment $\boldsymbol{m}_i$, and the summation runs over all magnetic moments. Plugging, in a Monte-Carlo simulation, the crystallographic structure, the magnetic structure and the muon site one can compute the local field at the muon site for any type of magnetic structure. The calculation is usually performed for several thousands of muons placed in all crystallographically equivalent sites, for ideal samples i.e. no depolarization of the μSR signal due to crystalline defects is taken into account.

RESULTS AND DISCUSSIONS

1. Commensurate magnetic structures.

If the components of ***k***, in Eq. 3, are rational numbers (with respect to the lattice parameters), the magnetic structure is *commensurate* with the crystallographic unit cell i.e. the magnetic unit cell is a "multiple" of the crystallographic unit cell.

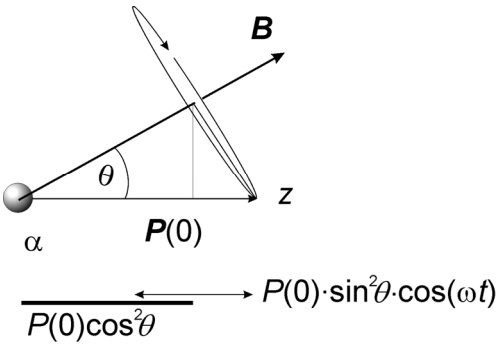

Fig. 1. Larmor precession of the muon spin around the local magnetic field.

In such a case the computed dipolar magnetic field distribution at the muon site is a delta function or a collection of characteristic delta functions, depending on the muon site. In the simplest case all the muons sense the same magnetic field ***B***, see Figure 1. This situation might occur for simple F or AF samples, in ideal single-domain single-crystals with one (magnetically equivalent) muon site. The time dependence of the μ^+ polarization as seen in one of the detectors (backward - with respect to the muon momentum) is then, see Eq. 2:

$$P_z(t) = \cos^2\theta + \sin^2\theta\cos(\gamma_\mu B_\mu t + \varphi) \tag{5}$$

where θ is the angle between the magnetic field and $\boldsymbol{P}(0)$ (defines the z axis). $\omega = \gamma_\mu B_\mu$ is the Larmor precession frequency of the muon spin around the local magnetic field and φ is the initial phase of the precession (0 in this case). A simulated μSR spectrum (B = 50 G, θ = 30°) is presented in Figure 2. By fitting the μSR spectrum to Eq. 4, information about the magnitude and orientation of the local field in the laboratory coordinates can be obtained. In the case of a polycrystalline sample the average over all θ angles yields:

$$P_z(t) = 1/3 + 2/3\cdot\cos(\gamma_\mu B_\mu t + \varphi). \tag{6}$$

The one-third term in the above equation can be easily understood by considering that since the magnetic fields can have all the orientations, on the average one third of the muons will sense magnetic fields parallel to their initial polarization and will not precess while two thirds of them will sense magnetic fields perpendicular to their initial polarization and will precess around them with $\omega = \gamma_\mu B$. The rule is sometimes valid also for multidomain single crystals.

2. Incommensurate magnetic structures.

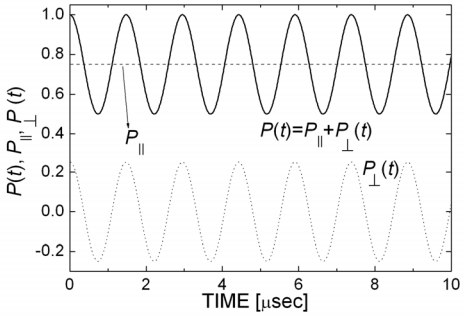

Fig. 2. mSR spectra simulated for the situation presented in Figure 1.

If at least one of the components of $\boldsymbol{k}$ is an irrational number, the magnetic and the crystallographic unit cell are incommensurate in that direction of the direct space. The Monte-Carlo simulation [3] of the local field at the muon site for an incommensurate magnetic structure yields a quite unexpected result: the local fields at the different crystallographically equivalent muon sites lie in a plane and define an ellipse (see Figure 3). The corresponding field distribution $f(B)$ is presented in Figure 4 (in this particular case the field distribution was simulated for one of the 2-2 (96*g* in Wickoff notation) muon sites in $CeAl_2$ [4].

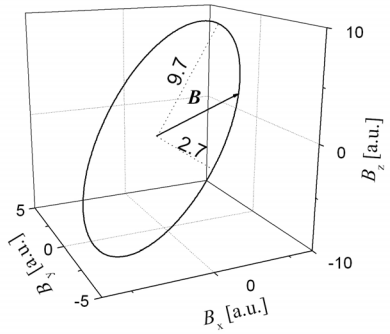

Fig. 3. Dipolar fields at the muon site for an incommensurate magnetic structure.

Using Eq. (4) and the notations from Figure 5 one can calculate the dipolar field at the muon site:

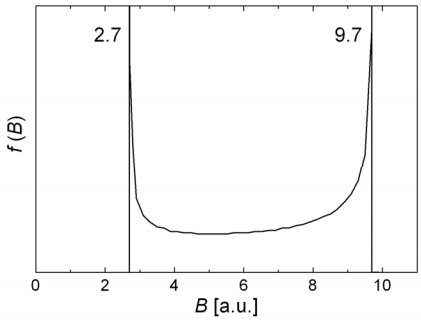

Fig. 4. Magnetic Field distribution for an incommensurate magnetic structure.

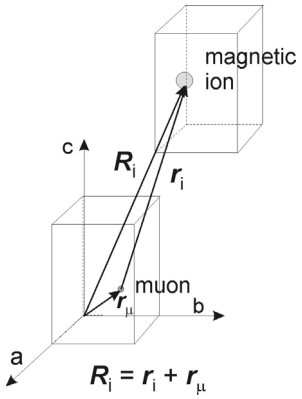

Fig. 5. Notations used for the calculation of B_{dip}

$$\boldsymbol{B}_{\text{dip}} = \sum_i M \cdot \cos\left(2\pi\, \boldsymbol{k} \cdot \boldsymbol{R}_i + \varphi\right)\left[\frac{3\left(\boldsymbol{1}_M \cdot \boldsymbol{r}_i\right)\boldsymbol{r}_i}{r_i^5} - \frac{\boldsymbol{1}_M}{r_i^3}\right], \tag{7}$$

where $\boldsymbol{1}_M$ is a unit vector in the direction of the magnetic moment $\boldsymbol{M}$: $\boldsymbol{M} = M \cdot \boldsymbol{1}_M$.

By making the substitution $\boldsymbol{R}_i = \left(\boldsymbol{r}_i + \boldsymbol{r}_\mu\right)$ [5], see Figure 5 and using simple trigonometric relations we obtain:

$$\boldsymbol{B}_{\text{dip}} = \cos 2\pi\left(\boldsymbol{k}\cdot\boldsymbol{r}_{\mu}\right)\sum_{i} M\cdot\cos\left(2\pi\,\boldsymbol{k}\cdot\boldsymbol{r}_{i}+\varphi\right)\left[\frac{3\left(\boldsymbol{1}_{M}\cdot\boldsymbol{r}_{i}\right)\boldsymbol{r}_{i}}{r_{i}^{5}}-\frac{\boldsymbol{1}_{M}}{r_{i}^{3}}\right]$$
$$-\sin 2\pi\left(\boldsymbol{k}\cdot\boldsymbol{r}_{\mu}\right)\sum_{i} M\cdot\sin\left(2\pi\,\boldsymbol{k}\cdot\boldsymbol{r}_{i}+\varphi\right)\left[\frac{3\left(\boldsymbol{1}_{M}\cdot\boldsymbol{r}_{i}\right)\boldsymbol{r}_{i}}{r_{i}^{5}}-\frac{\boldsymbol{1}_{M}}{r_{i}^{3}}\right] \tag{8}$$

Since the terms under the sums in the above equation do not depend on the muon site one can easily observe that the magnetic fields at the muon site generated with Eq. 8, lie in a plane defined by two lattice sums (vectors) and their ends lie on an ellipse (see Figure 3) with a corresponding field distribution $f(B)$ as presented in Figure 4. Thus Eq. 8 provides an easy way of calculating field distributions at the muon site for both commensurate and incommensurate magnetic structures and drastically reduces the computing time of such calculations. The two lattice sums on the right hand side of Eq. 8 can be calculated separately. We will denote them $\boldsymbol{S}_{\cos}$ and $\boldsymbol{S}_{\sin}$:

$$\boldsymbol{B}_{\text{dip}} = \boldsymbol{S}_{\cos}\cdot\cos\left(2\pi\,\boldsymbol{k}\cdot\boldsymbol{r}_{\mu}\right)-\boldsymbol{S}_{\sin}\cdot\sin\left(2\pi\,\boldsymbol{k}\cdot\boldsymbol{r}_{\mu}\right) \tag{9}$$

No matter the value of $\boldsymbol{k}$, the shape of the ellipse is determined solely by the lattice sums $\boldsymbol{S}_{\cos}$ and $\boldsymbol{S}_{\sin}$. In the case of an incommensurate magnetic structure, all the points on the ellipse are generated and each of them only once since for an incommensurate structure $\boldsymbol{k}\boldsymbol{r}_{\mu} \neq \boldsymbol{k}(\boldsymbol{r}_{\mu} + \boldsymbol{R}_{\text{n}})$ for all direct lattice vectors $\boldsymbol{R}_{\text{n}} = n_1\boldsymbol{a} + n_2\boldsymbol{b} + n_3\boldsymbol{c}$ where n_1, n_2 and n_3 are integers. Therefore in that case one can write:

$$\boldsymbol{B}_{\text{dip}} = \boldsymbol{S}_{\cos}\cdot\cos\alpha - \boldsymbol{S}_{\sin}\cdot\sin\alpha$$

which describes *all* the points of an ellipse.

The field distribution at the muon site can be easily computed if $\boldsymbol{S}_{\cos}$ and $\boldsymbol{S}_{\sin}$ are perpendicular to each other (we denote them $B_{\min}$ and $B_{\max}$: $B_{\min} < B < B_{\max}$):

$f(B) = \dfrac{2}{\pi}\dfrac{B}{\left(B^2 - B_{\min}^2\right)^{1/2}\left(B_{\max}^2 - B^2\right)^{1/2}}$, see Figure 4. At this point we have to mention that a similar formula was used by [6] to describe field distribution for an incommensurate magnetic structure but with no further comments.

Conclusions

It was shown that the dipolar magnetic fields at the muon sites, for an IMS lie on a plane where they define an ellipse. The field distribution has a characteristic two peak shape and intrinsic field distribution even for an ideal sample (different from the δ functions of the commensurate case). An easy way of computing such field distributions is proposed, which drastically reduces the computation time.

REFERENCES

1. A. Schenck, "Muon Spin Spectroscopy: Principles and Applications in Solid State Physics", Adam Hilger, Bristol, England, 1985.
2. A. Amato and D. Andreica, "Muon Spin Rotation" in Encyclopedia of Condensed Matter Physics, edited by G. Bassani, G. Liedl and P. Wyder, Elsevier, 2005, p. 41.
3. D. Andreica, Ph.D. thesis, IPP/ETH-Zurich, 2001
4. A. Schenck, D. Andreica, F. N. Gygax, H. R. Ott, *Physical Review B*, **2001**, 65, 024444
5. M. Pinkpank, private communication
6. G. M. Kalvius, D. R. Noakes, A. Kratzer, K.H. Miinch, R. Wäppling, H. Tanaka, T. Takabatake, R.F. Kiefl, *Physica B*, **1995**, 206-207, 205

STUDIA UNIVERSITATIS BABEŞ-BOLYAI, PHYSICA, LV, 1, 2010

SURFACE MAGNETIC STRUCTURE OF NEARLY ZERO MAGNETOSTRICTIVE AMORPHOUS GLASS-COATED MICROWIRES

TIBOR-ADRIAN ÓVÁRI, SORIN CORODEANU, MIHAELA LOSTUN, HORIA CHIRIAC[a]

ABSTRACT. Nearly zero magnetostrictive amorphous glass-coated microwires are very versatile due to their very good soft magnetic properties and to the appearance of sensitive application-related effects, such as the large Barkhausen and the giant magneto-impedance effects. Their specific magnetic behavior and properties originate in their unique core-shell magnetic domain structure. In this paper we address two very important aspects related to the surface magnetic structure of these materials: (i) – the necessity to include the interdomain wall that separates the inner core and the outer shell in any analysis of high frequency phenomena, and (ii) – the structure of the outer shell. Both these aspects have very important consequences as concerns the sensor applications of microwires, especially those based on the giant magneto-impedance effect.

Keywords: *amorphous microwires, domain wall, giant magneto-impedance, magnetic domain structure*

INTRODUCTION

Amorphous glass-coated microwires consist of a metallic nucleus with diameters from 1 to 50 μm, embedded in a Pyrex glass coating with the thickness ranging between 1 and 40 μm. They are prepared at high cooling rates in a continuous process called glass-coated melt spinning [1], the resulting microwires displaying lengths in the range of 10^3 m. The magnetic properties and behavior of such microwires are mainly decided by the magneto-mechanical coupling between internal stresses induced during preparation and the magnetostriction of the employed metallic alloys. Microwires with positive, negative, and nearly zero magnetostriction display a specific magnetic behavior each, correlated with the sign and magnitude of their magnetostriction constant. They are all suitable for various sensor applications [2], however the most versatile microwires are the nearly zero magnetostrictive ones, which display the softest magnetic properties and offer the appropriate conditions for the appearance of the most important application-related effects, such as the large Barkhausen effect and the giant magneto-impedance (GMI) effect.

[a] *National Institute of Research and Development for Technical Physics, 47 Mangeron Boulevard, RO-700050 Iaşi, Romania, hchiriac@phys-iasi.ro*

Their sensitive GMI response originates in the peculiar domain structure, composed mainly of an inner core (IC) and an outer shell (OS). The IC can display either transverse or axial anisotropy, depending on the microwire dimensions (radius of the metallic nucleus – R and glass coating thickness – t), whilst the OS displays a circumferential easy axis. The OS is the main region involved in the GMI effect, due to the skin effect that occurs at high frequencies. There are two key factors that lead to a large GMI response: (i) a suitable domain structure, i.e. a region with circumferential easy axis of magnetization, and (ii) enhanced soft magnetic properties. Both factors have to be met in the GMI responding region, i.e. within the surface region determined by the skin depth at frequencies where GMI effect takes place. Microwires that are the closest to both requirements are the nearly zero magnetostrictive $(Co_{0.94}Fe_{0.06})_{72.5}Si_{12.5}B_{15}$ ones, having the saturation magnetostriction constant $\lambda_S = -1 \times 10^{-7}$.

The core-shell representation of the domain structure is rather simplistic, since it does not offer much information about the transition zone between the two main regions and the effects it might have on various high frequency phenomena, such as GMI or ferromagnetic resonance. Therefore, our first aim is to demonstrate the necessity to go deeper into the complexity of the domain structure and to consider elements that have been disregarded until recently, in order to fully understand the GMI response of amorphous microwires. It has been recently shown that the width of the interdomain wall between the IC and the OS in amorphous microwires can reach to quite large values, especially in samples with low magnetostriction [3]. Under these circumstances, the interdomain wall is expected to reach within the region that responds in the high frequency GMI effect, i.e. the region determined by the skin effect through the magnetic skin depth, d.

On the other hand, the circumferential OS has been found to display a bamboo-like structure with consecutive rings circumferentially magnetized in opposite directions [4], in spite of earlier theoretical studies which predicted an OS with uniform magnetization [5]. Consequently, our second aim is to clarify these contradictory results and to establish the circumstances in which each of these potential structures may appear.

EXPERIMENT

Amorphous glass-coated microwire samples have been prepared by means of glass-coated melt spinning at the National Institute of Research and Development for Technical Physics, Iaşi, Romania. The employed alloy composition was $(Co_{0.94}Fe_{0.06})_{72.5}Si_{12.5}B_{15}$. The amorphous state was checked by X-ray diffraction measurements.

GMI measurements have been performed at frequencies of the ac driving current between 10 and 500 MHz using an Agilent E4991A impedance analyzer. GMI has been measured on both as-cast samples and on samples with the glass coating completely removed, using a current amplitude of 0.5 mA. Glass removal was achieved using hydrofluoric acid solution.

Magneto-optical Kerr effect (MOKE) surface hysteresis loops have been measured using a NanoMOKE2 Kerr effect magnetometer with a built-in optical microscope made by Durham Magneto Optical Ltd.

RESULTS AND DISCUSSION

Figure 1 illustrates the dependence of the impedance magnitude, $|Z|$ on the applied dc magnetic field, *H*, for an as-cast glass-coated amorphous microwire (Figure 1a), and for the same microwire after the complete removal of the glass coating (Figure 1b), with the frequency of the driving ac current as a parameter. In case of the glass-coated sample, the impedance magnitude displays a maximum at each value of the frequency, its position being symmetric with respect to the applied dc magnetic field.

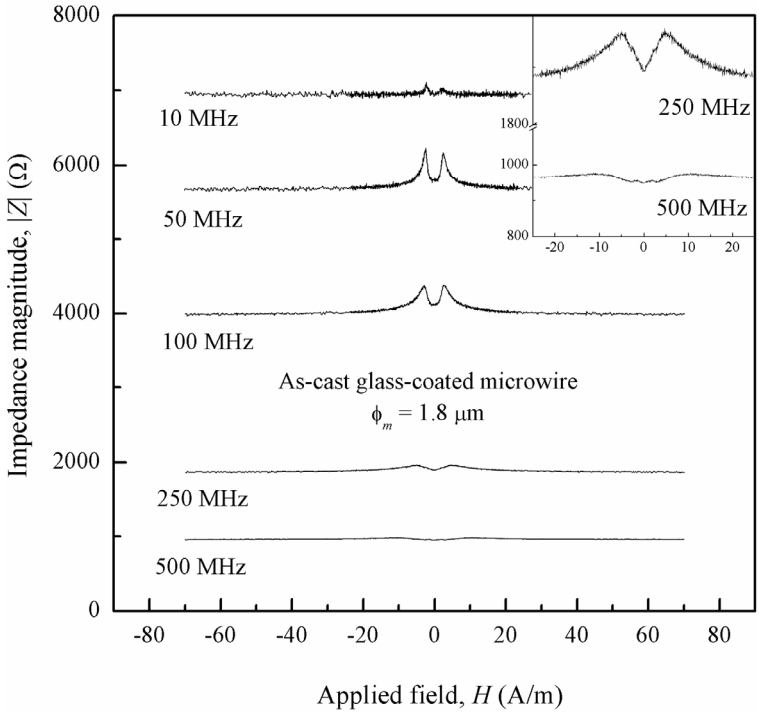

Fig. 1a.

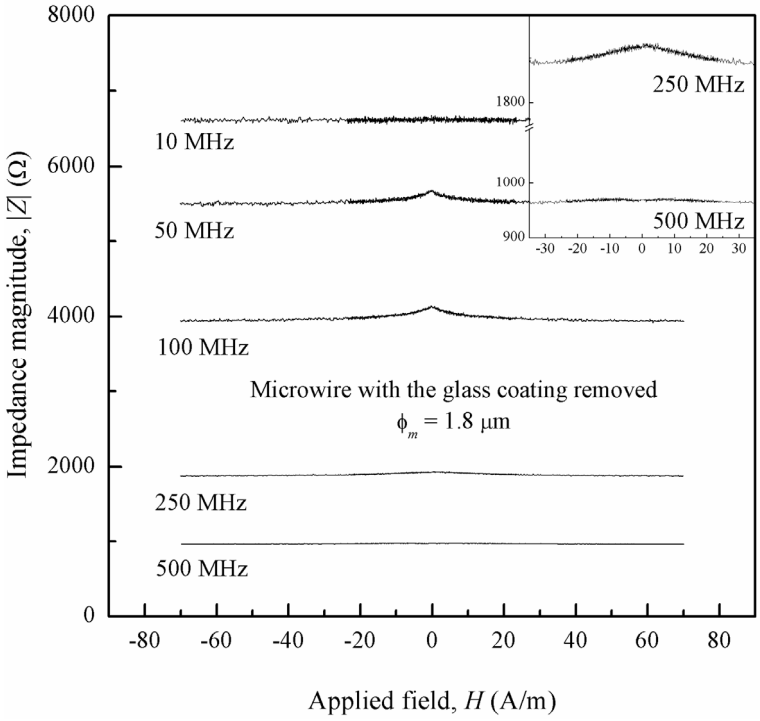

Fig.1b.

Fig. 1. Impedance magnitude, $|Z|$, vs. applied dc magnetic field, H, for an as-cast glass-coated amorphous microwire with the metallic nucleus diameter of 1.8 μm (Figure 1a) and for the same sample after glass removal (Figure 1b), at frequencies between 10 and 500 MHz.

Such maxima are linked to the circumferential anisotropy field within the OS, i.e. once the axially applied dc field overcomes it, the GMI response becomes the largest, since the magnetic moments are free to follow the reversal of the circumferential ac magnetic field created by the driving ac current. The largest and most sensitive impedance variations are obtained at the frequencies of 50 and 100 MHz.

After glass removal, the largest and most sensitive impedance variations are also obtained at 50 and 100 MHz. However, glass removal leads to a significant change in the shape of the GMI curves: the impedance magnitude decreases monotonically with the applied dc field, without passing through a maximum. This change is associated with the important stress relief caused by glass removal. Although the circumferential anisotropy field within the OS is expected to decrease abruptly, an explanation based solely on the simple IC+OS domain structure does not clarify the absence of any effect the circumferential anisotropy field might have on GMI.

To fully understand the impedance behavior with glass removal, one has to consider the complex magnetic structure in the surface region which is involved in the GMI effect due to the skin effect. The GMI responding region is delimited by the magnetic skin depth, *d*, which limits the flow of the driving ac current to the surface region of the microwire. Therefore, it is important to understand which elements of the domain structure are located within this region and what are the exact changes induced by glass removal. Usually, specifically in case of Co-based amorphous microwires with nearly zero magnetostriction, it is implied that the OS with circumferential easy axis of magnetization is mostly the responding region from the surface [6], [7]. However, in the light of very recent results on the interdomain wall in such microwires [3], one also has to consider the role of this wall in the GMI effect, since it is expected to be part of the GMI responding region.

We have calculated the width of the interdomain wall in a microwire with the metallic nucleus diameter (ϕ_m) of 1.8 μm and the glass coating thickness of 7.5 μm starting from the analysis of internal stresses induced during preparation, following the procedure described in [3]. The analysis of internal stresses reveals the coordinate of the middle of the interdomain wall at the radial coordinate r = 0.725 μm. From this coordinate toward the center of the microwire there is a region in which axial tensile stresses are dominant, whilst toward the surface there is a small region in which radial tensile stresses dominate, followed by a larger region in which circumferential compressive stresses dominate.

The width of the interdomain wall, δ, is given by $(\pi/2)\sqrt{A/2K}$, in which A is the exchange parameter for Co-based alloys (3×10^{-11} J/m) and K is the magnetoelastic anisotropy constant in the wall region, given by $(3/2)\lambda\langle\sigma\rangle$, where $\langle\sigma\rangle$ is the average value of internal stresses across the transition region in which the direction of the dominant stress changes. Calculations show that, in this case δ is 282 nm, large compared to the 0.9 μm radius of the metallic nucleus. Thus, the parameters of the wall are determined, and one can represent a schematic of the domain structure (Figure 2): the IC has a radius of 584 nm and the OS is extremely thin at just 34 nm, however it displays a quite large circumferential anisotropy; between the IC and the OS, from r = 584 nm to r = 866 nm lies the 282 nm wide interdomain wall.

Therefore, for an average value of the magnetic skin depth $d \approx 0.5$ μm at 100 MHz (see for instance [8], in which an estimated 0.8 μm is given for a Co-based ribbon at the same frequency, and considering that the permeability of a microwire is larger due to its more convenient domain structure and symmetry), it is plausible to state that, besides the OS, the interdomain wall plays a very important role in the GMI effect of microwires.

The GMI responses at 50 and 100 MHz are the closest to the situation depicted in Figure 2. The responding region consists mainly of the OS and interdomain wall. The OS is responsible for the appearance of the peaks associated with the large circumferential anisotropy of the OS, while the interdomain wall is responsible for

the large impedance variation, due to the high degree of spread in the local anisotropies, which results in softer magnetic properties at high frequencies. At 250 and 500 MHz, the GMI responding region is closing on the OS, and consequently, the impedance variation is much smaller, but the peaks determined by the large circumferential anisotropy of the OS are visible.

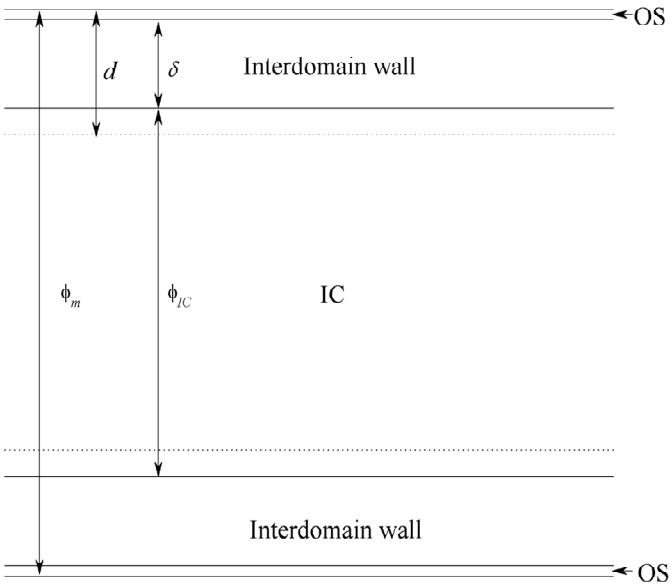

Fig. 2. Schematic of the domain structure within the metallic nucleus of an as-cast amorphous glass-coated microwire with ϕ_m = 1.8 μm and a 7.5 μm glass coating thickness. The dimensions of the IC, OS, and interdomain wall width are proportional to their calculated values. Dotted line indicates a potential value of the magnetic skin depth *d*.

After glass removal, the maximum values of stresses decrease significantly (e.g., maximum axial tensile stress decreases by almost 50%) and the radial coordinate of the middle of the interdomain wall is moving toward the center of the microwire with 25 nm, to r = 0.700 μm. Nonetheless, the width of the interdomain wall, δ, increases by 40% due to the significant decrease of stresses, and reaches to almost 400 nm. Under these circumstances, the thin OS practically vanishes, which is in agreement with the experimentally observed GMI response of the microwire with the glass coating removed (Figure 1b). There are no maxima associated with the circumferential anisotropy from the OS, as there is no clearly delimited OS, and the frequency dependence of the magnitude of the impedance variation is similar to that observed in the case of as-cast microwires.

The microwire with the glass removed displays an altered domain structure, made up of an IC, a very wide interdomain wall, and an extremely thin region with helical anisotropy, which is a remnant of the OS. Such a structure is in agreement with previous reports on the helical anisotropy from the surface region of Co-based amorphous glass-coated microwires with very thin glass coating [9].

As concerns the structure of the OS, in order to compare the magnetostatic energies of the bamboo structure (configuration C1) and uniform magnetization (configuration C2), we have divided the OS in thin disks of length l on the axial direction, and then each disk in disk sectors of opening $\mathrm{d}\theta$ on the circumferential direction. A schematic representation of both configurations is illustrated in Figure 3. The radial dimension is given by the thickness of the OS, t_{OS}. The circumferential anisotropy energy is the same in both configurations and it results from the coupling between magnetostriction and internal stresses, the Zeeman term is null in the absence of an applied field, whilst the exchange term has been neglected at such large scale.

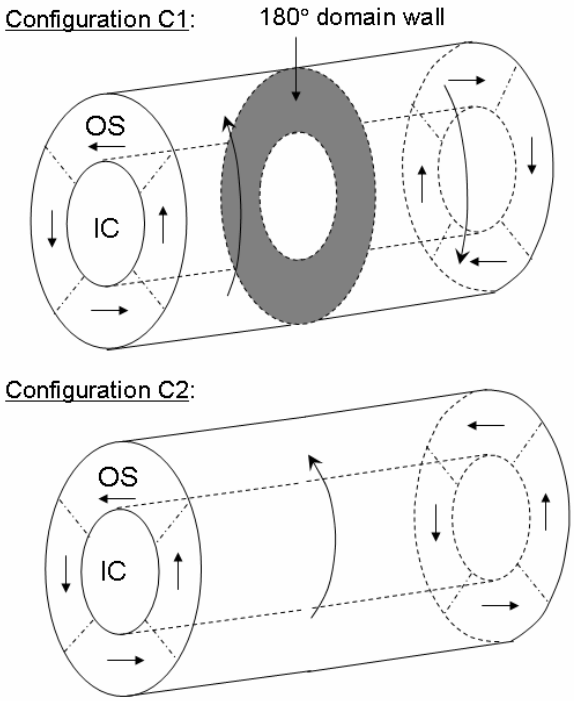

Figure 3. Schematic representation of the simplified configurations of the outer shell (OS) employed to calculate the variation of the magnetostatic energy between the OS with bamboo structure (configuration C1) and the OS with uniform circumferential magnetization (configuration C2).

The dipolar field created by the *j*-th element (disk sector) at the place of the *i*-th element is given by:

$$\vec{H}_d(i) = \frac{3\left(\vec{m}_j \cdot \frac{\vec{r}_{ij}}{|\vec{r}_{ij}|}\right)\frac{\vec{r}_{ij}}{|\vec{r}_{ij}|} - \vec{m}_j}{|\vec{r}_{ij}|^3}$$ in which $\vec{m}_j$ is the magnetization of the *j*-th element and $\vec{r}_{ij}$ is the distance between elements *i* and *j*.

If the sum of all the dipolar fields created by all the *j* elements from the OS ($j \neq i$) at the place of element *i* is denoted by $\vec{H}_d^{tot}(i)$, then the scalar product between $\vec{m}_i$ and $\vec{H}_d^{tot}(i)$ gives the part of the magnetostatic energy, E_{ms}, that results from the interaction of $\vec{m}_i$ with the dipolar field created by all the other elements from the system. The total magnetostatic energy is then obtained by summing over *i*.

For the simple case illustrated in Figure 3, we have found the following expressions for E_{ms} in configurations C1 and C2:

$$E_{ms}^{C1} = 8m^2V(A + B - C - D) \text{ and } E_{ms}^{C2} = 8m^2V(A - B + C + D)$$

where *m* is the magnetization within an element, *V* the volume of an element, while *A*, *B*, *C*, and *D* are coefficients which depend only on distances and geometry as follows:

$$A = \frac{1+6\sqrt{2}}{(R+r)^3}, \qquad B = \frac{1}{l^3}, \qquad C = \frac{6\sqrt{2}(R+r)^2}{\left(\sqrt{(R+r)^2+2l^2}\right)^5}, \qquad \text{and}$$

$$D = \frac{1}{\left(\sqrt{(R+r)^2+l^2}\right)^3}$$ in which *R* is the radius of the metallic nucleus, *l* the axial dimension of a disk sector, and *r* the radial coordinate at which the OS begins ($r = R - t_{OS}$).

Consequently, the difference in magnetostatic energy between configurations C1 and C2 in this case is:

$$\Delta E_{ms} = E_{ms}^{C1} - E_{ms}^{C2} = 16m^2V(B - C - D)$$

A simple verification shows the $\Delta E_{ms} = 0$ for any typical dimensions of microwires. *l* has been considered of the order of the microwire diameter, while t_{OS} has been calculated based on the internal stress distribution in microwires [10], by taking into account the interdomain wall between the IC and the OS.

Thus, the two configurations are identical from the point of view of the magnetostatic energy. However, in configuration C1 there is also a 180° domain wall whose energy increases the total energy of the OS. Therefore, configuration C2, with the uniformly magnetized circumferential OS is energetically favored over configuration C1 with the bamboo-like structure of the OS.

Figure 4 shows the MOKE surface hysteresis loops for a glass-coated sample (Figure 4a) and for the same sample after glass removal (Figure 4b).

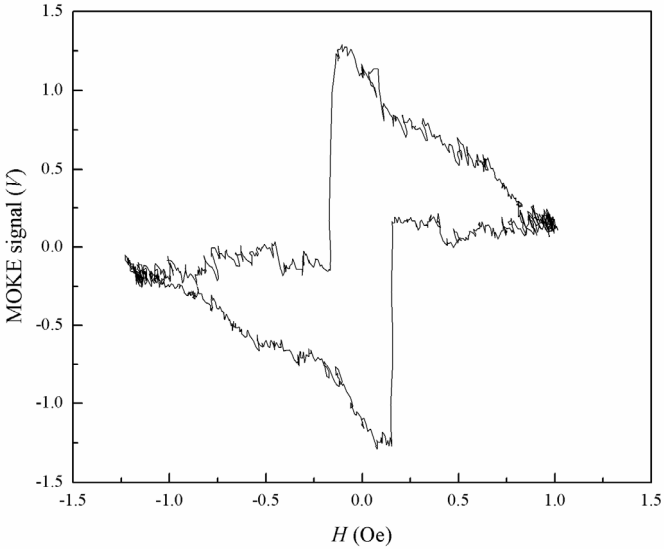

Fig. 4a.

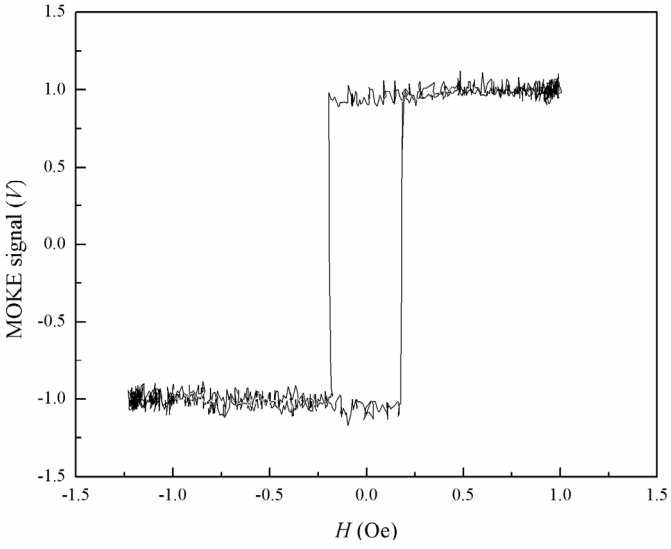

Fig. 4b.

Figure 4. MOKE surface hysteresis loops for an as-cast glass-coated microwire (Figure 4a) and for the same sample after glass removal (Figure 4b).

The hysteresis loop illustrated in Figure 4a is consistent with the uniformly magnetized circumferential OS. The Kerr signal, which is proportional to the axial component of the magnetization, M_Z, in the employed longitudinal MOKE configuration, reaches maximum just around reversal. The reversal mechanism is the following: the IC with axial magnetization reverses due to the applied axial field H, and it drags the magnetization from the OS to reverse through the interdomain wall, which also suffers reversal. What we are seeing is just what happens in the surface region, i.e. no M_Z component until reversal, since before and after reversal the magnetization is in the circumferential direction.

Glass removal induces significant changes in the structure of the OS, as proven by the rectangular MOKE surface hysteresis loop shown in Figure 4b. This surface loop is consistent with a magnetization in the θ-z plane, i.e. a helical magnetization, whose z-component reversal is observed. Such a situation reflects neither configuration C1 nor configuration C2. The reversal mechanism is the same: the IC with axial magnetization reverses due to H, and it drags the magnetization from the surface region to reverse through the interdomain wall, which also suffers reversal, but in this case M_Z is constant. The most plausible explanation for the changes induced by glass removal is that the magnetoelastic anisotropy decreases significantly due to the associated stress relief, which causes the OS to vanish, being replaced by a region with helical magnetic anisotropy, that blends at its inner boundary with the expanded interdomain wall and continues on its outer side towards the surface of the microwire. This result is also consistent with the GMI response of the microwire with the glass coating removed.

The helical surface structure is characterized by very low anisotropy and it is very plausible to expect the formation of various maze-like domain patterns at the surface caused by surface defects or imperfections. Such domain patterns could resemble the bamboo structure. One argument in favor of this explanation is the one pointed out by Rakhmanov et al.[5], i.e. that the bamboo structure has only been observed in partially polished microwires or in microwires with the glass coating removed.

CONCLUSIONS

The role of the complex surface magnetic structure in glass-coated Co-based amorphous microwires has been investigated. An element that has been disregarded until now – the interdomain wall between the IC and the OS – has been proven to significantly affect the GMI response of microwires, since it is located within the region delimited by the magnetic skin depth at high frequencies. Glass removal determines a strong stress relief, reflected in an expanded interdomain wall and a corresponding vanishing of the OS with circumferential anisotropy.

A uniformly magnetized outer shell with circumferential easy axis has been proven to exist in the surface region of nearly zero magnetostrictive glass-coated amorphous microwires. In microwires with the glass coating removed, the vanishing OS is replaced by a region with helical magnetization, which reaches towards the microwire surface.

ACKNOWLEDGMENTS

Work supported by the Romanian National University Research Council (CNCSIS) under Contract No. 526/2009 (Project ID 1610).

REFERENCES

1. M. Vázquez, *Physica B*, **2001**, *299*, 302-313.
2. A. Zhukov, *J. Magn. Magn. Mater.*, **2002**, *242*, 216-223.
3. H. Chiriac, T.-A. Óvári, S. Corodeanu, G. Ababei, *Phys. Rev. B*, **2007**, *76*, 214433.
4. E.E. Shalygina, V.V. Molokanov, M.A. Komarova, *J. Experim. and Theor. Phys.*, **2002**, *95*, 511.
5. A.A. Rakhmanov, A.S. Antonov, N.A. Buznikov, and A.F. Prokoshin, *J. Magn. Magn. Mater.*, **2006**, *300*, e37-e40.
6. K. Mandal, S. Puerta, M. Vázquez, and A. Hernando, *Phys. Rev. B*, **2000**, *62*, 6598-6602.
7. D.P. Makhnovskiy, L.V. Panina, and D.J. Mapps, *Phys. Rev. B*, **2001**, *63*, 144424.
8. D. de Cos, A. García-Arribas, and J.M. Barandiarán, *Sensor. Actuat. A-Phys.*, **2004**, *115*, 368-375.
9. A. Chizhik, J.M. Blanco, A. Zhukov, J. Gonzalez, C. Garcia, P. Gawronski, and K. Kulakowski, *IEEE. Trans. Magn.*, **2006**, *42*, 3889-3892.
10. H. Chiriac, T.-A. Óvári, and Gh. Pop, *Phys. Rev. B*, **1995**, *52*, 10104-10113.

INFLUENCE OF THE GADOLINIUM IONS ON THE STRUCTURAL AND CRYSTALLIZATION PROPERTIES OF THE GADOLINIUM-TELLURATE-VANADATE GLASS CERAMICS

EUGEN CULEA[a], SIMONA RADA

ABSTRACT. The present study provides information concerning the devitrification behavior of the $xGd_2O_3 \cdot (100-x)[7TeO_2 \cdot 3V_2O_5]$ vitreous system with $0 \leq x \leq 60$mol% in which the $Te_2V_2O_9$ and $GdVO_4$ crystalline phases occur.

The presence of multiple cations (gadolinium, tellurium) in the glasses to attract the $[VO_4]$ structural units for charge compensation yield a competition between these cations showing the drastic reduction of the characteristic features corresponding to the $[VO_4]$ units (bandwidth, position and intensity). After the heat treatment applied at 400^0C for 48h, two crystalline phases appear, namely the $Te_2V_2O_9$ and $GdVO_4$. The $Te_2V_2O_9$ crystalline phase is characteristic of the host glass ceramic. The strong affinity of the Gd^{+3} ions towards the vanadium units containing non-bridging oxygen is responsible for the disappearance of the $Te_2V_2O_9$ crystalline phase. The addition of higher Gd_2O_3 contents produce the gradual depolymerization of the vanadate chains and the formation of the $GdVO_4$ crystalline phase.

We propose a possible structural model of building blocks for the formation of the continuous random $7TeO_2 \cdot 3V_2O_5$ network glass based on DFT calculations.

Keywords: *Gadolinium-tellurate-vanadate glass ceramics, FTIR spectroscopy, DFT calculations.*

INTRODUCTION

Tellurium dioxide is a conditional glass former. It is very difficult to form pure vitreous TeO_2 and it has been suggested that this is due to the lone pair of electrons in one of the equatorial positions of the $[TeO_4]$ polyhedron [1]. The structure and the properties of the oxide glasses are dependent strongly on the nature and concentration of the constituent oxides. In normal glass systems, the modifier atoms cause the break of the network. In tellurate glasses, the modifier atoms cause the modification of the basic structural units such as $[TeO_4]$ trigonal bipyramidal and $[TeO_3]$ trigonal pyramidal units with the equatorial position occupied by a lone pair of electrons.

A lone pair of electrons occupies one equatorial site of the Te sp^3d hybrid orbitals in the $[TeO_4]$ structural unit and also the apex of the sp^3 hybrid orbitals in the $[TeO_3]$ structural unit. The axial Te-O bonds of the $[TeO_4]$ structural units are

[a] *Department of Physics, Technical University of Cluj-Napoca, 400641 Cluj-Napoca, Romania, eugen.culea@phys.utcluj.ro*

longer than the equatorials bonds. Several studies of tellurate glasses [1] give some indications for additional O sites at larger distances than these typical Te-O bonds which are also known to from crystal structures [2, 3]. When network modifier oxides are added, the broke of Te-O-Te network bridges is accompanied by the formation of non-bridging oxygen sites. The effect appears reduced for tellurite glasses modified by the conditional glass formers V_2O_5 [4] and WO_3 [5].

Although the existence of binary and ternary V_2O_5 glasses is well established and the structure of vanadate glasses remains a subject of interest because there is no clear picture as to the exact nature of the oxygen polyhedra surrounding the vanadium atoms or the role played by the other glass components.

On the other hand, rare earth ions doped glasses have been widely used for many purposes such as laser materials and on line optical amplificators [6-8]. Whereas the local structure of gadolinium ions sites seems to be similar in different types of glasses, the correlation between the doping level and clustering depends on the glass type and composition [9, 10].

In brief, the structure of TeO_2-V_2O_5 glasses is still subject to discussion from at least two motives: (i) adding to the network modifier oxides occur the broke of the Te-O-Te network bridges accompanied by the formation of non-bridging oxygen sites, and (ii) there is no clear picture of the exact nature of the oxygen polyhedra surrounding the vanadium atoms or of the role played by the other glass components. Moreover, the structure of the vanadate glasses can be related to the nature of the network formers as well as of the network modifiers.

The presence of some rare earth ions in the host vitreous matrix may modify the glass structure. Thus, our target in the present investigation is to explore changes in vanadate-tellurate glasses doped with gadolinium ions. A glass ceramics system of the $xGd_2O_3 \cdot (100\text{-}x)[7TeO_2 \cdot 3V_2O_5]$ composition where $0 \leq x \leq 60$mol% has been studied using FTIR spectroscopy and DFT calculations. The correlation between structure and the properties is also presented.

RESULTS AND DISCUSSION

XRD diffraction

After heat treatment some structural changes were observed and the $Te_2V_2O_9$ crystalline phase appeared in the structure of the samples with up to 15%molGd_2O_3 (Fig.1). Note that since in the samples with x<20%mol Gd_2O_3 the $Te_2V_2O_9$ crystalline phase was observed, in the samples with higher contents of Gd_2O_3 ($x \geq 60\%$) the $GdVO_4$ crystalline phase was found.

FTIR spectroscopy

The FTIR spectra for the heat treated samples exhibit changes, namely those illustrated by the narrowing of the previous bands and the appearance of some new bands in the spectra (Fig. 2). A simple inspection of the observed FTIR bands for the

investigated ternary glasses with various x values up to 60mol% permit their assignement to the Te-O linkage vibration in [TeO_4] and [TeO_3] structural units [11-13] and to the V-O linkage vibration in [VO_5] [13-16] and [VO_4] structural units [17-19]. In the FTIR spectrum of the glass ceramics appear strong changes for a content of gadolinium oxide within the $0 \leq x \leq 20$ and $50 \leq x \leq 60$mol% Gd_2O_3 ranges due to the apparition of the $Te_2V_2O_9$ and $GdVO_4$ crystalline phases, in agreement to the X ray data.

The examination of the FTIR spectra of the $xGd_2O_3(100\text{-}x)[7TeO_2 \cdot 3V_2O_5]$ glass ceramics shows the following modify of the characteristic IR bands:

i) The prominent band centered at about 460cm^{-1} splits into four components located at 420, 446, 490 and 525cm^{-1} for x between 0 and 15mol%Gd_2O_3. After that, the intensity of this band increases with the increase of the Gd_2O_3 content up to 60mol%. All these bands are assigned to the bending mode of Te-O-Te or O-Te-O linkages [9-13];

ii) The intensity of the band centered at about 650cm^{-1} increase with the increase of the Gd_2O_3 content and shift to 670cm^{-1}. For $0 \leq x \leq 20$mol% this band splits into some components. This band is attributed to the stretching vibrations in [TeO_4] structural units;

iii) The intensity of the band centered at ~780cm^{-1} increases slowly with the increase of the gadolinium ions content up to 60mol%, while for small gadolinium ions contents ($0 \leq x \leq 15$mol%) the band splits into two components located at ~785 and ~820cm^{-1}. All these bands are corresponded to the stretching vibrations in [TeO_3] structural units [9-13];

iv) A new band appears at about 870cm^{-1} into glass ceramic with 60mol%Gd_2O_3, which are attributed to the presence of vibration of the V-O bonds of orthovanadate units [9-13].

v) The band centered at about 970cm^{-1} splits into two components located at ~940 and 953cm^{-1} at a small content of Gd_2O_3 ($0 \leq x \leq 15$mol%). These intense bands are assigned to the stretching vibrations of the terminal V=O bonds and the bands at ~785 and 815cm^{-1} are due to the stretching vibrations of the V-O-V bonds [29]. The bands located at about 660, 530 and 490cm^{-1} are probably ascribed to the vibrations of V-O, Te-O or Te-O-V bonds. After that, by increase of rare earth content from 20 to 60%, this band shifts to higher wavenumber at ~985cm^{-1} and finally becomes the dominant feature of the spectrum. These bands are due to the V-O stretching vibrations in [VO_4] structural units.

The structural changes observed by increasing the Gd_2O_3 content in the $xGd_2O_3(100\text{-}x)[7TeO_2 \cdot 3V_2O_5]$ glass ceramics and evidenced by the XRD and FTIR investigation suggest that the gadolinium ions play a network modifier role.

Thus, drastic structural modification occurs with the apparition of the $Te_2V_2O_9$ crystalline phase for x between 0 and 20mol%Gd_2O_3. The content of $Te_2V_2O_9$ crystalline phase decreases drastically up to its disappearance with the increase of gadolinium oxide concentration.

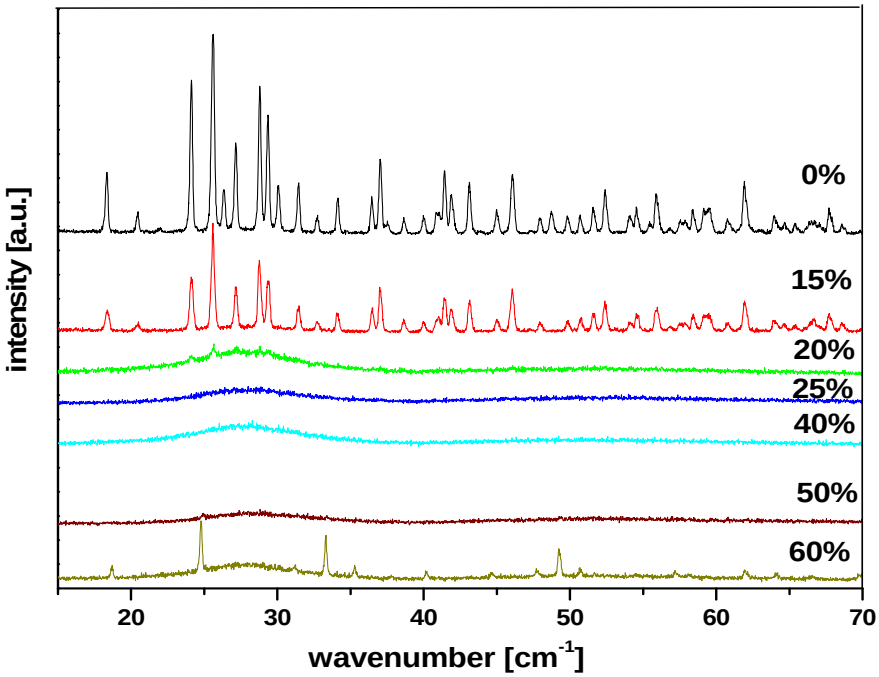

Fig. 1. X-ray diffraction patterns for $xGd_2O_3(100-x)[7TeO_2 \cdot 3V_2O_5]$ glass ceramics samples with x=0-60% Gd_2O_3.

The presence of multiple oxides in the glasses increases the tendency of the network formers to attract oxygen ions due to a competition between the cations themselves. The unit that has higher electronegativity value picks up oxygen ion and gets modifier. For Gd_2O_3 content up to 20mol%, the gadolinium ions are firstly inserted in the trivalent state and they can be considered as modifiers because they have a strong affinity towards these groups containing non-bridging oxygens, which are negative-charged. Presence of multiple cations, gadolinium and tellurium in the glass ceramic to attract oxygen ions yield a competition between these cations.

For x>20mol%Gd_2O_3, gadolinium ions will participate in the network as modifiers for $[VO_4]$ structural units from the $Te_2V_2O_9$ crystalline phase yielding its disappearance. This may be attributed to the electrostatic field of the strongly polarizing Gd^{+3} ions. The increase of Gd^{+3} content leads the formation of $[VO_4]$ orthovanadate units, and consequently causes a shift of the bands corresponding to the $[VO_4]$ structural units to lower wavenumber ($870cm^{-1}$). This effect yields the formation of the $GdVO_4$ crystalline phase. Accordingly, the gadolinium oxide plays a particular role on the homogeneity of the glasses and in accommodation of the networks with the excess of oxygen.

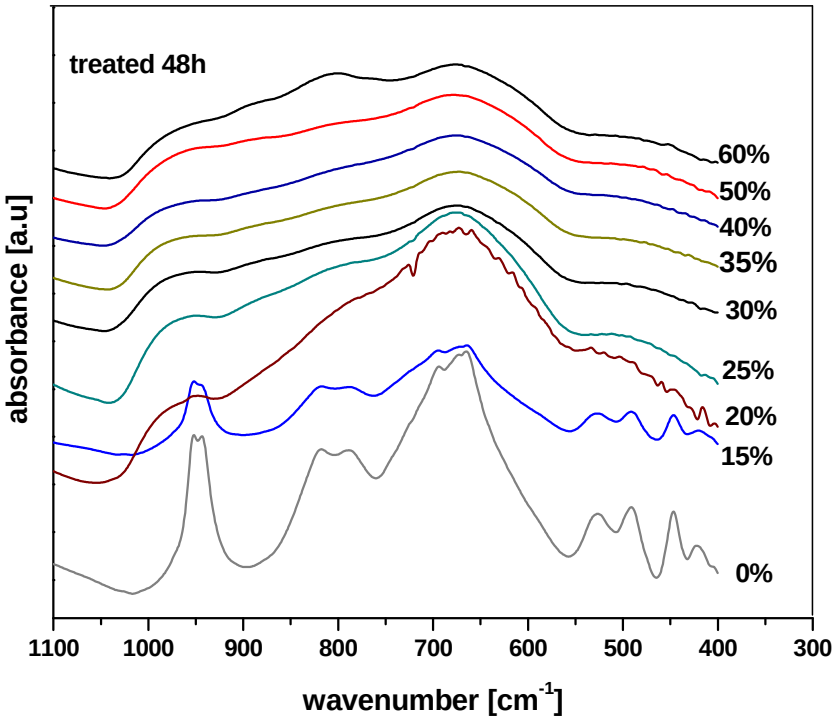

Fig. 2. FT-IR spectra of the $xGd_2O_3 \cdot (100\text{-}x)[7TeO_2 \cdot 3V_2O_5]$ glass ceramics (with x=0-60mole%).

The changes of the IR spectral features produced by devitrification suggest that the competition between cations of gadolinium and tellurium explains the drastic reduction of the characteristic features corresponding to the $[VO_4]$ structural units in bandwidth, position and intensity.

DFT cluster calculations on structure of $7TeO_2 \cdot 3V_2O_5$ glass network

The IR data are used in the present research in order to compute a possible structural model of the $7TeO_2 \cdot 3V_2O_5$ glass network. Similar methodology has previously been reported to study other glasses [13, 17-21]. The structural model consists of a $7TeO_2$-$3V_2O_5$ mixture.

The simulation method used by us is able to provide a realistic description of the vanadate-tellurate network structure, which consists of three types of structural units: (i) $[TeO_4]$ trigonal bipyramidal units (in which all the oxygen atoms are involved in bridge bonds), (ii) $[TeO_3]$ units (in which the oxygen involved in the double bond Te=O is nonbridging, and the other two oxygen are involved in bridging bonds) [39, 40] and (iii) $[VO_5]$ square pyramidal units (with terminal oxygen in the

apical position and four bridging oxygen atoms linking to four tellurium atoms [41]) and (iv) [VO_4] tetrahedral units (in which all the oxygen atoms are involved in bridge bonds).

Symmetric stretching vibrations of those bridges give rise to a large and intense band situated near ~430cm^{-1}, whereas the asymmetric stretching have weak intensities and are located at about 700cm^{-1}. The inter-chain linkages are realized via standard Te-O-Te bridges, which are formed by the so-called axial bonds having 2.10-2.15Å and equatorial bonds having 1.85-1.90Å. These linkages are similar to the Te-O-Te linkages in the α- and β-TeO_2 lattice as well as in many tellurate structures, whose symmetric and asymmetric vibrations are situated near 480 si 660cm^{-1}, respectively.

The model of clusters that can form the continuous random network of the $7TeO_2 \cdot 3V_2O_5$ glass, is shown in Fig. 3. There are three types of Te atoms in our proposed model (Fig. 3), namely:

i) Tellurium is in tetragonal coordination. Three bonds have short interatomic distances (1.97-2.09Å) and one has longer interatomic distance (2.32 or 2.50Å). This Te-O bond is longer than the Te-O covalent bond (2.15Å) but significantly shorter than the sum of the van de Waals radii (3.58Å). The mean Te-O distances 2.12-2.16Å are comparable to that the Te-O covalent bond distance (2.15Å) and the tellurium atom are strongly bonded to four oxygen atoms giving to a trigonal bipyramide arrangement. This geometry of Te^{+4} ions show an asymmetric coordination due to the active lone-pair electrons.

ii) Tellurium is in tetragonal coordination. The Te-O bond has very short interatomic distance (1.66Å), two have normal interatomic distances (1.94-1.96Å) and one has longer interatomic distance (3.44Å). The mean Te-O distance 2.25Å is easy longer than Te-O covalent bond but it is significantly shorter than the sum of the van de Waals radius.

iii) Tellurium site is coordinated with three O atoms. All Te-O distances are comparable the Te-O bond distances of the [TeO_3] structural units (1.81-2.03Å).

The asymmetrical unit of the proposed model in the Fig. 3 shows two enviroments for the vanadium atoms. The vanadium (V) site shows a distorted [VO5] square pyramidal geometry, with terminal oxygen in the apical position (1.77Å) and four bridging oxygen atoms (the mean V-O distance is 1.92Å) linking to three tellurium atoms and a vanadium atom. The vanadium (IV) sites are tetracoordinated with oxygen atoms and exhibit [VO4] folded square geometry, only with some differences between bond lengths and bond angles. The V-O bond lengths vary from 1.65 to 2.18 Å. The O-V-O angles are in the range of 32.4 to 142.2^0.

The optimized geometry was followed by second derivate calculations using the same method and basis set to verify the structure found as true minime. The evolution of vibrational spectrum of the proposed model is important for understanding broadening-effect of the glasses from experimental FTIR spectrum. The simulated IR spectra of proposed model together with experimental FTIR spectrum are shown in Fig. 4. Comparing the theoretical and experimental IR spectra data, we conclude that the proposed model in Fig. 3 predicts very well the vibrational modes of the experimental FTIR spectrum.

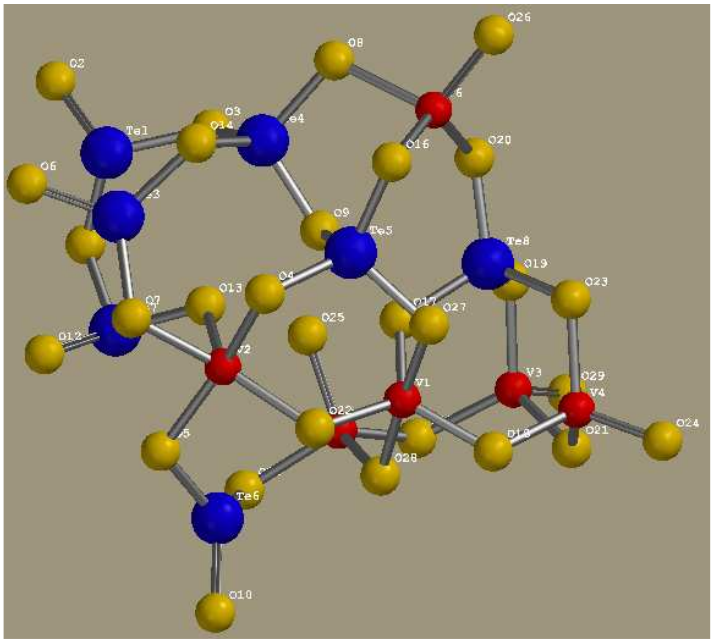

Fig. 3. Optimized structure of the proposed model for binary $7TeO_2 \cdot 3V_2O_5$ glassy network.

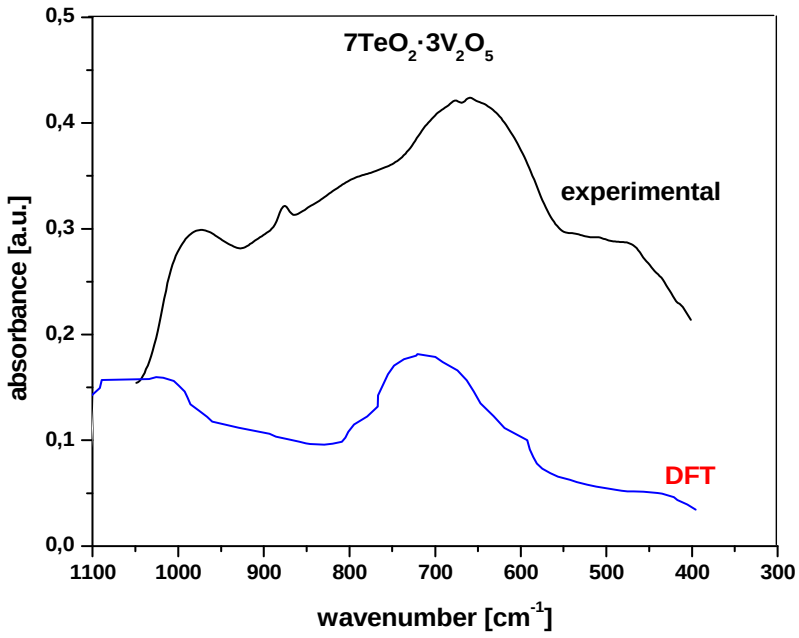

Fig. 4. Experimental and simulated IR spectra of the proposed model for the binary $7TeO_2 \cdot 3V_2O_5$ glassy network.

Our results show that the Te-O, and V-O stretching vibration region of proposed model is similar to the same region of the glasses. The vibrational modes corresponding to the $[VO_4]$, $[VO_5]$, $[TeO_3]$ and $[TeO_4]$ structural units are significantly broadened in the disordered phase. Comparing the theoretical and experimental data, we conclude that the performance of the method/basis sets used on the prediction of the structural data and vibrational modes is good.

CONCLUSIONS

Glass ceramics of the $xGd_2O_3\cdot(100\text{-}x)[7TeO_2\cdot 3V_2O_5]$ system (where $0\leq x\leq 60$mol%) were obtained and investigated by X-ray diffraction and infrared spectroscopy. The X-ray diffraction patterns show the presence of the $Te_2V_2O_9$ and $GdVO_4$ crystalline phases. The $Te_2V_2O_9$ crystalline phase is characteristic of the host glass ceramic. The strong affinity of the Gd^{+3} ions towards the $[VO_4]$ vanadate units containing non-bridging oxygen is responsible for the disappearance of $Te_2V_2O_9$ crystalline phase and the formation of the $GdVO_4$ crystalline phase.

We used the FTIR spectroscopic data in order to compute a possible model of the glass matrix. The structural and vibrational properties of the proposed model of binary $7TeO_2\cdot 3V_2O_5$ glass network are determined by DFT calculations.

DFT calculations show that tellurium atoms occupy three different sites and there are two environments of the vanadium atoms in the proposed model. Comparing the theoretical and experimental data, we conclude that the performance of the method/ basis sets used on the prediction of the structural data and vibrational modes is good.

EXPERIMENTAL SECTION

Glasses with the $xGd_2O_3(100\text{-}x)[7TeO_2\cdot 3V_2O_5]$ composition where x=0, 15, 20, 25, 30, 35, 40 , 50, 60mol% were prepared by mixing appropriate amounts of tellurium dioxide, vanadium pentaoxide and gadolinium trioxide. The mixtures were melted at 850^0C for about 10 minutes in corundum crucibles in an electric furnace and after that were rapidly quenched at room temperature. Then, the glassy samples were subject of a heat treatment applied at 400^0C for 48h.

The samples were analyzed by means of X-ray diffraction using a XRD-6000 Shimadzu diffractometer, with a monochromator of graphite for the Cu-Kα radiation (λ=1.54Å) at room temperature. The position and intensity of diffraction peaks of the polycrystalline powder $xGd_2O_3(100\text{-}x)[7TeO_2\cdot 3V_2O_5]$ systems are consistent with that of the powder diffraction file (PDF) 170260 and 181330, which indicates that the sample crystalized well.

The structure of the $xGd_2O_3(100\text{-}x)[7TeO_2\cdot 3V_2O_5]$ glasses and glass ceramics was investigated by IR spectroscopy using the KBr pellet technique. The IR spectra were recorded in the 400-1100cm^{-1} range using a JASCO FTIR 6200 FT-IR spectrometer.

The starting structures have been built using the graphical interface of Spartan'04 and preoptimized by molecular mechanics. The geometry optimization of the proposed model structure was carried out using density functional theory (DFT). The DFT computations were performed with B3PW91/CEP-4G/ECP method using Gaussian'03 program package [22]. It should be noticed that only the broken bonds at the model boundary were terminated by hydrogen atoms.

Frequency analysis followed all optimizations in order to establish the nature of the stationary points found, so that all the structures reported in this study are genuine minima on the potential energy surface at this level of theory, without any imaginary frequencies. Accordingly, frequency calculations were performed to ensure that the stationary points were minima and to calculate infrared (IR) spectra.

REFERENCES

1. J. Pisarska, *J. Non-Cryst. Solids*, **2004**, *345&346*, 382-385.
2. H Afifi, S. Marzouk, N. Abd el Aal, *Physica B: Condesed Matter*, **2007**, *390*, 65-70.
3. El-Mallawany R., *Mater. Chem. Phys.*, **2007**, *53*, 93-120.
4. A.K. Varshneya, Fundamentals of Inorganic Glasses, **1994**, Academic Press, San Diego.
5. T.A. Mohameda, I. Shaltout, K.M. Al Yahyaei, *Spectrochimica Acta Part A*, **2006**, *64*, 106-115.
6. R. El-Mallawany, M.D. Abdalla, I.A. Ahmed, *Mater. Chem. Phys.*, **2008**, *109*, 291-296.
7. L.M. Fortes, L.F. Santos, M.C. Goncalves, R.M. Almeida, M. Mattarelli, M. Montagna, A. Chiasera, M. Ferrari, A. Monteil, S. Chaussedent, G. C. Righini, *Optical Materials*, **2007**, *29*, 503-509.
8. R. Rolli, K. Gatterer, M. Wachtler, M. Bettinelli, A. Speghini, D. Ajo *Spectrochimica Acta Part A*, **2001,** *57*, 2009-2017.
9. S. Rada, E. Culea, *J. Molec. Struct.*, **2009**, *929*, 141-148.
10. S. Rada, M. Culea, M. Rada, E. Culea, *J. Mater. Sci.*, **2008**, *43*, 6122-6125.
11. S. Rada, E. Culea, M. Culea, *J. Mater. Sci.*, **2008**, *43*, 6480-6485.
12. S. Rada, M. Culea, E. Culea, *J. Phys. Chem. A*, **2008**, *112(44)*, 11251-11255.
13. J.C. Sabadel, P. Armand, D. Cachau-Herreillat, P. Baldeck, O. Doclot, A. Ibanez, E. Philippot, *J. Solid State Chem.*, **1997**, *132*, 411-419.
14. B. Jeansannetas, S. Blanchandin, P. Thomas, P. Marchet., J.C. Champarnaud-Mesjard, T. Merle-Mejean, B. Frit, V. Nazabal, E. Fargin, G. Le Flem, M.O. Martin, B. Bousquet, L. Canioni, S. Le Boiteux, P. Segonds, L. Sarger, *J. Solid State Chem.*, **1999**, *146*, 329-335.
15. B.L. Shivachev, I.P. Mincov, E.P. Kashchieva, Y.B. Dimitriev, R. Smith, T. Troev,
16. *J. Non-Cryst. Solids*, **2004**, *345&346*, 108-111.

17. S. Rada, M. Culea, M. Rada, P. Pascuta, V. Maties, E. Culea, *J. Molec. Struct.*, **2009,** *937*, 70-74.
18. S. Rada, M. Culea, M. Neumann, E. Culea, *Chem. Phys. Lett.*, **2008,** *460*, 196-199.
19. S. Rada, T. Ristoiu, M. Rada, I. Coroiu, V. Maties, E. Culea, *Mater. Res. Bull.*, **2010**, *45*, 69-73.
20. M. Valant, D. Suvoroy, *J. Amer. Ceram. Soc.*, **2004**, *85*, 355-358.
21. S. Rada, P. Pascuta., M. Bosca, M. Culea, L. Pop, E. Culea, *Vibrat. Spectrosc.*, **2008**, *48*, 255-258.
22. M.J. Frisch, G.W. Trucks, H.B. Schlegel, G.E. Scuseria, M.A. Robb, J.R. Cheeseman, J.A. Montgomery, Jr., T. Vreven, K.N. Kudin, J.C. Burant, J.M. Millam, S.S. Iyengar, J. Tomasi, V. Barone, B. Mennucci, M. Cossi, G. Scalmani, N. Rega, G.A. Petersson, H. Nakatsuji, M. Hada, M. Ehara, K. Toyota, R. Fukuda, J. Hasegawa, M. Ishida, T. Nakajima, Y. Honda, O. Kitao, H. Nakai, M. Klene, X. Li, J.E. Knox, H.P. Hratchian, J.B. Cross, C. Adamo, J. Jaramillo, R. Gomperts, R.E. Stratmann, O. Yazyev, A.J. Austin, R. Cammi, C. Pomelli, J.W. Ochterski, P.Y. Ayala, K. Morokuma, G.A. Voth, P. Salvador, J.J. Dannenberg, V.G. Zakrzewski, S. Dapprich, A.D. Daniels, M.C. Strain, O. Farkas, D.K. Malick, A.D. Rabuck, K. Raghavachari, J.B. Foresman, J.V. Ortiz, Q. Cui, A.G. Baboul, S. Clifford, J. Cioslowski, B.B. Stefanov, G. Liu, A. Liashenko, P. Piskorz, I. Komaromi, R.L. Martin, D.J. Fox, T. Keith, M.A. Al-Laham, C.Y. Peng, A. Nanayakkara, M. Challacombe, P.M.W. Gill, B. Johnson, W. Chen, M.W. Wong, C. Gonzalez, and J.A. Pople, Gaussian 03, Revision A.1, Gaussian, Inc., Pittsburgh PA, **2003**.

STUDIA UNIVERSITATIS BABEŞ-BOLYAI, PHYSICA, LV, 1, 2010

GLASSY MAGNETIC BEHAVIOR IN THE PEROVSKITE TRANSITION METAL OXIDES $Pr_{0.7}Ca_{0.3}TMO_3$ (TM = Mn, Co)

IOSIF G. DEAC[a]*, ADRIAN V. VLĂDESCU

ABSTRACT. Polycrystalline perovskites $Pr_{0.7}Ca_{0.3}MnO_3$ and $Pr_{0.7}Ca_{0.3}CoO_3$ have been investigated by magnetization and ac susceptibility measurements. The magnetic measurements data indicate that the samples have, at low temperatures, similar properties to the frustrated magnets. The origin of this glassy behavior, in these phase separated perovskites, was found to be different in the manganite and cobaltite samples. While in $Pr_{0.7}Ca_{0.3}MnO_3$ the phase separation consists in ferromagnetic clusters embedded in an antiferromagnetic matrix, in $Pr_{0.7}Ca_{0.3}CoO_3$ the ferromagnetic clusters are surrounded by a paramagnetic (or spin glasslike) matrix.

Keywords: *manganites, cobaltites, phase separation, spin glass*

INTRODUCTION

The transition metal oxides display remarkable magnetic and transport properties of interest for technical applications. In manganites with perovskite structure, the mixed valence Mn^{3+}/Mn^{4+} is absolutely necessary for the appearance of these magnetotransport properties. The spin states of the manganese ions do not depend on temperature because the Hund energy is higher than the crystal field energy. Both double and superexchange interactions are present in these compounds. The competition of different kinds of interactions leads to a highly inhomogeneous ground state due to the coexistence of a ferromagnetic (FM) metallic phase and an antiferromagnetic (AFM) charge-ordered (CO) phase and this phase separation governs many of the observed physical properties of these materials. The phase separation tendencies suggest that there should be glassy behavior associated with the frustration of the different interactions. For example, irreversibilities in the magnetization, frequency dependent peaks in the real or imaginary parts of the ac susceptibility, negative sharp minimum in the real part of the nonlinear ac susceptibility, and aging and memory effects on the resistivity and magnetization were observed in manganites [2, 3]. These phenomena are rather similar in appearance to those observed in classical spin glasses [4].

[a] *Universitatea Babeş-Bolyai, Facultatea de Fizică, Str. Kogălniceanu, Nr. 1, RO-400084 Cluj-Napoca, Romania, * ideac@phys.ubbcluj.ro*

Doped cobaltite perovskites $Ln_{1-x}A_xCoO_3$, have as a unique feature among some other perovskites the change of the Co ions spin-state [5]. In these compounds there are various spin states for trivalent (low-spin LS: $t^6_{2g}e^0_g$; intermediate-spin IS: $t^5_{2g}e^1_g$; high-spin HS: $t^4_{2g}e^2_g$) and tetravalent cobalt ions (LS: $t^5_{2g}e^0_g$; IS: $t^4_{2g}e^1_g$; HS: $t^3_{2g}e^2_g$). The spin-states of undoped $LnCoO_3$ exhibit a gradual crossover with increasing temperature, from the low-spin (LS) state ($t^6_{2g}e^0_g$) to the intermediate-spin (IS) state ($t^5_{2g}e^1_g$) or to the high-spin (HS) state($t^4_{2g}e^2_g$). Upon doping A^{2+} ions into $LnCoO_3$, some of trivalent Co ions become tetravalent. The Co ion spin states are determined by the two competing energies, namely, crystal field and Hund coupling, respectively [5]. The hole-doped cobaltites, such as $La_{1-x}Sr_xCoO_3$, have been proved to exhibit a particularly clear picture of phase separation [5]. Through Sr doping, the material segregates into Sr-rich, ferromagnetic (FM) metal regions and La-rich, non-FM insulator matrix. If phase separation scenario applies to cobaltites a magnetic glassy behavior is also expected for these compounds.

In this paper we analyze the magnetic glassy behavior in some phase separated manganites ($PrCa_{0.7}Mn_{0.3}O_3$) and cobaltites ($Pr_{0.7}Ca_{0.3}CoO_3$). We found that the phase separation scenario in cobaltites is different from that in manganites. While in the manganite $PrCa_{0.7}Mn_{0.3}O_3$ this phase consists in FM clusters embedded in an AF matrix, in the cobaltite Pr0.7Ca0.3CoO3

EXPERIMENTAL

High-quality polycrystalline samples with nominal composition $Pr_{0.7}Ca_{0.3}MnO_3$ and $Pr_{0.7}Ca_{0.3}CoO_3$, compounds were prepared by conventional solid state reactions at high temperatures. The powder x-ray diffraction patterns were recorded by using a Bruker D8 Advance AXS diffractometer with Cu Kα radiation. Data were refined by the Rietveld method using the program FULLPROF. The samples were found to be single perovskite phase of orthorhombic *Pbnm* symmetry. A cryogen free VSM magnetometer (Cryogenic Ltd.) was used for magnetization and ac susceptibility measurements in the temperature range 5 - 300 K and up to 12 T. The amplitude of the ac field was 1 Oe and the ac susceptibility was measured in the frequency range from 10 to 10000 Hz. Zero-field-cooled (ZFC) and field-cooled (FC) magnetization was measured at various applied fields, from 0.005 to 1 T.

RESULTS AND DISCUSSION

Magnetization measurements show that $Pr_{0.7}Ca_{0.3}MnO_3$ has a charge ordering transition (CO) in the range 200–250 K, followed by antiferromagnetic and ferromagnetic transitions at about 120 and 105 K, respectively [3]. Spin glass-like features were seen in magnetic measurements on this sample, at low temperatures. As described in Figure 1, the temperature dependence of magnetization has different behaviors as it was measured in ZFC and FC regimes. The real part of the complex magnetic susceptibility $\chi'(T)$ shows a frequency dependent cusp at about $T_f \sim 82$ K, as

depicted in the inset of Figure 1. The peaks shift to lower temperatures at lower frequencies. We found that T_f is linear in the logarithm of the frequency with a normalized slope $p = \Delta T_f / T_f \Delta \log_{10} \omega$ and $p = 0.0022$. This value is much lower than the typical values (between 0.0045 and 0.28) of canonical spin glasses [3,4]. The data could be fitted to a Vogel-Fulcher law $\omega = \omega_0 e^{-E_a/k_B(T_f - T_0)}$ which presumes correlations between spin clusters [4]. In order to check the presence of an AFM phase in the ground state, we measured the magnetization *M(H)*, in high magnetic fields. As depicted in Figure 2, the methamagnetic transition seen in low temperature *M(H)* curves, indicate the coexistence of the FM and AFM phases. In other words, the AFM component is turned to be FM starting from a high value of the magnetic field that finally leads to the saturation of magnetization. In the frame of a phase separation scenario, the FM clusters grow, below 110 K, inside of an AFM phase, as the temperature decreases.

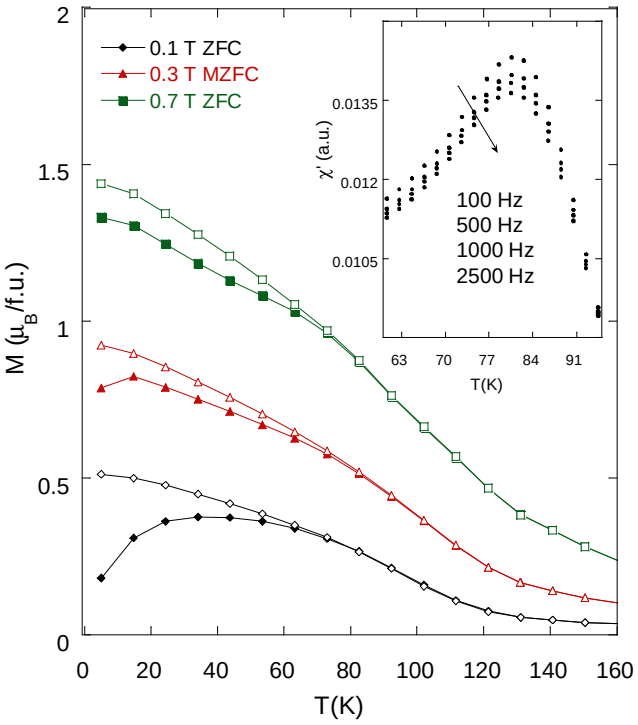

Fig. 1. Field cooled (open symbols) and zero field cooled (closed symbols) magnetizations of $Pr_{0.7}Ca_{0.3}MnO_3$ as a function of temperature. In the inset, $\chi'(T)$ is plotted at selected frequencies.

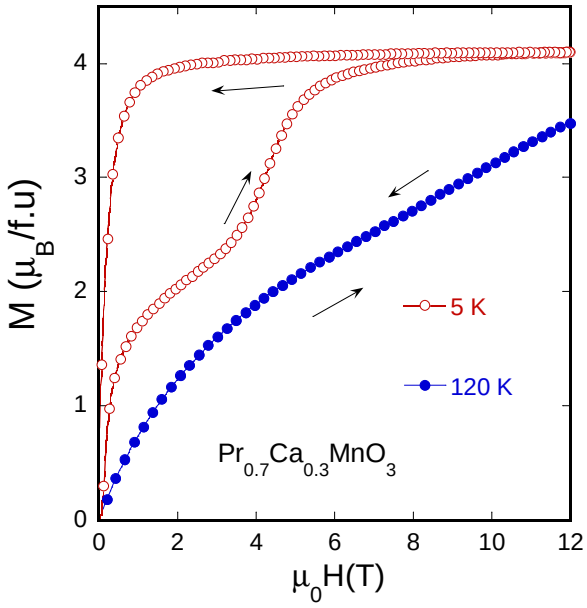

Fig. 2. *M(H)* curves for the sample $Pr_{0.7}Ca_{0.3}MnO_3$ taken at 5 K, and 120 K.

The cobaltite $Pr_{0.7}Ca_{0.3}CoO_3$, shows also the features of glassy behavior, indicating an inhomogeneous magnetic system. The temperature dependence of magnetization has history dependence with a bifurcation between ZFC and FC curves at an irreversibility temperature T_{irr}, as illustrated in Figure 3. The shape of the *M(T)* curve is rather complex, not typical for pure ferromagnets. This suggests the presence of the preformed clusters well above the Curie temperature (estimated to be T_C~ 25 K). The ac susceptibility is again frequency dependent showing sharp maxima, both in the real part χ'(T) and in the imaginary part χ"(*T*). In the inset of Figure 3, χ'(T) is plotted at selected frequencies. Here again, the temperature T_f ~ 16 K corresponding to the peak was found to be linear in the logarithm of the frequency.

T_f's shift to lower temperatures as the frequency decreases. The data could be fitted to a Vogel-Fulcher law, but the fit parameters have unphysically large values. These data suggest that the glassy behavior in this compound is not only the result of the correlations between the spin clusters [6], as in the case of the manganite $Pr_{0.7}Ca_{0.3}MnO_3$.

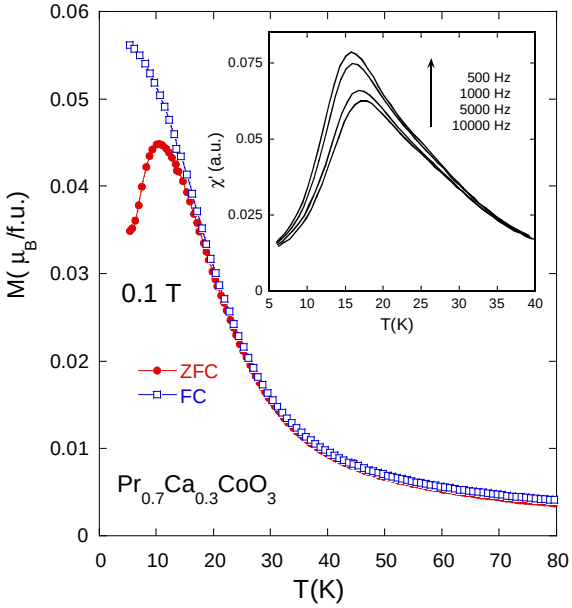

Fig. 3. Field cooled and zero field cooled magnetizations of $Pr_{0.7}Ca_{0.3}CoO_3$ as a function of temperature.

In the inset, χ'(T) is plotted at selected frequencies.

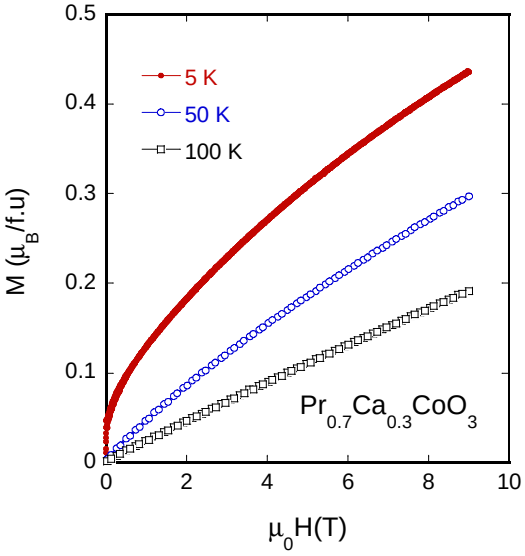

Fig. 4. *M(H)* curves for the sample $Pr_{0.7}Ca_{0.3}CoO_3$ taken at 5 K, 50 K and 100 K.

The *M(H)* curves, depicted in Figure 4, indicate another type of phase separation that is different from the case of the manganite compound. The magnetization increases monotonously with increasing magnetic field and it do not show any sign of saturation up to 9 T and at low temperatures. This behavior suggests the presence of isolated ferromagnetic clusters in a paramagnetic (or spin glass-like) matrix [4,6].

CONCLUSIONS

The origin of the magnetic glassy behavior in phase separated perovskites $Pr_{0.7}Ca_{0.3}MnO_3$ and $Pr_{0.7}Ca_{0.3}CoO_3$ was analyzed by using magnetic measurements. The data suggest that the pictures of phase separation in the two systems are different. While in $Pr_{0.7}Ca_{0.3}MnO_3$ the phase separation consists in ferromagnetic clusters embedded in an antiferromagnetic matrix, in $Pr_{0.7}Ca_{0.3}CoO_3$ the ferromagnetic clusters are surrounded by a paramagnetic (or spin glasslike) matrix.

ACKNOWLEDGMENTS

This work was supported by the grant IDEI 2590 of CNCSIS, Romania.

REFERENCES

1. J.M.D. Coey, M.Viret, and S.von Molnar, *Adv.Phys.* **1999,** *48*, 167-293.
2. R.S. Freitas, L. Ghivelder, F. Damay, F. Dias, and L.F. Cohen, *Phys. Rev. B* **2001,** *64*, 144404-1-6.
3. I.G. Deac, J. F. Mitchell and P. Schiffer, *Phys. Rev. B* **2001,** *63*, 172408-1-5
4. J.A. Mydosh, “Spin Glasses: An Experimental Introduction”, Taylor& Francis, London, **1993**.
5. M. A. Señarís-Rodríguez, J.B. Goodenough, *J. Solid State Chem.* **1995**, *118*, 323-336.
6. Y.K. Tang, Y. Sun, and Z.H Cheng, *Physical Review B*, **2006,** *73*, 012409-1-4.

MAGNETIC PROPERTIES OF 3D TRANSITION METALS-(Fe, Co, Ni) ALLOYS FROM *AB INITIO* CALCULATIONS

ANDREI ILIES, ADRIAN NEDELCU, VASILE CRISAN[a]

ABSTRACT. Electronic properties of 3d transition metal-(Fe wi, Co, Ni) with both bcc and fcc crystalline structures are analyzed based on *ab initio* band structure calculations. The effect of chemical ordering as in MnNi and FeNi systems are investigated in the framework of disordered local moment model and using arguments based on charge transfer, exchange splitting and hybridization arguments.

Keywords: *transition metal, band calculation, DFT, KKR*

I. Introduction

An enormous amount of experimental and theoretical investigations have been carried out to have a proper understanding of the nature of magnetism in solids [1, 2]. Transition metals itself Mn, Fe, Co and Ni have drawn considerable attention due to the interesting magnetic properties as pure elements or alloying with other 3d transition metals. The experimental investigations have provided a variety of information about the magnetic properties of these systems *e. g.:* variation of magnetization with band filling [3, 4] moment distribution in alloys at low [5 –9] as well as at finite temperatures, local environmental effects on magnetic properties [14, 17] chemical ordering and short-order effects [19] spatial distribution and thermal variation of hyperfine fields [18, 24], magnetic layers [25], concentration dependence of high field susceptibility [26], low temperature specific heat [26] and magnetic phase stability, leading eventually to magnetic phase diagrams [27, 28]. The transition metal series as the number of valence electrons ***N*** increases from **3** to 11 was explained quantitatively by the total one-electron band structure energy (***N*** is the number of d- and outer s-electrons per atom) combined with some hard-core contribution even in 1969. The structure trend change from hcp to bcc and for the late elementsof 3d serie through hcp again to fcc.

The total energy of a transition metal [29, 30] can be written where ε_{abs} is the absolute position of the d electron resonance level, E_{bs} is the total one electron band structure measured relative to the d-electron level - obtained from summing over all occupied energy levels, E_{es} is the electrostatic potential energy of their lattice taking into account the self energy and the double counting, E_{core} is the

[a] *Universitatea Babes –Bolyai,Facultatea de Fizica, Str. Kogălniceanu, Nr. 1, RO-400084 Cluj-Napoca, Romania, vcrisan@phys.ubbcluj.ro*

contribution of the ion core to the total energy, E_{xc} contains all the exchange and correlation effects not included in the resonance parameters, which in the nonmagnetic transition metals are of secondary importance.

$$E_{total}=N\varepsilon_{abs}+E_{bs}+E_{es}+E_{core}+E_{xc} \quad (1)$$

The terms of the total energy (1) can be evaluated by using an combination of the tight binding and nearly free electron approximations [29, 30]. E_{bs} will be determined by the tight binding overlap parameters and by hybridization elements all of which depending on the resonance parameters Γ and ε_{abs} which defined the resonance scattering of the l=2 component of a plane wave from the atomic potential, (Γ is the width of this resonance)

Augmented plane wave (APW), [31] and KKR [32, 33] schemes have been applied also successfully to the transition metals, but the eigenvalues take a long time to be calculated because the matrix elements themselves are dependent on the energy.

The interpolation schemes [34-37] were motivated primarily by a desire to remove this energy dependence and this was achieved by writing the secular equation for the eigenvalues *E* as follows

$$\det(\bar{O}-El) = 0 \quad (2)$$

where I is the unit matrix and $\bar{O}$, is an energy-independent model Hamiltonian of the hybrid nearly-free-electron tight-binding form; that is

$$\overline{O}=\begin{pmatrix} C & H \\ H^{+} & R \end{pmatrix}$$

where ***C*** represents the conduction block written in the NFE pseudopotential formalism, R represents the resonance block written in the tight-binding form between the localized resonant states (i. e. d states for the transition metals), and the block H represents the hybridization of the localized states with the plane waves. H^{+} is the hermitian conjugate of H. The good fitting to previously calculated first-principle energy levels achieved by these interpolation schemes numerically verified that *the band structure of the transition metals could be described quantitatively by the overlapping and hybridization of the conduction s-electron band with a tight-binding d-electron band*. In addition, not only was the model Hamiltonian written in terms of such physical parameters as the tight-binding overlap integrals, but it also yielded a convenient representation of the wave functions [35] and hibridisation parameters [37].

The band theory has achieved a considerable progress by density functional theory (DFT), [38] so that it is possible to calculate *ab initio* the band structure of magnetic alloys with sufficient accuracy to discuss their magnetism, chemical and spin ordering within the limit of the one-electron model.

In DFT the total energy is functional of the particle density n(r):

$$E_{tot} = \int v(\vec{r})n(\vec{r})d\vec{r} + T[n] + E_H[n] + E_{xc}[n] \quad (4)$$

where T[n] is the kinetic energy of the interacting particles sistem $v(\vec{r})$ external potential and $E_{xc}[n]$ the exchange-correlation energy. The exchange and correlation computed in the local density approximation (LDA) reduces the many-body quantum-mechanical problem to the solution of a set of coupled one-electron equations with periodic boundary conditions. Accurate determinations of the total energy (4) as a function of volume yeld binding curves which determine the ground state of a system. The system is in equilibrium at zero pressure only at volumes corresponding to the minima of the energy. Thus the effect of the external pressure P is simulated by forcing the system to have a given volume.

The spin-polarized form of LDA, LSDA allows the extension of electronic structure calculations, including magnetic moments, to the magnetic materials [39, 40]. Such calculations involve the simultaneous determination of both the total energy and the magnetic moment. In practical *ab inito* calculations we deal always with systems that are constrained in one or another way. Usually we force a system to have some specific crystallographic structure and lattice parameters, or in spin-polarized calculations to be nonmagnetic, ferromagnetic or antiferromagnetic by suitable manipulation of charge and state density. By introducing various forms of an external potential [41] one can force the system to have a predetermined value of magnetic moment (method called Fix-Spin-Moment, FSM). The total energy of a system is determined with a fixed volume per atom, V, and a fixed magnetic moment per atom, M. In this case the total energy functions determined in a parameter space of M and V, resulting in a binding surface. The equilibrium corresponds to M and V loci where the pressure $P = -(\partial E/\partial V)_M$ and an external applied magnetic field $H = (\partial E / \partial M)_V$ are both zero. Other points on the binding surface correspond to total energies at finite applied pressure or magnetic field. Thus, forcing the magnetic moment to have a given, nonequilibrium value simulates an applied field in the same way that forcing the system to have a given volume simulates an applied pressure. Many properties depend on the total energy of a system as equilibrium lattice constants, bulk moduli, elastic constants, phase transitions, bonding, and more complex property as INVAR[42]. It was shown [2, 58] that the magnetovolume instabilities in 3d elements, alloys and compounds are quite common, but for Invar alloys the energy difference, ΔE, between the high-spin (HS), high volume phase and low-spin (LS), low volume phase is very small.

II. 3d transition metal elements

The magnetic phases of fcc and bcc forms of Fe, Co and Ni were studied by total energy calculations in moment-volume parameter space obtained from energy-band calculations[43]. The results show that bcc Co is ferromagnetic, fcc

Co either nonmagnetic (LS) or ferromagnetic (HS) an there is a range of volumes where the two phases coexist. For Fe, the bcc form exhibits a stable ferromagnetic phase, but the fcc form can exist in any of three phases: nonmagnetic, low-spin and high-spin states-all of which can coexist in a limited volume range. For Ni the fcc form exhibits a stable ferromagnetic phase, but the bcc form can exist in both nonmagnetic and ferromagnetic phases.

The magnetic moment, in a very simple picture, depends weakly on the crystal structure, and decreases almost linearly with an increasing number of electrons. As a matter of fact, this kind of trend is displayed already for the free atoms -if the orbital moment is assumed to be quenched. This is a clear illustration of the fact that the magnetic moment of 3*d* transition-metal alloys is formed by quite localized *d*-electron states with a bandwidth of 3–4 eV. This picture, of course, breaks down when one considers the earlier transition-metals and is definitely more complicated.

The localized electron picture has to be substituted by an itinerant model where the existence of magnetism is related to whether the Stoner criterion is fulfilled or not

$$IN(E_F)>1$$

where N (E_F) is the alloy density of states (DOS) at the Fermi level (E_F) in the paramagnetic phase, while I denotes the so-called Stoner parameter- an intra-atomic quantity known to depend only little on crystal environment. The Stoner criterion states that ferromagnetism appears when the gain in exchange energy is larger than the loss in kinetic energy. Therefore, there is always a competition between FM and paramagnetic solutions, and magnetic properties are determined by the state which has lowest energy.

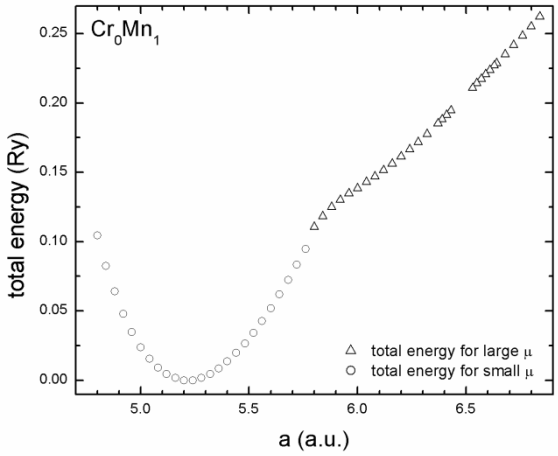

Fig. 1. Total energy/f. u. for fcc Mn.

For fcc Mn the total energy calculations is shown in Figure 1 and the magnetovolume effect in Figure 2. We have obtained a FM high-spin phase (HS) and a low spin state (LS). No coexistence of the phases was found.

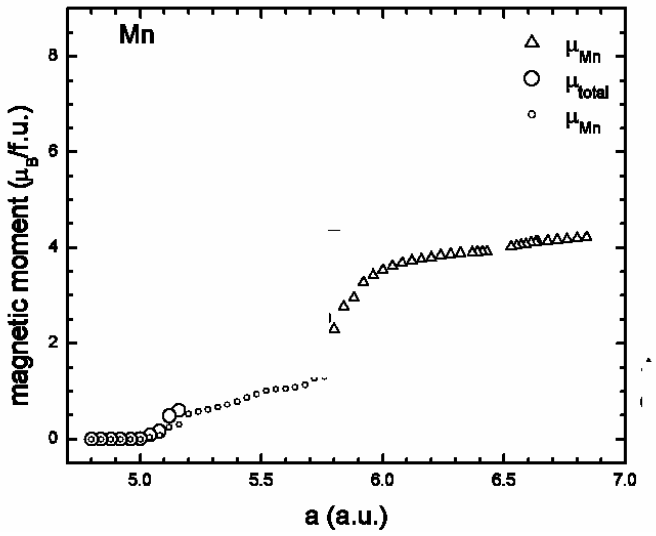

Fig. 2. Magnetic moment vs volume for fcc Mn. HS states are denoted by(Δ)and LS by(o)

The variation with the volume of the magnetic moments shows a new phase in the LS range. The elemental fcc Mn exhibit an anti-Invar behavior due to the magnetovolume instability, as was observed in fcc Fe. Total energy calculations have shown that bcc Mn have antifferomagnetic ordering [44]

Recently by using the FSM method Moruzzi et. al. studied AF for all 3d [44] transition metals in fcc and bcc structures. The total energies of the encountered AF phases were usualy lower than the nonmagnetic (NM) energies, but in no case was the AF ground state found. It seems therefore that the noncolinearity of magnetic moments or tetragonal lattice distortion are essential ingredients of experimental AF ground states of elemental metals. However by using a floating magnetic method it is obtained that bcc Mn has AF ordering [45].

III. Transition metal alloys

Concerning the magnetic properties of binary transition metal alloys the most relevant experimental information is contained in the so-called Slater-Pauling curve showing a linear increase of the average magnetic moment for early transition-metal alloys when plotted as a function of the increasing electron per atom ratio, followed by a linear decrease of the moments when the average *d* occupation increases for the latter transition-metal alloys, with a maximum for an average *d* occupation situated close to iron. However, some very interesting exceptions from this rule are known to exist. For instance, the magnetic moment of the fcc FeNi alloys is zero

over a concentration interval of Fe between 100 and 75%. The same type of quenched moment has been observed in the fcc FeCo alloy, artificially fabricated by precipitation in a Cu matrix. In general, the possibilities to investigate experimentally the magnetic properties of transition-metal alloys as a function of structure, lattice parameter or degree of chemical order are very limited which in turn limits the available data base for a complete coverage of the phenomena.

Magnetic 3d alloys with fcc cristalline structure within certain electron concentrations per atom e/a exhibit the Invar effect. For FM alloys 8. $5<e/a<9$, while for AF ones 7. $3<e/a<7$. 8, for $T<T_c$ and $T<T_N$ respectively. On the other hand fcc 3d alloys with $e/a<8$. 5 in the paramagnetic state have a thermal-expansion coefficient larger than that described by a Gruneisen lattice [52, 53]. This is referred to as anti-Invar behavior. The fcc Mn (see figs 1 and 2) exhibits this behavior.

The magnetic moment, in a very simple picture, depends weakly on the crystal structure, and decreases almost linearly with an increasing number of electrons. As a matter of fact, this kind of trend is displayed already for the free atoms (if the orbital moment is assumed to be quenched). This is a clear illustration of the fact that the magnetic moment of 3*d* transition-metal alloys is formed by quite localized *d*-electron states.

III. 1. Fe based alloys

Fe is among the most abundant elements on Earth, and is probably the major alloy component for the modern industry. Its structural and magnetic phase diagrams are enormously rich. At ambient conditions, it is stable in the bcc phase, which is ferromagnetic. With increasing temperature it first becomes paramagnetic above the Curie temperature of 1043 K, and then transforms structurally into the fcc phase at 1183 K. Just before melting, Fe re-enters the paramagnetic bcc phase. At relatively low temperatures, it transforms into the hexagonal closed-packed structure (hcp) at pressure above 13 GPa. A competition between antiferromagnetism and superconductivity was reported for iron at these conditions. With alloying the situation becomes even more complicated. Different elements may stabilize the bcc or fcc structures modifying the mechanical as well as the magnetic properties of Fe.

FeCr alloys

The addition of Fe to AF cromium reduces the Neel temperature gradually, the SDW disapearing at aproximately 19 at% Fe [54].

Between 16% and 19% a spin glass type behavior is observed [56].

There is evidence that the iron moments acts largely independently of the SDW [55]. Friedel and Hedman [56] interprets this behavior in terms of a strong coupling between isolated Fe moments and the SDW, but with clusters of iron moments remaining largely uncoupled to the SDW.

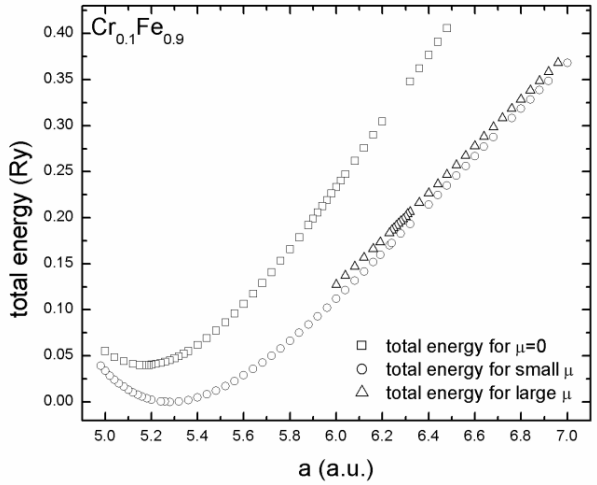

Fig. 3. Total energy/f. u. for $Cr_{0.1}Fe_{0.9}$ alloy

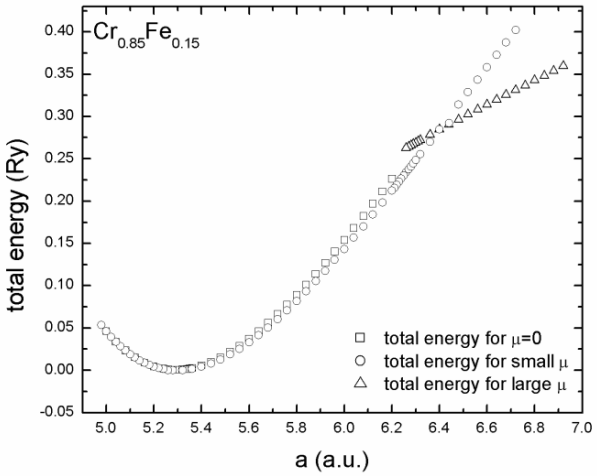

Fig. 4. Total energy/f. u. for $Cr_{0.85}Fe_{0.15}$ alloy

For low cromium concentration the total energy looks the same as for elemental fcc Fe which sustain the Fridel model of Fe clusters noninteracting with SDW. Moreover, an nonmagnetic state is only few mRy apart from the small magnetic moment branch of total energy. When the cromium concentration is large the nonmagnetic and low magnetic moments branches are degenerate. No coexistence at the equilibrium was found of the HS state.

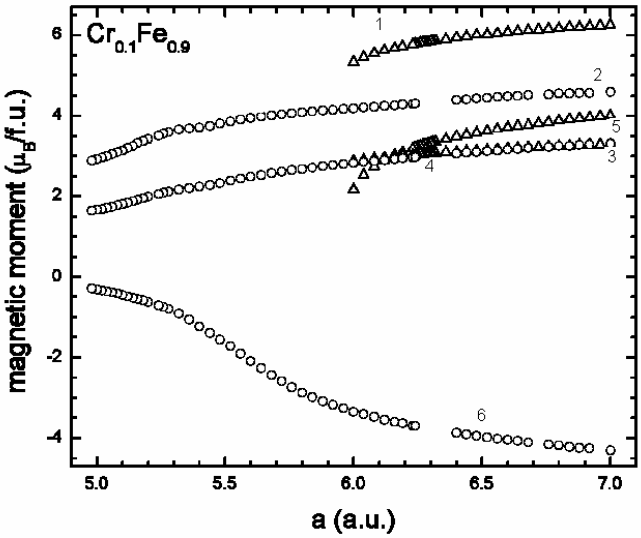

Fig. 5. Magnetic moments/f. u. for HS state (1), and intermediate sate(2) as well as for Fe HS state (3) and intermediate state (4), and for Cr atoms in HS state (5) and intermediate state(6) for$Cr_{0.1}Fe_{0.9}$. The symbols are the same as in Fig. 3.

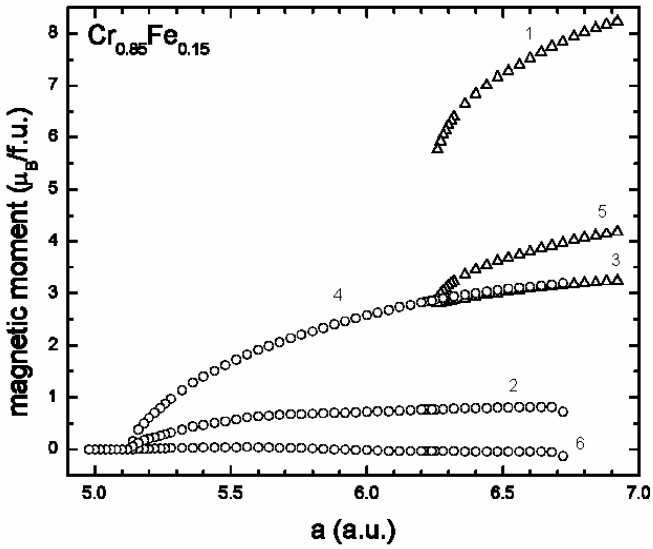

Fig. 6. Magnetic moments /f. u. for $Cr_{0.85}Fe_{0.15}$ for HS state (1) and LS state (2) as well as for Fe atoms in HS state(3) and inLS state (4), for Cr atoms in HS state (5) and in LS state (6). The symbols are the same as in Fig. 4.

As is seen from Fig's 3 and 5, the clusterisation of Fe atoms is large and the SDW is not interacting with.

The small Fe concentration prevent clusterisation and Fe-SDW interactions are expected. Indeed the AF Cr ordering is not seen(see Fig. 6). The desapearing of SDW state was found already at 0. 15at% Fe in rather good agreement with experimental data and other calculations [54]

FeMn alloys

The measurements of the thermal expansion coefficient on $Fe_{1-x}Mn_x$ alloys with $15<x<60$ at% show an anomalously enhanced in the high temperature range [57]. In contradiction with the FM Invar alloys, where the HS-LS transition entangles all constituents of the alloys [58] it was found that in AF-Invar FeMn alloys the moment instability affects only Fe moments leaving the Mn moments intact in contradiction with the Mn sensitivity to the volume variation (see fig. 2) In MnFe alloys, ferromagnetic phase is stable only up to $x = 0{:}2$ and the crystallizes in bcc lattice. For $x > 0.2$, several phases with AF ordering get stabilized [59].

The results obtained with TB-LMTO, [62] and Hartree-Fock-CPA [71] are in agreement with experimental data [72] i. e. the Mn local moment linearly decreases with increasing Mn concentration. The Fe moment weakly increases and the average moment decreases with the Mn concentration which is in qualitative agreement with the experimental Slater-Pauling curve [72]. These variations can be explained by using band-filling arguments and density of states (DOS). The DOS shows an almost constantly filled Fe up and down bands across the concentration regime thereby supporting the weak variation in Fe local moment. In case of Mn, the filling accommodates a greater number of electrons in the minority band. As a result, the minority band of the alloy gets gradually filled up while a loss of electrons from the majority bands occurs. For majority spin states, the filling of the majority band at Fe site reduces the density of sates at the Fermi level $\eta(E_F)$ for the corresponding band, while increasing Mn content shifts the Fermi level to regions of low spin up density of states and high spin down density of states because of a gradual filling of minority electrons.

Among the FeMn fcc alloys Fe_2Mn_2 is an AF Invar. The volume dependence of the magnetic properties of MnFe in AuCu I crystalographic structure was calculated by Podgorny[63] for colinear magnetic structure while Kübler et. al. [74] investigated collinear and noncollinear AF at the experimental lattice parameter.

FeNi alloys

Because of the intriguing properties the FeNi alloys were studied for a century. Chemical ordering (Ni rich), vanishing thermal expansion (Invar), and fcc to bcc structural transformations (Ni poor). *Ab initio* calculations confirmed the existence of several energetically competing states and showed that one can relate the Invar

effect to the population of antibonding electronic states near the Fermi level E_F causing large internal pressure favoring a large volume and nonbonding states with lower internal pressure tending to a smaller volume. However, this theoretical picture is unsatisfactory because it predicts a first-order HM-LM transition of the magnetic moments vs *composition* in Fe-Ni, in contrast to experiment, and the softness of the fcc Fe-Ni alloys is not found.

In particular the calculations based on the Korringa-Kohn-Rostoker method within the coherent-potential approximation (KKR-CPA) showed that chemical and magnetic disorder represented by the disordered local-moment (DLM) theory leads to multiple competing magnetic states and allows for additional lattice softening in the Fe-Ni alloys. KKR-CPA-based thermodynamic linear-response calculations showed the importance of magnetocompositional interactions for the observed atomic short-range order of $L1_2$ type of FM permalloy.

The magnetic order is shown in Figure 7.

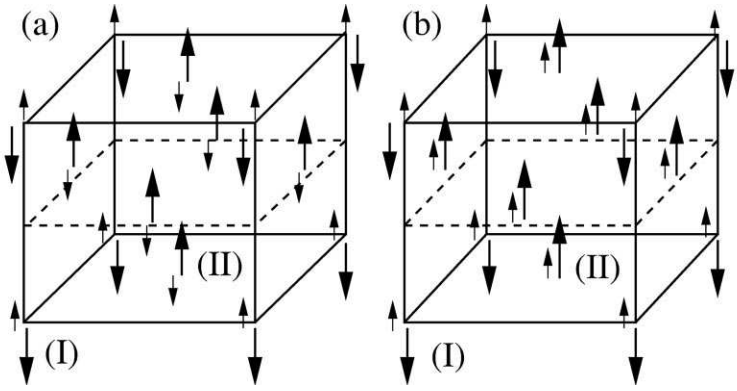

Fig. 7. The magnetic order for Fe-Ni alloys as resulted from KKR-CPA-MS calculations [19] for the two cases, increasing the local concentration of (a) Ni and (b) Fe on site II compared to site I by an amount *S*. Large arrows: Fe moments, small arrows: Ni moments.

The softening of the lattice is the same as obtained in the canted spin model [51].

III. 2. Co based alloys

CoMn alloys

Neutron studies performed for MnCo alloys show twotypes of magnetic behavior: FM-SRO for Co-25 at % Mn and coexistent FM and AF-SRO for Co-30 at. % Mn [79]. The atomic (chemical) ordering is still a subject of controvercy. Adachi et al. [76] concluded that the alloy is completely disordered while Bacon and Cowlam [77] and Wildes[78] have found a slight preference for unlike first

neighbors in agreement with other ASRO determinations [10, 77]. An extensive study of the system was made by Menshikov et al. [79] who used magnetisation and neutron diffraction techniques and find FM-LRO below25at. %Mn andAF-LRO above 43at. %Mn. Above 36 at%Mn the AF-SRO is observed which is transform at 43 at. %Mn to AF-LRO.

Due to the strong dependence of the Mn atom to the volume we computed the magnetic moment as function of the unit cell volume [80]. At large lattice parameters the system is FM while at smaller one is AF for the whole range of concentration. In the Co rich side of the system the Mn atoms are coupled AF with Co atoms as well as with other Mn atoms located in other lattice sites. For Mn rich side of the alloy system the Mn atoms are coupled FM with Co atoms for large lattice parameters and AF for small one.

The Fermi level is pinned on the minority spin channel. The DOS of $Mn_{0.3}Co_{0.7}$ (see Figure 8) can be used to explain the magnetic moment of Mn atoms with composition in a rigid band model.

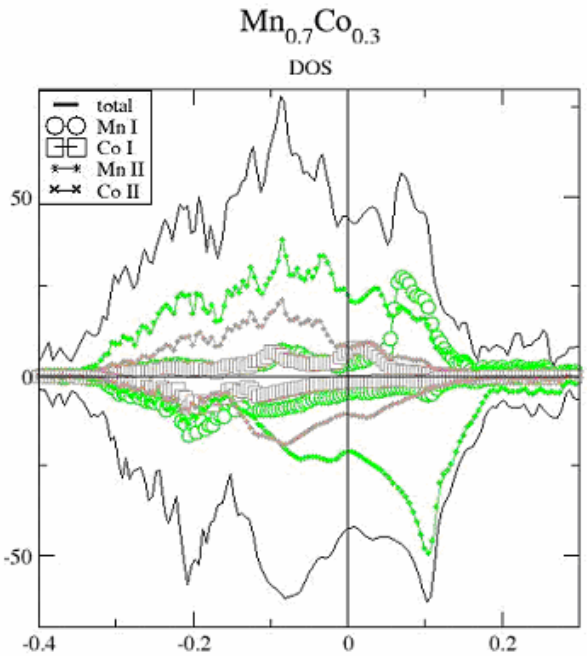

Fig. 8. DOS for $Mn_{0.3}Co_{0.7}$. The 0- value on the x axes correspond to the Fermi level, full line to the total DOS, while open circle to the Mn DOS. The upper plan correspond to the majority spin channel while the negative one to the monority spin channel.

CoFe alloys

Alloys of iron and cobalt constitute an important class of soft magnetic materials with a wide and important range of technological applications where high magnetic flux densities are required. Fe-Co alloys find application in data storage, high performance transformers, and pole tips for high field magnets [41, 42] The effect of magnetism on structural stability and ordering in Fe-Co alloys has been extensively studied in the past, and it has been established that in random Fe-rich Fe-Co alloys magnetism stabilizes the bcc structure relative to the close-packed fcc and hcp structures, and that the ordering of B2-phase originates from the ferromagnetism. [43] Similarly, in the two-dimensional analogs of the Fe-Co bulk alloys, the electronic and magnetic interactions enable the formation of the ordered $L1_0$ superlattice on nonmagnetic e. g. Cu (001) substrates. [44] Fe local moment increases with increasing Co content up to $x = 0.3$ beyond which it tends towards a saturation while the Co moment remains almost constant over the whole concentration regime, [36], in agreement with experimental data [39, 40] This system is very sensitive to the change in local atomic environment: structural instability and transformation into low-symmetry $L1_0$ structure or sheared $L1_2$ structure can be caused by reduced dimensionality or applied shear stress, respectively [42].

CoNi alloys

The magnetic diffuse scattering of neutrons from a series of cobalt-nickel alloys indicate individual 3d moments at Co and Ni and no short range order. The magnetic moments of Co and Ni do not differ significantly from the values of pure metals. Cobalt shows complete solid solubility in nickel from 100 to about 30% nickel. At higher cobalt concentrations a hexagonal close-packed phase appears at room temperature. The randomness of atomic arrangement is somewhat surprising because the isomorphous iron-nickel alloy with the same mean number of electrons per atom and saturation magnetization shows marked ordering effects over very wide ranges of composition even after quenching from 1000^0 C, [47, 49].

Our calculations based on the KKR-CPA method have shown no SRO of the $L1_2$ kind. The total energy calculations show no modification of the shape of the curves with magnetic canceling of the Co and Ni magnetic moments. Also there are very small variations of the magnetic moment as the lattice parameter is changed. In Figure 9 and 10 the magnetic moment variations with lattice parameter are shown.

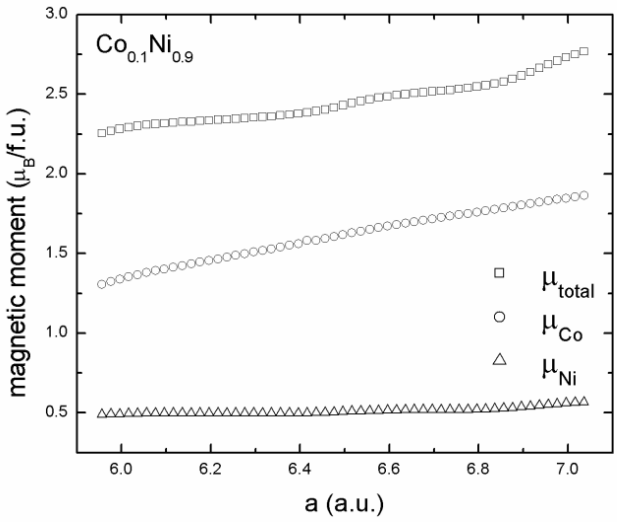

Fig. 9. Magnetic moments of atoms and total magnetic moment/f. u. for $Co_{0.1}Ni_{0.9}$ alloy.

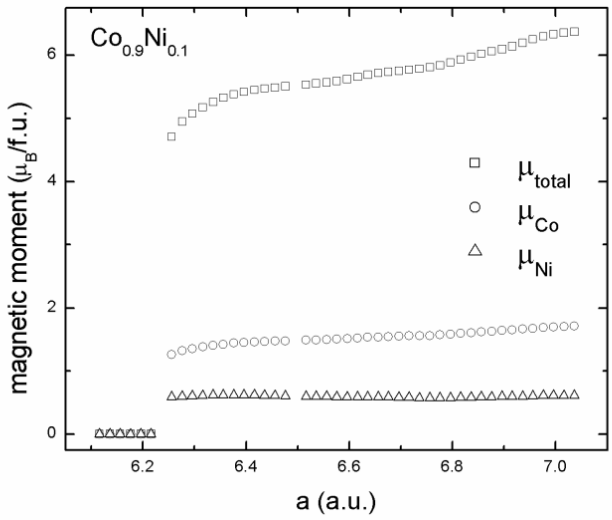

Fig. 10. The total and atomic magnetic moments for $Co_{0.9}Ni_{0.1}$ alloy. For the $Co_{0.9}Ni_{0.1}$ it is seen the magnetovolumic instability induced by the Co atoms because the large Co content. The magnetic moments of both Ni and Co atoms are almost insensitive to the unit cell volume. This is seen also from the total energy calculation (see fig. 11)

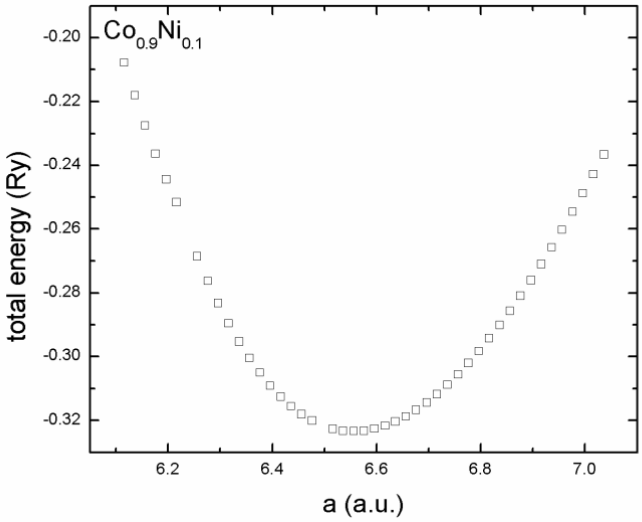

Fig. 11. Total energy as function of lattice parameter for $Co_{0.9}Ni_{0.1}$ alloy.

It seems that the orbital overlapping in CoNi alloys is not so significant. The new charge distribution after the magnetovolume effect is not producing a significant total energy change. The behavior is consistent with the lack of the SRO in this alloy system.

For the thin films it was observed a structural change from fcc structure to the hcp one accompanied by a magnetic hardening as function of the method used for deposition, [48].

Ni based alloys

NiFe alloys

In the Fe rich side the fcc FeNi alloys the magnetic structure is determined by a competition between the collinear and noncollinear magnetic states. It was found a series of transitions between these magnetic structures, in particular disordered local moment configurations, spin spiral states, the double layer antiferromagnetic state, and the ferromagnetic phase, as well as the ferrimagnetic phase with a single spin flipped with respect to all others [50].

In the concentration region with INVAR properties these alloys have almost similar properties [51] apart from an fcc to bcc transition at the $Fe_{65}Ni_{35}$. In the bcc phase the alloys are nonmagnetic. Also the antiferromagnetic ordering with a local ordering tendency was found [9].

NiMn alloys

Neutron studies, [23] performed on MnNi alloys show two types of magnetic behavior: coexistent FM long range order (LRO)and AF short range order (SRO) for Ni-24at. % Mn; and AF-SRO for Ni-28 at. % Mn. The sublattice moments are of about 3. 5 μ_B [9, 10]. If we accept the LDA calculations for AF Ni systems [11] the moments of fcc Ni will vanish than the average moment is associated only to Mn sites and therefore correspond to 4 μ_B/Mn.

Other experimental results [21] claim LRO above 32 at. % Mn with spin glass behavior in the intermediate region. In all fcc Mn alloys a discontinous change from LS to HS state with increasing lattice constant is found[12] and ASRO increase the FM tendencies.

In the $MnNi_{3.5}$ ASRO, producing a change in the local environment, the Mn atoms are AF coupled. [13]. The atomic(chemical) degree of order was found to be the reason for the magnetic moment of 1. 15 μ_B/cell for less disordered system compared with 2. 67 μ_B/cell for more ordered one. Moreover the AF arrangement of Mn atoms lower the total energy by forming a pseudo-gap in the density of states [22]. For small as well as high Mn concentration the magnetovolume instability is present for fcc structure as is seen in Figures 7.

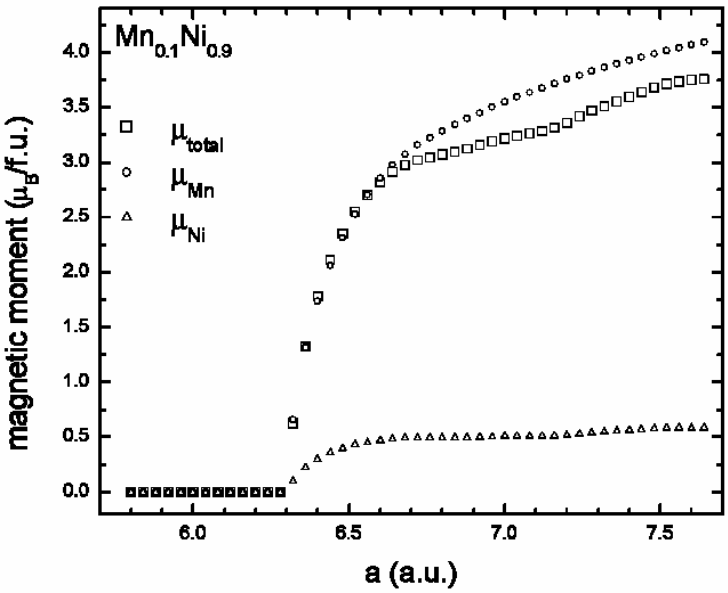

Fig. 12. The atomic and total magnetic moment for fcc $Mn_{0.1}Ni_{0.9}$ vs lattice parameter.

The total energy for the same alloy composition is shown in Fig. 8.

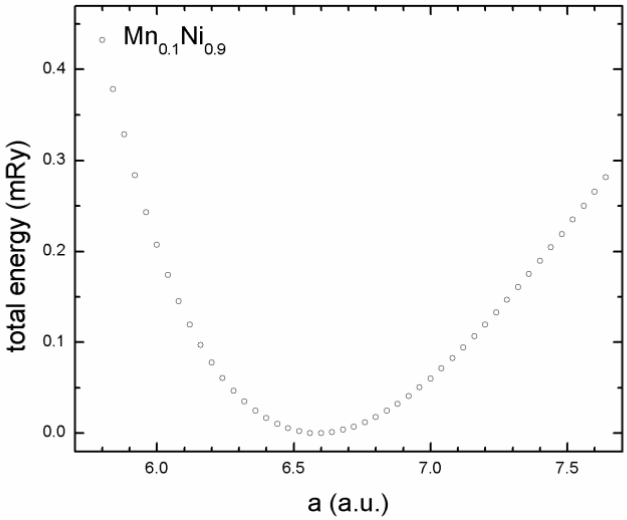

Fig. 13. Total energy/f. u. for $Mn_{0.1}Ni_{0.9}$ as function of lattice parameter.

The slope of the right branch is different from the left one. It was not seen any coexistence of the HS and LS states. The charge distribution in the unit cell can be computed by the muffin-tin charge calculation at each lattice point. The results for the alloy $Mn_{0.1}Ni_{0.9}$ are shown in Figure 14.

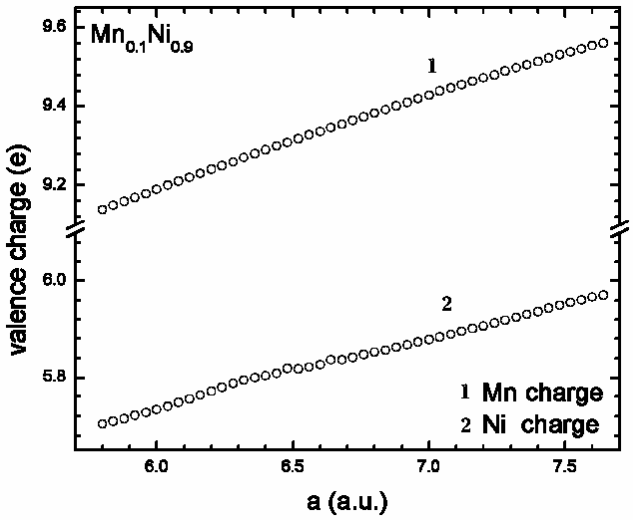

Fig. 14. The muffin tin charge at the Mn and Ni sites for $Mn_{0.1}Ni_{0.9}$

The increase of the charge is produced by the increase of the muffin-tin radius as a result of the increase of the lattice parameter. The slope of both lines are the same which means that no charge transfer is taking place.

For the increase concentration of Mn atoms the total energy, magnetic moment and charge transfer as function of lattice parameter are shown in Figures 15-17.

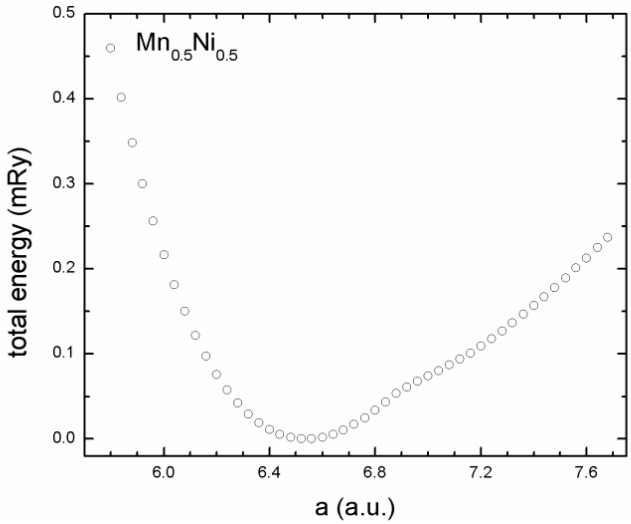

Fig. 15. Total energy/f. u. as function of lattice parameter for $Mn_{0.5}Ni_{0.5}$ alloy.

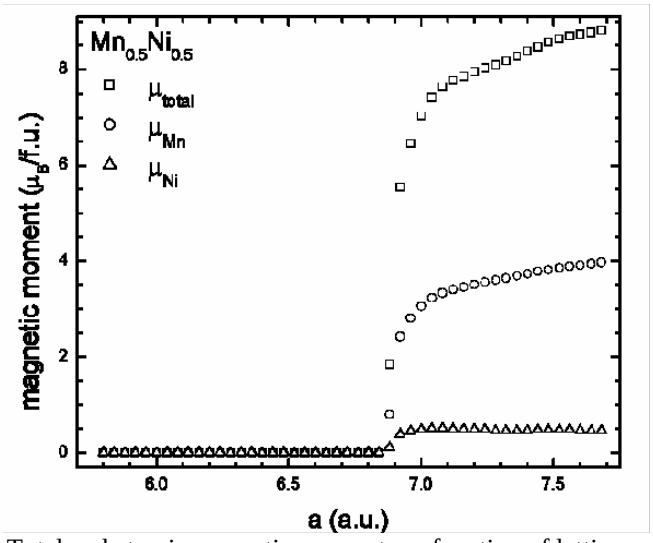

Fig. 16. Total and atomic magnetic moments as function of lattice parameter for $Mn_{0.5}Ni_{0.5}$ alloy.

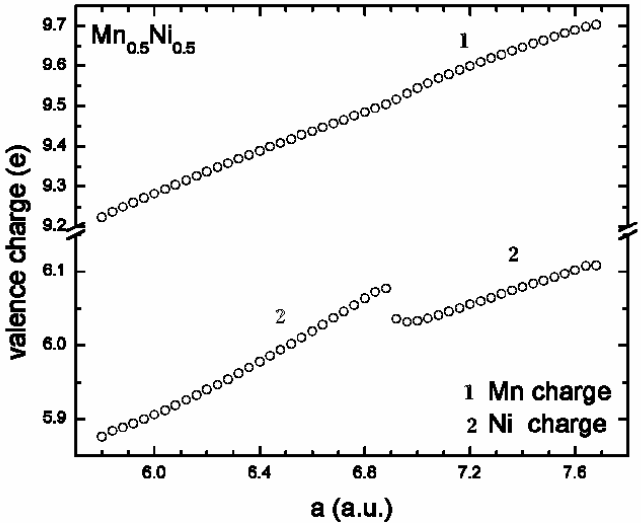

Fig. 17. Muffin tin charge for Ni (1) and Mn(2) as function of lattice parameter for $Mn_{0.5}Ni_{0.5}$ alloy.

The change in the magnetic moment from LS state to HS state is accompanied by a delocalisation of Mn muffin tin charge. The extra charge was not found around the Ni atoms. The charge delocalisation of Mn atom which produces the drop in the magnetic moment of Mn atom will produce also a modification of bonding which could be relevant for the INVAR property.

REFERENCES

1. Ferromagnetic Materials, edited by E.P. Wohlfarth, K.H. Buschow, Vol. 1-7 (North-Holland, Amsterdam, 1980-1993).
2. E.H. Wassermann, Ferromagnetic Materials, ed. K. H. J. Burdow, E. P. Wohlfarth (North-Holland, Amsterdam, 1990)
3. C.G. Shull, M.K. Wilkinson, Phys. Rev. **97**, 304 (1955). (fost 6)
4. D.I. Bardos, J. Appl. Phys. **40**, 1371 (1969) (fost 7)
5. M.F. Collins, G.G. Low, Proc. Phys. Soc. **86**, 535 (1965)
6. M.F. Collins, J.B. Forsyth, Philos. Mag. 8, 401 (1963)
7. H.R. Child, J.W. Cable, Phys. Rev. B **13**, 227 (1976)
8. G.G. E. Low, M.F. Collins, J. Appl. Phys., **34**, 1995 (1963)

9. J.W. Cable, H.R. Child, Phys. Rev., B10, 4607 (1974)
10. J.W. Cable, Phys. Rev. B 25, 4670 (1982)
11 L.M. Sandratskii, J. Kubler, J. Phys. Condens. Matter. 4, 6927 (1992)
12. N.E. Brener, G. Fuster, J. Callaway, J. L. Fryand, Y. Z. Zhao, J. Appl. Phys., 63, 4057 (1988)
13. C. Petrillo, F. Saccheti, M. Scafi, J. Mag. Mag. Mat., 104, 2015 (1992)
14. P. Radhakrishnan, F. Livet, Solid State Commun. **25**, 597 (1978)
15. F. Kajzar, G. Parette, Phys. Rev. B **22**, 5471 (1980)
16. M. Hennion, B. Hennion, Phys. Rev., **B19**, 348 (1979)
17. O. Moze, T.J. Hicks, J. Phys. F: Metal Phys., **14**, 221 (1984)
18. V. Arp., D. Edmonds, R. Peterson, Phys. Rev. Lett. **3**, 212 (1952)
19. V. Crisan, P. Entel, H. Ebert, H. Akai, D.D. Johnson, J.B. Staunton, Phys. Rev. **B66**, 014416, (2002)
20. O. Moze, T.J. Hicks, J. Phys. F: Metal Phys., 11, 1471, (1981)
21. J.W. Cable, Y. Tsunoda, J. Mag. Mag. Mat., 140, 93 (1995)
22. A. Sakuma, J. Mag. Mag. Mat., 187, 105 (1998)
23. J.W. Cable, Y. Tsunoda, Phys. Rev., 50, 9200 (1994)
24. H Akai, J. Phys.: Condens. Matter **1,** 8045 (1989) 8045
25. X-T Tang, G-C Wang, M. Shima, J. Mag. Mag. Mat., 309, 188(2007)
26. Y.A. Abdu, T. Ericsson, H. Annersten, J. Mag. Mag. Mat. **280**, 395 (2004)
27. C.M. Van Baal, Physica **64**, 571 (1973).
28. Y.A. Abdu, T. Ericsson, H. Annersten, J. Mag. Mag. Mat. **280**, 395 (2004)
29. D.G. Pettifor, J. Phys**.** C(Sol. Stat. Phys.), 2, 1051 (1969)
30. D.G. Pettifor J. Phys. C (Sol. Stat. Phys.), 3, 367(1970)
31. T.L. Loucks, The Augmented Plane Wave Method (New York, Amsterdam: Benjamin 1967).
32. J. Koringa, Physica, **19,** 392, (1947)
33. W. Kohn., N. Rostoker, . Phys. Rev., **94,** 1111, (1954)
34. N.L. Hodges, H. Ehrenreich., N.D. Lang, Phys. Rev., **152,** 505, (1966).
35. F.M. Mueller, Phys. Rev., **153,** 659, (1967)
36. V. Crisan, A. Vernes, L. Dulca, V. Popescu, D. Kapusi, Int J. Mod. Phys. B 7, 546, (1993)
37. V. Crisan, M. Muresan, Studia Universitatis Babes-Bolyai 2, 28 (1977).
38. W. Kohn, L. Sham, Phys. Rev., 140, A1133 (1965)
39. V.L. Moruzzi, J.F. Janak, A.R. Williams, Calculated Electronic Properties of Metals (Pergamon, New York, 1978)
40. O.K. Andersen, J. Madsen, U. K. Poulsen, O. Jepsen, J. Kollar, Physica86&&88B, 249 (1977)
41. P.H. Dederichs, S. Blugel, R. Zeller, H. Akai, Phys. Rev. Lett. 53, 2512(1984)
42. E.H. Wassermann, M. Acet, W. Pepperhoff, J. Magn. Magn. Mater., 90-91, 126 (1990)
43 V.L. Moruzzi, P. M. Marcus, K. Schwartz, P. Mohn, Phys. Rev., 34, 1784 (1986)

44. V.L. Moruzzi, P. M. Marcus, Phys. Rev., B 42, 8361 (1990)

45. Kubler, J. Magn. Magn. Mater. 20, 107 (1980)

46. K. Shimizu, T. Kimura, S. Furomoto, K. Takeda, K. Kontani, Y. Onuki, K. Amaya, Nature London **412**, 316 (2001)

47. M.F. Collins, R.V. Jones, D. Lowde, *J. Phys.* ***Soc.*** *Japan (SuPPl.* BIII), 17, 19 (1962).

48. S. Pane, E. Gomez, J. Garcia-Amoro´s, D. Velasco, E. Valle´s Applied Surface Science 253, 2964, (2006)

49. I. N. Shabanova, N. V. Keller, Surf. Interface Anal. 32, 114 (2001)

50. I.A. Abrikosov, A. E. Kissavos, F. Liot, B. Alling, S. I. Simak, O. Peil, A. V. Ruban, Phis. Rev. B **76**, 014434 (2007)

51. M. van Schilfgaarde, I. A. Abrikosov, B. Johansson, Nature London **400**, 46 (1999).

52. M. Acet, T. Schneider, H. Zahres, E. F. Wassermann, W. Pepperhof, J. Appl. Phys. 75, 7015 (1994)

53. W. Bendick, H. H. Ettwig, W. Peperrhoff, J. Phys. F, 8, 2525 (1978)

54. S. K. Burke B. D. Rainford 1978 *J.* Phys. F. Metal Phys. **8** L239, (1978) [5531g] J.0. Strom-Olsent, D. F. Wilfordt, **S. K.** Burke, B. D. Rainford, J. phys. F: Metal Phys., 9, L95, (1979)

56. J. Friedel, L.E. Hedman, Journal de Physique, 39, 1225(1978)

57. T. Schneider, M. Acet, B. Rellinghaus, E. H. Wassermann, W. Pepperhoff, Phys. Rev., 51, 8917 (1995)

58. M. Podgorny, Phys. Rev., B 45, 797 (1992)

59. Y. Endoh, Y. Ishikawa, J. Phys. Soc. Jpn., **30**, 1614 (1971).

60. E. Fawcet, Rev. Mod. Phys. 60, 209 (1988)

61. E. Fawcett, H.L. Alberts, V. Yu. Galkin, D. R. Noakes, J.V. Yakhmi, Rev. Mod. Phys. 66, 25 (1994)

62. S. Gho, B. Sanyal, C.B. Chaudhuri, A. Mookerjee Eur. Phys. J. B **23**, 455 (2001)

63. D.I. Bardos, J. Appl. Phys. **40**, 1371 (1969).

64. M.F. Collins, J. B. Forsyth, Phil. Mag. **8**, 401 (1963).

65. I. Turek *et al.*, Phys. Rev. B **49**, 3352 (1994)

66. R. Richter, H. Eschrig, J. Phys. F **18**, 1813 (1988).

67. A. Díaz-Ortiz, 1, 2 R. Drautz, 3 M. Fähnle, 2 H. Dosch, 2 and J. M. Sanchez, Phys. Rev., B **73**, 224208 (2006)

68. C.L. Fu, M. Krčmar, Phys. Rev. B **74**, 174108 (2006)

69. I.A. Abrikosov, P. James, O. Eriksson, P. Söderlind, A.V. Ruban, H.L. Skiver, B. Johansson, Phys. Rev. B **54**, 3380 (1996). 70G. A. Farnan, C. L. Fu, Z. Gai, M. Krcmar, A. P. Baddorf, Z. Zhang, and J. Shen, Phys. Rev. Lett. **91**, 226106 _2004_.

71. H. Hasegawa, J. Kanamori, J. Phys. Soc. Jpn **33**, 1607 (1972).

72. H. Fisher et al., in Magnetic Ultrathin Films, Multilayers and Surfaces, edited by A. Fert et al. (Materials Research Society, Pittsburgh, 1995)

73. M. Podgorny, Phys. Rev., 45, 797 (1992)

74. J. Kübler, K-H. Höck, J. Sticht, A.R. Williams, J. Phys. F, 18, 469 (1988)

75. R.S. Fishman and W. -T. Lee, S.H. Liu, D. Mandrus and J.L. Robertson, K.J. Song and J.R. Thompson, Phys. Rev. B 61, 12159 (2000)

76. K. Adachi, K. Sato, M. Matsui, S. Mitani, J. Phys. Soc. Jpn. 35, 426 (1973)

77. G.E. Bacon, N. Cowlam, J. Phys. C 3, 675 (1970)

78. A.R. Wildes, S.J. Kennedy, L.D. Cussen, T.J. Hicks, J. Phys. Condens. Matter 4, 8961 (1992)

79. A.Z. Menshikov, G.A. Takzei, Yu. A. Dorofeev, V.A. Kazantsev, A.K. Kodtyshin, I. I. Sych, Sov. Phys. JETP, 62, 734 (1985)

80. A. Nedelcu, V. Crisan, Studia UBB, Phys. LIV, 2, 97 (2009)

MICROSTRUCTURE EVOLUTION OF $(Pr,Dy)_2Fe_{14}B/\alpha$-Fe NANOCOMPOSITE COUPLED BY EXCHANGE INTERACTIONS

OLIVIER ISNARD[a], VIOREL POP[b*], EUGEN DOROLTI[b], SIMONA GUTOIU[b], ALBERT TAKACS[b], IONEL CHICINAS[c]

ABSTRACT. (Pr,Dy)2Fe14B/α-Fe hard/soft nanocomposites were obtained by mechanical milling and subsequent annealing. The influence of the milling and annealing conditions on the structural, microstructural and magnetic properties of $(Pr_{0.92}Dy_{0.08})_2Fe_{14}B/\alpha$-Fe nanocomposite have been investigated. The crystallites mean size was deduced from the Full – Width – at – Half – Maximum - FWHM of the diffraction α-Fe peaks according to Scherrer's formula. The crystallites mean size, for the iron phase, increases when increasing the annealing temperature.

Keywords: *Nanocomposite magnetic materials, microstructure, mechanical milling*

INTRODUCTION

Nanocomposites exchange-enhanced magnetic materials of a hard and a soft magnetic phase have a substantial potential for permanent magnets applications due to a higher remanent magnetizations compared to the isotropic single-phase hard magnetic materials. Remanence enhancement arises from the exchange coupling of magnetic moments across interfaces between the hard and soft magnetic phases, causing the magnetic moments of the soft magnetic phase to become aligned with those of the hard magnetic phase. Skomski and Coey [1] first predicted that a giant energy product $(BH)_{max}$ over 1 MJ/m^3 might be attainable in oriented exchange coupled $Sm_2Fe_{17}N_3/Fe_{65}Co_{35}$ nanocomposites. Similarly, a potential $(BH)_{max}$ of 720 kJ/m^3 was predicted in $Nd_2Fe_{14}B/\alpha$-Fe nanocomposite [2]. It has been demonstrated on several occasions [3-5] that the crystallite size of both phases, in particular, the soft phase, is important in determining remanence enhancement and coercivity. Optimum magnetic coupling of the hard and soft components is achieved in materials with grain sizes of about 10–20 nm, which is of the same order of magnitude as the domain-wall width in the hard magnetic material. The refinement of microstructure becomes a key factor for the enhancement of the magnetic properties.

[a] *Institut Néel, CNRS, Université J. Fourier, BP166, 38042 Grenoble, Cedex 9, France*
[b] *Faculty of Physics, Babes-Bolyai University, 400084 Cluj-Napoca, Romania*
[*] Corresponding author*: viorel.pop@phys.ubbcluj.ro*; +40746 201051
[c] *Materials Sciences and Technology Dept., Technical University of Cluj-Napoca, 103-105 Muncii ave., 400641 Cluj-Napoca, Romania*

An efficient way to optimize the magnetic properties of nanocomposites is the adjusting the composition [6-9]. For the $Nd_2Fe_{14}B$ hard phase it has been shown that a small substitution of Nd by Dy increases the anisotropy field which favours the improvement of coercivity. On the other hand, a decrease of the magnetization is observed due to the antiparallel coupling between Fe and Dy moments [10]. Praseodymium is very similar to neodymium in elemental state and also in the $R_2Fe_{14}B$ compounds. Both $Pr_2Fe_{14}B$ and $Nd_2Fe_{14}B$ have the same tetragonal structure with a space group P4mnm. The Curie temperature of both compounds is similar, 585 K ($Nd_2Fe_{14}B$) compared with 569 ($Pr_2Fe_{14}B$). The saturation magnetization of $Pr_2Fe_{14}B$ is also comparable to that of $Nd_2Fe_{14}B$ (1.56 T compared with 1.60 T) [11]. However, in $Nd_2Fe_{14}B$ a spin reorientation occurs at around 140 K [12], and this has a detrimental effect upon the low temperature magnetic properties [13], whereas $Pr_2Fe_{14}B$ exhibits no spin reorientation down to 4.2 K [14] and therefore at low temperatures, exhibits superior magnetic properties to those of $Nd_2Fe_{14}B$. Furthermore, the $Pr_2Fe_{14}B$ compound possesses a larger magnetocrystalline anisotropy field of 8.7 T [15] compared to 6.7 T for $Nd_2Fe_{14}B$ [15], indicating a somewhat higher theoretical limit intrinsic coercivity in $Pr_2Fe_{14}B$. All these factors lead Pr–Fe–B magnets to be attractive for broad temperature range applications.

In our previous works, we have successfully obtained hard/soft type magnetic nanocomposite with coercivity ranging from 3.7 to 8.2 kOe [16-18]. A few percent of Dy, substituted for Nd in the Nd-Fe-B hard magnetic phase proved to refine the microstructure and enhance the anisotropy field [19-21]. This increase of magnetic anisotropy favours on improvement of the coercivity. Based on the earlier results concerning the higher anisotropy of $Pr_2Fe_{14}B$ compared to $Nd_2Fe_{14}B$ compound [15] and our previous results concerning the evolution of the magnetic properties of $Nd_2Fe_{14}B/\alpha$-Fe nanocomposite when a small quantity of Nd is replaced by Dy [16], in this article we report the results of a study on the microstructures evolution and magnetic properties of nanocrystalline $(Pr_{0.92}Dy_{0.08})_2Fe_{14}B/\alpha$-Fe nanocomposite obtained by mechanical milling and subsequent annealing.

EXPERIMENTAL

The hard magnetic phase $(Pr_{0.92}Dy_{0.08})_2Fe_{14}B$ was prepared by arc melting under argon atmosphere. The ingots were re-melted several times to promote homogeneity. The used started materials had a purity superior to 99.9%. An excess amount of 1 wt% Pr was added in order to compensate the weight loss during the preparation. The ingot was crushed into small pieces and subsequently mechanically milled for 3 hours in a Frisch high energy planetary mill under helium atmosphere. The $(Pr_{0.92}Dy_{0.08})_2Fe_{14}B$ powder, obtained after milling, was mixed with iron powder (≤ 40 μm) in a ration of 78 wt % $(Pr,Dy)_2Fe_{14}B$/22 wt % α-Fe. The mixture was mechanically milled from 4 up to 12 hours. The structure and the microstructure were modified by appropriate heat treatments performed under vacuum between 450

and 800 °C, for a duration ranging from 5 min to 1.5 hours. X-ray diffraction (XRD) was carried out on a Bruker D8 Advance diffractometer with Cu Kα radiation in the angular range 2θ = 20- 90°. The crystallites mean size was deduced from the line broadening by means of the Scherer's formula [22]. The magnetisation curves were recorded at room temperature, using the so-called extraction method [23] in a DC magnetic field of up to 10 T.

RESULTS AND DISCUSSIONS

Figure 1a shows XRD patterns comparing the structure of the $(Pr_{0.92}Dy_{0.08})_2Fe_{14}B$ hard phase milled for 3 hours and $(Pr_{0.92}Dy_{0.08})_2Fe_{14}B$ /α-Fe composite as-milled for 4 and 6 hours. The Bragg peaks corresponding to the hard and soft magnetic phases are broadened by milling, but no additional peaks are evidenced. Upon a heat treatment at 550 °C for 1.5 hours (figure 1b), the respective peak intensity ratios for both hard and soft phases are more easily observed. Furthermore, as can be seen from figure 1b, the heat treatment induces an evolution of the microstructure but no additional Bragg peaks have appeared. These aspects prove that the initial phases present in the composite were kept after milling and annealing and no supplementary phases were formed. After annealing the width of the diffraction peaks decreases in comparison to the corresponding milled samples as a consequence of diminishing of the second-order internal stresses and of the defects density.

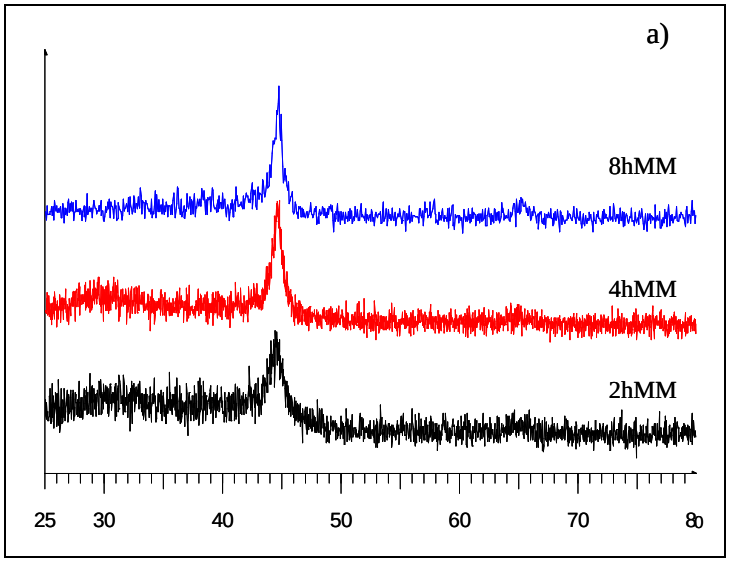

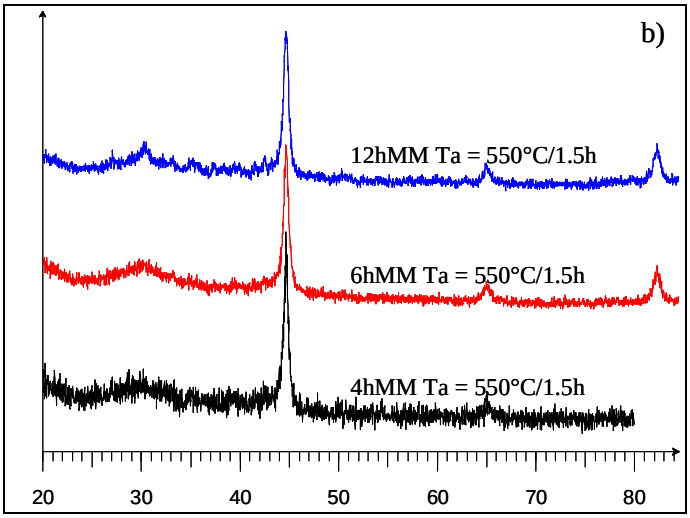

Fig. 1. X-ray diffraction patterns of the $(Pr_{0.92}Dy_{0.08})_2Fe_{14}B/\alpha$-Fe composite sample milled for 4 and 8 h in comparison with the $(Pr_{0.92}Dy_{0.08})_2Fe_{14}B$ hard phase milled for 2 h (a) and nanocomposites milled for 4, 6 and 12 hours and annealed at 550°C for 1.5 hours (b).

X-ray diffraction line-broadening analysis was performed for samples milled for two different times (6 and 12 hours) and heat treated in temperature ranging from 550 °C to 800 °C. The crystallite size was computed from the line broadening by means of the Scherer's formula [22]. For two different milling time, annealing at temperature greater than 600 °C (figure 2) show a little narrowing of XRD peaks which proves that this temperature is close to the recrystallization temperature for the studied samples. Moreover, a heat treatment at 800 °C for 5 minutes produces a recrystallization of the samples, which results in a clear narrowing of the diffraction peaks in good agreement with our previous results [16], confirming that the recrystallization temperature is below 800 °C. Values of the crystallite size of the soft phase calculated from the diffractions peaks are given in table 1.

A continuous increasing of the crystallite size was obtained for samples annealed between 550 and 800 °C. It is important to note that the nanoscale (16-37 nm) grain size of the soft phase is higher that the theoretically estimations for an optimum soft/hard exchange coupling.

The isothermal hysteresis curves for $(Pr_{0.92}Dy_{0.08})_2Fe_{14}B/\alpha$-Fe 6 h milled samples and subsequently annealed at 550, 600 and 800 ºC, recorded at room temperature, are plotted in figure 3. For comparison, the hysteresis curve of $(Nd_{0.92}Dy_{0.08})_2Fe_{14}B/\alpha$-Fe 6 h milled samples and annealed at 550 ºC for 1.5 h, is also given. The hysteresis curve of $(Nd_{0.92}Dy_{0.08})_2Fe_{14}B/\alpha$-Fe samples, against the low remanence and coercivity, is rather smooth and testify for a good exchange coupling between hard and soft phases. The poor remanence and coercivity for $(Pr_{0.92}Dy_{0.08})_2Fe_{14}B/\alpha$-Fe samples are explained by a low inter-phase coupling as witnessed by the non uniform shape of the demagnetisation curves. This aspect is clearer in the *dM/dH* vs.

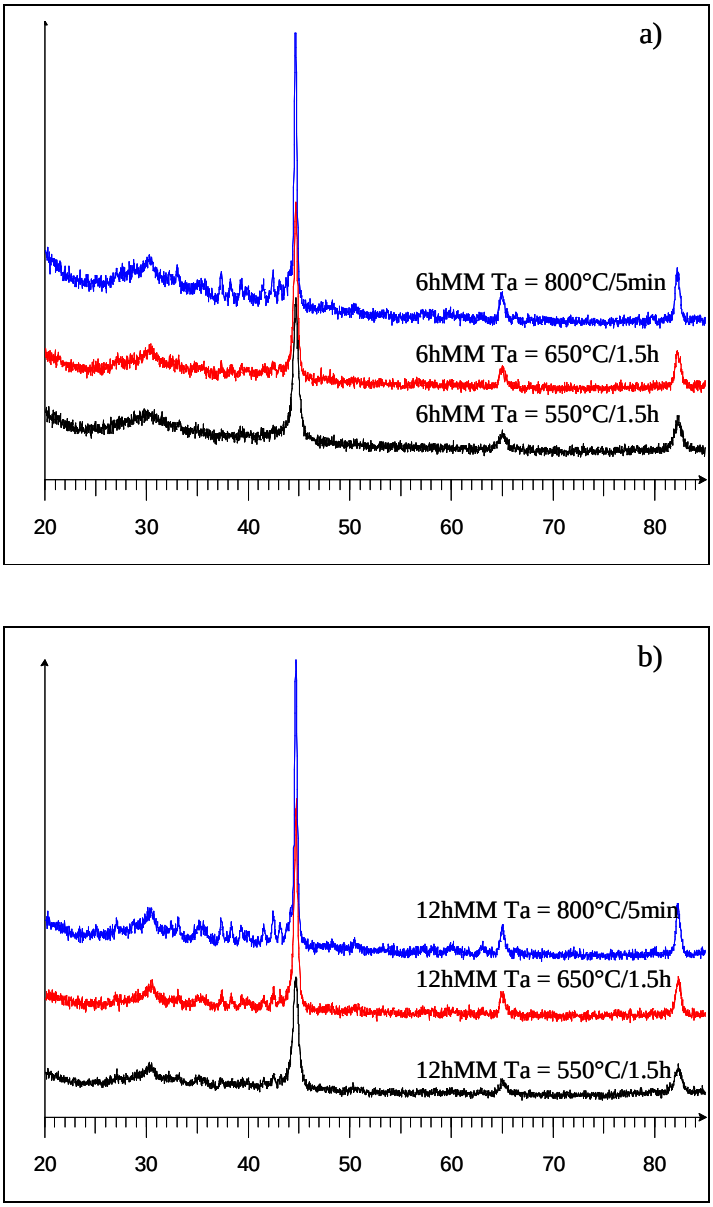

Fig. 2. X-ray diffraction patterns of the $(Pr_{0.92}Dy_{0.08})_2Fe_{14}B$/α-Fe composite milled for 6 h (a) and 12 h (b) and annealed at different temperatures in the range 550-800 °C for 1.5 h or 5 minutes.

Table 1.
The nanocrystallites mean sizes of α-Fe, for $(R_{0.92}Dy_{0.08})_2Fe_{14}B$/α- Fe samples milled for 6 and 12 h and annealed at different temperature

Annealing Temperature (°C)	$(Pr_{0.92}Dy_{0.08})_2Fe_{14}B$ /α-Fe-6hMM (nm)	$(Pr_{0.92}Dy_{0.08})_2Fe_{14}B$ /α-Fe-12hMM (nm)	$(Nd_{0.92}Dy_{0.08})_2Fe_{14}B$ /α-Fe-6hMM (nm)
550	20	18	16
650	24	29	26
800	33	34	37

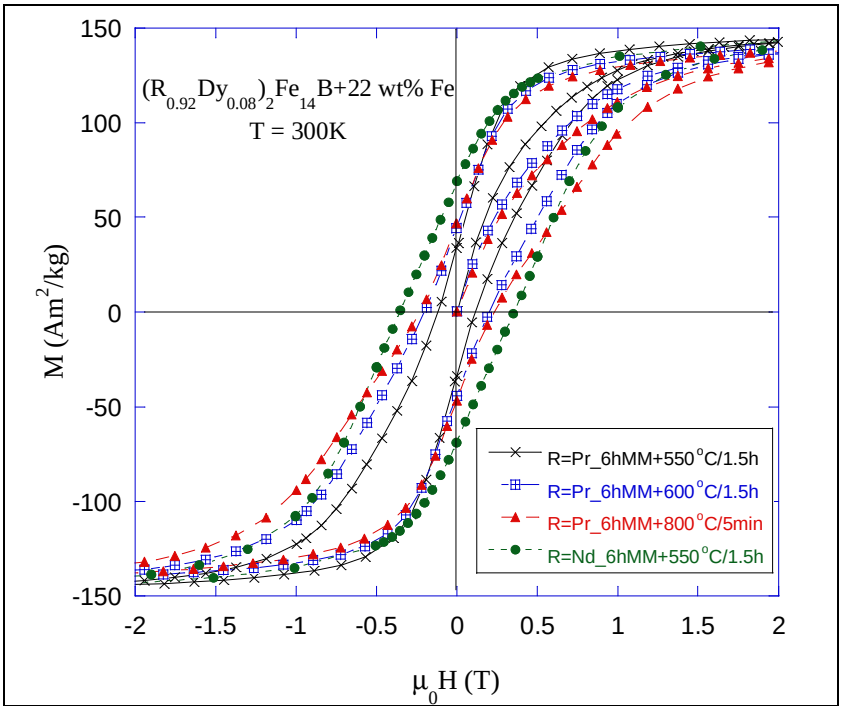

Fig. 3. Hysteresis loops measured at room temperature for $(R_{0.92}Dy_{0.08})_2Fe_{14}B$/α-Fe (R = Nd or Pr) nanocomposite milled for 6 hours and annealed for the indicated time and temperature.

H curves, figure 4. The observed peaks in *dM/dH* vs. *H* curves are directly linked to the coercivity which results from the inter-phase exchange coupling. Broaden and large peaks can be given by a large distribution of the α-Fe crystallite sizes, which gives different degree of inter-phase exchange coupling. When the *dM/dH* peak is thin and is observed at high negative field, this corresponds to a narrow crystallite grain distribution, a good anisotropy of hard phase and a strong inter-phase exchange

coupling. For the $(Nd_{0.92}Dy_{0.08})_2Fe_{14}B$/α-Fe nanocomposite the corresponding peak *dM/dH* is broad with two maxima, the higher negative maxima being bigger. The first one, at very low field, corresponds to the weakly coupled α-Fe crystallites and the second one, at about 0.5 T corresponds to the well exchange coupled soft/hard composite. This behaviour explains both the smooth demagnetisation curves in figure 3 for this composite, the low remanence and poor coercivity. The large *dM/dH* peaks and the long tails testify about the percentage of crystallites which are not well coupled by inter-phase exchange. The very big peak near zero field for $(Pr_{0.92}Dy_{0.08})_2Fe_{14}B$/α-Fe samples proves both, the low coercivity of hard phase and the existence of non coupled Fe crystallites. This behaviour could be understood by the large Fe crystallites (table 1) and the poor anisotropy of $(Pr_{0.92}Dy_{0.08})_2Fe_{14}B$ hard phase. The evolution of the two peaks vs. annealing temperature, the diminution of the low field peak and the development of a *dM/dH* peak at higher field by increasing the annealing temperature, proves the hypothesis that the microstructure of the hard phase, damaged by milling, is not completely recovered by annealing at temperature smaller than 600 ºC. This behaviour proves the weakness in the preparation of this composite.

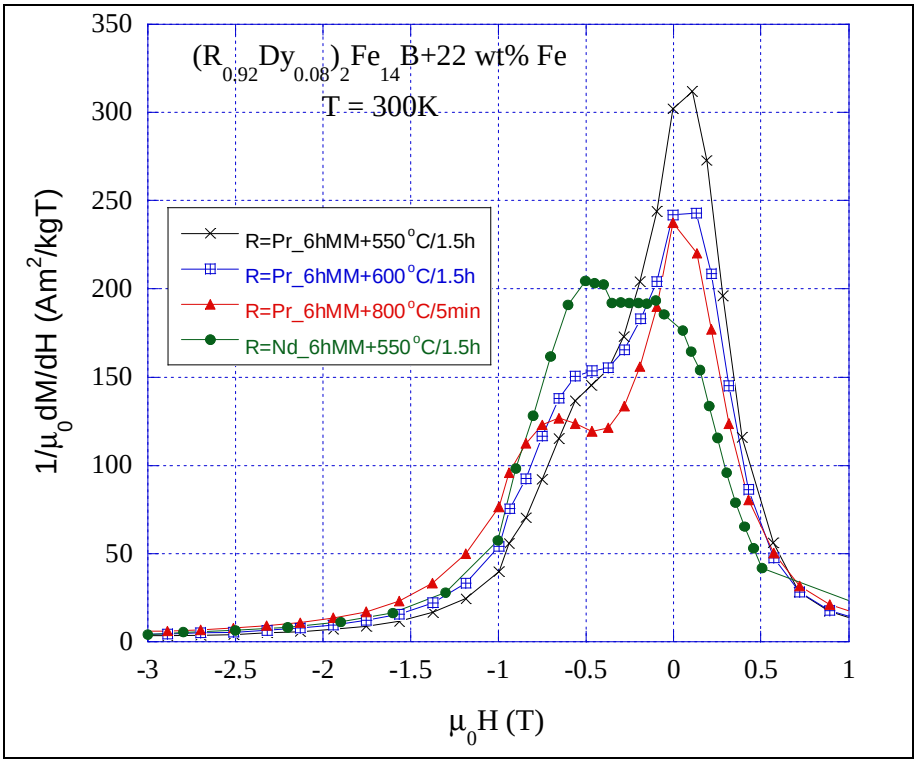

Fig. 4. The *dM/dH* vs. *H* curves of $(R_{0.92}Dy_{0.08})_2Fe_{14}B$ + 22 wt% Fe (R = Nd or Pr) nanocomposite milled for 6 hours and annealed for the indicated time and temperature.

CONCLUSIONS

Mechanical milling and annealing has been applied in order to obtain $(Pr_{0.92}Dy_{0.08})_2Fe_{14}B/\alpha$-Fe exchange coupled magnetic nanocomposite. The influence of the milling and the annealing conditions on the structural and microstructural behaviour of the $(Pr_{0.92}Dy_{0.08})_2Fe_{14}B/\alpha$-Fe composite powder has been studied. The annealing conditions have a direct influence on the efficiency of the exchange coupling between hard and soft magnetic phases. Heat treatments at 550 °C on the powder milled for 4, 6 and 12 hours refine the crystal structure. The α-Fe grain size measured for samples heat treated at 550 °C is between 16-20 nm, smaller than that of those annealed at 650 or 800 °C, indicating that annealing at 650 °C or more can induce the recrystallization of soft α-Fe phase. However, the magnetic measurements prove that also the crystallite size of 550 °C annealed composite are still too large for an optimum inter-phase exchange interactions. Further microstructural and magnetic investigations are in progress in order to well understand these evolutions and to increase the magnetic properties toward the theoretical predictions.

ACKNOWLEDGEMENTS:

The scientific discussions with M. Coldea are gratefully acknowledged. This work has been partly supported by Romanian Ministry of Education, grant PNCD II 72-186/2008.

REFERENCES

1. R. Skomski, J.M.D. Coey, Phys. Rev. B 48, 15812 (1993)
2. T. Lieneweber, H. Kronmüller J. Magn. Magn. Mater. 176, 145 (1997)
3. E.F. Kneller and R. Hawig, IEEE Trans. Magn. 27, 3588 (1991).
4. T. Schrefl, J. Fidler, and H. Kronmüller, Phys. Rev. B 49, 6100 (1994).
5. W.F. Miao, J. Ding, P.G. McCormick, and R. Street, J. Appl. Phys. 79, 2079 (1996).
6. S. Hirosawa, H. Kanekiyo, and M. Uehara, J. Appl. Phys. 73, 6488 (1993).
7. N. Sano, T. Tomida, S. Hirosawa, N. Uehara, and Kanekiyo, Mater. Sci. Eng., A 250, 146 (1998).
8. D.F. Ping, K. Hono, H. Kanekiyo, and S. Hirosawa, J. Appl. Phys. 85, 2448 (1999).
9. Z.H. Cheng, H. Kronmüller, and B. G. Shen, Appl. Phys. Lett. 73, 1586 (1998).
10. A. Bollero et all, J. Alloys Comp. 315 243 (2001).
11. E.P. Wohlfarth, K.H.J. Buschow (Eds.), Ferromagnetic Materials, 4, 20 (1988).
12. M.Q. Huang, E. Oswald, E.B. Boltich, S. Hirosawa, W.E. Wallace, E. Schwab, Phys. Stat. Sol. (b) 130 319 (1985).
13. S. Heisz, G. Hilscher, J. Magn. Magn. Mater. 67 20 (1987).

14. E.B. Boltich, W.E. Wallace, Solid State Commun. 55 529 (1985).
15. S. Hirosawa, Y. Matsuura, H. Yamamoto, S. Fujimura, M. Sagawa, H. Yamauchi, J. Appl. Phys. 59 873 (1986).
16. E. Dorolti, V. Pop, O. Isnard, D. Givord, I. Chicinaş, J. of Opt. and Adv. Mat., 9, 1474 (2007).
17. V. Pop, O. Isnard, I. Chicinaş, D. Givord, J. M. Le Breton, J. of Opt. and Adv. Mat. 8 494 (2006).
18. V. Pop, O. Isnard, I. Chicinaş, D. Givord J. Magn. Magn. Mat. 310 2489 (2007).
19. M. Sagawa, S. Hirosawa, K. Tokuhara, H. Yamamoto, S. Fujimura, Y. Tsubokawa, R. Shimizu, J. Appl. Phys. 61, 3559 (1987).
20. Z. Liu, H.A. Davies, J. Magn. Magn. Mater. 290-291, 1230 (2005).
21. B.E. Meacham, D.J. Branagan, J.E. Shield J. Magn. Magn. Mater. 277, 123 (2004).
22. P. Scherrer Göt. Nachr. 2, 98 (1918).
23. A. Barlet, J.C. Genna, P. Lethuillier, Cryogenics 31, 801, (1991).

STUDIA UNIVERSITATIS BABEŞ-BOLYAI, PHYSICA, LV, 1, 2010

MAGNETIC AND DIELECTRIC BEHAVIOUR OF MAGNETIC FLUIDS IN ELECTROMAGNETIC FIELD

IOSIF MĂLĂESCU[a], PAUL C. FANNIN[b], CĂTĂLIN N. MARIN[a], NICOLETA ŞTEFU[a]

ABSTRACT. The frequency dependencies of the complex dielectric permittivity, $\varepsilon = \varepsilon' - i\varepsilon''$ and of the complex magnetic permeability, $\mu = \mu' - i\mu''$, over the range *100 Hz – 6 GHz*, of a kerosene-based magnetic fluid are presented.

Using the Sillars theory for heterogeneous dielectrics, we have determined the permittivity, electric conductivity and shape factor of the colloidal particles within the magnetic fluid, in microwave range.

From the magnetic relaxation measurements, the Brownian relaxation time τ_B, the hydrodynamic radius r, the Nèel relaxation time τ_N, the effective anisotropy field H_A and the effective anisotropy constant K_{eff} of the magnetic colloidal particles were determined. In addition, these measurements give useful information about the colloidal stabilization of the particles within the magnetic fluid in zero polarizing field.

Based on the ferromagnetic resonance measurements the effective anisotropy constant, anisotropy field, gyromagnetic ratio, γ, damping parameter, α and spectroscopic splitting factor, g of the magnetite colloidal particles are determined.

The paper demonstrates how the investigation of the dielectric and magnetic behaviour of magnetic fluids in electromagnetic field can be employed to determine theirs microscopic and macroscopic properties.

Keywords: *Magnetic fluid, Complex dielectric permittivity, Complex magnetic permeability, Relaxation processes, Ferromagnetic resonance*

INTRODUCTION

Magnetic fluids, also known as ferrofluids, are colloidal systems consisting of single-domain magnetic nanoparticles dispersed in a carrier liquid and stabilized by means of a suitable surfactant [1], [2]. Apart from their multiple applications [1], ranging from instrumentation to medicine [3], the magnetic fluids are convenient model systems to explore fundamental properties of magnetic nanoparticles. Following these reasons, an investigation of the magnetic and dielectric properties of magnetic fluids in electromagnetic field is of great interest.

[a] *West University of Timisoara, Faculty of Physics, Bd. V. Parvan #4, 300223 Timisoara, Romania*
[b] *Department of Electronic and Electrical Engineering, Trinity College, Dublin 2, Ireland*

This paper is a review of the dielectric and magnetic relaxation processes and of the ferromagnetic resonance phenomenon in magnetic fluids, with the aim to show how the complex permittivity and permeability measurements can be used to determine certain properties of magnetic fluids, as well as specific parameters of nanoparticles.

EXPERIMENTAL

For dielectric and magnetic measurements we have used a commercial kerosene-based magnetic fluid with magnetite particles, having the saturation magnetization M_∞=*11.32 kA/m* and the mean magnetic diameter of the particles d_m=*11.1 nm*.

The colloidal particles from the investigated sample have been obtained by chemical co-precipitation and the stabilization of the magnetic colloidal particles was done by hydrofobization with technical oleic acid in the absence of the dispersion medium [4].

The components of the complex magnetic permeability have been measured by means of the toroidal technique, over the frequency range 100Hz – 1MHz [5]. The dielectric and magnetic measurements (over the frequency range *0.4* to *6 GHz*) were made by means of the coaxial transmission line technique [6, 7] in the presence of an external magnetic field. The biasing field, H, was changed in the approximate range *0* to *105 kA/m*.

RESULTS AND DISCUSSIONS

The dielectric behaviour

The magnetic fluids have a complex structure consisting of colloidal particles electrically charged by adsorbed or chemisorbed ions dispersed in a dielectric liquid. Therefore, the magnetic fluids behave as heterogeneous dielectric materials and several dielectric relaxation processes occur. As theoretically described [8] and experimentally confirmed [9, 10], in low frequency field the deformation of the counter-ions atmosphere surrounding the colloidal particles, due to an electric field, is responsible for the dielectric behaviour. The mobility of ions from the counter-ions atmosphere surrounding the colloidal particles is not large enough to follow the change of the high frequency electric field. Consequently, the interfacial relaxation process is expected to occur in high frequency field. This is usually explained in terms of the Maxwell-Garnett-Sillars theory [11, 12].

Depending on the dielectric parameters and on the conductivity of its constituents, a magnetic fluid may or may not exhibit an interfacial relaxation peak. For those magnetic fluids that exhibit such a relaxation peak, the Sillars model [13] in the biphase approximation can be used to determine the dielectric permittivity and the conductivity of the colloidal particles.

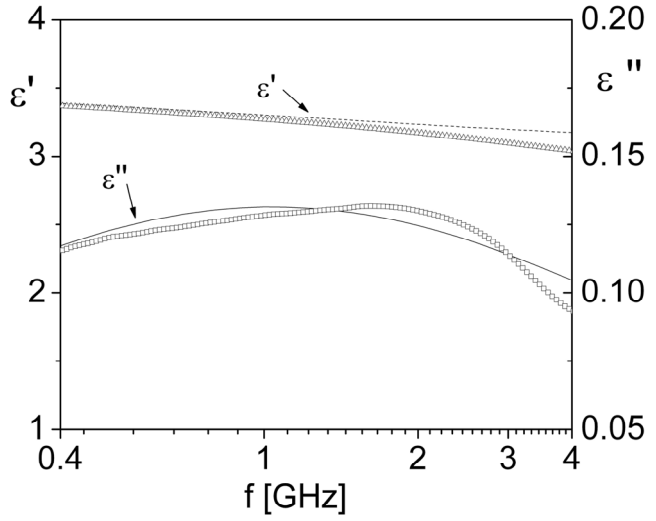

Fig. 1. Frequency dependence of the real part (ε') and of the imaginary part (ε") of the complex dielectric permittivity of the sample

The frequency dependence of the complex dielectric permittivity of the investigated sample is presented in figure 1. The frequency dependences of the complex dielectric permittivity of kerosene and oleic acid are presented in figure 2.

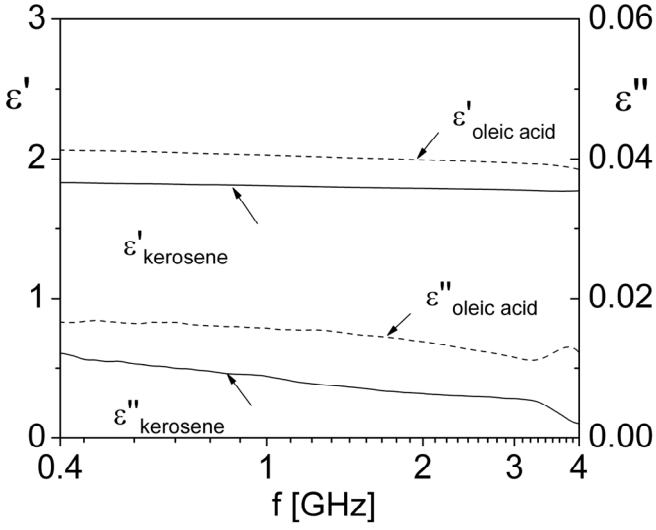

Fig. 2. Frequency dependence of the real part (ε') and of the imaginary part (ε") of the complex dielectric permittivity of kerosene and oleic acid

As it can be observed in figure 2, no relaxation peak occurs for either kerosene or oleic acid in the investigated frequency range. This allows us to assume that the relaxation peak observed for the magnetic fluid (figure 1) is due to the interfacial relaxation process.

The magnetic fluids can be considered as being biphase systems in which one phase consists of surfacted colloidal particles electrically charged by adsorbed or chemisorbed ions and the other phase consists of the carrier liquid. Using the Sillars theory for heterogeneous dielectrics [13], in the biphase approximation, the complex dielectric permittivity of the magnetic fluid can be rewritten in Debye form,

$$\varepsilon_{eff} = \varepsilon_{\infty} + \frac{\Delta\varepsilon}{1 + i\omega\tau} - i\frac{\sigma_{eff}}{\omega\varepsilon_0} \tag{1}$$

with the notations (2) - (5).

$$\Delta\varepsilon = \frac{1}{n}\frac{(\varepsilon_2'\sigma_{1eff} - \varepsilon_1'\sigma_{2eff})^2\Phi(1-\Phi)}{\left[\varepsilon_2' + (1/n)(1-\Phi)(\varepsilon_1' - \varepsilon_2')\right]\cdot\left[\sigma_{2eff} + (1/n)(1-\Phi)(\sigma_{1eff} - \sigma_{2eff})\right]^2} \tag{2}$$

$$\varepsilon_{\infty} = \varepsilon_2' \cdot \left(1 + \Phi\frac{\varepsilon_1' - \varepsilon_2'}{\varepsilon_2' + (1/n)(1-\Phi)(\varepsilon_1' - \varepsilon_2')}\right) \tag{3}$$

$$\sigma_{eff} = \sigma_{2eff} \cdot \left(1 + \Phi\frac{\sigma_{1eff} - \sigma_{2eff}}{\sigma_{2eff} + (1/n)(1-\Phi)(\sigma_{1eff} - \sigma_{2eff}}\right) \tag{4}$$

$$\tau = \varepsilon_0 \cdot \left(\frac{\varepsilon_2' + (1/n)(1-\Phi)(\varepsilon_1' - \varepsilon_2')}{\sigma_{2eff} + (1/n)(1-\Phi)(\sigma_{1eff} - \sigma_{2eff}}\right) \tag{5}$$

In equations (1) - (5), Φ is the volume fraction of the colloidal particles; n is the particle shape factor; ε_0 is the permittivity of the free space; ω is the angular frequency of the electromagnetic field; ε_1' and ε_1'' are the real and the imaginary part of the complex permittivity of the magnetite colloidal particles; σ_1 and σ_{1eff} are the d.c. conductivity and the effective conductivity (including the relaxation losses) of the magnetite colloidal particles; ε_2' and ε_2'' are the real and the imaginary part of the complex permittivity of kerosene; σ_2 and σ_{2eff} are the d.c. conductivity and the effective conductivity (including the relaxation losses) of kerosene.

Due to the particle size and shape dispersion, the magnetic fluid is characterized by a distribution of relaxation times. Fitting the theoretical dependencies (6) and (7) to the experimental data (see figure1), the relaxation time was determined, resulting in $\tau = 4.71 \cdot 10^{-10}$ s.

$$\varepsilon'_{eff} = \int_0^{\infty} \left(\varepsilon_{\infty} + \frac{\Delta\varepsilon}{1+\omega^2\tau^2} \right) \cdot f(\tau) d\tau \tag{6}$$

$$\varepsilon''_{eff} = \int_0^{\infty} \left(\frac{\omega\tau \cdot \Delta\varepsilon}{1+\omega^2\tau^2} + \frac{\sigma_{eff}}{\varepsilon_0 \omega} \right) \cdot f(\tau) d\tau \tag{7}$$

The shape factor *n*, the real part of the dielectric permittivity, ε'_1 and the effective conductivity, σ_1 for the magnetite colloidal particles were obtained by means of equations (2) - (5), using the following values: i) $\varepsilon_{\infty} = 3.08$ (experimental value for the magnetic fluid, see figure 1); ii) $\Delta\varepsilon = 0.4319$ and $\tau = 4.71 \cdot 10^{-10}$ *s* (resulted from fit); iii) $\varepsilon'_2 = 1.84$ (experimental value for kerosene, see figure 2); iv) $\sigma_{2eff} = \sigma_2 + \omega\varepsilon_0\varepsilon''_2 = 5.5 \cdot 10^{-4}\,\Omega^{-1}m^{-1}$ computed for a frequency of *1GHz*, considering $\sigma_2 = 10^{-14}\ \Omega^{-1}m^{-1}$ [14] and $\varepsilon''_2 = 0.01$ (experimental value, see figure 2). The following results were obtained: $n = 3.57$, $\sigma_{1eff} = 0.537\,\Omega^{-1}m^{-1}$ and $\varepsilon'_1 = 22.2$. The determined parameters *n*, ε'_1 and σ_{1eff} do not correspond only to the magnetite particles. They are effective parameters corresponding to the biphase model in which one phase consists of magnetite colloidal particles surfacted with oleic acid and surrounded by an electric double layer, and the other phase is the carrier liquid. Therefore, these parameters may differ from one magnetic fluid to another, depending on the obtaining method, even if the same materials are used.

The magnetic behaviour

a) The relaxation processes

The magnetization of magnetic fluids in a variable magnetic field is realized either by rotating the particles in the carrier liquid or by rotating the magnetic moment inside the particles [15-17]. Consequently, two magnetic relaxation processes are possible in magnetic fluids: the Brownian relaxation process and the Néel relaxation process. Due to the relaxation processes, the imaginary component μ'' of the complex magnetic permeability shows a maximum at a certain frequency f_m. According to the Debye theory [18], the relaxation time τ is correlated with this frequency through the relation:

$$2\pi f_m \tau = 1 \tag{8}$$

The time corresponding to the Brownian relaxation process, τ_B, depends on the viscosity η, of the carrier fluid and on the hydrodynamic radius *r*, of the particle, by the relation:

$$\tau_B = \frac{4\pi\eta r^3}{kT} \tag{9}$$

where k is the Boltzmann's constant and T is the absolute temperature of the system. Taking into account the viscosity of kerosene, $\eta=1.2\cdot10^{-3}\ Pa\cdot s$, and the typical value of the mean hydrodynamic diameter of particles, *15nm* [1, 2], the equation (9) allows us to estimate the Brownian relaxation time, resulting in $\tau_B=1.5\mu s$.

For the sample investigated in low frequency field, the frequency dependencies of μ' and μ'' are presented in figure 3.

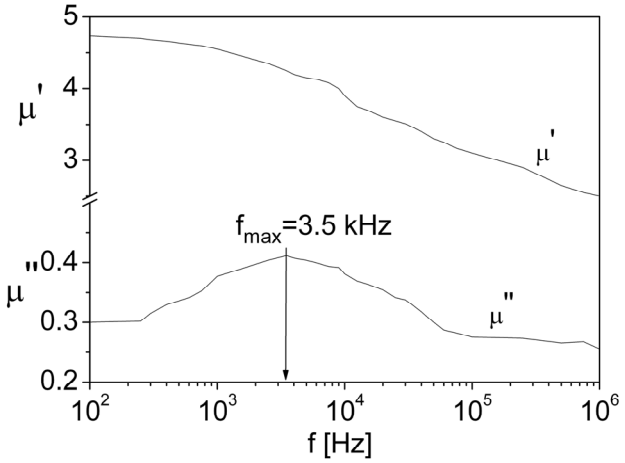

Fig. 3. The frequency dependence of μ' and μ'' for the sample in low frequency field

As shown in figure 3, the magnetic fluid presents a maximum for the imaginary component μ'' of the complex magnetic permeability. The frequency corresponding to the maximum is *3.5 kHz*. Using this frequency and the equation (8), the relaxation time was calculated, resulting in $\tau_B=45.49\ \mu s$. Based on this value of the relaxation time, one can assert that the maximum of μ'' corresponding to the low frequencies is assigned to the Brownian relaxation process.

From the Eq. (9) and using the value obtained for τ_B, the mean hydrodynamic radius of the particles was calculated, resulting in $r_{exp}=23.2\ nm$. Taking into account the average value of the magnetic diameter of particles within the investigated magnetic fluid, ($d_m=9.30\ nm$), and assuming a nonmagnetic shell of approximately *3 nm* (including the surfactant layer), we have calculated a theoretical value, r_{th}, for the mean hydrodynamic radius of particles, resulting in $r_{th}=7.65\ nm$. The experimental value for the hydrodynamic radius is much larger than the calculated value. This allows us to assert that within the investigated sample large particle agglomerations are formed.

The time corresponding to the Néel relaxation process, τ_N, is given by the equation:

$$\tau_N = \tau_0 \exp\left(\frac{K_{eff}V_m}{kT}\right) \tag{10}$$

where K_{eff} is the effective anisotropy constant (including magnetocrystalline, shape and surface effects); V_m is the magnetic volume of the particle and τ_0 is a constant having the magnitude 10^{-9} *s*.

Using a typical value for the mean magnetic diameter of the particles within magnetic fluids, in order of *10 nm* and the effective anisotropy constant of magnetite particles, in order of 10^4 *J/m*^{3}, the equation (10) gives an estimated value for τ_N, resulting in τ_N=*3.5 ns* [15-17].

For the sample investigated in radiofrequency field, the frequency dependencies of μ' and μ'' are presented in figure 4.

As shown in figure 4, the magnetic fluid presents a maximum for the imaginary component μ'', of the complex magnetic permeability. The frequency corresponding to the maximum is *32 MHz*. Using this frequency and the equation (8), the relaxation time was calculated, resulting in *5 ns*. Based on this value of the relaxation time, one can assert that the maximum of μ'' is assigned to the Néel relaxation process.

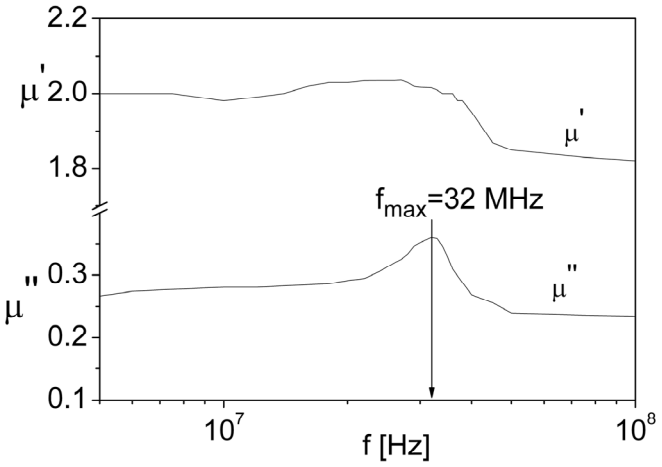

Fig. 4. The frequency dependence of μ' and μ'' for the sample in radiofrequency field

From the equation (10) and using the value obtained for the Néel relaxation time (τ_N=*5 ns*), one obtains the effective anisotropy constant of the particles within the investigated magnetic fluid, K_{eff}=$15.7 \cdot 10^3$ *J/m*^{3}. The large value of K_{eff} for the colloidal magnetite particles, can be assigned to the strong magnetic interactions between the particles due to possible particle agglomerations. This result is in agreement with the result obtained from the Brownian relaxation measurements. Therefore, the measurements of relaxation times allow obtaining information about the colloidal stabilization of the magnetic particles within the investigated magnetic fluid sample in zero polarizing fields.

b) The ferromagnetic resonance

The magnetic resonance phenomenon in magnetic fluids is determined from measurements of complex magnetic permeability, $\mu(\omega) = \mu'(\omega) + j\mu''(\omega)$ at a constant polarizing field [19, 20]. The resonance is indicated by a transition in the value of the real part of complex magnetic permeability, $\mu'(\omega)$, from a supraunitary to a subunitary quantity at a frequency f_{res}. The imaginary component $\mu''(\omega)$ exhibits a maximum at a frequency f_{max}, which is always smaller than f_{res} [21] (figure 5).

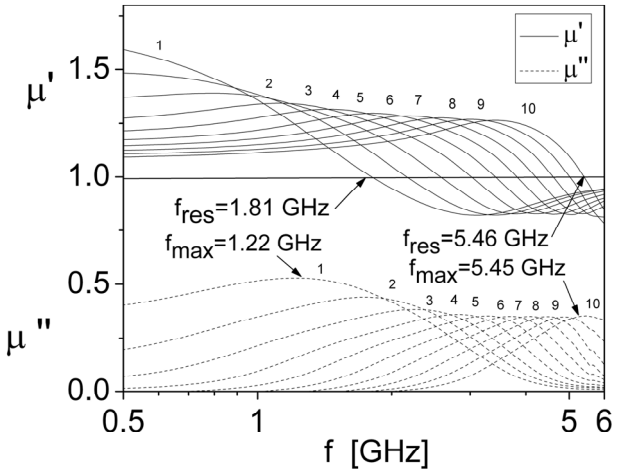

Fig. 5. Frequency and field dependence of μ' and μ'', for the sample in microwave range; the polarizing field strengths are approximately: (1) 0 kA/m, (2) 15.23 kA/m, (3) 24.47 kA/m, (4) 35.28 kA/m, (5) 46.18 kA/m, (6) 57.07 kA/m, (7) 68.49 kA/m,(8) 79.33 kA/m, (9) 90.66 kA/m, (10) 102.40 kA/m.

In a constant polarizing field, H, the resonance condition is given by the expression [21]:

$$f_{res} = \frac{\gamma(1+\alpha^2)^{1/2}}{2\pi}(H + H_A) \tag{11}$$

where $\gamma = \mu_0 g \gamma_e$, is the gyromagnetic ratio; $\gamma_e = e/2m_e$ is the electronic gyromagnetic ratio; α is the damping parameter of the Landau-Lifshitz equation; g is the spectroscopic splitting factor, which is correlated with the Lande factor, g_L, by relation $2 - g_L = g - 2$ [22]; μ_0 is the free space permeability and

$$H_A = \frac{2K_{eff}}{\mu_0 M_S} \tag{12}$$

is the effective anisotropy field, M_S, being the spontaneous magnetization of the bulk material of particle.

By fitting the equation (11) to the experimental dependence $f_{res}(H)$ (see Fig. 6) the anisotropy field, H_A, was determined, resulting in: $H_A=48.14$ *kA/m*. Using Eq. (12) and the value $M_S=480$ *kA/m* [22], the effective anisotropy constant was computed. The obtained value $K_{eff}=14.4\cdot10^3 J/m^3$ is larger than the reported value of bulk magnetite ($K=11\cdot10^3 J/m^3$ [22]) due to the interparticle interactions [23] and is in agreement with the conclusion drawn from the Néel relaxation measurements.

As demonstrated in Ref. [21], the ratio f_{max}/f_{res} increases with the polarizing field, H, approaching unity for $H>H_A$. In a strong polarizing field ($H>H_A$) the damping parameter of the Landau-Lifshitz equation satisfies the equation (13) [21].

$$\alpha = \sqrt{\frac{1-(f_{\max}/f_{res})^2}{1+(f_{\max}/f_{res})^2}} \tag{13}$$

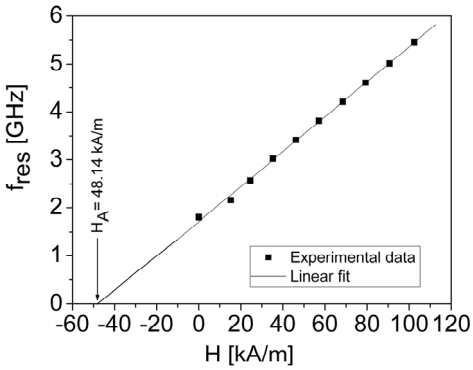

Fig. 6. Polarizing field dependence of f_{res}

From the dependence of f_{max}/f_{res} on H for $H>H_A$ (see figure 7) the mean value for α was computed, resulting in $\alpha = 0.13$.

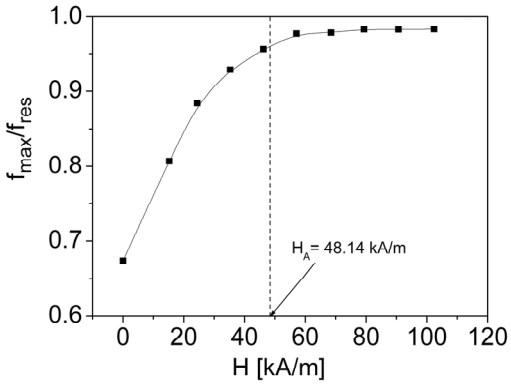

Fig. 7. The polarizing field dependence of the ratio f_{max} / f_{res}

Using the value (obtained from the fit) for the slope $\frac{\gamma(1+\alpha^2)^{1/2}}{2\pi}$ of the linear dependence of $f_{res}(H)$ (see Fig.6) and the value of α obtained above, we have computed the gyromagnetic ratio, resulting in $\gamma=2.271\cdot10^5\ s^{-1}A^{-1}m$. Taking into account the expression of γ (i. e. $\gamma=\mu_0 g\gamma_e$), the spectroscopic splitting factor was computed, resulting in $g=2.056$. This value of g obtained for the magnetite nanoparticles lays between 2 (corresponding to the free spins [22]) and 2.17 (corresponding to the bulk magnetite [24]).

CONCLUSIONS

Using the Sillars theory and the dielectric measurements in microwave range, we have determined some parameters of the magnetite colloidal particles within the investigated magnetic fluid such as: the dielectric permittivity, electric conductivity and the shape factor.

Based on the magnetic relaxation measurements, we have determined the Brownian relaxation time, τ_B, and the Nèel relaxation time, τ_N, of the investigated magnetic fluid, as well as the hydrodynamic radius, r, and the anisotropy constant of the magnetite colloidal particles, K_{eff}. The measurement of relaxation times also gives useful information about the colloidal stabilization of the magnetic particles within the investigated magnetic fluid sample in zero polarizing fields.

From the ferromagnetic resonance measurements, the values of the anisotropy constant, anisotropy field, the damping parameter, α the gyromagnetic ratio, γ and the spectroscopic splitting factor, g, of the magnetite colloidal particles were determined.

The complex permittivity and permeability measurements are therefore powerful tools in the investigation of the magnetic fluids, in determining their macroscopic and microscopic properties.

REFERENCES

1. E. Luca, Gh. Calugaru, R. Badescu, C. Cotae and V. Badescu, “Ferofluide si aplicatiile lor in industrie”, Ed. Tehnica, Bucuresti, **1978**
2. J.C Bacri and R. Perzynski, “Magnetic fluids and applications handbook”, Ed. B. Berkovski and V. Bashtovoy, New York, Begell House Inc., **1996**
3. Q.A. Pankhurst, J. Connolly, S.K. Jones and J. Dobson, *J. Phys. D: Appl. Phys.,* **2003,** 36, R167
4. I. Malaescu, L. Gabor, F. Claici, N. Stefu, *J. Magn. Magn. Mater*., **2000,** 222, 8

5. Fannin, P.C, Scaife, B.K.P, and Charles, S.W, *J. Phys. E. Sci. Instrum.*, **1986**, 19, 238
6. P.C. Fannin, B.K.P. Scaife, S.W. Charles, *J. Magn. Magn. Mater.*, **1990**, 85, 54
7. I. Hrianca, I. Malaescu, *J. Magn. Magn. Mater.*, **1995**, 150, 131
8. G. Schwarz, *J. Phys. Chem.*, **1962**, 66, 2636
9. M. M. Radulescu, *J. Magn. Magn. Mater.,* **1990***,* 85, 144
10. I. Malaescu, C.N. Marin, *J. Colloid Interface Sci.*, **2002**, 251, 73
11. O. Derriche, L. Jorat, G. Noyel, J. Monin, *J. Magn. Magn. Mater.*, **1991**, 102, 255
12. R. Pelster, A. Spanoudaki, T. Kruse, *J. Phys. D: Appl. Phys.*, **2004**, 37, 307
13. R.W. Sillars, *Journal of Institution of Electrical Engineers,* **1937**, 80, 378
14. G. Kronkalns, *Magnetohydrodynamics*, **2004**, 40, 297
15. I. Hrianca, I. Malaescu, *J. Magn. Magn. Mater.*, **1995**, 150, 131
16. P.C. Fannin, B.K.P. Scaife, S.W. Charles, *J. Phys. D: Appl. Phys.*, **1988**, 21, 533
17. P.C. Fannin, B.K.P. Scaife, S.W. Charles, *J. Magn. Magn. Mater*., **1993**, 122, 159
18. P. Debye, "Polar Molecules (The Chemical Catalog Company)", New York, **1929**
19. P.C. Fannin, *J. Mol.Liquids*, **2004**, 79, 87
20. P.C. Fannin, *Adv. Chem.Phys.,* **1998,** 104, 181
21. P.C. Fannin, C.N. Marin, I. Malaescu, *J. Phys.: Condens. Matter.*, **2003**, 15, 4739
22. S.V. Vonsovski, "Magnetismul", Ed. St. si Encicl., Bucuresti, **1981**
23. C.N. Marin, I. Malaescu, A. Ercuța, *J.Phys.D: Appl. Phys*. **2001**, 34, 1466
24. L.R. Bickford, *Phys. Rev*. **1950**, 78, 449

STUDIA UNIVERSITATIS BABEŞ-BOLYAI, PHYSICA, LV, 1, 2010

STRUCTURAL AND ELECTRIC PROPERTIES OF Bi:2212 THIN FILMS OBTAINED BY THE OPTIMIZATION OF D. C. SPUTTERING PARAMETERS AND SUBSTRATE TEMPERATURE

A. V. POP[a]*, AL. OKOS[a], I. POP[a], S. MANOLACHE[a]

ABSTRACT. The target and growth conditions (sputtering pressure, substrate temperature, d. c. plasma power and sputtering gas composition) for the deposition of thin Bi:2212 films by d. c. magnetron sputtering have been optimized.

X-ray diffraction shows that the films are single phase, oriented with their c-axis perpendicular to the substrate surface. Transport properties investigated by electrical resistivity function of temperature show the influence of substrate temperature on the intergrowth defects.

Keywords: *Bi:2212 thin film, DC magnetron sputtering, growth conditions, XRD, resistivity.*

INTRODUCTION

Among the high Tc superconductors (HTS) cuprates, $Bi_2Sr_2CaCu_2O_y$ (Bi:2212) superconductor exhibits the largest anisotropy, which is function of temperature and doping. The intrinsic Josephson effect exists in highly anisotropic Bi:2212 superconductor. The films with c-axis aligned to the film plane appear to to be suited for the fabrication of sandwich type SNS and SIS Josephson junction and quasiparticle tunnel junctions [1]. Much attention has been given to the Bi:2212 thin films from the viewpoint of their utilization as artificial intrinsic Josephson junction for THz- wave generation [2], buffer layer for fabrication of Bi:2212 and Bi:2223 thin films [3]. For the deposition of BSCCO films difficulties arise from possible phase mixture and oxygen overdoping. Thin films of Bi:2212 grow epitaxially depending on the substrate material, thermodynamic and kinetic growth conditions. The epitaxial growth of Bi:2212 thin films has been realized on substrates like $SrTiO_3$, $LaAlO_3$ and MgO [4-7]. The 2D nature of the superconductor-insulator transition in Bi:2212 and Bi:2201 nanoscale thin films was examined [5, 6]. Usually these films were grown with their c-axis perpendicular to the substrate surface, since c-axis growth is the thermodynamically favored growth direction. Sputtering is one of the most common vacuum techniques currently applied for superconducting

[a] *Faculty of Physics, University Babes-Bolyai, Cluj-Napoca, Romania, * avpop@phys. ubbcluj. ro*

oxide thin film growth. The sputter deposition technique can tolerate quite high gas pressure, while still giving controllable growth rates, as long as the targets surface is insensitive to oxidation. The key requirements for HTS thin films quality are: precise control of the growth conditions such as growth temperature and oxidizing gas pressures etc., meaning that a variety of thermodynamic factors should be optimized [7].

Here we present the optimization of the dc sputtering deposition parameters for the fabrication of epitaxial Bi:2212 films. The thin films were characterized by X-ray diffraction and electrical resistivity measurements versus temperature.

EXPERIMENTAL

Bi:2212 thin films were deposited onto (100) $SrTiO_3$ heated single crystal substrate using a DC magnetron sputtering system. A major problem that appears during the deposition of Bi:2212 thin films is the Bi losses. The film composition function of temperature shows that the Bi ratio gradually diminishes for temperatures above 600 ^{0}C [8]. In order to compensate this loss, a bismuth enriched target has been synthesized with chemical effective composition $Bi_{2.6}Sr_{1.9}Ca_{0.9}Cu_{2.4}O_y$. For the synthesis of target the solid state reaction route was used. The target composition was measured by EDAX analysis normalized to the Cu. The resulting material is superconducting with Tc=82K. XRD shows that Bi:2212 is the majority phase with some traces of Bi:2201 and CuO. The in-situ thin films were obtained by on-axis d. c. magnetron sputtering. The optimal parameters used for the fabrication of epitaxial quality Bi:2212 thin films were: sputtering gas pressure of 0. 9 mbar (with a ratio 1/1 between the argon and oxygen partial pressures), the substrate temperature 790 ^{0}C and d. c. plasma power between 20W and 30W. The growth rates of the films is of the order 10-15 Å/min. The increase of Tc for the Bi:2212 thin films arises by optimizing the oxygenation of BiO bilayers [9]. The oxygen content of our thin films was adjusted by an oxygenation treatment after the high temperature annealing. The oxygen pressure was of 0. 1 mbar, the substrate temperature of 500 ^{0}C and the oxygenation time of 45 minute.

RESULTS AND DISCUSSIONS

Figure 1 shows the X-ray diffraction pattern obtained for the best quality Bi:2212 thin film deposited in optimal conditions. This figure provides a 20× magnification of baseline. No additional peaks can be distinguished from the background, a good indication that the film are free from bulk secondary phases. The peak indexation indicates only (00l) reflexions for thin films and (h00) reflexions for $SrTiO_3$ substrate. This behavior suggest that the film is oriented with their c-axis perpendicular to the substrate surface.

The informations about the perpendicular misorientation of the microcrystallites composing the film was investigated by the measurement of rocking curve. The θ–2θ angle is fixed on the reference (00$\underline{10}$) peak for all measured samples.

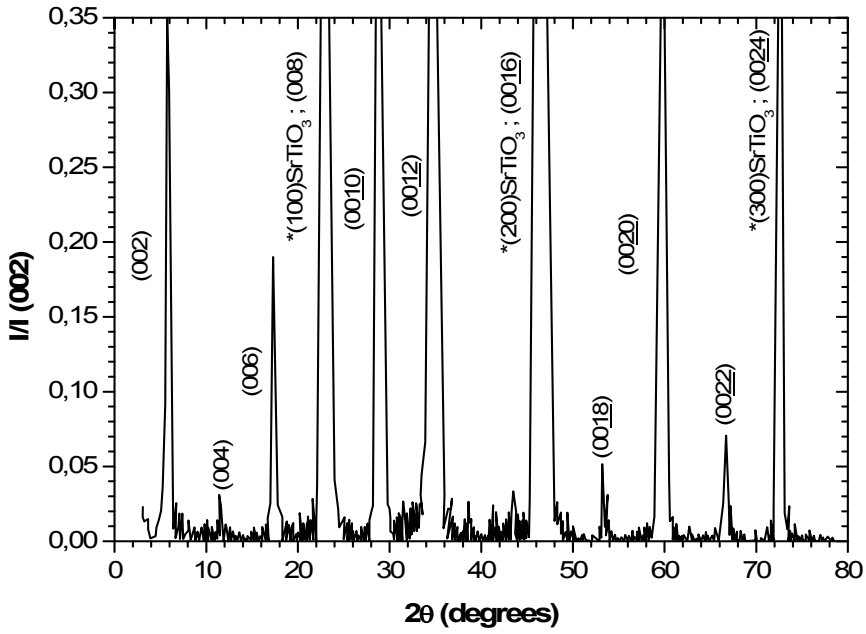

Fig. 1. X-ray diffraction pattern of Bi:2212 film deposited on $SrTiO_3$ substrate. The intensity of baseline is enlarged 20 times. The substrate (h00) reflexions are labeled by asterisk.

Figure 2 shows the rocking curve for the Bi:2212 film deposited under optimal conditions. The FWHM (full width for high maximum) of rocking curve is equal to 0. 39^0 and confirmed the high orientational quality of sample. For epitaxial thin films, typical values of the FWHM are of the order of 1^0, sometime lower, depending on the composition of the deposited material and/or the growth conditions. The effect of the sputtering pressure on the orientation of Bi:2212 film has been investigated by the deposition of many thin films under various total pressures ranging from 0. 5 to 1. 2 mbar. Above 1mbar the plasma becomes increasingly unstable In order to prevent target damage, the depositions were carried out at a total pressure of 0. 9 mbar. In the pressure range 0. 5 to 0. 9 mbar no change in the average FWHM of the rocking curve could be observed. The substrate temperature is one of the most important parameter for obtained high quality films, because of the influence on the stability of Bi:2212 phase and on the Bi losses.

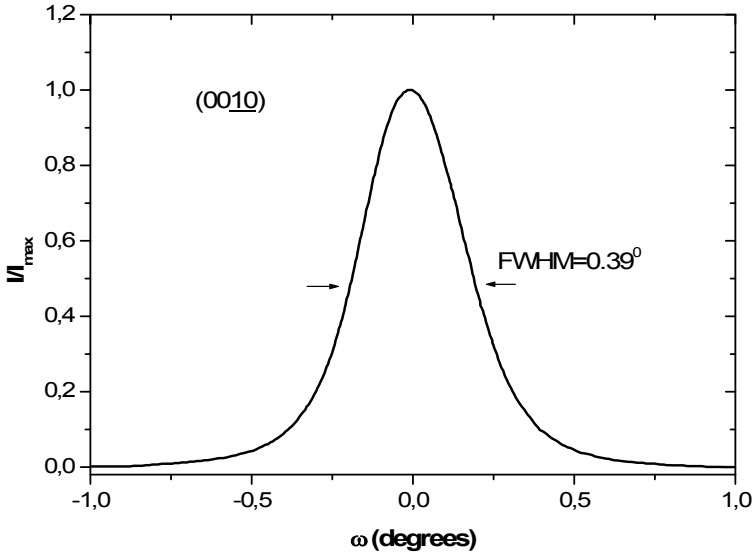

Fig. 2. The rocking curve around the (00$\underline{1}$0) line of Bi:2212 thin films obtained in optimal conditions on $SrTiO_3$ substrate.

Fig. 3 shows the effect of substrate temperature on the (002) line of θ –2θ X ray diffraction pattern of thin films deposited on $SrTiO_3$ substrate. A narrow and symmetric (002) peak of Bi:2212 phase is measured for the optimal temperature of 790 ^{0}C. Below the optimal temperature Bi:2201 intergrowth begins to appear [10]. At temperatures higher than 790 ^{0}C, the Bi:2223 phase intergrowth is favored and the epitaxial quality is reduced. The intergrowth is the dominant stacking fault in the BSCCO system. In the intergrowth, layers of Bi:2201, Bi:2212 and Bi:2223 appear in the overall structure. In our films with the chemical composition corresponding to the Bi:2212 phase, inserted 2201 and 2223 layers may appear in the 2212 matrix without causing any compositional change.

Since low densities of intergrowth are difficult to detect by X-ray diffraction, but have a prominent effect on the electrical resistance.

Fig. 4. show the temperature dependence of electrical resistance for two Bi:2212 thin films obtained for the substrate temperature t_s=795 ^{0}C (optimal conditions) and a temperature t_s=815 ^{0}C slightly higher than the optimal one. The optimal sample with T_c = 85K shows an extrapolated ρ(T=0K)=7% ρ(T=300K) with ρ(T=300K) =750 μΩ.cm. This value characterizes the pure Bi:2212 superconducting system [4, 11]. The kink around 110K (arrow in fig. 4 and first derivative in insert) indicates the presence of a small quantity of Bi:2223 intergrowth in the film at a substrate temperature of 815 ^{0}C. This result agrees with the shift of the (002) diffraction line from the optimal position to links (around 2θ =5 degrees) in fig. 3.

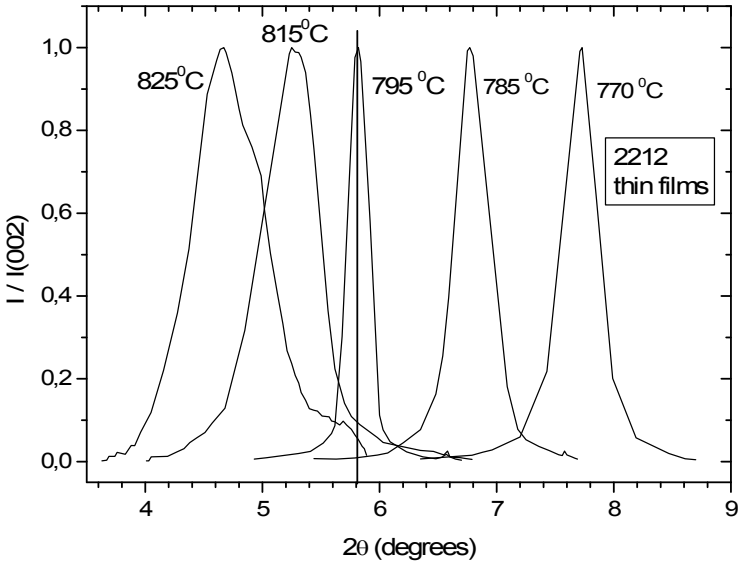

Fig. 3. The variation of the normalized (002) peak obtained by X-ray diffraction on Bi:2212 samples deposited on $SrTiO_3$ at different temperatures

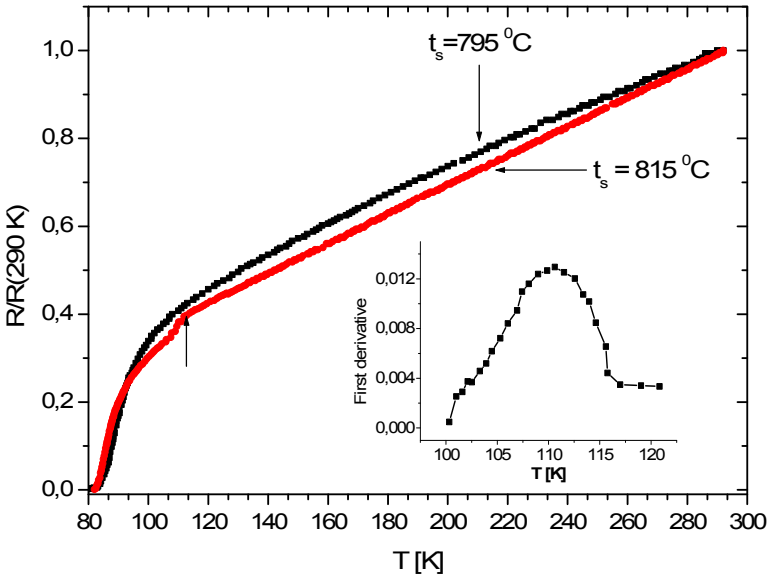

Fig. 4. The normalized resistance R/R(300K) versus temperature for thin film with optimal tempearature of substrate (t_s=790 ^{0}C) and the film with t_s=820 ^{0}C. The insert show first derivative dR/dT in the region of the kink.

For these samples containing a few intergrowth of Bi:2223, the XRD peaks are only slightly displaced away from the pure Bi:2212 pattern. The sample obtained for the substrate temperature t_s=815 ^{0}C shows a critical transition temperature T_c =85K and a tresidual resistivity lower than in sample obtained for t_s=795 ^{0}C.

CONCLUSIONS

The target composition and growth conditions for the deposition of Bi:2212 films by d. c. magnetron sputtering have been optimized, by the precise control of the growth conditions (substrate temperature and oxidizing gas pressures)

XRD shows that the synthesized films in optimal conditions were single Bi:2212 phase and well oriented with c-axis perpendicular to substrate surface. Electrical resistivity shows in normal state a metallic behavior and a sharp superconductive transition.

The increase of substrate temperature above optimal temperature t_s=790 ^{0}C lead to a few intergrowth of Bi:2223 (with T_c =110K). The presence of intergrowth is related by the kink around 110 K in the resistivity curve versus temperature and by the decrease of residual resistivity.

ACKNOWLEDGEMENTS

We thanks to PN II Romania for financial support (grant 71-140).

REFERENCES

1. J. Geerk, X. X. Xi, G. Linker, Z. Phys. **B73**, 1327 (1988).
2. T. Tachiki, A. Sugawara, T. Uchida, Physica C 469, 1604 (2009).
3. T. Satoh, J. Fujita, T. Yoshitake, H. Igarashi, S. Miura, N. Matsukura, H. Tsuge, Physica **C 185-189**, 2059 (1991).
4. P. Wagner, F. Hillmeyer, U. Frey, H. Adrian, T. Steinborn, L. Ranno, A. Elschner, I. Heyvaert, Y. Bruynserade, Physica **C215**, 123 (1993).
5. L. X. You, A. Yurgens, D. Winkler, C. T. Liu, B. Liang, Supercond. Sci. Technol. **19**, S205 (2006)
6. A. V. Pop, G. Ilonca, M. Pop, JOAM **8**, 480 (2006)
7. R. Rossler, J. D. Pedarnig, Ch. Joos, Physica **C361**, 13-21 (2001)
8. T. Onishi, N. Fujiwara, S. Kishida, Physica **C426-431**, 1439 (2005),
9. J. M. Grace, D. B. McDonald, M. T. Reiten, J. Olsen, R. T. Kampwirth, K. E. Gray,
10. J. Appl. Phys. **70**, 3867 (1991).
11. T. Watanabe, T. Fuji, A. Matsuda, Phys. Rev. Lett. **79**, 2113 (1997).
12. L. Ranno, D. Marquez-Garcia, J. Perriere, P. Barboux, Phys. Rev. **B 48**, 13945 (1993).
13. S. Labdy, S. Megtert, H. Raffy, Sol. State Commun. **85**, 491 (1993).

STUDIA UNIVERSITATIS BABEŞ-BOLYAI, PHYSICA, LV, 1, 2010

X-RAY DIFFRACTION STUDIES OF $CeNi_5$ POWDER OXIDIZED IN AIR

LIDIA REDNIC[a, b], MARIN COLDEA[a], VASILE REDNIC[b], NICOLAE ALDEA[b]

ABSTRACT. Synthesis and dimensionality studies for $CeNi_5$ powder, oxidized in air at different temperatures, up to 800^{o}C, are reported. Powder X-Ray Diffraction (XRD) and Transmission Electron Microscopy (TEM) measurements were used in order to determine resulting products morphology. The average crystalline size was obtained by X-Ray line broadening investigations from the integral breadth or the full width at half maximum (FWHM) of the diffraction profile. The approximation and decomposition of experimental X-Ray line profiles were analytically calculated using four fitting methods: Gauss, Cauchy, Voigt and Generalized Fermi Function (GFF).

Keywords: *CeNi5, powder,X-ray diffraction*

INTRODUCTION

As advanced technologies are expanding, the need for novel functional materials significantly increases. Materials containing or consisting of nanosized metal particles have gained considerable attention in the last decades. Nanosized particles of ferromagnetic metals (Fe, Co, Ni) have been widely studied as they present an interest both for fundamental physics and potential applications such as catalysis, high density magnetic recording media, ferrofluids and medical diagnostics [1-4]. The nanophase materials perform more efficiently than their bulk counterparts due to the outstanding properties emerging from the so-called size effects [5-10]. However, synthesis, handling and storage of such materials give rise to problems related both to their size control and to the stabilization of the highly reactive resulting product. Several methods have been used for the production of such particles: evaporation [11-14], sputtering [15], and various chemical methods [16-18]. Evaporation techniques allow producing isolated particles whereas the others are used to produce particles dispersed in an insulating matrix.

Magnetic nanoparticles covered with a layer of antiferromagnetic oxide exhibit large coercitive forces due to the exchange anisotropy at the ferromagnetic-antiferromagnetic interface [19]. This anisotropy could lead to improved permanent magnets if antiferromagnetic coating materials with a Néel temperature above room temperature can be produced (T_N=525K for NiO).

[a] *Babes-Bolyai University, Faculty of Physics, 4000084 Cluj-Napoca, Romania*
[b] *National Institute for Research and Development of Isotopic and Molecular Technologies, P. O. Box 700, 400293Cluj-Napoca, Romania*

Rare earth oxides are potentially useful materials for various optical and electronic applications. One such material is cerium dioxide (CeO_2) due to his high refractive index (~2), high transparency in the visible and near-infrared region and large dielectric constant (~26) [20].

The $CeNi_5$ compound crystallizes in the hexagonal $CaCu_5$ structure type, space group P6/mmm with Ce occupying the 1a site (0, 0, 0), Ni(1) in the 2c site (1/3,2/3,0) and Ni(2) in the 3g sites (1/2,0,1/2); with the Ni-Ni distances very close to those from pure metallic Ni. This compound is an exchange-enhanced Pauli paramagnet and Ce ions are in the intermediate valence state [21, 22]. The magnetic susceptibility of $CeNi_5$ arises mainly from the Ni 3d electrons which are very close to the onset of ferromagnetism [23].

Generally it is not easy to obtain accurate values of the crystallite size without extreme care in the experimental measurements and analysis of X-Ray Diffraction (XRD) data. XRD line profile analysis is a versatile nondestructive method that can be used in obtaining nanostructural information. Usually the nano-crystallite size is determined by classical Scherrer equation [24]. For a better accuracy in the determination of full width at half maximum (FWHM) of the X-Ray line profile (XRLP) approximation methods like Cauchy [25], Gauss [26], Voigt [27] or Generalized Fermi Function (GFF) [28] are used.

EXPERIMENTAL

The starting material $CeNi_5$ was prepared by argon arc melting method. In order to aid homogenization the sample was inverted and re-melted several times in the same atmosphere. The weight loss of the final sample was found out to be less than 1%. High purity elements have been used for the sample preparation 99.9% for both Ce and Ni. The obtained sample was crushed and heat treatments in air up to 800^{o}C were performed.

X-Ray powder diffraction measurements, for initial and treated samples, were collected using a Bruker D8 Advance diffractometer, in the Bragg-Bretano (BB) geometry, with Ni filtered CuK_α radiation, λ = 1.54178Å, at room temperature. The typical experimental conditions were 5 sec for each step, initial angle $2\theta = 20^o$ and step 0.05.

The crystallite size of initial $CeNi_5$ compound was calculated from the (002) profile of XRD pattern using several approximation methods like Cauchy, Gauss, Voigt or generalized Fermi function (GFF).

For some of the treated samples ($CeNi_5$ oxidized in air at 300^{o}C, 400^{o}C, 500^{o}C and 600^{o}C) the Ni (200) and NiO (110) X-Ray diffraction profiles were processed in order to evaluate the average crystalline size of Ni core and NiO layer formed on Ni particles surface. The same four methods were adopted in the approximation of XRLP. The doublet correction $K\alpha_2$ was realized by the installation soft. The background approximation was necessary in order to obtain a correct value of the FWHM; this approximation was realised using a regression line defined on the two XRD lobes.

In order to observe the particle features, microstructure analysis was also performed using a TESLA BS-500 transmission electron microscope.

RESULTS AND DISCUSSION

XRD pattern showed that the initial compound is single phase and all peaks can be indexed according the characteristic lines of expected structure type with the following lattice parameters a ≈ 0.487nm and c ≈ 0.402nm (**Fig. 1**). The theoretical $CeNi_5$ XRD pattern was generated using PowderCell 2.3 program [29]. The Ni-Ni distances in $CeNi_5$ are 0.244nm very close to those of pure metallic Ni, 0.249nm, respectively.

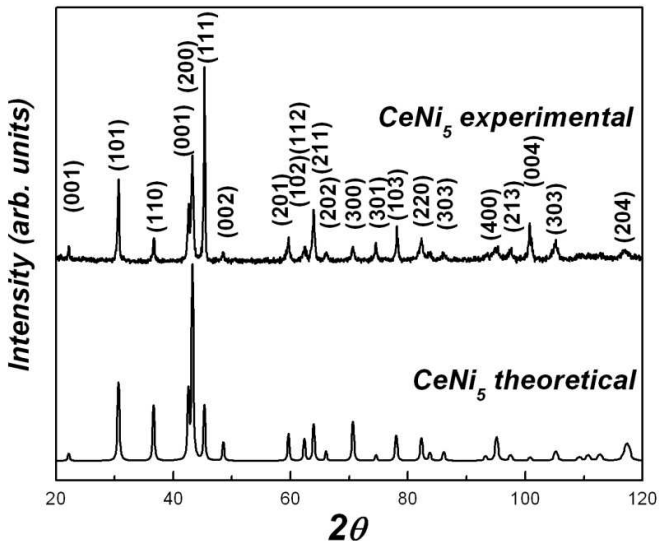

Fig. 1. $CeNi_5$ theoretical and experimental XRD patterns

Fig. 2. shows the (002) XRD line profile of $CeNi_5$ approximated using Cauchy, Gauss, Voigt and generalized Fermi function (GFF) methods, together with the differences between the experimental pattern and each approximation.

The global structural parameters of investigated compound obtained using the four approximation methods are summarized in **Table 1**.

Table 1. Global structural parameters of initial compound $CeNi_5$

	Gauss	Cauchy	Voight	GFF
d(nm)	**30.6**	**40.9**	**45.4**	**34.7**
FWHM($2\theta^o$)	**0.33**	**0.23**	**0.27**	**0.27**
χ^2	**997**	**903**	**864**	**839**

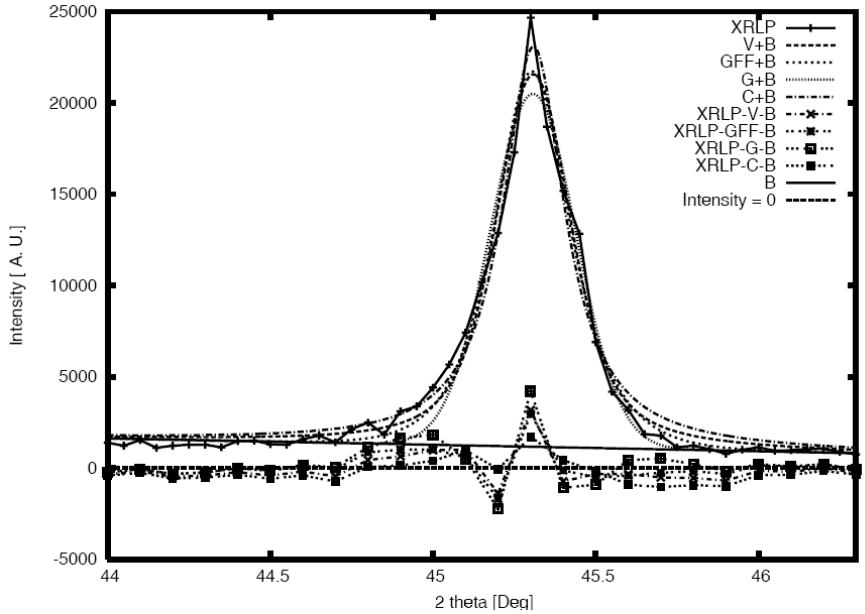

Fig. 2. Experimental (002) XRLP of initial compound $CeNi_5$ superposed with Cauchy, Gauss, Voigt and GFF approximation results

χ^2 is the root squares of residuals, which represents de difference between the experimental and calculated results. In case of initial compound $CeNi_5$ the FWHM was calculated using the Scherrer's equation from the GFF approximation results for which we have a minimum value of the root squares of residuals. The average crystallite size of the starting material was about 34.7nm.

Taking into account the great oxygen affinity of Ce and the strong magnetic interactions between Ni atoms in this compound, we tried to obtain isolated single domain particles of Ni by mechanically transforming the bulk $CeNi_5$ in a very fine powder followed by a thermal treatment in air at different temperatures up to 800^{o}C.

The $CeNi_5$ powder becomes magnetic upon exposure to air for 40 min. at 100 °C. Is well known that Ce is much more sensitive to oxygen than Ni, this result suggest that Ni atoms diffuse into particles to form magnetic clusters, due to the strong magnetic interactions between the nearest - neighbors Ni atoms, and Ce ions migrate to the surface of the particles during heat treatment to form the oxide layers of CeO_2 and Ce_2O_3. The Ce oxide layers and in a very small quantity; NiO formed on the surface of Ni particles are not continuous and consist of very small crystallites. The surface of Ni particles is completely oxidized after a new heating for 1 h at 600 °C.

The experimental relative intensities with respect to 2θ values for the investigated samples as well as theoretical patterns of $CeNi_5$, pure metallic Ni, NiO, Ce_2O_3 and CeO_2 are presented in **Fig. 3**. All theoretical XRD pattern were generated using PowderCell 2.3 program.

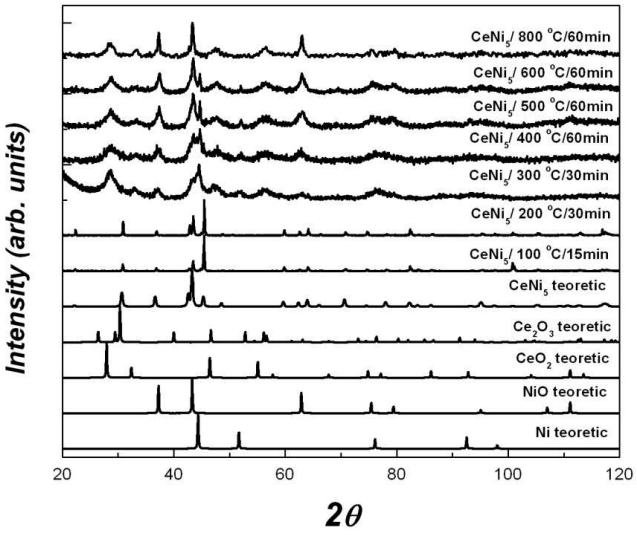

Fig. 3. XRD patterns for $CeNi_5$ oxidized in air at different temperatures and theoretical patterns corresponding to pure metallic Ni, NiO, CeO_2, Ce_2O_3 and $CeNi_5$

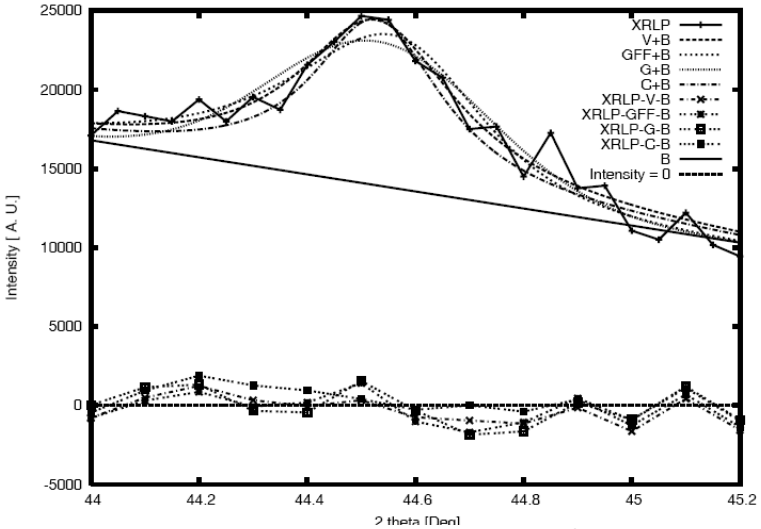

Fig. 4. Ni (200) XRLP of $CeNi_5$ oxidized in air at 300°C for 30 minutes, processed using Cauchy, Gauss, Voigt and GFF approximations

For some of the investigated samples, $CeNi_5$ oxidized in air at 300°C, 400°C, 500°C and 600°C, the Ni (200) and NiO (110) X-Ray diffraction profiles were processed in order to evaluate the average crystalline size of Ni core and NiO layer formed on Ni particles surface.

Fig. 4. shows the Ni (200) XRD line profile of $CeNi_5$ oxidized in air at 300°C for 30 minutes processed using Cauchy, Gauss, Voigt and GFF approximations, together with the differences between the experimental pattern and each approximation.

The associated numerical results are synthesised in **Table 2**. The crystalline average size of Ni clusters increases with temperature due to recrystallization processes that occur during the heat treatment from 34nm to 77nm. These dimensions were determined using Scherrer's equation from the Voigt approximation for which the values of χ^2 is minimum.

Table 2. XRD parameters corresponding to Ni average crystallite size

		$CeNi_5$/300/30 min	**$CeNi_5$/400/60 min**	**$CeNi_5$/500/60 min**	**$CeNi_5$/600/60 min**
GFF	**d(nm)**	23	24	54	57
	FWHM(2θ°)	0.41	0.40	0.17	0.16
	χ^2	1223.32	1249.62	1358.34	1906.12
Cauchy	**d(nm)**	32	31	63	68
	FWHM 2θ°)	0.29	0.30	0.15	0.13
	χ^2	1223.13	1429.16	1386.81	1163.26
Gauss	**d(nm)**	20	22	43	55
	FWHM(2θ°)	0.47	0.43	0.22	0.17
	χ^2	1268	1197.14	1365.99	2138.27
Voigt	**d(nm)**	34	30	60	77
	FWHM(2θ°)	0.36	0.40	0.20	0.23
	χ^2	1119.76	1176.12	1333.56	1178.03

The same Cauchy, Gauss, Voigt and GFF facilities were used in order to analytically evaluate the thickness of NiO layer formed on Ni particles surface. To this end the (110) X-Ray diffraction profile of NiO was processed. **Fig. 5** shows the experimental XRD pattern of $CeNi_5$ oxidized in air at 500°C for an hour, superposed with Cauchy, Gauss, Voigt and GFF approximations results. The numerical results are contained in **Table 3**.

The thickness of NiO layer also increases with temperature, from 9nm, in case of $CeNi_5$ oxidized in air at 300°C for 30 min, up to 19nm, for $CeNi_5$ treated at 600°C for one hour. These values were determined using Scherrer's equation applied to Voigt approximation results, for which χ^2 has its minimum value.

In order to determine the composition of investigated samples, microstructure analysis was also performed using a TESLA BS-500 transmission electron microscope. TEM imagine (**Fig. 6**) shows the presence of darker particle centers surrounded by

a light colored coating in most of the particles. This could be attributed to a core-shell type of structure, where the core consists of metallic cores. The mean Ni particle diameters are in good agreement with those obtained from XRD measurements.

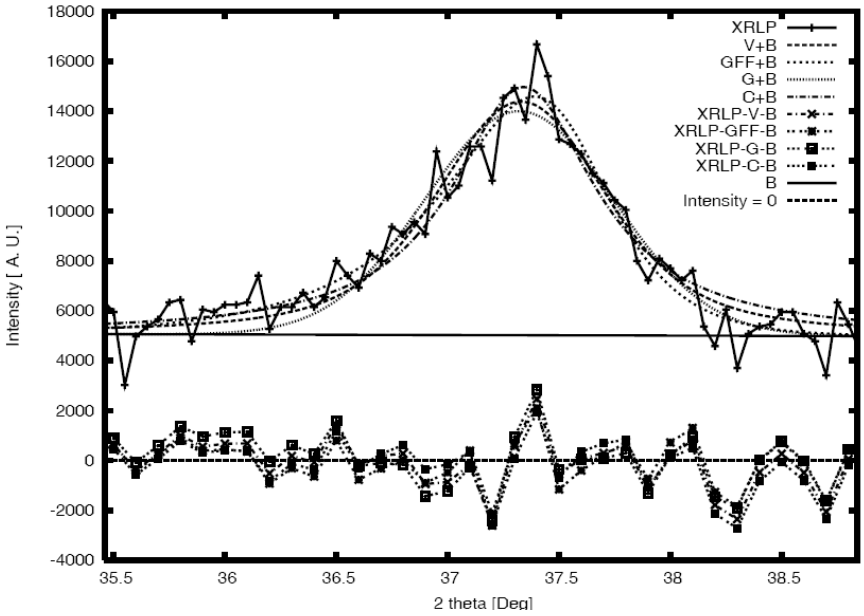

Fig. 5. NiO (110) XRLP of $CeNi_5$ oxidized in air at 500°C for an hour, processed using Cauchy, Gauss, Voigt and GFF approximations

Table 3. XRD parameters corresponding to NiO layer

		$CeNi_5$/300/30min	**$CeNi_5$/400/60min**	**$CeNi_5$/500/60min**	**$CeNi_5$/600/60min**
GFF	**d(nm)**	10	8	11	19
	FWHM(2θ°)	0.95	1.08	0.88	0.49
	χ^2	813.137	1188.48	899.206	1526.7
Cauchy	**d(nm)**	9	9	11	23
	FWHM 2θ°)	0.86	0.98	0.78	0.40
	χ^2	826.051	1195.84	1016.09	1555.79
Gauss	**d(nm)**	9	7	9	16
	FWHM(2θ°)	1.06	1.20	0.99	0.56
	χ^2	804.748	1183.2	1036.05	3604.03
Voigt	**d(nm)**	10	9	12	19
	FWHM(2θ°)	1.02	1.11	0.90	0.56
	χ^2	804.618	1174.56	989.28	1689.74

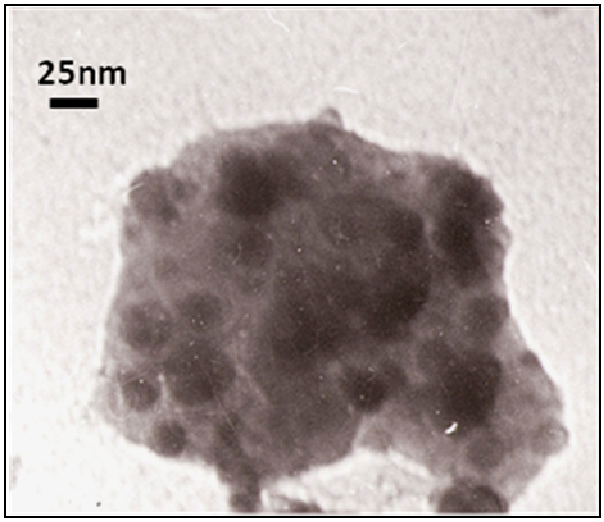

Fig. 6. TEM imagine of $CeNi_5$ powder oxidized in air at 800 ^oC for 1h

CONCLUSIONS

XRD studies results of $CeNi_5$ powder oxidized in air at different temperatures up to 800^oC, suggest that during the heat treatment Ni metallic clusters surrounded by NiO, Ce_2O_3 and CeO_2 appear. The average crystallite size of Ni core and the thickness of NiO oxide formed at the surface was evaluated by means of Cauchy, Gauss, Voigt and GFF approximations. The obtained results suggest that both Ni and NiO average crystallite size increase with temperature due to recrystallization processes from 34nm to 77nm and from 9nm to 19nm respectively. TEM imagines confirm the approximation results.

REFERENCES

1. L. Schultz, K. Schitzke, and J. Wecker, Appl. Phys. Lett. **1990**, *56*, 868
2. L. Lu, M. L. Sui, and K. Lu, Science **2000**, *287*, 1463
3. M. Ozaki, Mater. Res. Bull. XIV, **1989**, *35*
4. H. Gleiter, Nanostruct. Mater., **1992**, *1*, 1
5. D. Kumar, J. Narayan, T.K. Nath, A.K. Sharma, A. Kvit, and C. Jin, Solid State Commun. **2001**, *119*, 63
6. D. Kumar, J. Narayan, A.V. Kvit, A.K. Sharma, and J. Sankar, J. Magn. Magn. Mater. **2001**, *232*, 161

7. A.S. Edelstein and R.C. Cammarata, "Nanomaterials: Synthesis, Properties and Applications", **1998**, Institute of Physics, Bristol,

8. W. Luo, S.R. Nagel, T. F. Rosenbaum, and R.E. Rosensweig, Phys. Rev. Lett. **1991**, *67*, 2721

9. R.W. Chantrell, N.S. Walmsey, J. Gore, and M. Maylin, Appl. Phys. Lett. **1999**, *85*, 4320

10. J. Gonzalo, R. Serna, C.N. Afonso, J. Bosbach, T. Wenzel, F. Stietz, F. Tranger, D. Babonneau, and D.E. Hole, J. Appl. Phys. **2001**, *89*, 5734

11. S. Gangopadyay, G.C. Hadjipanagis, C.M. Sorebsen, K.J. Klabunde, MRS Symp. Proc. **1991**, *20*, 655

12. W. Gong, H Li, Z. Zhao, J. Chen, J. Appl. Phys. **1991**, *69*, 5119

13. T. Hayashi, T. Ohno, S. Yatsuya, R. Uyeda, Japanese J. Appl. Phys. **1977**, *16*, 705

14. M. B. Stern, Y. Cheng, J. Appl. Phys. **1994**, *75*, 6894

15. A. Gavrin, C. L. Chien, J. Appl. Phys. **1933**, *73*, 6949

16. J.M. Broto, J.C. Ousset, H. Rakoto, S. Askenazy, Ch. Dufor, M. Brien, P. Mauret, Solid State Commun. **1993**, *85*, 263

17. J.P. Wang, D.H. Han, H.L. Luo, N.F. Gao, Y.Y. Liu, J. Magn. Mater. **1994**, *135*, L251

18. C. Estournes, T. Lutz, J. L. Guille, J. Non-Cryst. Solids **1996**, *197*, 192

19. A.H. Morrish, *"The Physical Principles of Magnetism"*, John Wiley & Sons, Inc., New York, **1965**

20. K.B. Sundaram, P.F. Wahid, O. Melendez, J. Vac. Sci. Technol. **1997**, *A15* , 52

21. M. Coldea, D. Andreica, M. Bitu, V. Crisan, J. Magn. Mater. **1996**, *157/158*, 627

22. L. Nordström, M.S.S. Brooks, and B. Johansson, Phys.Rev. **1992**, *B 46*, 3458

23. D. Gignoux, F. Givord, R. Lemaire, H. Launois, F. Sayetat, J. Physique **1982**, *43*, 173

24. C. Estournes, T. Lutz, J.L. Guille, J. Non-Cryst. Solids **1996**, *197*, 192

25. H.P. Klug and L.E. Alexander, *"X-Ray Diffraction Procedures – For Polycrystalline and Amorphous Materials"*, John Wiley & Sons, Inc., **1974**

26. B.E. Warren, *"X-Ray Diffraction"*, Dover Publications, Inc., New York, **1990**

27. D. Balzar, J. Res. Natl. Inst. Stand. Technol. **1993**, *98*, 321

28. N. Aldea, A. Gluhoi, P. Marginean, C. Cosma, Xie Yaning, Spectrochim. Acta Part B, **2000**, *55*, 997

29. G. Nolze and W. Kraus, *PowderCell 2.3 Program*, BAM Berlin **2000**

GADOLINIUM EFFECT ON THE MAGNETIC PROPERTIES OF HEAVY METAL GLASSES AND GLASS-CERAMICS

S. SIMON[a]

ABSTRACT. Heavy metal bismuthate glass and glass-ceramic samples with gadolinium oxide were obtained by quick undercooling of melts and later heat treatments. Magnetic susceptibility data suggest that beside homogeneously distributed Gd^{3+} ions, both in the glass and glass-ceramic samples, there are clustered Gd^{3+} ions experiencing antiferromagnetic interactions. In all cases the magnetic moments are smaller than the value corresponding to free Gd^{3+} ions and decrease with gadolinium content. The decrease is linear and the slope depends on the glass matrix composition.

Keywords: *Glass; glass-ceramics; heavy metals; magnetic properties.*

INTRODUCTION

Heavy metal oxide glasses might be defined as glasses containing over 50 cation percent of bismuth and/or lead, which mainly participate in the glass structure as network formers [1]. Although the bismuth oxide is an unconventional glass network former, a series of binary and multicomponent nonconventional bismuthate glasses with interesting properties have been synthesised [2-4].

Glasses with a high content of heavy metals, like Bi_2O_3 and PbO, are intensely investigated because of their properties such as high density, high refractive index, excellent IR transmission and high polarisability [5-8]. All of these properties are exploited in applications such as thermal and mechanical sensors [8], wave-guides in nonlinear optics, scintillation detectors in high-energy physics [9, 10]. At the same time the study of glasses containing small amounts or no classical glass network formers such as SiO_2, B_2O_3 or P_2O_5 is important for the understanding of the way in which stable glasses may be realized in the absence of the classical glass network formers.

Bismuthate glasses doped with rare earth exhibit new magnetic properties, particularly when gadolinium or europium are used as dopants [4,11-14], and their investigation can be extended using the EPR spectroscopy.

Germanium bismuthate glasses and ceramics have been widely investigated also due to their various applications in optical devices based on their high optical non-linear susceptibility and scintillating properties [15-18]. The use of these glasses as active media for Raman fiber and optical amplifiers, as materials for low loss fibers and IR transmitting windows, has been also recommended [19].

[a] *Babes-Bolyai University, Faculty of Physics*

The aim of the present work is to present the magnetic properties of gadolinium containing glasses and glass-ceramics of Bi_2O_3-GeO_2 and Bi_2O_3-PbO systems.

EXPERIMENTAL

Glasses belonging to $xGd_2O_3 \cdot (100-x)$ [$85.7Bi_2O_3 \cdot 14.3GeO_2$] system, with $0.5 \leq x \leq 10$ mol %, were prepared by using reagent grade Bi_2O_3, GeO_2 and Gd_2O_3. The components, in amounts corresponding to the desired composition, were mixed thoroughly to prepare the batches melted at 1250°C for 15 minutes and air quenched at room temperature. According to the DTA data [20], a heat treatment at 600^0C was applied for 24 hours on the glass samples in order to obtain glass-ceramic samples.

Glasses of $(100-x)[4Bi_2O_3 \cdot PbO]xGd_2O_3$ and $(100-x)[3Bi_2O_3 \cdot 2PbO]xGd_2O_3$ systems, where x = 1, 5, 10 and 20 mol %, were obtained by melting at 1100°, for 10 minutes, and quick undercooling to room temperature. The starting materials used to prepare the samples were analytically pure reagents $(BiO)_2CO_3$, PbO and Gd_2O_3.

The magnetic susceptibility was measured between 80 K and 300 K with a Faraday-type magnetic balance of 10^{-8} emu/g sensitivity. Corrections for the diamagnetism of the sample holder and of the ion cores were applied.

RESULTS AND DISCUSSION

The vitreous state of all as-prepared samples was proved by XRD analysis. After heat treatment of germanium-bismuthate glasses, different crystalline phases were evidenced, depending on Gd_2O_3 content. For the samples with $x \leq 1$ the sillenite $Bi_{12}GeO_{20}$ crystalline phase was identified, while for the sample with x = 10, surprisingly, the $Bi_{24}GeO_{38}$ crystalline phase. The structure of samples with intermediate Gd_2O_3 concentration is of a BiLa type [21].

The temperature dependence of the reciprocal magnetic susceptibility for glasses and glass-ceramics is presented in Fig. 1. For the sample with x = 1 the reciprocal magnetic susceptibility shows a paramagnetic behaviour of Curie type, while the samples with x > 1 follows a Curie-Weiss type behaviour. After heat treatment, the crystallised samples exhibit similar magnetic behaviour to that of the vitreous samples, no significant changes being observed [22].

The paramagnetic Curie temperature θ_p from the Curie - Weiss law, is a rough indicator of magnetic interaction between Gd^{3+} ions. This temperature for the samples with x > 1 is negative and increases in absolute value with increasing of Gd_2O_3 content.

The effective magnetic moment for the gadolinium ions was calculated in Bohr magnetons, μ_B, with the formula $\mu_{Gd}^{3+} = 2.827\sqrt{C_M / 2x}$, where C_M is molar Curie constant. The effective magnetic moment per gadolinium ion for all samples is lower than 7.94 μ_B, the value of the magnetic moment for the free gadolinium [23, 24]. In general, this value decreases with the increasing of the rare earth amount in the sample. The molar Curie constant C_M, effective magnetic moment per gadolinium

ion and the paramagnetic Curie temperature for the glass and glass-ceramic samples are summarised in Table I. These data suggest the presence of the weak antiferromagnetic interaction between the Gd^{3+} ions.

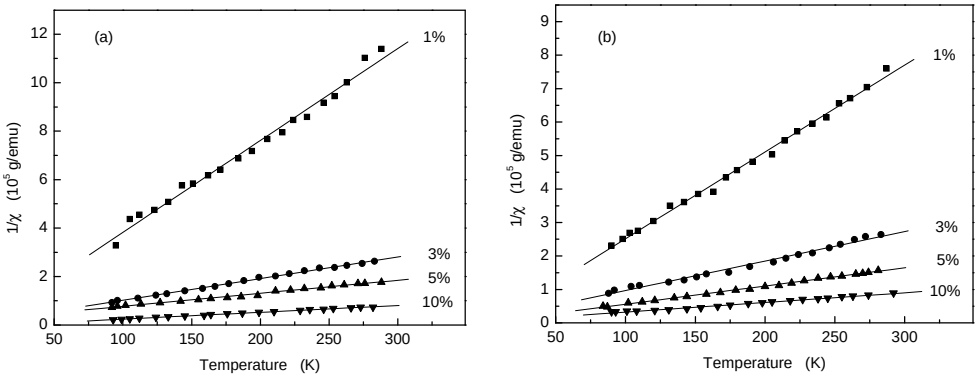

Fig. 1. Temperature dependence of the reciprocal magnetic susceptibility of $xGd_2O_3 \cdot (100\text{-}x)\ [85.7Bi_2O_3 \cdot 14.3GeO_2]$ glasses (a) and glass-ceramics (b).

The temperature dependence of the reciprocal magnetic susceptibility in Bi_2O_3-PbO glasses (Fig. 2) shows for samples containing x = 1 mol % Gd_2O_3 a paramagnetic behavior of Curie type. Samples with x > 1 mol % Gd_2O_3 exhibit negative paramagnetic Curie temperatures suggesting antiferromagnetic interactions between these ions.

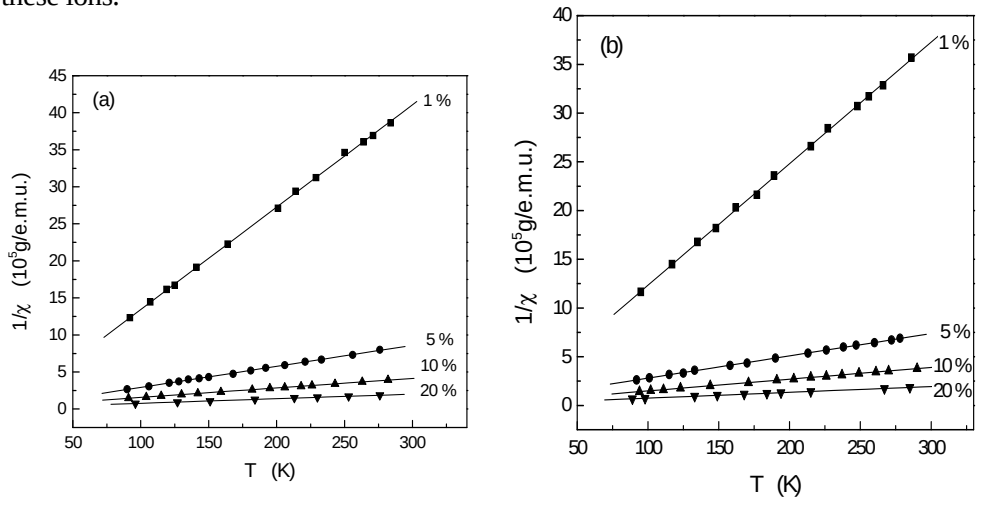

Fig. 2. Reciprocal susceptibility versus temperature for (a) $xGd_2O_3(100\text{-}x)[4Bi_2O_3 \cdot PbO]$ and (b) $xGd_2O_3(100\text{-}x)[3Bi_2O_3 \cdot 2PbO]$.

Table I. The molar Curie constant, effective magnetic moment and paramagnetic Curie temperature for the glass and glass-ceramic samples.

x (mol %)	Glasses			Glass-ceramics		
	C_M (uem·K/mol)	μ_{eff} (μ_B)	$-\theta_p$ (K)	C_M (uem·K/mol)	μ_{eff} (μ_B)	$-\theta_p$ (K)
1	0.157	7.93	0	0.158	7.94	0
3	0.462	7.85	10.4	0.467	7.89	15.2
5	0.761	7.80	24.7	0.755	7.77	25.4
10	1.463	7.65	32.7	1.421	7.54	33.1

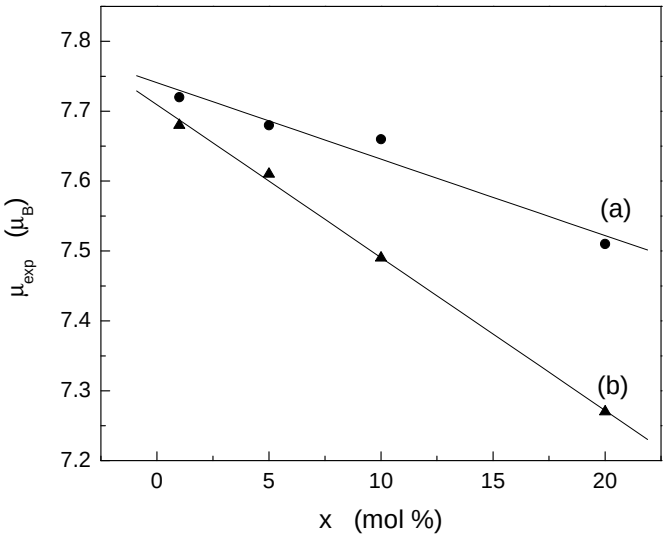

Fig. 3. Variation of the experimental magnetic moment as a function of x for (a) $xGd_2O_3(100\text{-}x)[4Bi_2O_3{\cdot}PbO]$ and (b) $xGd_2O_3(100\text{-}x)[3Bi_2O_3{\cdot}2PbO]$ glasses.

The unique valence state of gadolinium is Gd^{3+}, and the magnetic moment corresponding to the free ion is $7.94{\cdot}\mu_B$, but in all samples lower values were determined (Table II). The lowering of the magnetic moments with increasing Gd^{3+} content in the two lead-bismuthate glass matrices is shown in Fig. 3. The decrease of μ_{exp} is linear in $4Bi_2O_3{\cdot}PbO$ and $3Bi_2O_3{\cdot}2PbO$ with slopes of –0.011 and –0.022 μ_B/mol %, respectively. Decreased values of the magnetic moment of gadolinium were also reported for other glasses [25, 26]. The negative value of the paramagnetic Curie temperature indicates that in these samples the interaction between gadolinium ions, like between iron and manganese ions, is mainly of short range as superexchange

via oxygen ions. Aggregates of these Gd^{3+}-O-Gd^{3+} coupled pairs lead to the appearance of magnetic clusters, each having an effective magnetic moment. The values obtained from magnetic susceptibility measurements are average values. In the samples some gadolinium ions behave as free Gd^{3+} ions, while others occur as antiferromagnetically coupled pairs with a certain angle between the magnetic moments. Close to 0 K this angle is 180^o and becomes, on an average, smaller at higher temperatures so that magnetic moments corresponding to coupled pairs are lower than for uncoupled ions. The more pronounced decrease of the magnetic moment in the second matrix shows that in this matrix, having a lower ratio of bismuth to lead, coupling is more pronounced than in the matrix with higher bismuth content [27]. The same contribution to the decreasing of experimental magnetic moment value for all samples with high paramagnetic ions content has to be taken into account before estimating the reduction or the oxidizing effect of glass matrix on the paramagnetic ions.

Table II. Experimental magnetic moments per gadolinium atom, paramagnetic Curie temperatures and Curie molar constants for $xGd_2O_3 \cdot (100\text{-}x)[4Bi_2O_3 \cdot PbO]$ and $xGd_2O_3 \cdot (100\text{-}x)[3Bi_2O_3 \cdot 2PbO]$ glasses.

Matrix	x (mol %)	μ_{exp} (μ_B)	$-\theta_p$ (K)	C_M (emu·K/mol)
4:1	1	7.72	0	0.148
	5	7.68	15.2	0.736
	10	7.66	23.8	1.140
	20	7.51	32.1	2.810
3:2	1	7.68	0	0.147
	5	7.61	16.1	0.733
	10	7.49	25.5	1.400
	20	7.27	34.2	2.630

CONCLUSIONS

For $xGd_2O_3 \cdot (100\text{-}x)$ $[85.7Bi_2O_3 \cdot 14.3GeO_2]$, $xGd_2O_3(100\text{-}x)[4Bi_2O_3 \cdot PbO]$ and $(100\text{-}x)[3Bi_2O_3 \cdot 2PbO]xGd_2O_3$ heavy metal glass systems the temperature dependence of reciprocal magnetic susceptibility is of Curie type only for the samples with $x \leq 1$. As Gd_2O_3 content exceeds 1 mol %, a Curie-Weiss type behaviour is evidenced, that denotes the occurrence of antiferromagnetic interactions between Gd^{3+} ions.

In all gadolinium containing samples, the experimental values of the magnetic moments are lower than the value for free Gd^{3+} ions. This result is explained by assuming the formation of coupled pairs in which the ions are coupled by superexchange. The decrease of the magnetic moment with increasing gadolinium content is well fitted by a linear function and depends also on the ratio between bismuth and lead in Bi_2O_3-PbO glass matrices.

REFERENCES

1. W.H. Dumbaugh, J.C. Lapp, J. Am. Ceram. Soc., 75, 2315 (1992)
2. N. Ahlawat, S. Sanghi, A. Agarwal, N. Kishore, S. Rani, J. Non-Cryst. Solids, 354, 3767 (2008)
3. S. Bale, S. Rahman, A.M. Awasthi, V. Sathe, J. Alloy Compd., 460, 699 (2008)
4. E. Culea, L. Pop, S. Simon, Mat. Sci. & Engin. B, 112, 59 (2004)
5. K. Ohura, M. Ikenaga, T. Nakamura, T. Yamamuro, Y. Ebisawa, T. Kokubo, Y. Kotoura, M. Oka, J. Appl. Biomaterials, 2, 153 (1991)
6. S. Hazra, A. Ghosh, Phys. Rev, B 51, 851 (1995)
7. Y. Dimitriev, V.T. Mihailova, J. Sci. Lett, 9, 1251 (1990)
8. S. Hazra, A. Ghosh, Phys. Rev, B 56, 13 (1997)
9. C. Stehle, C. Vira, D. Hogan, S. Feller, M. Affatigato, Phys. Chem. Glasses, 39, 2, 836 (1998)
10. S.E. Van Kirk, S.W. Martin, J. Am. Ceram. Soc., 75, 4, 1028 (1992)
11. D.L. Griscom, "Electron Spin Resonance"; pp.151-251 in Glass Science and Technology, Vol. 4B, *Advances in Structural Analysis*. Edited by D. R. Uhlman and N. J. Kreidl. Academic Press, Inc., 1990.
12. M.F. Carrasco, S.K. Mendiratta, L. Marques, A. S. B. Sombra, J. Mater. Sci. Lett., 21, 963 (2002)
13. S. Takeda, K. Sugiyama, Y. Waseda, Jpn. J. Appl. Phys., 32, 5633 (1993)
14. Y.B. Saddeek, E. R. Shaaban, E. S. Moustafa, H. M. Moustafa, Physica B, 403, 2399 (2008)
15. M.J. Weber, R. R. Monchamp, J. Appl. Phys., 44, 5495 (1973)
16. P.P. Lottici, I. Manzini, G. Antonioli, G. Gnappi, A. Montenero, J. Non-Cryst. Solids, 159, 173 (1993)
17. Z.S. Macedo, A. C. Hernandez, J. Am. Ceram. Soc., 85, 1870 (2002).
18. Z.S. Macedo, R. S. Silva, M. E. G. Valerio, A. L. Martinez, A. C. Hernandez, J. Am. Ceram. Soc., 87, 1076 (2004)
19. D.W. Hall, M.A. Newhouse, N.F. Borrelli, W.H. Dumbaugh, D.L. Weidman, Appl. Phys. Lett., 54, 1293 (1989)
20. V. Simon, O. Ponta, S. Simon, D.A. Udvar, M. Neumann, Phys. Status Solidi A, 205, 1139 (2008)
21. Natl. Bur. Stand. (US) Monogr., 25, 48 (1965)
22. S. Simon, A.D. Udvar, J. Am. Ceram. Soc., 1–4 (2010) DOI: 10.1111/j.1551-2916.2010.03783
23. D. R. Lide, The Handbook of Chemistry and Physics, 78th Edition, 1997-1998.
24. I. Ardelean, E. Burzo, D. Mitulescu-Ungur, S. Simon, J. Non-Cryst. Solids 146, 256 (1992)
25. M.A. Valente, S.K. Mendiratta, Phys.Chem. Glasses, 33, 149 (1992)
26. J.E. Shelby, S.R. Shelby, Phys.Chem. Glasses, 40, 207 (1999)
27. S. Simon, R. Pop, V. Simon, M. Coldea, J. Non-Cryst. Solids. 331, 1 (2003).

STUDIA UNIVERSITATIS BABEŞ-BOLYAI, PHYSICA, LV, 1, 2010

EVIDENCES OF MARTENSITIC TRANSFORMATION IN SOME Ni-Fe-Co- Ga ALLOYS

M. VALEANU, M SOFRONIE[a]

ABSTRACT. The martenitic transformation characteristics in two series of cobalt substituted Ni-Fe-Ga Ferromagnetic Shape Memory alloys have been studied by differential scanning calorimetry, X-ray diffraction, electrical resistivity and thermomagnetic measurements. Co substitution for Fe or Ni promotes an increase of the Curie temperatures but the changes of the martensitic transformation temperatures are in accord with the valence electron concentration and unit cell volume variations. A large hysteresis observed between cooling and heating curves as feature of a first order phase transition was evidenced by ρ(T) and thermomagnetic measurements.

Keywords: *Ferromagnetic Shape Memory alloys; Martensitic transformation; Magnetic properties*

The development of more efficient materials for sensors and actuators is attaining increasing interest in the materials science community. These materials allow their shape to be changed, producing a displacement, during thermal activation of a structural transition. The shape-memory effect (SME) is associated with a thermoelastic reversible structural phase transition between high and low symmetric phases, the so called martensitic transformation (MT). An induced deformation in the lower symmetry, martensite phase can be recovered upon transformation to a higher symmetry, austenite phase with the increasing temperature. For all until now known SMA, the parent austenite phase has a cubic crystalline structure (bcc or fcc). Close to the transition, the lattice deformation along one of any tree directions generates some variants of structural units with the same deformation, the so called twin variants. The martensite microstructure is a characteristic one, composed of variable volume fractions of the twin variants to accommodate the elastic strain. The high mobility of twin boundary is exploited in the temperature driven shape memory effect. The velocity of shape recovering is restricted by the heating and cooling processes which are slow. Therefore a way to drive the shape change with a faster response would be desirable for many applications. This can be achieved by taking the magnetic freedom degree into play.

Ferromagnetic Shape Memory Alloys (FSMA) are materials in which MT lie in the temperature region of magnetic order. The large magnetic field induced strain (MFIS), the high frequency response and the shape memory effect evidenced in FSMA has drawn attention as promising materials for magnetically controlled

[a] *National Institute of Materials Physics, 077125 Bucharest, Romania*

actuators. The MFIS derives from the large magnetic anisotropy installed in the low symmetry martensite phase. By applying an external magnetic field it is energetically favorable to move the twin boundaries instead to rotate the twin magnetization direction. The martensite variants that have their easy axis along the applied field direction grow at the expense of other variants giving rise to a large strain. A huge MFIS, of about 10% was observed on Ni2MnGa, the FSMA prototype [1]. The high fragility of this alloy was the driving force to search for new FSMA as Fe-Pt, Fe-Pd or other Heusler alloy like Co-Ni-Al(Ga), Ni-Mn-Al [2-5]. Recently, a thermoelastic martensitic transformation in the ferromagnetic state, associated with a shape memory effect was evidenced Ni-Fe-Ga off-stoichiometric Heusler type alloy [6]. For the stoichiometric Ni2FeGa, MT is around 145K being ferromagnetic until 693K. For the off-stoichiometric compounds, the martensitic transition sifts to higher temperature with increasing Ni content. The advantage, in field of application, of Ni-Fe-Ga alloys is its better ductility which is associated with the presence of a second phase γ –(face –centered cubic A1 structure) [6].

The purpose of this work is to put in evidence the martensitic transformation via different type of physical measurements and to analyse the effect of cobalt substitution of iron or respectively of nickel in some Ni-Fe-Ga off-stoichiometric Heusler alloys.

EXPERIMENTAL

The polycrystalline samples with nominal composition $Ni_{55}Fe_{20-x}Co_xGa_{25}$ (x=0, 1) and $Ni_{54-y}Co_yFe20Ga26$ (y= 1, 2) were prepared by arc melting in argon atmosphere. The alloys were remelted three times to ensure the homogeneity. Subsequently, a thermal treatment was performed in high vacuum for 25h at 950^oC followed by a quenching in iced water.

Room temperature X-ray diffractions were performed using a Seifert diffractometer (Cu Kα radiation). The temperature induced structural transformations were also evidenced by low-temperature energy-dispersive x-ray diffraction (EDXRD) using synchrotron radiation (HASY-LAB, F2.1 beam line). The phase transformation measurements were performed by differential scanning calorimeter (DSC- 204 F1 Phoenix, Netzsch) with a scanning rate of 10K/min. The temperature dependences of the electrical resistivity were carried out by standard four-probe measurements in a measuring platform from Cryogenic Ltd. The low temperature magnetic measurements were performed with a High Field measurement system (Cryogenic Ltd.) in the VSM mode. Above room temperature, the magnetic measurements were done using a Weiss-type home made balance.

RESULTS AND DISCUSSIONS

The most accessible method to check the existence of a first order transition is via calorimetric measurements. The DSC results presented in fig 1 evidence the reversible martensite transformation for all reported samples. By cooling, at a temperature Ms

(martensite start), the free energy of the martensite state become lower than the free energy of the austenite state and the transformation is initiated. The transformation continues to evolve as the temperature is lowered until the structural transformation is completed at a temperature denoted by Mf (martensite finish). The reverse transformation takes place by heating; it begins at a temperature As (austenite start) and continues until the entire material reaches the austenite phase at a temperature denoted by Af (austenite finish). Throughout the transformation a latent heat is release (exothermic process) during the A-M transformation and absorbed (endothermic process) during the reverse M-A transformation. The characteristic transformation temperatures (Ms, Mf, As, Af), enthalpies (ΔH_M and ΔH_A) together with the valence electron concentrations (e/a) and the Curie temperatures for the studied alloys are presented in Table 1.

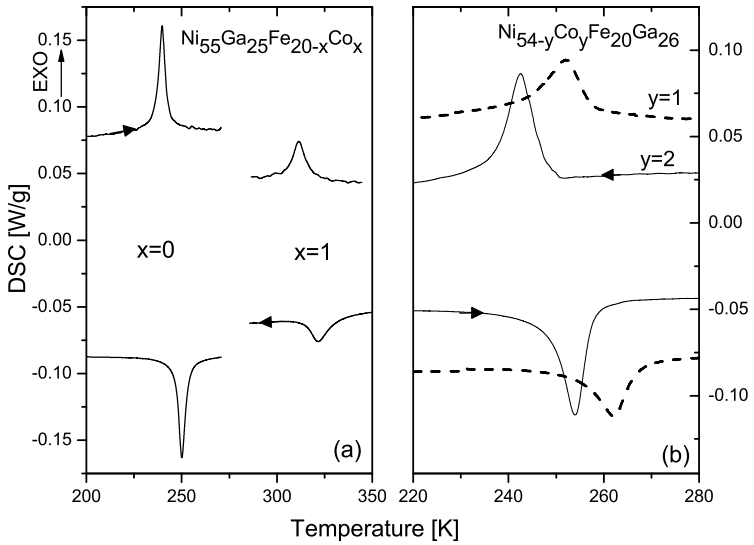

Fig. 1. DSC curves of $Ni_{55}Fe_{20-x}Co_xGa_{25}$ (a) and $Ni_{54-y}Co_yFe_{20}Ga_{26}$ (b) alloys. The MT shifts to higher temperatures for the alloys with cobalt substituting iron and to lower temperatures for those with cobalt substituting nickel.

Table 1. Composition, characteristic temperatures - Martensite start (Ms) and finish (Mf), Austenite start (As) and finish, (Af), transformation enthalpies (ΔH_M and ΔH_A), valence electron concentrations (e/a) and Curie temperatures (Tc) for all the studied alloys

Sample	**M_s (K)**	**M_f (K)**	**ΔH_M (J/g)**	**A_s (K)**	**A_f (K)**	**ΔH_A (J/g)**	e/a	Tc [K]
$Ni_{55}Fe_{20}Ga_{25}$	244.5	235	2.055	246	254.5	-2.066	7.85	305
$Ni_{55}Fe_{19}Co_1Ga_{25}$	322	302	1.21	307	333	-1.39	7.86	329

Sample	M_s (K)	M_f (K)	ΔH_M (J/g)	A_s (K)	A_f (K)	ΔH_A (J/g)	e/a	Tc [K]
$Ni_{53}Co_1Fe_{20}Ga_{26}$	257	244	2.53	255	267	-2.77	7.77	324
$Ni_{52}Co_2Fe_{20}Ga_{26}$	248	237	2.69	249	257	-2.61	7.76	345

By analyzing the DSC measurements can be concluded that the MT temperatures increase dramatically (~80^o) for the alloy in which iron is substituted by cobalt, the effect being opposite and less pronounced (~10^o) in those alloys were nickel is replaced by Co. It is general accepted that MT temperatures increase with the augment of valence electron concentration per system and with the reducing of the volume of the unit cell [7,8]. The observed changes in the MT temperatures are in qualitative agreement with the valence electron concentration variation for both series of alloys. It is worth mentioning that the valence electron concentrations given in Table 1, were estimated based on the atomic concentration per formula unit and considering for the number of valence electrons 10, 9, 8 and 3 for nickel, cobalt, iron and gallium, respectively. To understand the more pronounced Ms increase in the alloys with Co substitution for Fe, the atomic size factor had to be taken into account; the atomic radii are 0.1246nm for Ni, 0.1252nm for Co and 0.1274nm for Fe [9]. Thus, substitution of Fe atoms by Co would cause a larger unit-cell volume reduction than the volume increase created by replacing Ni atoms by Co, which can stand for the higher change of MT temperatures in $Ni_{55}Fe_{20-x}Co_xGa_{25}$ alloys.

Previous studied concluded that [10] crystalline structure for Ni-Fe-Ga changes from austenite with B2 (disordered Heusler –type) or $L2_1$ (Heusler –type) structure to different martensitic structure, depending on composition. There are two basic martensitic symmetries: tetragonal and orthorhombic named non-layered martensite. In addition, the basic structure may by modulate by a shuffling of atomic planes; the (110) plane undergoes a periodic shuffling in the [1, -1,0] direction, while every 5^{th} (or 7^{th}) (110) plane remains in its original position giving rise to the so cold 5 (or 7)- modulated structure. The abbreviations 5M (or 7M) or 10M (14M) seen in literature stand for monoclinic unit cell, considering the B2 and respectively L21 atomic ordering of the cubic austenite phase [11]. The problem of martensite nomenclature arises from the fact that martensite has a long ordering period structure and in the interest of describing more precisely the crystal structure, the stacking order must be specified too.

Room temperature X-ray diffraction measurements of the alloys treated at 950 ^{0}C reveal a bi-phase structure (Fig. 2). Common for all the compounds, is the presence of a γ face centered cubic (fcc) phase. Besides this secondary fcc phase, the main phase is in agreement with the DSC results. For the alloy with MT above room temperature (RT), the main phase show the characteristic peaks of the martensite non–layered tetragonal phase (L10). When the austenite is the stable phase at room temperature (Ms being lower than RT), the XRD patterns point out to a B2 structure.

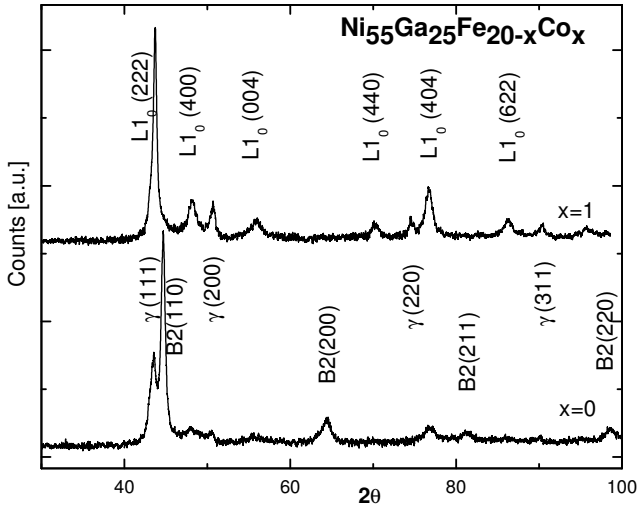

Fig. 2. Room temperature XRD patterns of $Ni_{55}Fe_{20-x}Co_xGa_{25}$ (x=0 and x=1). Apart from the peaks attributed to a secondary, un-transforming, face centered cubic phase, γ, the main peaks are indexed with a non-modulated tetragonal structure ($L1_0$ - martensite) or with a B2 (austenite) structure, in concordance with the DSC results.

Low-temperature energy-dispersive x-ray diffraction (EDXRD) using synchrotron radiation was also performed to evaluate the structural changes induced by the MT. For a more comprehensively comparison with room temperature X-ray diffraction measurements the data were transformed from λsynch = 0.12328516 A to Cu K_α radiation. Fig.3 shows the diffraction patterns recorded during cooling from room temperature down to 180K on $Ni_{53}Co_1Fe_{20}Ga_{26}$ alloy. As a general remark, the diffraction patterns contain some Bragg reflections for which the intensity remain unchanged during cooling (corresponding to the un-transforming fcc phase) and others which disappear by cooling, belonging to the active phase. In concordance with DSC results, the diffraction patterns at 300K and 275K show the characteristic peaks of the austenite phase with B2 structure. For the sample in discussion, the MT occurs at Ms=257K and the diffraction scans recorded at lower temperatures point out the appearance of new peaks ascribed to the martensite phase. Calculations concerning the type of modulated martensite are in progress.

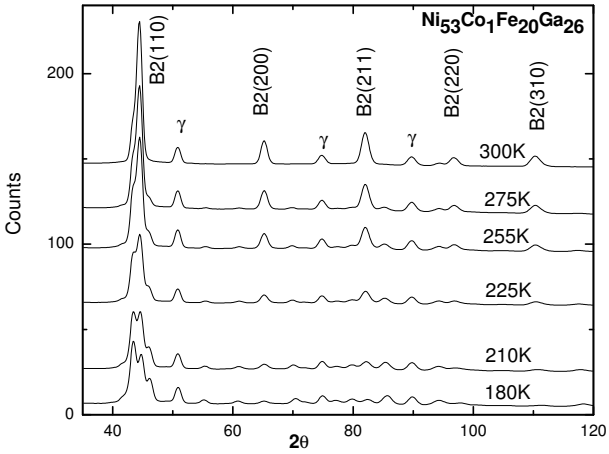

Fig. 3. XRD patterns of Ni_{53} $Co_1Fe_{20}Ga_{26}$ recorded during cooling from room temperature down to 180K. By cooling the Bragg reflections corresponding to the austenite phase diminish and new peaks ascribed to the martensite phase become visible.

A first order phase transition may strongly influences the transport properties. Particularly, in the temperature range of MT, the experimentally observed ρ(T) data shows anomalies for the FSMAs [12] but also for the nonmagnetic SMA like NiTi [13]. In fig 4 is presented the temperature dependence of resistivity for $Ni_{52}Co_2Fe_{20}Ga_{26}$ alloy. A large hysteresis observed between cooling and heating curves is the feature of a first order phase transition. The DSC measurements, presented for comparison in the same graph, validate the fact that the hysteresis appears in the temperature region where the two phases coexist.

By cooling and passing from austenite to martensite phase, at Ms, the resistivity shows an augmentation of about 20%. (In variance, by heating the sample through As, the resistivity shows a reduction). The abrupt variation of the electrical conductibility in the MT vicinity had to be due to an important change in the processes that influences the transport properties: electron –phonon and electron–magnon scattering cross-sections or the residual resistivity. According to Bloch- Gruneisen function, the electron –phonon contribution is mainly controlled by the Debye temperature, θ_D. From specific heat measurements [14] one can deduce that θ_D is larger for the martensite than for the austenite state consequently giving rise to an opposite resistivity variation at MT. The electron –magnon scattering depends on both the magnetic moment and the Curie temperature. For the martensite state the last one is difficult to evaluate but the magnetic moment is only slightly higher in the martensite state [15]. Since the mentioned effects are small, the residual resistivity must play an important role. The crystalline disorder appearing once nucleation of the martensite (phase) begins and the low symmetry of the new established phase are valuable reasons to justify the suddenly resitivity increase at Ms and its hysteretic behavior.

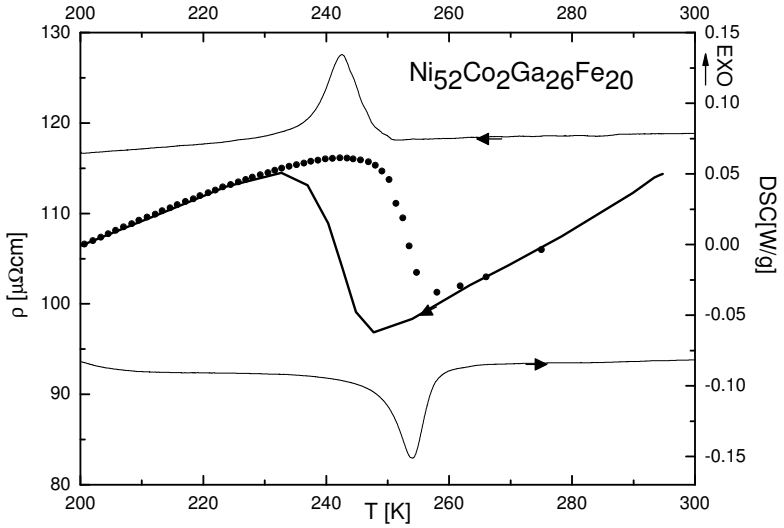

Fig. 4. Thermal variationof the electrical resistivity and DSC curves for Ni_{52} $Co_2Fe_{20}Ga_{26}$ alloy. A good correspondence between all the involved transition temperatures in the DSC curves and the ρ(T) scans can be observed.

Low field thermo-magnetic measurements were done by cooling down the samples in constant magnetic field of 0.04 T, from room temperature to a temperature well below the transformation temperature and warming them up again, until vanish the magnetization. Measurements performed on the alloys with MT below room (Fig. 5) evidenced two magnetic phases. The majority phase shows an order–disorder magnetic transition temperature above room temperature which slightly rises with cobalt content, in good agreement with other reported results [16]. The secondary phase, with higher Curie temperature, was assigned to the γ-fcc phase appearing in X ray diffraction patterns. The thermo-magnetic experimental data suggest an increase of the volume fraction of this secondary phase, with the cobalt content.

In the temperature region of MT a hysteretic anomaly is evidenced in the thermal variations of the magnetization between the cooling and heating curves. Figure 6 is a detailed view of the thermo magnetic data points in the vicinity of MT. By cooling at a certain temperature, magnetization shows a distinct drop and than by warming up at a slightly higher temperature shows an augmentation. The location of the critical points of this thermo- magnetic hysterezis correspond well with all the involved transition temperatures between the high temperature austenite phase and the low temperature martensite phase revealed by DSC measurements. Therefore, the thermo-magnetic measurements represent a powerful tool to study the influence of the magnetic field on phase transitions in FSMA.

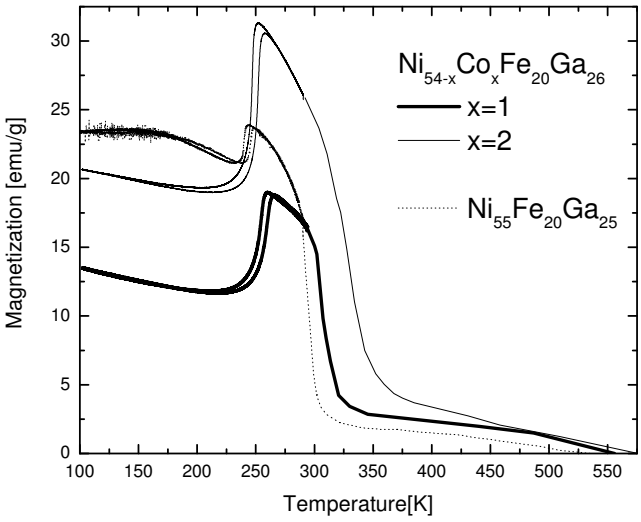

Fig. 5. Low field VSM thermo-magnetic scans for $Ni_{55}Fe_{20}Ga_{25}$ and $Ni_{55}Fe_{20-x}Co_xGa_{25}$ alloys evidence two magnetic phases. The Curie temperatures of the both phases, the majority austenite phase and the fcc secondary one increase with cobalt content.

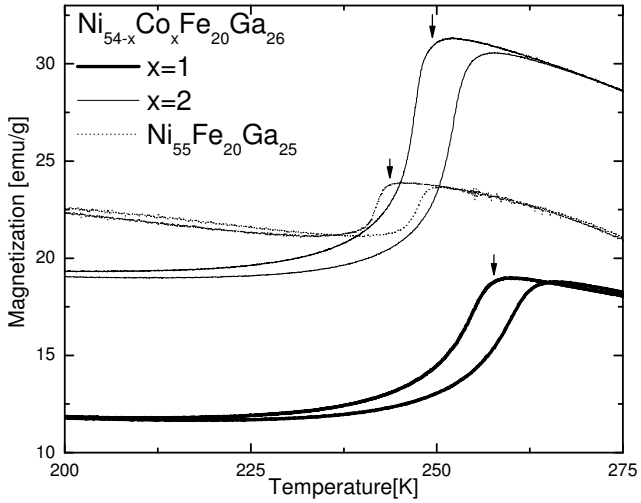

Fig. 6. Detailed view of the thermo-magnetic measurements (at constant magnetic field of 40mT) on cooling and heating for $Ni_{55}Fe_{20}Ga_{25}$ and $Ni_{55}Fe_{20-x}Co_xGa_{25}$ alloys. The magnitude of magnetization drop by passing from austenite to martensite is a measure of the difference in magnetic hardening between the two phases. The arrows mark Ms temperatures obtained by DSC measurements.

This evident change of the magnetization value by passing from austenite to martensite state certainly proves a change of magnetocrystalline anisotropy during the transformation. At low fields, due to its smaller magnetocrystalline anisotropy, the austenite phase is easier magnetized than the martensite ones, giving rise to a higher magnetization. By cooling the sample and passing in the martensite state with higher anisotropy, the low magnetic field do not succeeds to rotate the magnetic moments in the field direction, or to produce enough driving force to move the twin boundary of the variant whose easy axis is aligned with the field. Therefore, the measured martensite magnetization is small. The higher the difference between the austenite and martensite magnetization, the stronger martensite magnetocrystalline anisotropy is. The results presented in fig 6 suggest that by increasing the cobalt content martensite magnetocrystalline anisotropy is higher. This assumption is also supported by the results obtained by Morito et al [17,18] on $Ni_{51}Fe_{18}Ga_{27}Co_3$ and $Ni_{49}Fe_{18}Ga_{27}Co_6$ alloys. They found that the magneto-crystalline constants, evaluated on monocrystals in single–variant martensite phase near the transition temperature, increase from $4.7x10^5 erg/cm^3$ to $1.2x10^6 erg/cm^3$ with the cobalt content.

CONCLUSION

Ni-Fe-Ga intermetallic compounds with Co substitutions at Ni and Fe sites were prepared and characterized with respect to their structural, resistivity and magnetic behavior during the martensitic transformation.

The opposite variation (deviation) of the phase transition temperatures, in the alloys with cobalt substitution for nickel or iron, is in agreement with valence electron concentration and unit cell volume change. It was evidenced a hysteretic behavior on the $\rho(T)$ data and on the thermo-magnetic measurements in the temperature region of martensite transformation. The increased resistivity in the martensite phase was ascribed to the rise of the residual resistivity due to the decrease of the carriers' mobility as the carriers are scattered at martensite twin boundaries. The magnetization jumps in the temperature region of martensitic transition were discussed with respect to the magnetic anizotropies of the austenite and martensite phases.

ACKNOWLEDGEMENTS

This work has been carried out with the financial support of the Romanian Ministry of Education (Projects PN09-450103 and PN71-116/ 2007**)**

REFERENCES

1. K. Ullakko, J.K. Huang, C. Kantner, R.C. O'Handley, V.V. Kokorin, Appl. Phys. Lett. **69**, 1966 (1996).
2. R.D. James, M. Wuttig, Philos. Mag. A **77**, 1273 (1998).

3. M. Wutting, J. Li, C. Craciunescu, Scr. Mater. **44**, 2393 (2001).
4. K. Oikawa, L. Wulff, T. Iijima, F. Gejima, T. Ohmori, A. Fujita, K. Fukamichi, R. Kainuma, K. Ishida, Appl. Phys. Lett. **81**, 1657 (2002).
5. A. Fujuta, K. Fukamichi, F. Gejima, R. Kainuma, K. Ishida, Appl. Phys. Lett. **77**, 3054 (2001).
6. K. Oikawa, Y. Ota, T. Ohmori, Y. Tanaka, H. Morito, R. Kainuma, K. Fukamichi, K. Ishida, Appl. Phys. Lett. **81**, 5201 (2002).
7. Z. H.Liu, H. Liu, X.X. Zhang, M. Zang, X.F. Dai, H.N. Hu, J.L. Chen, G.H. Wu, Phys. Lett. A **329**, 214 (2004).
8. C. Picornell, J. Pons, E. Cesari, J. Dutkiewicz, Intermetallics. **16**, 751 (2008).
9. H. Zeng, M.Xia, J. Liu, Y. Huang, J.Li Acta Mater 53, 2005, 5125
10. T. Omori, N.Kamiya, Y. Sutou, K. Oikawa, R. Kainuma, K. Ishida, Mat. Sci. Eng. A **378**, (2004), 403
11. Otsuka. K, Ohba. T, Tokonami. M, and Wanyman C.M, *Scripta Metallurgica et Materialia* **29** (1993), 1359-1364.
12. Valeanu M, Filoti G, Kuncser V, Tolea F, Popescu B, Galatanu A, Schinteie G, Jianu AD, Mitelea I, Schinle D, Craciunescu CM, J. Mag. Mag. Mat. 320 (2008), E164-E167
13. H. Matsumoto, J All. and Comp. 370(2004)244-248
14. V.A. Chernenco, A. Fujita, S. Besseghini, J.I. Perez-Landazabal, J. Mag. Mag. Mat. 320 (2008),E156-E159
15. M. Sofronie, F. Tolea, V. Kuncser, M. Valeanu, J. Appl Phys. in press
16. Y. Imano, T. Omori, K. Oikawa, Y. Sutou, R. Kainuma, K. Ishida, Mat. Sci. Eng. A **438-440**, 970 (2006)
17. H. Morito, K. Oikawa, A. Fujita, K. Fukamichi, R. Kainuma, K. Ishida, Scripta Mater. **53** 1237 (2005).
18. H. Morito, K. Oikawa, A. Fujita, K. Fukamichi, R. Kainuma, K. Ishida, T. Takagi, J. Mag. Mag Mat. **290-291**, 850 (2005).

STUDIA UNIVERSITATIS BABEŞ-BOLYAI, PHYSICA, LV, 1, 2010

TiO_2 DOPING EFFECT ON SHORT RANGE ORDER OF $CaO{\cdot}P_2O_5$ GLASS MATRIX

R. CICEO LUCACEL, M. MAIER, V. SIMON[a]

ABSTRACT. Local order of ternary titanium-calcium–phosphate glasses prepared by classical melting method was characterized by X-ray diffraction (XRD), Scanning Electron Microscopy (SEM), Fourier transform infrared (FTIR) and Raman spectroscopy.

XRD results support the vitreous state of the samples and SEM analysis indicates no phase separation tendency. FTIR and Raman data reveal that the local network structure mainly consists of Q^1 and Q^2 tetrahedrons connected by P-O-P linkages. A gradual depolymerization of the phosphate chains was observed with the addition of the titanium dioxide.

Keywords: *calcium-phosphate glasses, titanium doping, XRD, FTIR, Raman analyses.*

INTRODUCTION

Phosphate glasses possess a series of attractive properties, like low glass transition and melting temperatures, high thermal expansion coefficient, and biocompatibility, which recommend them in many emerging applications, e.g. vitrification of radioactive waste [1], photonics [2], fast ion conductors [3], glass to metal seals [4] and most recently biomedical engineering [5]. All these applications require the optimisation of phosphate-based glass properties that is achievable by tuning their composition and structure.

In the last decades, studies on phosphate glasses have shown that their medical applications are limited not only by crystallization effect, but also in vitro studies have shown that too high solubility is detrimental to cell activity [6]. Franks et al. [7] have shown that glasses with 45 mol% P_2O_5 can be easily melt and own good compatibility as biomaterials.

Simple phosphate glasses do not have high chemical stability when compared with multicomponent phosphate-based glasses. In addition, soluble phosphate glasses with certain network modifiers slowly release active ingredients, like calcium ions, during dissolution process [8]. In this case, such active ingredients are used to cure the damaged bone tissues. It is well known that among the phosphate glass-based materials those containing calcium are preferred due to their bioactivity [9] or to unusual trends between the variation of composite versus physical properties [10]. The phosphate glasses containing calcium seems to be one of the best alternative approaches for

[a] *Faculty of Physics, Babes Bolyai University, Cluj-Napoca, 400084, Romania*

bone bonding since they have close chemical composition each with other and the glass can act as drug carriers and their crystallization can be controlled in order to improve the microstructure of the bioactive implant [11].

Titanium is an element that presents high physiological interest in the biomedical field. Due to its biocompatibility, titanium is considered the universal material for permanent implants, like dental implants of endosseous type. In some applications requiring special properties (higher mechanical strength, ductility or bioactivity) glasses or/and glass-ceramics containing titanium dioxide are preferred [12-15]. The role of TiO_2 in bioactive glasses and glass ceramics is still in discussion. The incorporation of TiO_2 the phosphate glasses not only improves their chemical durability but also increases nonlinear refractive index and modifies in a typical manner the thermophysical properties (density, molar volume, thermal expansion coefficient, glass transition temperature, etc.) [16]. Moreover, related to the P_2O_5-CaO based glasses, is recognized that the TiO_2 addition induces calcium-phosphates volume crystallization [12, 17].

Therefore, in this work we report results regarding the synthesis by melting method of glasses from $xTiO_2 \cdot (100-x)[CaO \cdot P_2O_5]$ system, and structural changes induced in $CaO \cdot P_2O_5$ glass matrix by TiO_2 doping.

EXPERIMENTAL PROCEDURE

The studied glasses have the composition expressed by the formula $xTiO_2 \cdot (100-x)[CaO \cdot P_2O_5]$ with x = 0; 0.1; 0.3; 0.5 and 1. They were prepared using the conventional melt quenching method. Appropriate quantities of reagent grade $NH_3 \cdot H_2PO_4$, $CaCO_3$, TiO_2 were mixed in an agate mortar. The batches were melted in air, in sintered corundum crucibles, in an electric furnace at 1200˚C for 45 minutes. The melts were quickly cooled at room temperature by pouring and stamping between two copper plates.

The structure of the samples was investigated by X-ray diffraction using a standard Bruker X D8 Advance diffractometer with a monochromator of graphite for CuK_α (λ = 1.54 Å). The diffractograms were performed in a 2θ degree range 10º- 80º with a speed of 2.4˚/ minute. A scanning electron microscope type Jeol JSM 5510 LV of 3.5 nm resolution with 100 kV accelerating voltage and $3x10^5$ magnification order was used to investigate the surface morphology. For performing the SEM measurements the samples were glued on an aluminum sample holder with conductive carbon cement. For FTIR measurements identical amounts of glasses were powdered and mixed with KBr in order to obtain thin pellets with a thickness of about 1 mm. The spectra were recorded at room temperature in the 350-4000 cm^{-1} range with a 6100 Jasco spectrometer with a maximum resolution of 0.5 cm^{-1} and signal/noise ratio 42,000:1. The Raman spectra were obtained with a micro-Raman setup (HR LabRam inverse, Jobin-Yvon-Horiba). The excitation wavelength 532 nm was delivered by a frequency-doubled Nd:YAG laser (Coherent Compass) with a laser power of 10 mW incident on the sample. The Raman signal was collected with a charge-coupled-device camera operating at 220 K.

RESULTS AND DISCUSSION

The X-ray diffraction patterns (Fig. 1) are characterized by broad diffraction lines which attest to the vitreous character of all $xTiO_2{\cdot}(100\text{-}x)[CaO{\cdot}P_2O_5]$ samples. SEM micrographs recorded from the powdered glasses (Fig. 2) do not reveal phase separation tendency in any of the random-sized particles. The room temperature FTIR absorption spectra (Fig. 3) were analyzed based on the method proposed by Tarte and Condrate [18, 19], by comparing the experimental data of glasses with those of related crystalline compounds. The FTIR spectrum of the glass matrix exhibits in the lower wavenumber domain bands that are due to overlapping of vibration modes coming from phosphate structural units as follows: the broad bands centred at ~ 510 cm^{-1} is assigned to fundamental frequencies of PO_4^{3-} or the harmonics of δ(O=P-O) and the wide band centered at ~ 745 cm^{-1} is assigned to the symmetric stretching vibration of P-O-P bonds occurring in ring type groups associated with $Q^2([P(OP)_2(O^-)_2])$ metaphosphate units [20, 21]. In terms of Q^n terminology, *n* represents the number of bridging oxygen atoms per PO_4 tetrahedron.

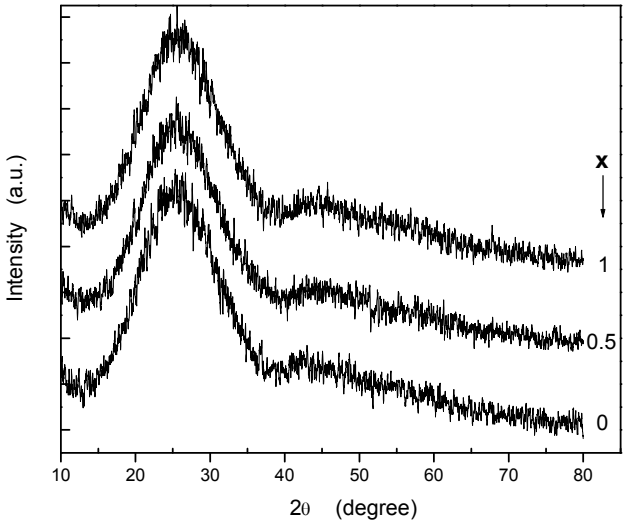

Fig. 1. X-ray diffraction patterns of the $xTiO_2{\cdot}(100\text{-}x)[CaO{\cdot}P_2O_5]$ glass system.

The infrared 800–1400 cm^{-1} spectral domain reveals the presence of three well defined bands centred at ~ 917, 1115 and 1270 cm^{-1}, along with a weak shoulder at ~1005 cm^{-1}. The band centred at ~913 cm^{-1} is due to the asymmetric stretching vibration of P-O-P bonds in short chains associated with Q^1 ($[P(OP)(OP^-)_3]$ pyrophosphate sites [20, 22, 23] while the band from ~ 1115 cm^{-1} comes from asymmetric stretching modes of PO_3 group associated with Q^1 phosphate units, and

that centered at ~ 1270 cm^{-1} is given by the asymmetric stretching vibration of doubly bonded oxygen υ_{as}(P=O) modes from Q^2 units [22]. The weak shoulder from ~1005 cm^{-1} is characteristic to the isolated 'P' tetrahedral $(PO_4)^3$ (Q^0 orthophosphate species) connected to calcium cations [23].

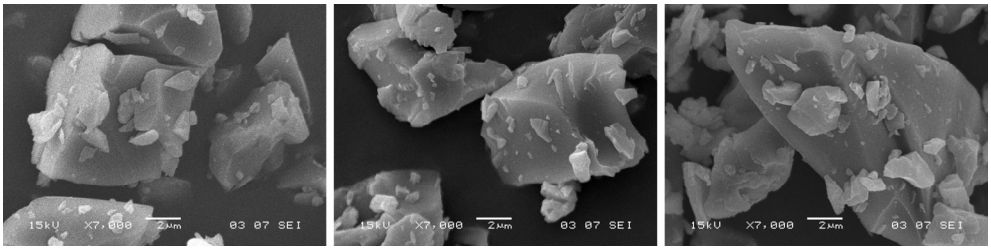

(a) (b) (c)

Fig. 2. SEM picture of $xTiO_2 \cdot (100\text{-}x)[CaO \cdot P_2O_5]$ sampls with x = 0 (a), x = 0.5 (b) and x = 1 mol% TiO_2 (c).

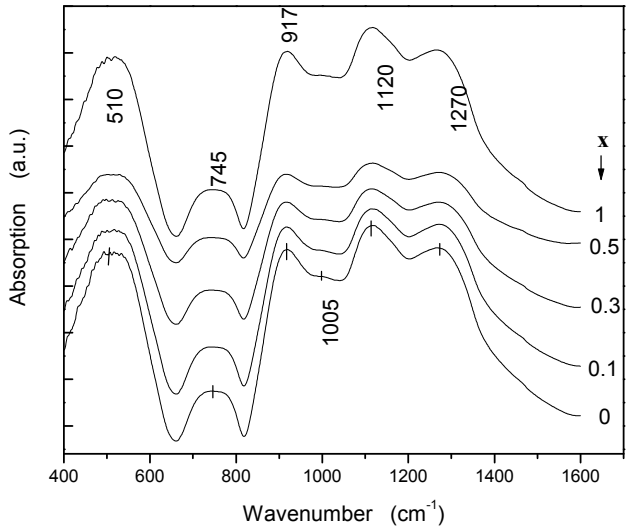

Fig. 3. FTIR spectra of $xTiO_2 \cdot (100\text{-}x)[CaO \cdot P_2O_5]$ glass system.

Having in view the above assignments of the infrared absorption lines from glass matrix spectrum one may consider that the local structure of $CaO \cdot P_2O_5$ host glass is mainly build by Q^1 and Q^2 units along with minor contribution from Q^0 units. Since vitreous P_2O_5 consist only in ultraphosphate Q^3 ($[P(OP)_3(O^-)_1]$) units with

three bridging oxygen atoms (P-O-P) and one double bounding by the phosphorous atom (P=O), is obviously that the presence in the P_2O_5-CaO glasses structure of meta- and pyro-phosphate units is given by the ability of Ca^{2+} cations to breakup the continuous 3D phosphorous network [21].

Adding gradually small quantities of titanium oxide into the glass matrix composition induces no major changes in terms of FTIR line shape. One aspect deserved to be point out is that in the 0.1-0.5 mol% TiO_2 compositional range the intensity of FTIR bands tend to decrease with the titanium oxide increase, while for the sample with 1 mol% TiO_2 the intensity of FTIR bands increases again and becomes similar to that of glass matrix. The progressively decreasing of the FTIR band intensity up to 0.5 mol% of TiO_2 can be explained in the following way: an initial introduction of TiO_2 in the matrix composition leads to the breaking of P-O-P and P-O-Ca bonds from calcium-phosphate network, forming stronger covalent Ti-O bonds and increasing the number of terminal oxygen atoms. It seems that first, until 0.5 mol%, titanium oxide acts as a modifier, probably titanium occurs five coordinated in a TiO_5 square-pyramids arrangement [24] causing the glass network depolimerization. A further addition of TiO_2 (> 0.5 mol%) in the glass network results in the creation of ionic cross-linking between non bridging oxygen atoms of two different chains, that reinforces the glass structure and in this case is possible that the titanium oxide acts as a network former oxide, probably titanium occurs six coordinated in TiO_6 octahedral arrangements [25]. The similarity between FTIR spectra of samples with 0 and 1 mol% TiO_2 suggests a possible double network in the case of sample with 1 mol%: one dominated by the Q^2, Q^1 phosphate structural units and one characteristic to titanium oxide, undetected through FTIR measurements.

The analysis of Raman spectra (Fig. 4) shows that the glass matrix presents two strong bands centered at ~ 700 cm^{-1} and 1162 cm^{-1} assigned as follows: the first one to the symmetric stretching of P-O-P linkages in Q^2 and Q^1 structural units [23, 26], and the second one to the symmetric and asymmetric stretching vibration of PO_2 groups (Q^2 structural units) [26]. At the same time, the Raman spectrum of the glass matrix presents four weak bands centered around 340 cm^{-1} (assigned to bending vibration of O-P-O linkages), 550 cm^{-1} (assigned to symmetric bending vibration of P-O-terminal bonds), 1025 cm^{-1} (ascribed to the symmetric stretching vibration of $-PO_3^{2-}$ terminal group groups from the Q^1 species) and 1265 cm^{-1} (ascribed to asymmetric stretching vibration of PO_2 groups in Q^2 units) [26, 27]. Based on the Raman bands assignment one may assume that the glass matrix network is mainly built by metha- and pyro-phosphate units.

As titanium oxide is added to the glass matrix two important changes in lines position and relative intensity are noticed:

(a) within 0.1 – 1 mol% TiO_2 content it can be observed a general decrease in intensity of all Raman bands, denoting a decrease in the depolymerization degree of the network;

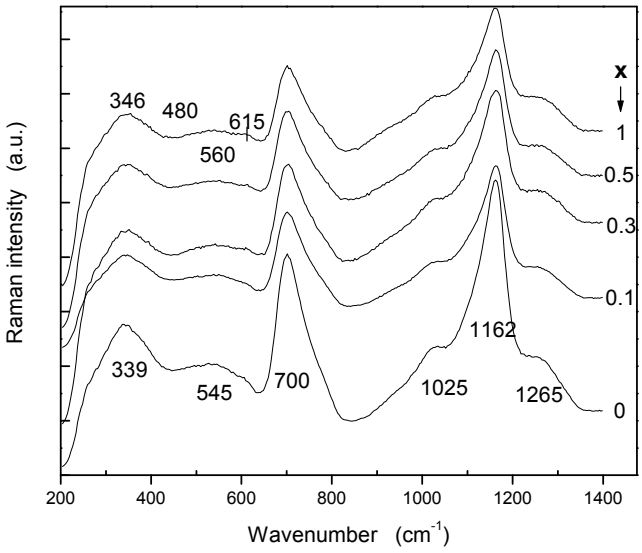

Fig. 4. Raman spectra of $xTiO_2 \cdot (100\text{-}x)[CaO \cdot P_2O_5]$ glass system.

(b) for the samples with 1 mol% TiO_2 one important aspect is related to the occurrence of the band at ~ 615 cm^{-1} assigned to the TiO_6 structural units vibrations [28]. Moreover, minor shifts are remarked for bands placed at 1025 cm^{-1} and 1265 cm^{-1} to 1030 cm^{-1} and 1260 cm^{-1}, respectively. These Raman bands are given by $\nu_{sym}(-PO_3^{2-})$ and $\nu(PO_2)$ vibrations from Q^1 and Q^2 species. According to previous studies [29] the peak frequency of $\nu(PO_2)$ band decreases as the metal-oxygen bond force constant decreases and/or the average of PO_2 angles increases. In this approach, it is obviously that in case of sample with 1 mol% TiO_2 a reorganization of the short and medium range network structure takes place.

CONCLUSIONS

Homogeneous samples of $xTiO_2 \cdot (100\text{-}x)[CaO \cdot P_2O_5]$ ternary glass system, with $0 \leq x \leq 1$ mol %, has been prepared by conventional melt quenching technique. X-ray diffraction analysis reveals the vitreous character of samples, and SEM micrographs show no evidence of phase separation tendency. FTIR and Raman results prove a local network structure mainly based on meta- and pyro-phosphate units, which are typical for glassy phosphate compounds.

Introducing and gradually increasing the titanium oxide content into the calcium-phosphate glass matrix causes a slow depolymerization of the infinite metaphosphate chains. As TiO_2 doping reaches 1 mol%, the Raman data indicate the development of TiO_6 octahedral units in the short range order structure of the glass matrix.

ACKNOWLEDGEMENTS:

This research was accomplished in the framework of PNII Idei PCCE-248/2008 project of CNCSIS Romania.

REFERENCES

1. P. Bergo, S.T. Reis, W.M. Pontuschka, J.M. Prison, C.C. Motta, J. Non-Cryst. Solids, 336 (2004) 159.
2. F.F. Sene, J.R. Martinelli, L. Gomes, J. Non-Cryst. Solids, 348 (2004) 63.
3. S. Kumar, P. Vinatier, A. Levasseur, K.J. Rao, J. Solid State Chem., 177 (2004) 1723.
4. J.Y. Wei, Y. Hu, L.G. Hwa, J. Non-Cryst. Solids, 288 (2001) 140.
5. A.G. Dias, J.M.S. Skakle, I.R. Gibson, M.A. Lopez, J.D. Santos, J. Non-Cryst. Solids, 351 (2005) 810.
6. V. Salih, K. Franks, M. James, J.M. Hastings, J.C. Knowles, J. Olsen, J. Mater. Med. 22 (2000) 615.
7. K. Franks, I. Abrahams, G. Georgiou, J.C. Knowles, Biomaterials, 22 (2001) 497.
8. U. Motohiro, M. Mizuno, Y. Kuboki Akio, A. Makishima, F. Watari, Biomaterials, 19 (1998) 2277.
9. L.L. Hench, J. Am. Ceram. Soc. 74 (1991) 1487.
10. E. Kordes, W. Vogel, R. Feterowsky, Z. Elektrochem. 57 (1953) 282.
11. R. Li, A.E. Clark, L.L. Hench, J. Appl. Biomater. 2 (1991) 231.
12. A.S. Monem, H.A. Elbatal, E.M.A. Khalil, M.A. Azooz, Y.M. Hamdy, J. Mater. Sci: Mater. Med. 19 (2008) 1097.
13. V. Rajendran, A.V.G. Devi, M. Azooz, F.H. El-Batal, J. Non-Cryst. Solids, 353 (2007) 77.
14. D.S. Brauer, C. Russel, J. Kraft, J. Non-Cryst. Solids, 353 (2007) 263.
15. A.M.B. Silva, R.N. Correia, J.M.M. Oliveira, M.H.V. Fernandes, J. Eur. Ceram. Soc., 30 (2010) 1253.
16. B. Tiwari, A. Dixit, G.P. Kothiyal, M. Pandey, S.K. Deb, BARC Newslett., 285 (2007) 167.
17. M. Navarro, M.P. Ginebra, J. Clement, M. Salvador, A. Gloria, J.A. Plannelll, J. Am. Ceram. Soc. 86 (2003) 1345.

18. P. Tarte, Physics of Non Crystalline Solids, Ed. I. A. Prins, Elsevier, Amsterdam, 1964, p. 549.
19. R.A. Condrat, Introduction to glass science, Ed. D. Pye, H. J. Stevens and W.C. LaCourse, Plenum Press, New York, 1972, p. 101-135.
20. J.J. Hudgens, R.K. Brow, D.R. Tallant, S.W. Martin, J. Non-Cryst. Solids, 223 (1998) 21.
21. J.E. Pemberton, L. Latifzadeh, J.P. Fletcher, S.H. Risbud, Chem. Mater. 3 (1991) 195.
22. M.A. Karakassides, A. Saranti, I. Koutselas, J. Non-Cryst. Solids, 347 (2004) 69.
23. A. Saranti, I. Koutselas, M. A. Karakassides, J. Non-Cryst. Solids, 352 (2006) 390.
24. M.A. Roberts, G. Sankar, J.M. Thomas, R.H. Jones, H. Du, J. Chen, W. Pang, R. Xu, Nature, 381 (1996) 401.
25. W. Wong-Ng, R.S. Roth, T.A. Vanderah, H.F. McMurdie, J. Res. Natl. Inst. Stand. Technol. 106 (2001) 1097.
26. Y.M. Moustafa, K. El-Egili, J. Non-Cryst. Solids, 240 (1998) 144.
27. D. Ilieva, B. Jivov, G. Bogacev, C. Petkov, I. Penkov and Y. Dimitriev, J. Non-Cryst. Solids, 238 (2001) 195.
28. A. Saboori, M. Rabiee, F. Moztarzadeh, M. Sheikni, M. Tahriri, M. Karimi, Mat. Sci. Eng. C, 29 (2009) 335.
29. D. Ilieva, B. Kirov, D. kovacheva, T. Tsacheva, Y. Dimitriev, G. Bogachev, Ch. Petkov, J. Non-Cryst. Solids, 293-295 (2001) 562.

STUDIA UNIVERSITATIS BABEŞ-BOLYAI, PHYSICA, LV, 1, 2010

STRUCTURAL AND MORPHOLOGICAL PROPERTIES OF SOL-GEL DERIVED BIOGLASSES PREPARED UNDER VARIOUS CONDITIONS

G. MELINTE, L. BAIA, S. SIMON[a]

ABSTRACT. Bioactive glasses belonging to the $60SiO_2$-$36CaO$-$4P_2O_5$ (mol %) system have been prepared by sol-gel method under various conditions, using different molar ratios of HCl:TEOS and replacing H_2O with H_2O_2. The obtained bioglasses were characterized by X-ray powder diffraction, BET analysis and Raman spectroscopy. Depending on synthesis conditions, crystalline Ca_2SiO_4 or hydroxyapatite phases are developed in some samples. At the same time, the preparation conditions influence the specific surface area and the connectivity of silica units in the structural network of these samples.

Keywords: *bioactive glasses; sol-gel; XRD; BET; Raman spectroscopy.*

1. INTRODUCTION

Sol-gel derived bioactive glasses were for the first time prepared in the early 1990s[1]. Using hydrolysis and polymerization of metal hydroxides, alkoxides and/or inorganic salts bioglasses with various textural properties could be prepared. [2] Sol–gel derived bioactive glasses tend to have more simple compositions than the melt-derived bioactive glasses and exhibit enhanced bioactivity and degradation/ bioresorption properties, due to the higher degree of purity, surface area, homogeneity and the presence of residual hydroxyl ions. [3, 4] Many processing variables can be used to control the pore network structure, such as glass composition, the type and concentration of the catalyst or sintering temperature. [5]

The main application of these bioglasses in the clinical field is the filling of osseous cavities, manufacture of small parts for middle ear bone replacement and maxilofacial reconstruction and dental applications. Thanks to advances in related medical technologies, bioactive glasses are now undergoing a new stage of development, resulting in different mechanical properties, drug delivery capabilities, bioactive coating of metallic implants, protein and/or cell activation for tissue regeneration and tissue engineering. [6]

[a] *"Babes-Bolyai" University, Faculty of Physics & Institute for Interdisciplinary Research in Bio-Nano-Science Cluj-Napoca, M. Kogalniceanu 1, 400084, Romania*

The aim of the present work is to determine structural and morphological particularities from silica based bioglasses when different preparation conditions are used.

2. EXPERIMENTAL

2.1. Sample preparation

The composition of the studied bioactive glasses belongs to the system $60SiO_2$-$36CaO$- $4P_2O_5$ (based on mol %). The sol-gel was prepared as follows: tetraethyl ortosilicate (TEOS:$C_8H_{20}Si$) was mixed with absolute ethanol (C_2H_5-OH). The molar ratio of Et-OH:TEOS was fixed at 4. Double distillated water (samples A and C) or hydrogen peroxide (sample B) were used to prepare solutions of calcium nitrate ($Ca(NO_3)_2 \cdot 4H_2O$) and dibasic ammonium phosphate ($(NH_4)_2HPO_4$). The $H_2O(H_2O_2$,30%):TEOS molar ratio for each sample was of 10:1. Each solution was consecutively added to TEOS solution under continuous stirring. For the sample C hydrochloric acid (HCl, 2N) in the molar ratio HCl:TEOS of 4:1 was added in the ammonium phosphate solution. The samples A and B was prepared by adding HCl in the final solution with a HCl:TEOS molar ratio of 20:1 and 4:1, respectively. The final solutions were kept at room temperature until gelation occurs (4 days). The obtained gels were aged for 10 days at room temperature. The dried gels were sintered at 550°C for 1/2h.

2.2. Sample characterization

The X-ray diffraction patterns were obtained with a Shimatzu XRD-6000 diffractometer, using CuKα radiation (λ = 1.5418 Å), with Ni–filter. The measurements were performed at a scan speed of 4°/min on a 2θ scan range of 10-80º and as calibrating material it was used quartz powder. Operating power of the X-ray source was 40 kV at 30 mA intensity.

The specific surface area, pore volume and pore radius of the samples were obtained from N_2-adsorption-desorption isotherms. by using a Sorptomatic 1990 apparatus. The BET method was used for calculation of surface area, and the BJH method for determination of porosity parameters.

The FT-Raman was recorded by using a Bruker Equinox 55 spectrometer with an integrated FRA 106 Raman module. Radiation of 1064 nm from a Nd:YAG laser was employed for recording the Raman spectra. The power incident on the sample was 350 mW and the spectral resolution was of 4 cm^{-1}.

3. RESULTS AND DISCUSSION

Fig. 1 shows the X-ray diffractograms of the sol-gel derived bioglass samples sintered at 550°C. In the XRD pattern of the sample A one can observe the main characteristics of the calcium silicate (Ca_2SiO_4) crystalline phase. [7] Nevertheless, in this sample the SiO_4 network remains preponderant in amorphous phase. For the

samples B and C the existence of crystalline hydroxyapatite (HA) in the glass network is clearly indicated by six diffraction peaks observed at 2θ= 25.7°, 31.78°, 38.8°, 46°, 49.3° and 63.7°. [8] One should mention that a few HA peaks (2θ=38.8°, 49.3° and 63.7°) are missing in the XRD pattern of the sample A, however, the presence of this crystalline phase can not be excluded.

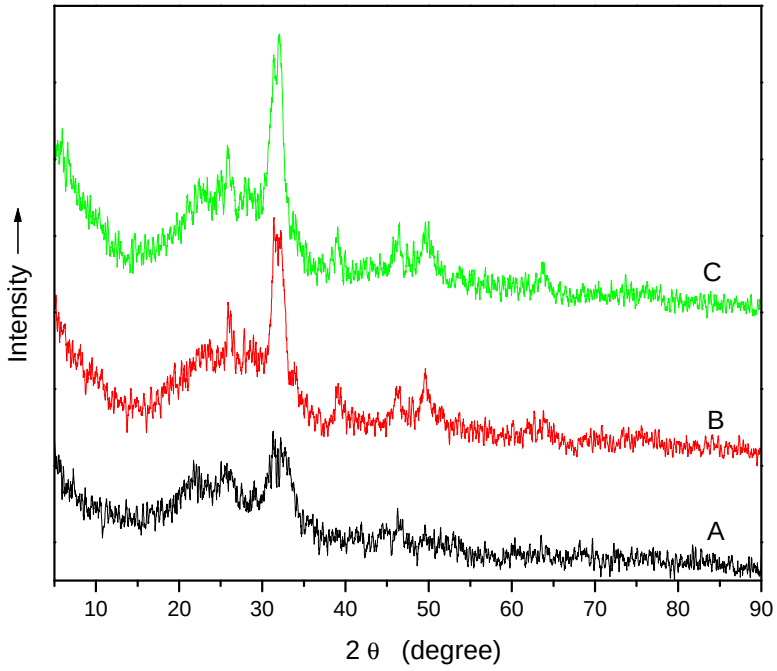

Fig. 1. XRD patterns of the sol-gel derived bioglasses sintered at 550°C as previously denoted.

Fig. 2 shows nitrogen adsorption and desorption isotherms of the bioglass samples sintered at 550°C. According to IUPAC classification [9] the sample A exhibits the type H4 hysteresis loop which is normally associated with narrow slit-like pores. In this case the shape of the isotherm, between Type I and Type II isotherms, is indicative of meso and micro porosity. The observed isotherms for samples B and C are Type IV isotherms, characteristic for the samples which contain meso and micro pores with a non-perfect cylindrical shape. These samples show H1 hysteresis loops, characterized by a narrow, step and parallel adsorption and desorption branches. Type H1 loops are given by adsorbents with a narrow distribution of uniform pores (e.g. open-ended tubular pores). [10]

The pore size distributions plot in Fig. 3, was obtained from BJH analysis of nitrogen desorption branches. Important differences in the shape of the pore distributions and the modal textural pores diameter of the samples can be observed.

The detailed data on specific surface area, pore volume and pore size of each sample are summarized in Table 1. Samples A and B exhibit a narrow and unimodal pore distribution and the modal pore diameter was 3.96 nm and 7.45 nm, respectively. Sample C shows a more broad distribution with a maximum pore diameter of 8.49 nm. From the shape of hysteresis loops and the Horvath and Kawazoe pore distribution (not presented) the existence of micropores in all the samples is proved. Also, it can be observed that micropores hold an important percentage in the pores distribution of sample A.

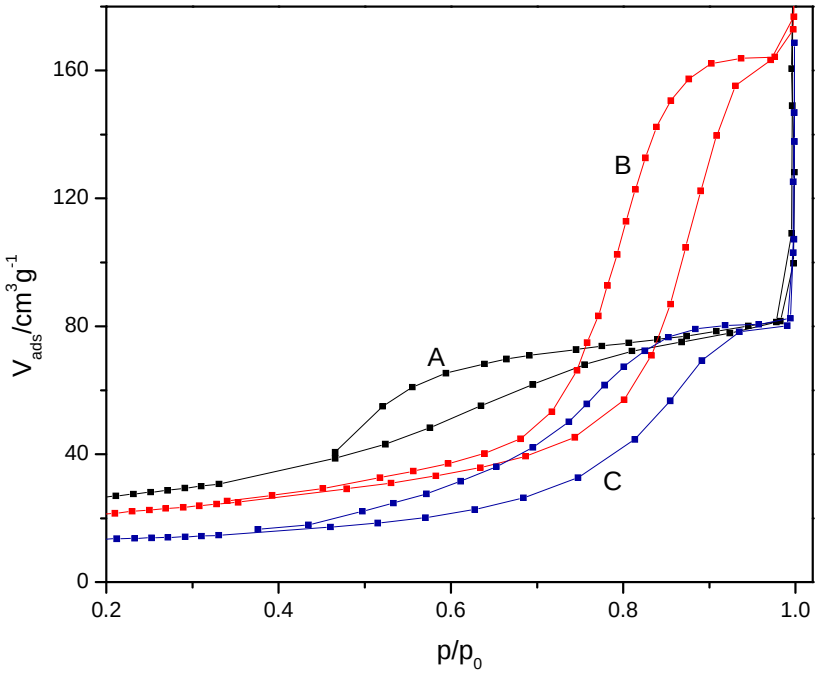

Fig. 2. Nitrogen adsorption isotherms of 60S bioglass samples prepared in various conditions.

Table 1 Textural properties of the bioglass powders sintered at 550°C .

Sample code	BET surface area (m^2g^{-1})	Pore volume (cm^3g^{-1})	BJH maximum pore diameter (nm)	BJH median pore diameter (nm)
A	90.216	0.1229	3.9662	4.2014
B	103.15	0.2676	7.4556	7.6896
C	42.235	0.1217	8.4912	7.9802

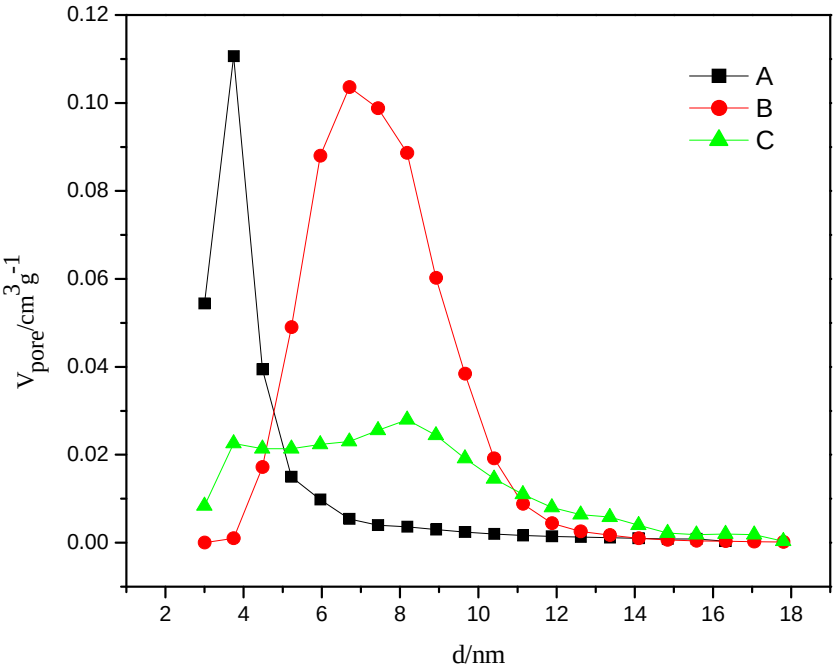

Fig. 3. Textural pore size distributions of 60S bioglass samples obtained from BJH analysis of nitrogen desorption branches.

The specific surface area and the pore volume reach the highest value for the sample prepared with hydrogen peroxide. Moreover, the textural properties of the samples A and C proved the relation existing between the surface area and the pore size. These samples have an equal pore volume, but different surface areas and pores size. The higher surface area exhibited by the sample A is related to the median pores diameter which is almost half of the median pores diameter of the sample C.

The network connectivity of a silica glasses can viewed through the structural units usually represented as Q_n, where Q represents the tetrahedral unit and n the number of bridging oxygen per tetrahedron (varies between 0 and 4) [11]. Raman spectroscopy has been established as a very powerful technique for identification of tetrahedral SiO_4 units.

The Raman spectra of the bioglass samples are presented in Fig. 4. Sample A exhibits two well defined peaks located at 724 and 958 cm^{-1} assigned to the Si-O bending motions and Q_3 unit vibrations, respectively. [11, 12,] These sharp peaks demonstrate the existence of the Ca_2SiO_4 phase, this result being in agreement with that obtained from X-ray diffraction data. The band centered at ~837cm^{-1} is made up from two overlapped bands attributed to the Q_2 and Q_1 unit vibrations. The Q_4 unit vibrations of SiO_4 tetrahedron give rise to a shoulder situated at ~1200cm^{-1}.[13]

The Raman spectrum of the sample B shows similar spectral features with those observed for sample A, the differences consisting in the broadening of the bands located at 724 and 837 cm^{-1}, the latter being shifted to lower wavenumbers (preponderantly Q_1 units), and the decrease in intensity of the peak attributed to the Q_3 units (958 cm^{-1}). Moreover, for the sample C the signal given by the Q_3 units becomes even larger and exhibits a drastic reduction in intensity. The band located at ~1060 cm^{-1}, which is attributed to the Q_4 units, is clearly defined only for the samples B and C, in the case of sample A this band diminishing. Thus, one can conclude that the more connected silica network built up the structure of bioglasses B and C.

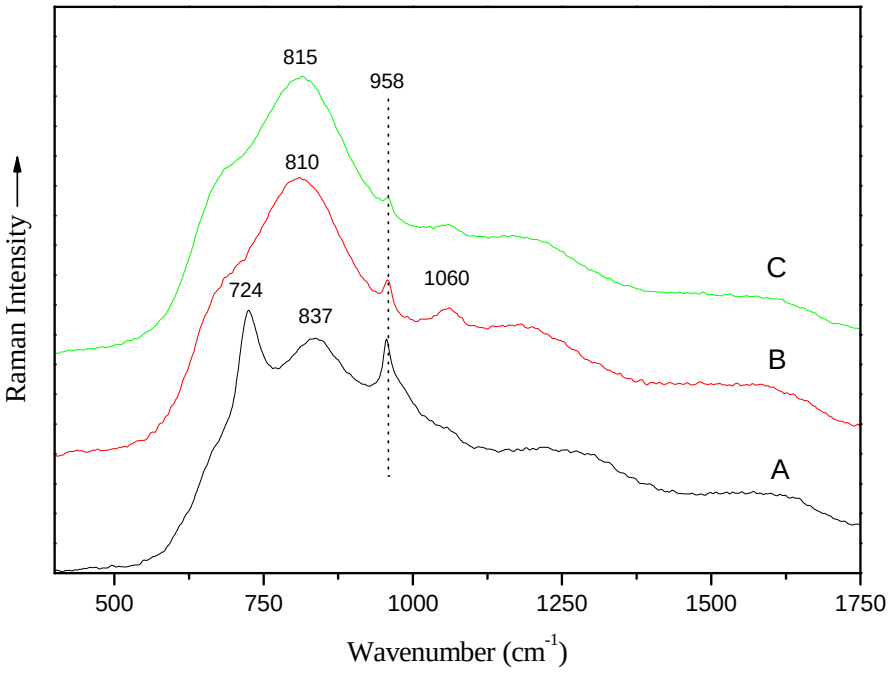

Fig. 4. Raman spectra of the sol-gel derived bioglasses sintered at 550°C as previously denoted.

4. CONCLUSIONS

Sol-gel method was used to prepare bioactive glasses belonging to the $60SiO_2$-$36CaO$-$4P_2O_5$ (mol %) system by using different molar ratios of HCl:TEOS (20:1 - sample A and 4:1 - sample C) and by replacing H_2O with H_2O_2 (sample B). XRD data revealed that crystalline Ca_2SiO_4 phase is embedded into the structure of sample A, while crystalline hydroxyapatite was found to be present in bioglasses B

and C. The N_2 adsorption measurements evidenced that the sample B presents has the highest surface area, attractive for biomedical applications. Raman spectra analysis indicates that B and C samples own a more connected silica network.

ACKNOWLEDGEMENTS:

This research was accomplished in the framework of PNII Idei PCCE-101/2008 project of CNCSIS Romania.

REFERENCES

1. R. Li, A.E. Clark, L.L. Hench, J. Appl. Biomater., 2, 231–9 (1991)
2. C.J.Brinker, G.W. Scherer, Sol–gel science. San Diego, CA: Academic Press; 1990
3. J.P.Zhong, D.G. Greenspan, J.Biomed. Mater. Res. (Appl. Biomater.), 53, 694-701 (2000)
4. M. Hamadouche, A. Meunier, D.C. Greenspan, C. Blanchat, J.P Zhong, G.P. LaTorre, et al., J. Biomed. Mater. Res., 54, 560–566 (2001)
5. J.R. Jones, L.L. Hench, J. Mater. Science, 38, 3783 – 3790 (2003)
6. M.V.Regi, C.V. Ragel, A.J. Salinas, Eur. J. Inorg. Chem., 1029-1042 (2003)
7. S. Tsunematsu, K. Inoue, K. Kimura, H. Yamada, Cement Concrete Res., 34, 717 (2004)
8. A. Balamurugan et al., Materials Letters, 60, 3752-3757 (2006)
9. F. Rouquerol, J. Rouquerol, K. Sing, Adsorption by Powder and Porous Solids, San Diego, (1998)
10. J.R. Jones, L.M. Ehrenfried, L.L. Hench, Biomaterials 27, 964–973 (2006)
11. H. Aquiar, J.Serra, P. Gonzalez, B. Leon, J. Non-Cryst. Solids, 355, 475-480 (2009)
12. R.H. Stolen, G.E. Walnfen, J. Chem. Phys., 64, 2623 (1976)
13. H. Aquiar, E.L. Solla, J.Serra, P.Gonzales, B.Leon, F. Malz, C.Jager, J. Non-Cryst. Solids, 354, 5004-5008 (2008)

STUDIA UNIVERSITATIS BABEŞ-BOLYAI, PHYSICA, LV, 1, 2010

ABSORPTION EXPERIMENTS OF β AND γ RADIATION IN POLYMERS

M. POP[a], L. DARABAN[a], P. VAN DEN WINKEL[b], M. TODICA[a]

ABSTRACT. In this paper, the absorption of β and γ radiation in different polymers was studied, in order to determine the absorption coefficients of the half life thickness in these type of materials. With the help of these experimental data, the global β and γ radioactivity of some radioactive waste, packed in different plastic bags, coming from nuclear medicine departments, can be estimated.

Also, the β spectrometry with huge plastic scintillators was established, in order to evaluate the global activity of β-pure radioactive waste by using a calibration in energy with Compton electrons.

The β global measurements were performed over regions of interest ROI, established for each determined radioisotope. It also was demonstrated that the γ radiation has a weak attenuation in such materials, its dependence of the thickness being almost linear.

Keywords: *Polymers degradation, Gamma irradiation and Spectroscopic methods*

1. Introduction

The Storage and assessment of radioactive waste from nuclear medicine departments (results obtained in the operations performed during medical investigations) is very important, the price of the storage for radioactive waste being proportional with its activity.

These waste are in general: radioactive plastic syringes infected with the respective radioactive trasor, absorbing filter paper, polyethylene bags, PET boxes, etc.

In terms of the emitted radiation, these emit γ or β radiation, but the most difficult to be measured are those which contain β pure radioisotopes (eg: ^{32}P, ^{14}C radionuclides from labeled compounds, etc...). It is necessary to assess some development methods for measuring the activity of this waste by γ and β spectrometry.

β activity measurements were performed with plastic scintillators [1, 2], where a large percentage was corrected due to the attenuation of the β radiation measured by radioactive infected waste material, but also in polyethylene bags and PET boxes, in which they are normally stored.

Previously, we have studied the problem of β spectrometry with plastic scintillators and the absorbtion of this radiation in various plastic materials.

[a] *Faculty of Physics, Univesity Babes-Bolyai Cluj-Napoca, Romania*
[b] *Enheid Cyclotron, Vrije Universiteit Brussel, Belgium*

2. Study of the characteristics of a large plastic scintillator

A large area (45x48.5x4 cm) plastic scintillator, sideways coupled to a single photomultiplier tube type Canberra, with preamplifier type 2007 B, and acqusition system (Acquspec-board and Acquspec-software, incorporated in Pentium II computer, type Hewlett Packard) were used (in the VUB Brussel Laboratory).

The detector dependence on the beta radiation energy was inspected. The energy-calibration has been made with Compton electrons and the end-point method from beta known spectra. When the gamma radiation energy is well known, the Compton edge value can be calculated with a classical formula (1) in which the condition θ is set to 180^o:

$$E_{emax} = \frac{E_\gamma}{1 + \frac{mc^2}{2E_\gamma}} \tag{1}$$

In the first tests, described in [1], it has been noticed that the large plastic scintillator has a weak energetically resolution and it's not able to make the difference of ~0.2 MeV energy between the two Compton edges enclosed in the Compton electrons distribution of Co-60. Nevertheless the detector has a good linear energy-dependence up to 2 MeV.

In publications in this domain there are many discussions about the technique of the E_{emax} edge positioning on the Compton electrons spectra as those from the Fig.1, [2-5].

A new method of differential-type [6] was applied by which a program, *Ducir* smooths the spectrum and performs a differentiation for locating the Compton edge on the most abrupt descendent part of the spectrum [2]. The following calibration curve was obtained: (Fig. 1.).

This method of calibration is in good agreement with the results obtained by others techniques from literature [7-10] for the position of the Compton edge localisation.

The plastic detectors system offers an other alternative for measuring some beta-radioactive contaminated wastes, which are sorted on radionuclides from the beginning of work, cut in pieces (if they are of paper) and homogenate and then introduced in a thin bag of polyethylene of fixed form. The superficial activity measured with plastic detectors, previously calibrated with the aide of packets containing known isotopes of a known activity, is proportional (or depends on a certain law [11]) with the global activity, of the packet volume. In this case we have a high efficiency of detection of the radioisotope. In the case when the waste products were unselectively collected (but we know what kind of radioactive isotopes they content) the beta active radionuclides can be measured on the spectrum regions (ROI) typical only to them, but the efficiency of detection and the sensibility is low, especially in superior energy regions (for ex. of P-32).

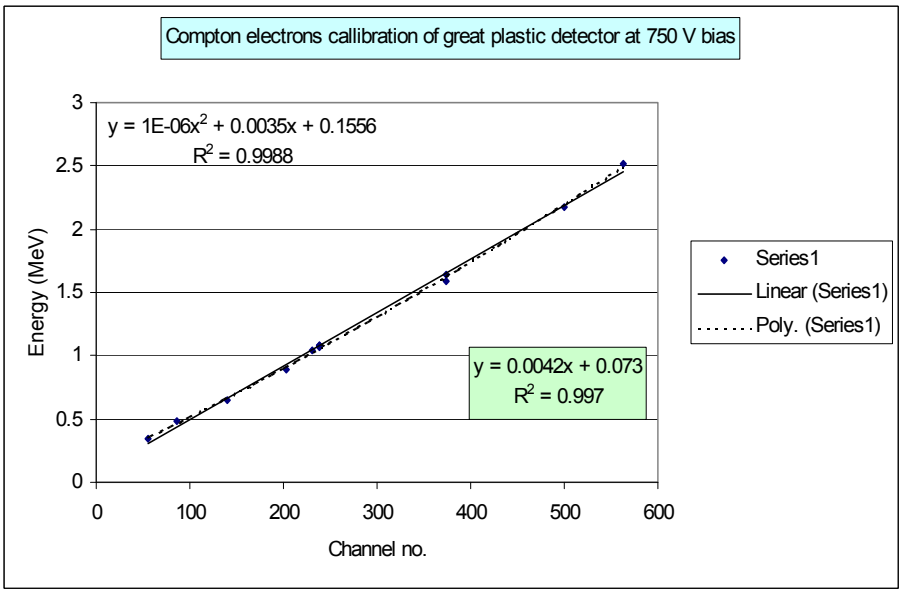

Fig. 1. Energy-calibration curve of the large plastic scintilator with the Compton electrons

Regions of Interest (ROI) were established, at different biases on the photomultiplier, for P-32, Cl-36 and C-14 nuclides measured from melange radioactive waste (Fig. 2.). At a bias of U = 900V the ROI are: for C-14 between channels 0-225, for Cl-36 between channels 225-1040 and for P-32 between channels 1040-2048 .

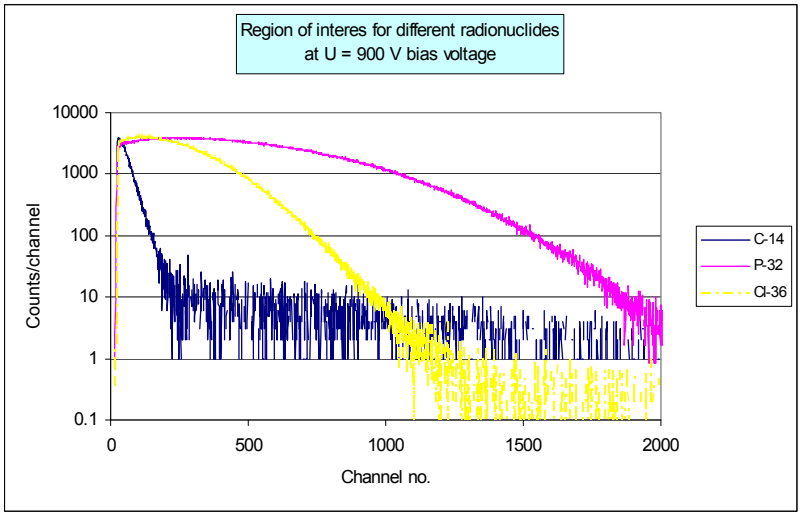

Fig. 2. The Region Of Interest (R.O.I) for the great plastic scintillator at bias U= 900 V on the photomultiplier

It can be adapted to measure in ROI. for beta-pure emitting known radionuclides with different energies from the large radioactive waste samples.

3. The ionizing radiation interaction with plastics

Through plastics, nuclear radiation produce ionization and the ions and electrons give rise resulted from free radicals that can cause various chemical reactions, which are directly proportioned with the dose of administered radiation. When passing through the matter, the radiation beam intensity is reduced, so the mitigating suffers a phenomenon that is the result of different mechanisms of interaction. Consequently, β radiation, consisting in electrically charged light particles (electrons and pozitironi), suffers a process of interaction in which predominantly occurs non-elastic collisions with electrons and nuclei crossed environment.

Instead, the X and γ -radiation causes mainly non-elastic interactions with the environment by passing electrons (internal fotoelectric effect and Compton effect). Considering these characteristics, the attenuation suffered with the ionizing radiation is mainly based on 3 types:

a) The *attenuation on the way*, R-specific for elastic or non-elastic collision processes in which the ionizing particle loses a small quantity of energy. In this case, spcific α particles, each particle is practically constant throughout the process, and the beam intensity is maintained constant until the end of the course, which drops sharply (Fig. 3a.) [12].

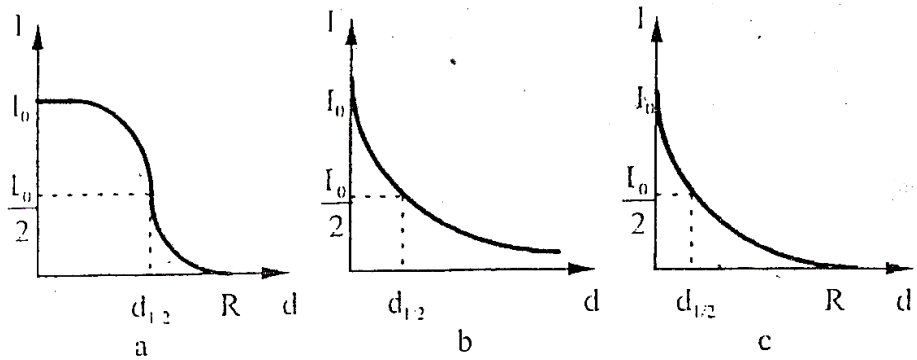

Fig. 3. Attenuation types: a) with range R; b) exponential; c) intermediar.

b) The *exponential attenuation*, characterized by the collision processes of X-rays and γ. Consequently, the photon loses all the energy (internal photoelectric effect), or most of its energy (Compton effect). Since the probability of absorption is constant at a certain point of energy, ionizing radiation beam intensity decreases with the exponential law (Fig. 3b.), characteristic X-rays and γ . (as will be seen in futhere Formula 3).

c) *Mitigation* is an *interimediar* nature radiation, but whose intensity gradually decreases as the beam is not monoenergetic and the collision process particle loses a significant part of its energy (Fig. 3c.). This case is a tipical β radiation.

All in all, it should be clear that in the latter case we deal with an exponential law of attenuation, like in the case of γ radiation, and therefore we cannot define a linear coefficient of absorption of the exponential mitigation law, but we can only define it as a so-called thick half range $d_{1/2}$ flow particule incident.

4. β – radiation interaction with plastic materials

Fast electrons emitted by radioactive isotopes or betatroane have, at the same amount of energy, a much greater speed than α particles because they have less mass.

This is the reason why have a specific ionization of about 100 times smaller than α particles, but also because of lower mass, it interacts strongly with electrons and atomic nuclei collision elastic spreading being important.

In addition, β radiation have a range of energies, and therefore suffer from interacting with a substance, an intermediate type of mitigation.

The environments which are composed of light elements, such as polymers, the spreading is due equally to elastic electrons and atomic nuclei. In the case of heavier elements (metal plates made of Al, Cu, Pb) and is the spreading increases due to the nuclei and it is so-called „bremstrahlung radiaton" of electrons (proportional to Z^2), a consequence of the interactions with non-elastic character. With this, we get to study the absorption of radiation β in various plastic objects.

4a. Polyethilene β-absorption experiments:

It has been measured, in parallel, the absorption of beta radiation emitted by P-32, Cl-36,

C-14 sources in different sorts of polyethylene for halving thickness determination, knowing that the radioactive wastes will be put in thinly sacs of polyethylene and measured. The curves concerning the absorption of the isotopes radiation P-32, Cl-36, in polyethylene are like in *Fig.4a.* and *4b*.

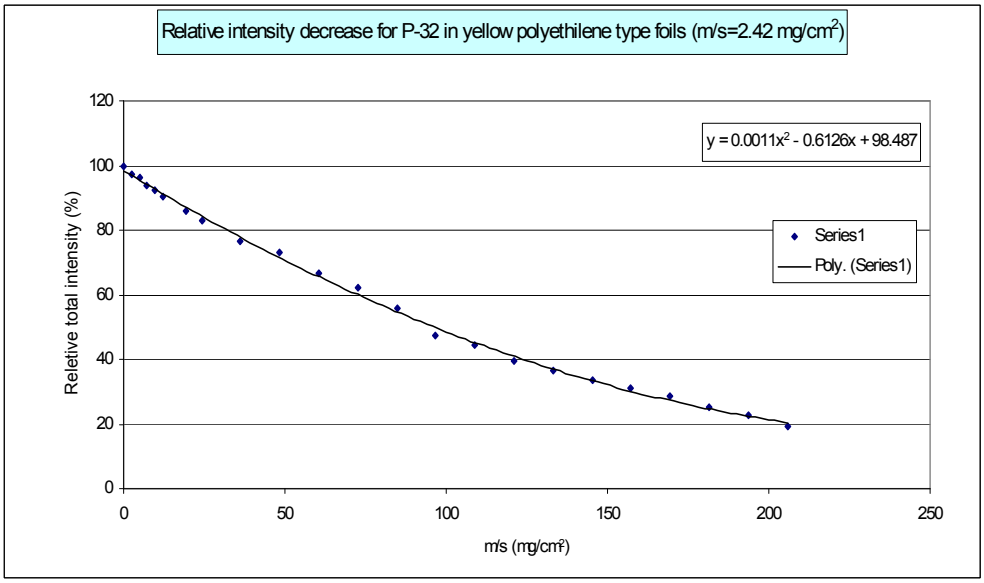

Fig. 4a. Relative intensity decrease curve for one case of absorption of P-32 beta radiation in polyethilene

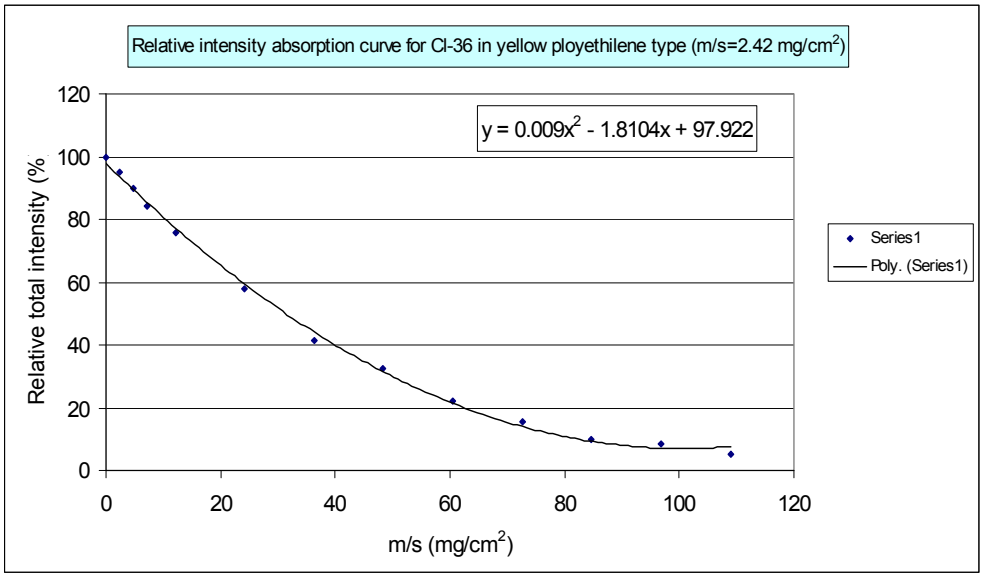

Fig. 4b. Relative intensity absorption curve for the absorption of Cl-36 beta radiation in polyethilene

The following values were obtained (Table No.1):

Table No.1. Results on the $x_{1/2}$ determination (for P-32 and Cl-36 β radiation) in different sort of polyethylene

Type of polyethylene	m/s of the 1 foil type (mg/cm^2)	$x_{1/2}$ estimation from exponential general law of absorption (mg/cm^2)		$x_{1/2}$ estimation by linear interpolation after de relative intensity $(I-I_b)/(I_0-I_b)$* decrease graphic (mg/cm^2)	
		P-32	***Cl-36***	***P-32***	***Cl-36***
White	1.2	99	33.5	98.6	29.58
Black	4.43	96.25	37.9	86.7	31.34
Yellow	2.42	110	33.5	93.4	31.77
Transp"type 1"	2.486	105	35	95	28.445
Transp"type 2"	2.2	103.4	32.7	98.6	31.41
Transp"type 3"	2.22	99	30.5	97.6	30.32
Transp"type 4"	2.32	103.4	33.6	99.5	33.41

Observation: *) values depend of the beam stopper characteristics

On the other hand we have 3 phenomenon:

-absorption of beta radiation in polyethylene

-backscattering of beta radiation inclusive on the shielding walls

-generation of bremsstrahlung radiation as increasing the polyethylene layer

We noticed that only one normal foil of polyethylene from the waste bag, does not modify very much (only a few percentage) the measured radiation intensity. Exception makes C-14, which has to be measured only in bags type white polyethylene with $x_{1/2} = 1.2$ mg/cm^2.

4b. Minimal Detectable β-Activity calculus

If we analyze the global efficiency curves as that from Fig.4 we observe that there is a minimal value of the detection efficiency at great m/s values, which will be done the MDA for that geometry of measurement.

From these measurements can be deduced the sensibility of detection of a radionuclid for both of the cases equal with minimal detectable activity (MDA) defined in [13] as the minimal activity yelding a signal with a level of 1σ above the ROI specific background (i.e. 1σ for 68% confidence, 2σ for 96% and 3σ for 99.7%). For a single measurement $\sigma = \sqrt{K}$ (K is the number of counts corresponding to

the an well-known activity). The measured counts K (of the MDA) in the ROI are hence equal to 1σ of the total counts of background spectrum for the same ROI.. The Lower Limit of Detection (LLD) of a radiological system for a particular nuclide is defined [13] as the counter rate of the nuclide that is discernible from its background count rate at a given level of confidence. In radioactivity analysis, the LLD's corresponding physical quantity would be termed as: Minimum Detectable Activity (MDA).

For the greatest confidence degree (around of 97% confidence), we used the formula:

$$LLD = 4.65\ \sqrt{B} \tag{2}$$

where B is the counting rate of the background in the delimited zone of the spectra.

The MDA was estimated on ROI (see Table no. 2) from the LLD by comparison with with known calibration source.

Table no. 2. The MDA for great plastic scintillator, calculated from measurements on selected waste of somme isotopes in the their ROI and for different geometry of detection (distance source-detector)

Geometry	MDA for C-14 on the ROI of (0-225channels) (MBq)	MDA for Cl-36 on the ROI of (225-1040channels) (kBq)	MDA for P-32 on the ROI of (1040-2048channels) (kBq)
D = 3 cm	3.398	0.272	0.502
D = 12.5 cm	4.989	0.356	0.435
D = 18 cm	6.176	0.48	0.57

4c. Polyethilene-therephtalate (PET) and polystyrene β-absorption experiments:

For other polimers we used a ^{90}Sr-^{90}Y β- source with maximum energy of 2.26 MeV.

We investigated the radiaition absorbtion at this greath energies for polyethylene-therephtalate (PET) and polystyrene materials.

The results is done in Fig. 5. and respectively Fig. 6.

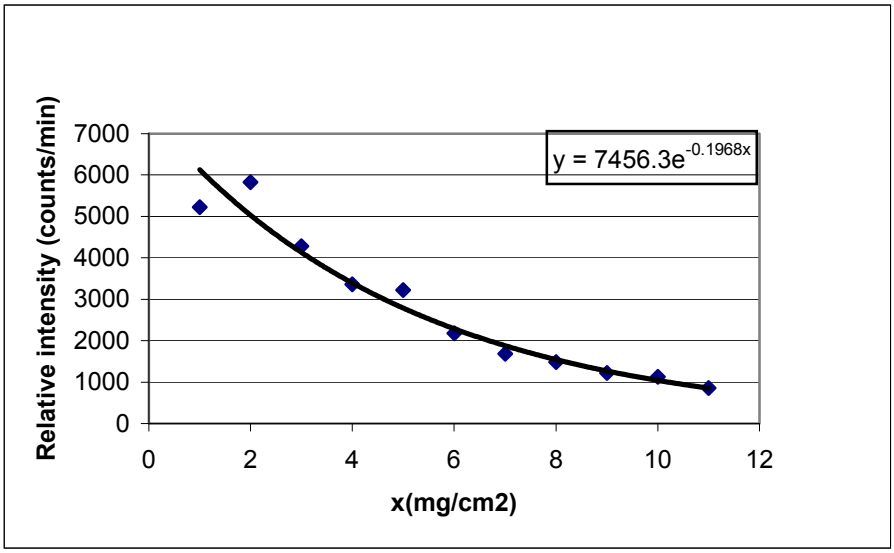

Fig. 5. The β-radiation from ^{90}Sr-^{90}Y radiation source absorbtion in PET.

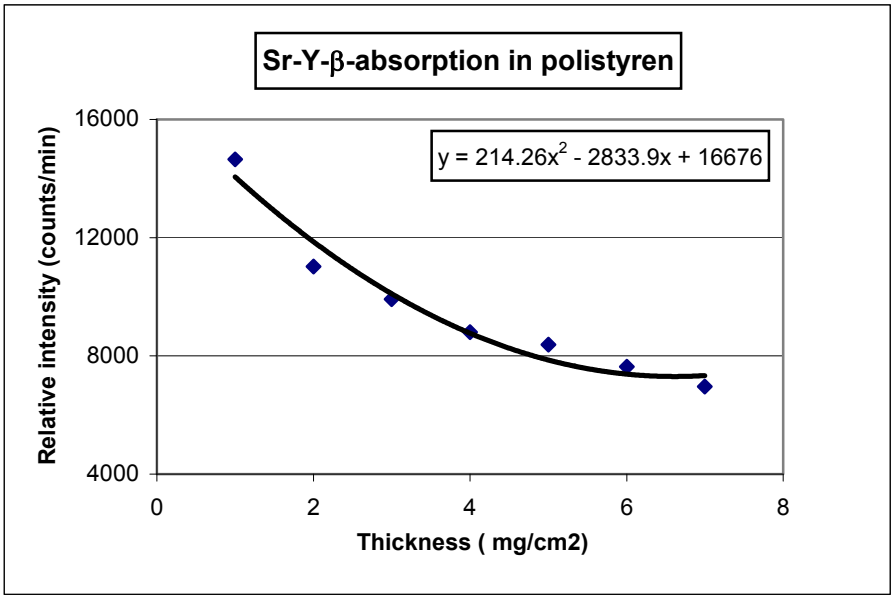

Fig. 6. The β-radiation from ^{90}Sr-^{90}Y radiation source absorbtion in polystyrene.

From these measurements we deduce the $d_{1/2}$ of materials for the energy of ^{90}Sr-^{90}Y. For polystiren $d_{1/2}$ = 36.5 mg/cm^2 and for polyethylene- therephtalate (PET) $d_{1/2}$ = 32.4 mg/cm^2.

5. The γ radiation interaction with polymers

Specific ionization of high-energy photons that comprise γ radiation is tens and even hundreds of times smaller than the electrons with comparable energies. Therefore, their pentration is more pronounced, the attenuation suffering with an exponential character.

As we know, [14], X-rays and γ can lose their energy in several ways when crossing the environment.

They can be absorbed totally by the atoms in the medium electrons (photoelectric effect), can be scattered from elastic collisions with orbital electrons (Compton effect) or can generate pozitirin electron pairs in the coulumbian field of a heavy nuclei.

These effects have different probabilities on different areas of photon energy incident. If γ radiation beam propagates parallelily a certain environment, its intensity decreases with distance by this law:

$$I = I_0 e^{-\mu \cdot x} \tag{3}$$

Where I_0 is the incident beam intensity, I is the intensity remaining after finishing the x distance and μ linear absorption coefficient of that environment, which depends on E_γ, as well as on Z [14]. The thickness of protection for the incident beam intensity is reduced halfly, this being called thick half-path:

$$d_{1/2} = \frac{0.693}{\mu} \tag{4}$$

For example in the case of γ radiation of ^{60}Co (with $\overline{E}_\gamma = 1.25$ MeV) half-path in water depth is 11.5 cm, and in Pb of only 1.085 cm.

For a weak absorbent material of γ radiation (such as polymers of polyethylene or polyethylene terephthalate) the exponential absorption law (3) is transcribed into a linear form by Taylor series decomposition:

$$I = I_0(1-\mu x) \tag{5}$$

Therefore absorption curve in figure 7 is more linear.

From Fig. 7. we deduced the γ- mass absorption coefficient for polyethylene terephthalate $\mu = 0.029$ cm^2/g at 662 keV gamma energy emitted from ^{137}Cs radionuclide.

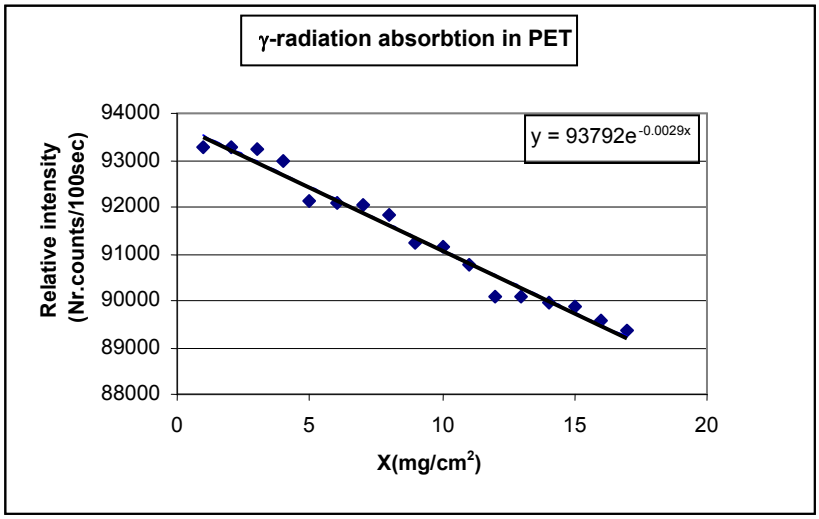

Fig. 7. The absorbtion of ^{137}Cs γ- radiation in polyethylene terephthalate (PET)

CONCLUSIONS

-The method, which uses detectors with plastic scintillators, is a beta-gamma global type.

It can be adapted to measure in ROI. for beta-pure emitting known radionuclides with different energies from the large radioactive waste samples.

-The plastic detectors system offer an alternative for measuring some beta-radioactive contaminated wastes, which are sorted on radionuclides from the beginning of work, cut in pieces (if they are of paper) and homogenate and then introduced in a thin bag of polyethylene of fixed form. The superficial activity measured with plastic detectors, previously calibrated with the aide of packets containing known isotopes of a known activity, is proportional (or depends on a certain law [11]) with the global activity, of the packet volume. In this case we have a high efficiency of detection of the radioisotope. In the case when the waste products were unselectively collected (but we know what kind of radioactive isotopes they content) the beta active radionuclides can be measured on the spectrum regions (ROI) typical only to them, but the efficiency of detection and the sensibility is low, especially in superior energy regions (for ex. of P-32).

For gamma radiation the absorbtion coefficient is verry low in polimers because of the low Z number elements content in sample.

Knowing the attenuation coefficients that are specific to a particular type of polymer is important in dosimetry and radioprotection (plastic screens against radiation β) and in radioactive waste management.

REFERENCES

1. L. Daraban, *Calibration of beta spectra by Compton electrons*, STUDIA Univ. B-B., ser. Physica, **46**,*1*, 77-82 (2002)
2. L. Daraban, P. Van den Winkel, *Experimental methods for the measurement of β-pure radionuclides used in nuclear medicine,* in *The 5-th International Conference on Isotopes, April 25-29, 2005, Brussel (Belgium),* conf.vol. pp.265-274 (2005).
3. E. Nardi,*Gamma ray measurements with plastic scintillators*, Nucl. Instr. Meth., **95**, 229-232 (1971)
4. I.T. Grissom, D.R. Koehler, Nucl. Instr. Meth., **37**, 336 (1965)
5. V.V. Verbinscki et al., Nucl. Instr. Meth., **65**, 8 (1968)
6. L. Daraban et al., Proc. Of the 2-nd Nat. Symp. *"Methods, Models and Techniques in Physics and Related Fields",* pp. 101-104, oct. 11-15, Cluj-Napoca, Romania, (1984)
7. F.K. Wohn, J.R. Clifford, G.H. Carlson, W.L. Tabert, Jr.*, A plastic scintillation detector for beta-ray spectrum measurements*, Nucl. Instr. Meth., **101**, 343-352 (1972)
8. N. Tsoulfanidis, B.W. Wehring and M.E. Wyman, *The use of an analitical response function for unfolding beta spectra,* Nucl. Instr. Meth., **73**, 98-102, (1969)
9. P.C. Rogers, G.E. Gordon, *Computer analysis of beta-ray and conversion electron spectra observed with low-resolution detectors*, Nucl. Instr. Meth., **37**, 259-264 (1965)
10. A.H. Wapstra, G.J. Nijgh, R. Van Lieshout, *Nuclear Spectroscopy Tables*, (in russian ed. pp.58-76), edit.: North-Holland Publ. Comp., Amsterdam (1959)
11. J.-H. Liang et al, *Parametric study of shell-source method for callibrating radwaste radioactivity detection sytems,* Appl. Radiat. Isot. **49**, 361-368,(1998)
12. T. Jurcut, M. Pop, Biofizica Medicala, Ed,. Univ. Oradea, pp.202-203 (1997)
13. L.A. Currie, *Limits for qualitative detection and quantitative determination*, *application to radiochemistry*, Anal. Chem., **40**, 586-593 (1968)
14. O.Cozar, Detectori de radiatii.Spectroscopie gama, Ed. Presa Universitara Clujeana, pp.29-45 (2007).

STUDIA UNIVERSITATIS BABEŞ-BOLYAI, PHYSICA, LV, 1, 2010

INVESTIGATION OF THERMAL EFFUSIVITY OF THIN SOLIDS IN A LAYERED SYSTEM. FPPE-TWRC APPROACH

M. N. POP[a], M. STREZA[a], D. DADARLAT[a], V. SIMON[b]

ABSTRACT. The front photopyroelectric (FPPE) configuration, together with the thermal-wave resonator cavity (TWRC) method was applied in order to measure the thermal effusivity of thin solids. The methodology is based on a detection cell in which the thin solid layer is inserted between two layers of identical liquids – one layer in contact with the pyroelectric sensor, acting as coupling fluid and the second one acting as backing layer. The value of the thermal effusivity is obtained as a result of a scan of the phase of the FPPE signal as a function of coupling fluid's thickness (TWRC method). The suitability of the method was demonstrated with investigations on a 50μm thick copper foil.

Keywords: *photothermal phenomena, photopyroelectric calorimetry, thin solids, thermal parameters*

INTRODUCTION

In the photopyroelectric (PPE) calorimetry one can combine two detection configurations ("back" or "front"), two sources of information (PPE amplitude or phase) and two scanning parameters (chopping frequency or one liquid layer's thickness), in order to obtain the dynamic thermal parameters of one layer of the detection cell [1-4].

If we restrict our attention to the front photopyroelectric (FPPE) configuration, it was largely used in the past to obtain thermal parameters of (semi)liquid and solid samples [3-7]. In the FPPE configuration, the radiation impinges on the front surface of the pyroelectric sensor, and the sample, in good thermal contact with its rear side, acts as a heat sink.

The thickness scanning procedure, called also thermal-wave resonator cavity (TWRC) method, was introduced about 10 years ago by Mandelis and co-workers and developed later by others groups [8-12]. Recently, the TWRC method, in the front configuration (FPPE) showed to be suitable for investigating thermal effusivity of solids, inserted as backing in the detection cell [13], but in such a configuration the solid sample must be semi-infinite.

[a] *National R&D Institute for Isotopic and Molecular Technologies, Donath Str. 65-103, POB-700, 400293 Cluj-Napoca, Romania*
[b] *Babes-Bolyai University, Faculty of Physics, 400084, Cluj-Napoca, Romania*

In this paper we propose an alternative PPE configuration useful for measuring the thermal diffusivity, or effusivity of a thin solid layer. We have to mention that one thermal parameter can be obtained, only if the other one is known (in the paper we consider thermal effusivity as an unknown parameter). The maximum thickness of the investigated samples is limited to several hundreds of microns (depending on their thermal properties).

THEORY

The schematic diagram of the detection cell is a classical one for FPPE configuration (Fig.1). It contains 5 layers: semi-infinite air (0), directly irradiated sensor (1), coupling fluid (2), thin solid layer (3) and a semi-infinite liquid layer from the same material as the coupling fluid (4).

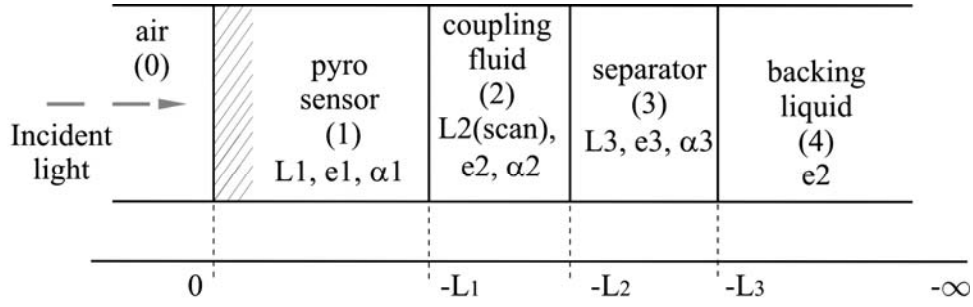

Fig. 1. Layout of the of the 5 layers detection cell.

For such a cell, the normalized FPPE complex signal is given by [14]:

$$V_n = \frac{1 - R_{21} e^{-2\sigma_1 L_1}}{1 - \rho_{21} e^{-2\sigma_1 L_1}} * \frac{\left(e^{-\sigma_1 L_1} - 1\right) - \rho_{21}\left(e^{-\sigma_1 L_1} - e^{-2\sigma_1 L_1}\right)}{\left(e^{-\sigma_1 L_1} - 1\right) - R_{21}\left(e^{-\sigma_1 L_1} - e^{-2\sigma_1 L_1}\right)} \tag{1}$$

where:

$$R_{21} = \frac{1 - b_{21}}{1 + b_{21}}$$

$$\rho_{21} = \frac{\left(1 - b_{21}\right) + \rho_{32}\left(1 + b_{21}\right) e^{-2\sigma_2 L_2}}{\left(1 + b_{21}\right) + \rho_{32}\left(1 - b_{21}\right) e^{-2\sigma_2 L_2}} \tag{2}$$

$$\rho_{32} = \frac{(1-b_{32}) + R_{23}(1+b_{32})e^{-2\sigma_3 L_3}}{(1+b_{32}) + R_{23}(1-b_{32})e^{-2\sigma_3 L_3}}$$

$$R_{23} = \frac{1-b_{23}}{1+b_{23}}$$

"Normalized signal" in Eq. (1) refers to the signal obtained with a 5 layers cell normalized to the signal obtained with semi-infinite coupling fluid.

In Eqs. (1-2) $\sigma_j = (1+i)a_j$, $\mu=(2\alpha/\omega)^{1/2}$, $b_{ij}=e_i/e_j$, α and e are the thermal diffusivity and effusivity, ω is the angular chopping frequency of radiation, σ and a are the complex thermal diffusion coefficient and the reciprocal of the thermal diffusion length ($a = 1/\mu$), respectively.

The normalized FPPE signal, described by Eq. (1), contains no approximation concerning the thermal thickness of the layers of the detection cell. It assumes only one-directional propagation of the heat and optical opacity for the sensor. In principle, Eq. (1) allows for the direct measurement of thermal diffusivity and/or effusivity of the layers 1-3 of the cell, and the thermal effusivity of the backing liquid, by performing a scan of the phase or amplitude of the signal, as a function of the coupling fluid's thickness.

In the paper we will use as source of information the phase of the PPE signal, which is more convenient from experimental point of view [13], and we will focus on the measurement of thin solid layer's thermal effusivity (its diffusivity is considered known). The most suitable method to obtain the value of the thermal effusivity of the thin solid material is a fit of the phase of the FPPE signal with the coupling fluid's absolute thickness and thin solid layer's thermal effusivity as fitting parameters. Mathematical simulations demonstrate that, in the thermally thin regime for the sensor and coupling fluid, the phase of the FPPE signal depends on the thickness and on the thermal parameters of the thin solid layer [13].

EXPERIMENTAL SET-UP

The experimental set-up is classical for FPPE calorimetry, and it was largely described before [13, 15-16]. Only some details will be presented here.

The pyroelectric sensor, a 100μm thick $LiTaO_3$ single crystal (e_1= 3.92x10^3 Ws$^{1/2}$m^{-2}K^{-1}; α_1= 1.56x10^{-6}m^{2}s^{-1}), provided with Cr-Au electrodes on both faces, is glued on a rotating stage. The backing liquid is accommodated by a 1cm thick and 1cm in diameter glass cylinder, situated on a micrometric stage. The coupling fluid fills the space between the rear side of the sensor and the thin solid foil, glued on the top of the glass cylinder. The coupling fluid's thickness variation is performed with a step of 0.03μm (9062M-XYZ-PPP Gothic-Arch-Bearing Picomotor™) and the data acquisition was taken each 30-th step. The modulated radiation (30 mW HeNe

laser) is partially absorbed by the front electrode of the sensor. The "rough" control of the coupling fluid's thickness and the parallelism between separator and sensor are assured by 3 and 6 –axis micrometric stages. During the scanning procedure, the sample's thickness variation is very rigorously controlled, but the absolute sample's thickness it is not precisely known. Its correct value is obtained, as explained in the theoretical section, only as a result of a fitting procedure.

All the measurements were performed at room temperature. The FPPE signal was processed with a SR 830 lock-in amplifier. The data acquisition, processing and analysis were performed with adequate software.

In our experiment, the coupling fluid and backing layer were the same liquid, ethylene glycol (e_2= 814Ws$^{1/2}$m^{-2}K^{-1}; α_2= 9.36x10^{-8}m^{2}s^{-1}) and the thin solid separator was a 50 μm copper foil with a thermal diffusivity α_3= 1.31x10^{-4}m^{2}s^{-1}.

RESULTS

The behaviour of the normalized phase of the FPPE signal, as a function of relative thickness of the coupling fluid, is presented in Fig 2. Fig.2 contains also the best fit performed with Eq. (1) on the experimental data.

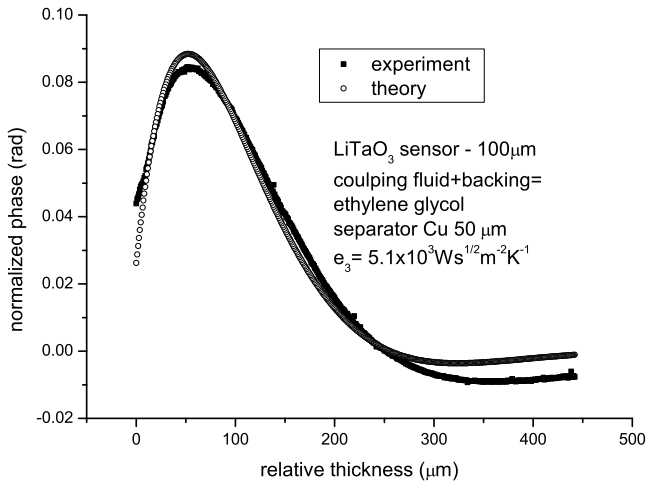

Fig. 2. The experimental behaviour of the normalized FPPE phase as a function of coupling fluid's thickness, for a detection cell with 50μm thick Cu foil as separator. The best theoretical fit is also displayed.

Concerning the accuracy of the method, as stated in previous papers [13, 17], for this type of investigations, it depends on the relative effusivity ratio solid layer/ coupling fluid (backing layer). The sensitivity map for our sample is displayed in Fig. 3.

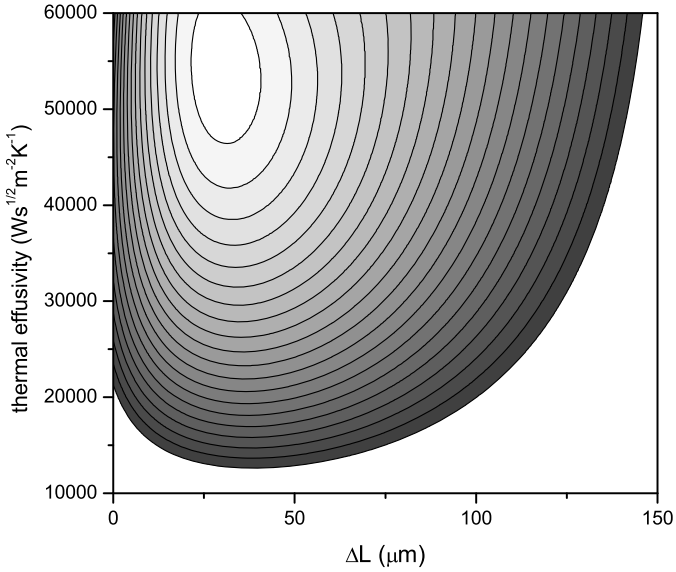

Fig. 3. Contour map of the precision of the fit performed with Eq. (1) on the experimental data obtained with Cu foil as separator. X-axis represents the correction term in the measurement of the absolute liquid's thickness.

CONCLUSIONS

The front photopyroelectric (FPPE) configuration, together with the thermal-wave resonator cavity (TWRC) method was applied in order to measure the thermal effusivity of thin solids. The new methodology is based on a FPPE detection cell in which the thin solid layer under investigation is inserted between two layers of identical liquids – one layer in contact with the pyroelectric sensor, acting as coupling fluid and the second one acting as backing layer.

The theory of this configuration predicts that, in the thermally thin regime for the sensor and coupling fluid, the phase of the FPPE signal depends on the thermal diffusivity and effusivity of the thin solid layer. If one parameter is known, the other one can be obtained as a result of a scan of the phase of the FPPE signal as a function of coupling fluid's thickness (TWRC method). In the paper we selected the thermal effusivity as an unknown parameter. The main result of the paper is the suitability of the method in investigations thin solid layers and not only thick ones, as requested by previous PPE procedures.

It is well known that the PPE method is a contact one and consequently, the coupling fluid, always necessary when investigating solids, plays often a disturbing role, reducing the accuracy of the results. The use of the TWRC method in the present investigation turns out the coupling fluid in a useful factor, due to the possibility of monitoring its geometrical (thickness) and thermal (type of liquid) properties.

The suitability of the method was demonstrated with investigations on a thin foil of copper. The result obtained for the thermal effusivity is in good agreement with reported data [18]. Concerning the accuracy of the method it is similar with that obtained by FPPE-TWRC technique for thermally thick solids [13, 17].

ACKNOWLEDGEMENTS:

Work supported in part by the Romanian Ministry of Education and Research through the National Research Programs PN09 44 02 03. M. N. Pop author wishes to thank for the financial support provided from programs co-financed by The Sectoral Operational Programme Human Resources Development, Contract POSDRU 88/1.5/S/60185 – „DOCTORAL STUDIES: THROUGH SCIENCE TOWARDS SOCIETY".

REFERENCES

1. A. Mandelis and M. M. Zver, Appl. Phys., 57, 4421-30 (1985)
2. M. Chirtoc and G. Mihailescu, Phys. Rev., B40, 9606-17 (1989)
3. D. Dadarlat, D. Bicanic, H. Visser, F. Mercuri, A. Frandas, J. Amer. Oil Chem. Soc., 72, 273-80 (1995)
4. D. Dadarlat, C. Neamtu, Acta Chim. Slovenica, 56, 225-36 (2009)
5. D. Dadarlat, M. Chirtoc, C. Neamtu, R. Candea, D. Bicanic, Phys. Stat. Sol., (a)121, K231-4 (1990)
6. D. Dadarlat, A. Frandas, Appl. Phys., A56, 235-8 (1993)
7. D. Dadarlat, H Visser, D Bicanic, Meas. Sci. Technol., 6, 1215-9 (1995)
A. Mandelis, A. Matvienko, Pyroelectric Materials and Sensors, D. Remiens (Ed.), Kerala, India (2007)
8. S. Delenclos , M. Chirtoc, A. H. Sahraoui, C. Kolinsky, J. M. Buisine, Rev. Sci. Instrum., 73, 2773-80 (2002)
9. J. Shen, A. Mandelis, Rev. Sci. Instrum., 66, 4999-5005, (1995)
10. P. C. Menon, R. N. Rajesh, C. Glorieux, Rev. Sci. Instrum., 80, 054904 (2009)
11. J.A. Balderas Lopez, A. Mandelis, J.A. Garcia, Rev. Sci. Instrum., 71, 2933-37 (2000)
12. D. Dadarlat, M. Streza, M.N. Pop, V. Tosa, S. Delenclos, S. Longuemart, A.H. Sahraoui, J. Therm. Analysis Calor., DOI 10.1007/S10973-009-0513-6 (2010)
13. A. Mandelis, Diffusion-Wave Fields: Mathematical methods and Green functions Springer, New-York (2001)
14. D. Dadarlat, Laser Physics, 19, 330-9 (2009)
15. M. Streza, M.N. Pop, K. Kovacs, V. Simon, S. Longuemart, D. Dadarlat, *Laser Physics,* 19, 1340-5 (2009)
16. D. Dadarlat, M. Streza, M.N. Pop, V. Tosa, *J. Phys- Conf. Series,* 182, 012023 (2009)
17. R. A. Bailey, Materials properties database (JAHM software) (1999)

STUDIA UNIVERSITATIS BABEŞ-BOLYAI, PHYSICA, LV, 1, 2010

DEUTERIUM ISOTOPIC CHARACTERIZATION OF PRECIPITATION WATER

R.H. PUSCAS, V. FEURDEAN[a]

ABSTRACT. This study was focussed on the analysis of isotopic compositions of hydrogen in samples from precipitation water. Stable isotope compositions of groundwater are principally controlled by the compositions of precipitation, evaporation, mixing of water mass and isotope fractionation with phases in the aquifer. The strong link between long-term monthly average values of the local surface air temperature and the deuterium abundance of precipitation fallen over Cluj-Napoca in the time period 1975-2004 was evidenced. These data are of large interest in studies of groundwater and water movement in wetland.

Keywords: *water isotopes; precipitation; Rayleigh model*

INTRODUCTION

Within the water cycle, temperature at the location where vapors condense to precipitation has been heralded as primary controlling factor in the fractionation of stable isotope in precipitations [1, 2]. Because atmospheric temperature dictates the pressure of aqueous vapor in the atmosphere and pressure controls the isotopic composition of atmospheric water vapours, changes in the temperature dictate different rates of fractionation. To describe how water fractionates between phases within an ideal cloud (under thermodynamic equilibrium) the Rayleigh model was established [3, 4]. The fundamental factors which control isotopic fractionation during precipitation have been identified as separate effects, but several are integrally related. The results focus on temporal distribution of deuterium content in the precipitation water.

The deuterium concentration in water brings valuable information in the investigation of the processes developed during the natural water cycle. The studies related to water transport in the water natural cycle are primary based on isotopic analysis of precipitations, using as natural tracers the stable isotopes of hydrogen and oxygen. The advantage to use the stable isotopes of water as tracers in earth and life sciences resides in the fact that they are available in the nature, they are not pollutant, non-invasive, space and time unlimited in use and can be investigated from micro- to macroscale.

[a] *National Institute for Research and Development of Isotopic and Molecular Technologies, 400293 Cluj-Napoca, Romania*

The strong link between long-term monthly mean values of the local surface air temperature and the deuterium abundance of precipitation fallen over Cluj-Napoca is used for the determination of deuterium content in precipitation from another site from Romania with reasonable confidence. These findings are necessary for studies of groundwater and water movement in wetland.

EXPERIMENTAL

The measurements related to deuterium concentration were carried out with an laser absorption spectrometer (TDLAS) for isotopic analyses in liquids. The isotope analyser delivers high accuracy data for ^{2}H/H ratio in water. The data obtained were compared with the international V-SMOW standard of AIEA Vienna.

The water samples refer to water derived from precipitations. They were collected with a pluviometer habitually used in the meteorology stations. The amount of precipitations is expressed in mm water column or in l/m^2. An amount of 1 l/m2 means that a surface of 1 m^2 is covered by a water layer with 1mm thickness. The precipitation water samples were collected once for every event. In each sample corresponding to a certain event, the deuterium concentration was determined by ^{2}H/H ratio. The data obtained were used for a data base containing the sampling date, the amount of fallen precipitations, and the deuterim concentration. New data computated using the average monthly, annual and multiannual experimental values were added to the data base. The monthly, annual and multiannual average data are not simple arithmetic avarages, but ponderated mean values, that take into account the precipitation amount and the deuterium concentration corresponding to each event. The avarage value is determined with the equation:

$$\overline{C^2H} = \frac{\sum C^2H_i \cdot Q_i}{\sum Q_i}$$

where C^2H_i and Q_i are the deuterium concentration and the precipitation amount corresponding to each event in the considered period, respectively. Subsequently the values are converted in δ units.

RESULTS AND DISCUSSION

With respect to the precipitations fallen in Cluj-Napoca in the period 1975-2004 the δ^2H momentary values of deuterium concentration are ranged between -221.88 % (121,20 ppm) and 64,74 % (166,00 ppm), while the monthly ponderated mean values are ranged between -169,74% (129,43 ppm) and -3,91% (155,15 ppm). The evolution of the δ^2H monthly ponderated mean values, and that of the monthly precipitation amount in the 1975-2004 time period [5] are illustrated in Fig. 1.

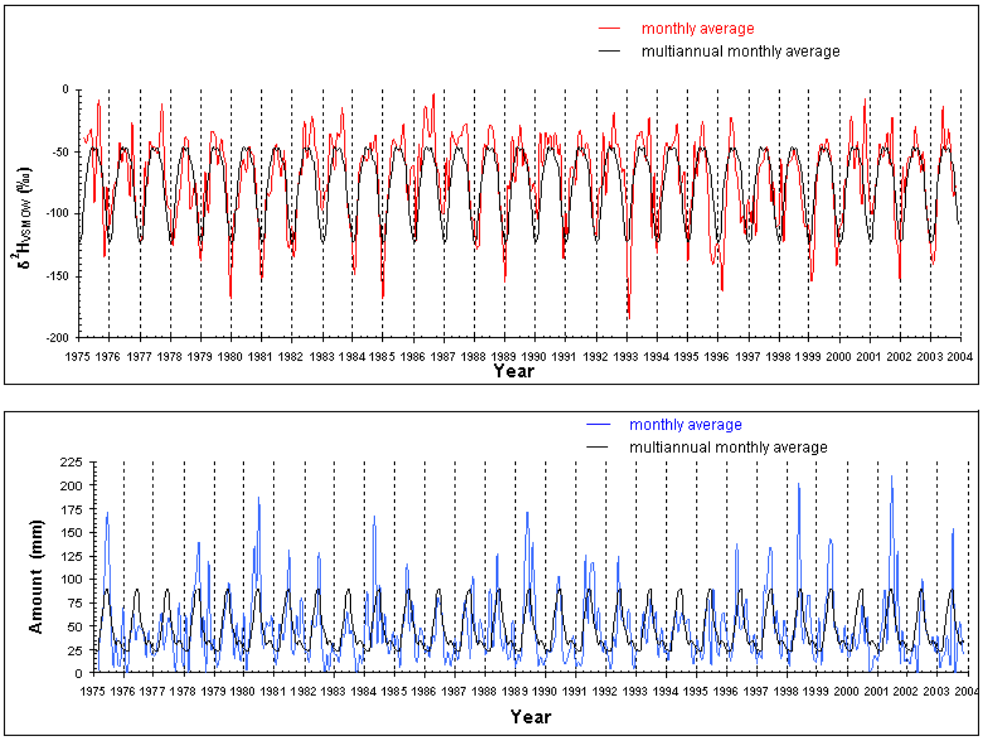

Fig. 1. Monthly ponderated mean values δ^2H (top), and monthly precipitation amount (botom) fallen in Cluj-Napoca in the time period 1975-2004.

The seasonal effect is very clear evidenced. During each year one remarks a succession of minima in the winter months and maxima in the summer months, and intermediate values for spring and autumn months.

On the other hand, an attentive inspection of δ^2H summer maxima evidences that they are also subjected to a periodical variation. In the years with more rain, i.e. in 1978, 1980, 1984, 1989 and 1998, these values are lower than that recorded in the years with less rain, i.e. 1977, 1983, 1986. At the same time, the absolute values for the winter minima are higher for the years with less precipitations, 1982/83, 1986/87, 1989/90.

The δ^2H values for the precipitations fallen in Cluj-Napoca seem to be determined by the precipitation amount (Fig. 2), although the correlation with the monthly precipitation amount is not high enough, but there is a good agreement between δ^2H and temperature (Fig. 3).

Based on the isotopic effects, the values of δ^2H in precipitations are indicatives for the provenance of the vapors and the temperature conditions under which they were produced. The precipitations characterized by high δ^2H values

occur from regions of lower latitudes and higher temperatures, while for low δ^2H values the provenance is from regions of higher latitudes and lower temperatures [6]. In this approach, one can appreciate that in Cluj-Napoca, the precipitations with high δ^2H values are preponderantly formed in the mediterranean region, while those with low δ^2H values are formed in the north region of Atlantic Ocean and very seldom in the north-east part of Siberia or Frozen Ocean.

The data base formed with δ^2H values referring to the precipitations fallen in a certain areal for a long time period is useful for climatology and weather prognoses, hydrology studies on surface water, groundwater aquifer, wetland, interactions occurring in hydrosphere, paleoclimatic studies, and even dendrology, with applications in agriculture [7].

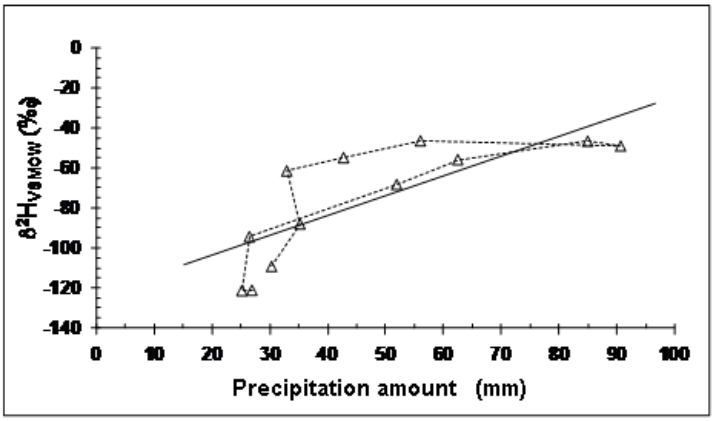

Fig. 2. Dependence of δ^2H average multiannual values on the amount of precipitations.

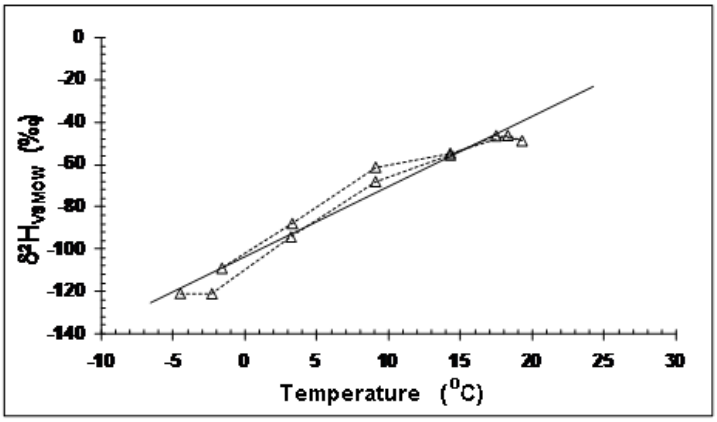

Fig. 3. Dependence of δ^2H average multiannual values on temperature.

CONCLUSIONS

The experimental and computed data reported in this study show that the deuterium isotope content in precipitations depend on the place where they are fallen, as well as on place and temperature at the originating region. The isotopic effects represent a large scale natural marker process. According to the experimental results recorded in Cluj-Napoca in the analysed time period the precipitations with high δ^2H values were preponderantly formed in the mediterranean region, while those with low δ^2H values were formed in the north region of Atlantic Ocean and very seldom in the north-east part of Siberia or Arctic Ocean.

The isotopic composition of precipitation water also shows a distribution in seasonal variation, with depleted isotopic composition during winter due to less active interflow of water masses in this season.

REFERENCES

1. Statistical Treatment of Data on Environmental Isotopes in Precipitation. Technical Reports Series No. 331, IAEA, Vienna (1992).
2. L. Merlivat, J. Jouzel, J. Geophys. Research, 84-C8, 5029 (1979).
3. W. Dansgaard S. J. Johnsen N. Reeh N. Gundestrup H.B. Clausen, C.U. Hammer Nature, 255, 24 (1975).
4. S.J. Johnsen, W. Dansgaard, J.W.C. White, Tellus B, 41 B, 452 (1989).
5. V. Feurdean, L. Feurdean, Atelier International sur l'Application des techniques Isotopiques aux Etudes Hydrologiques et Environnementales, Paris, France, 6 - 8 September, 2004.
6. H.-Y. Lu, T.-R. Peng, T.-K. Liu, C.-H. Wang, C.-C. Huang, Environ. Geol., 50, 885 (2006).
7. V. Feurdean, L. Feurdean, S. Apahidean, M. Apahidean, A. Lujerdean, R. Puscas, D. Ficior, XXXVII Annual Meeting of European Society for New Methods in Agricultural Research, 10-14 September 2007, Dubna, Russia.

STUDIA UNIVERSITATIS BABEŞ-BOLYAI, PHYSICA, LV, 1, 2010

Dedicated to Prof. M. Coldea, for his appreciated contributions to XPS research field [i-xvi].

XPS STUDIES ON AMORPHOUS AND NANOSTRUCTURED BIOMATERIALS SURFACE AND THEIR BIOFLUID INTERFACE

V. SIMON[a]

ABSTRACT. X-ray photoelectron spectroscopy (XPS) is extensively used to characterise the surface of materials used in bioengineering. Its ability to characterise both the elemental composition and structural characteristics of the surface makes it particularly useful, as it can identify the functional groups present on the surface of any material and implicitely give insight into biointerfacial interactions. The paper summarizes some XPS results obtained on compact and porous materials with potential biomedical applications, before and after their interaction with simulated body fluids.

Keywords*: biomaterial systems; interface changes; simulated body fluids; XPS.*

INTRODUCTION

A key issue in most applications of biomaterials is the way in which a given material influences and is influenced by the biological response that results from the contact between the biomaterial and the biological systems, particularly at the thin surface layers. It is widely accepted that the surface characteristics of the material has a critical influence on the biological response [1-4]. In recent years there has been a considerable increase in the use of the various surface analytical methods, including X-ray induced photoelectron spectroscopy (XPS). The XPS technique, in particular, provides information on the outer few tens of angstroms of the sample surface and it is a key tool in understanding the chemistry and physics taking place on surfaces and at interfaces. Usually the surface of biomaterials is nanostructurated, so that in biological media bio-nano-interfaces are developed.

Ferromagnetic glass ceramics are successfully applied to reinforce the curettaged bone and to decrease the recurrence of tumors by hyperthermic treatment because the hysteresis heating raises the temperature sufficiently to induce necrosis and significant delay of tumor growth [5, 6]. Yttrium aluminosilicate glasses have led to a special family of glasses used in radiotherapy [7]. Certain ions, among which silver ions are an eloquent example, can be rapidly or gradually released from glasses and glass-ceramics and they have an excellent antibacterial effect [8].

[a] *Babeş-Bolyai University, Faculty of Physics & Institute of Interdisciplinary Research in Bio-Nano-Sciences, 400084 Cluj-Napoca, Romania*

Biocompatibility depends on the manner in which the biomaterial surface interacts with blood constituents as well as the proteins [9]. Moreover, the biological properties of a materials surface depend strongly on the way proteins adsorb on the synthetic surface [10]. For example, serum albumin is mainly responsible for the maintenance of blood pH and is associated to the binding and transport of several small molecules such as fatty acids, dyes, metals, amino acids, drugs, as well as several pharmaceutical compounds [11]. The protein adsorption is the first event happening on the surface of any system implanted in biological environment [9]. Once adsorbed, a protein either keeps its native structure or undergoes changes in concentration, orientation or conformation. These properties of adsorbed protein layers determine the subsequent cellular interactions, which can significantly impact the performance of biomaterials in a biological environment. The extent of the protein rearrangement is affected by the nature and the properties of the surface. The behaviour of a protein at an interface is likely to differ considerably from its behaviour in the bulk or in lyophilized state. XPS became a very useful analysis tool for investigation and characterisation of materials surfaces and evidenced that very often the functional properties are determined by the outermost layers of the material [12].

In this paper are reviewed some XPS results of our research group obtained on compact and porous materials with potential biomedical applications.

EXPERIMENTAL

Glass samples of CaO-P_2O_5-SiO_2-Fe_2O_3, Y_2O_3-Al_2O_3-SiO_2-Fe_2O_3, P_2O_5-CaO-Na_2O-Fe_2O_3, P_2O_5-CaO-Na_2O-Ag_2O, SiO_2-Al_2O_3-Fe_2O_3, Ag_2O-CaO-Bi_2O_3-B_2O_3 systems, and hydroxyapatite, $Ca_{10}(PO_4)_6(OH)_2$, as well as other oxide systems with potential biomedical applications were prepared following the classic melting method or the sol-gel route [7, 17-31]. In some cases the as prepared samples were heat treated in order to develop certain structures for the envisaged applications.

XPS measurements were performed on both fresh fractured compact samples and on unfractured porous samples either using a PHI 5600ci Multi Technique system with monochromatized Al K_α radiation from a 250 W X-ray source ($h\nu$ = 1486,6 eV), with the pressure in the analysis chamber in the 10^{-9} Torr range, from University of Osnabrück, or the SPECS PHOIBOS 150 MCD system with monochromatised Al-Kα radiation from a 300 W X-ray source (hν=1486.6 eV), under ultra high vacuum conditions, of order 10^{-10} Torr, from IIRBNS of Babes-Bolyai University. In all measurements a low energy electron beam was used to achieve charge neutrality at the sample surface.

RESULTS AND DISCUSSION

XPS analysis on fractures of $29.04(3.34CaO{\cdot}P_2O_5){\cdot}58.06SiO_2{\cdot}12.9Fe_2O_3$ glass and glass-ceramic bulk samples considered for hyperthermia therapy indicate local composition changes induced by the applied heat treatment. According to the

data obtained from survey spectra analysis, the heat treatment carried out at different temperatures between 1000 and 1200°C for the same time and under similar conditions leads to differences in the elemental composition and therefore in the ratio of the component elements (Table 1). The most affected is the iron content which increases about 4.5 times at 1000°C and decreases by 35.31% at 1200°C relative to the untreated sample. The oxygen content practically does not change after heat treatment. In the investigated temperature range all applied heat treatments enhance the Ca/P ratio at the samples surface, as compared with the value corresponding to the untreated glass. The glass ceramic obtained at 1000°C has Ca/P = 3.89 and it contains the highest iron concentration in the thin surface layers investigated. Changes in the valence state of iron ions during the applied heat treatment were also evidenced, and this result is in good agreement with the XRD analysis of this sample that indicates the occurrence of iron in Fe_3O_4, Fe_2O_3 and FeO crystallites [16].

Table I. Atomic percentage of the elements and Ca/P ratio obtained from XPS analysis.

Element	Signal	Untreated sample	Heat treated at 1000°C	Heat treated at 1100°C	Heat treated at 1200°C	Expected elements in bulk sample
Si	2p	10.40	7.47	9.28	10.54	9.13
O	1s	65.94	65.64	64.92	65.01	62.43
P	2p	8.32	2.12	7.32	8.65	9.13
Ca	2p	11.63	8.24	12.53	13.40	15.25
Fe	2p	3.71	16.52	5.96	2.40	4.06
Ca/P		1.40	3.89	1.71	1.55	1.67

In Y_2O_3-Al_2O_3-SiO_2 glasses doped with Fe_2O_3 up to 1 mol % [22], the iron doping effect on the binding energies of core level electrons of the cations entering these glasses (Fig. 1-3) is correlated with changes in the next nearest neighbours of the cations. The full width at half maximum indicates an ordering tendency in the local structure by iron addition to the host yttrium aluminosilicate glass. Progressive iron doping causes the decrease of the effective electronic charge density on the other cations.

XPS is also very useful in the study of protein adherence to the biomaterials surface in order to accomplish their in vitro bioconjugation before to come in direct contact with the alive tissues in the human body. Further are presented data obtained for samples treated in a solution of simulated body fluid (SBF) enriched with bovine serum albumin (BSA). The C 1s core level spectra recorded from sol-gel derived aluminosilicate samples immersed in BSA-SBF solution contain the BSA signature even after one day soaking in the SBF solution with low BSA content [28, 30]. The deconvoluted C 1s photoelectron peaks (Fig. 4) provide more information. It is to be mentioned that the presence of carbon was evidenced in all survey spectra, but carbon adsorption occurs on all surfaces exposed to the atmosphere and is detected by the XPS technique.

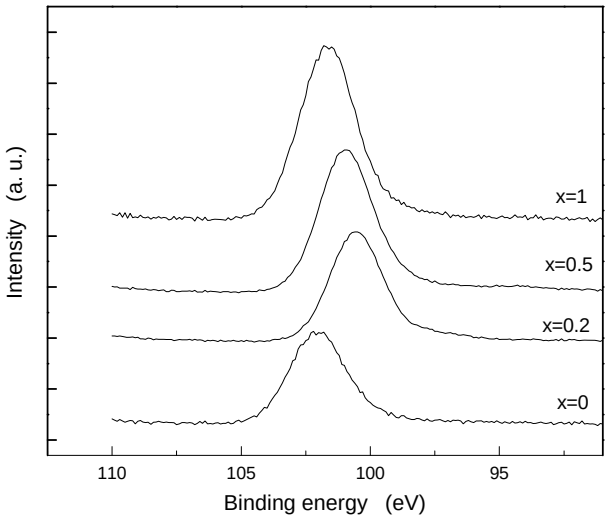

Fig. 1. Si 2p core level photoelectron spectra of $17Y_2O_3 \cdot 19Al_2O_3 \cdot (64\text{-}x)SiO_2 \cdot xFe_2O_3$ samples.

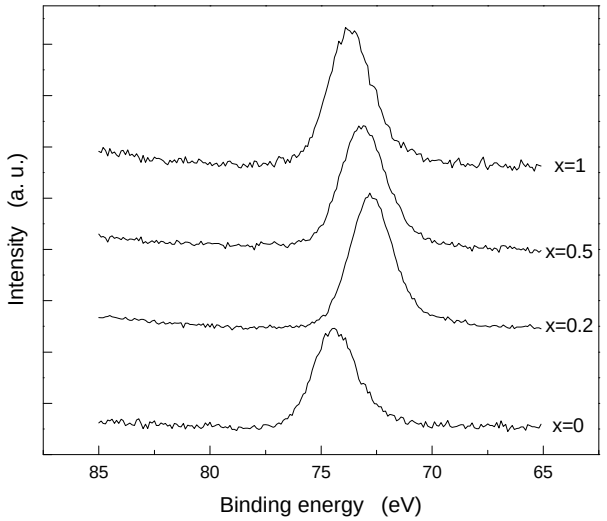

Fig. 2. Al 2p core level photoelectron spectra of $17Y_2O_3 \cdot 19Al_2O_3 \cdot (64\text{-}x)SiO_2 \cdot xFe_2O_3$ samples.

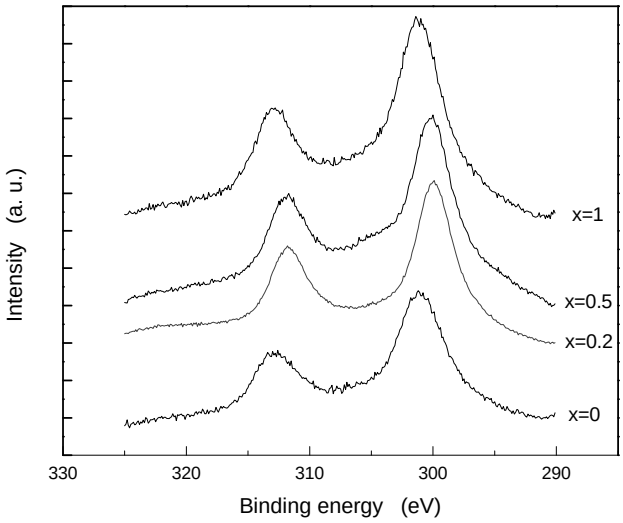

Fig. 3. Y 3p core level photoelectron spectra of $17Y_2O_3 \cdot 19Al_2O_3 \cdot (64\text{-}x)SiO_2 \cdot xFe_2O_3$ samples.

From the non-immersed sample only one single C 1s peak at 285.5 eV is recorded. Also after one day immersion in SBF the C 1s photoelectron peak is well fitted with a single line centered at 285.5 eV, but the peak is broadened, with 2.9 eV full width at half maximum (Fig. 4b), while the full width at half maximum for the non-immersed sample (Fig. 4a) is only 2.3 eV. The deconvolution of C 1s photoelectron peaks for the samples immersed in SBF solution enriched with BSA leads beside the peak at 285.5 eV to other two components centered at 286.7 and 288.6 eV, but their relative peak areas are notably different (Table II). It is beyond doubt that the increased contribution of higher binding energy components is arising from the BSA adhered to the surface of aluminosilicate samples. After immersion in BSA solutions, the relative concentrations of C, N and O suggests that the surface is nearly saturated in taking up BSA functional groups regardless of BSA concentration in SBF. The evolution of both C 1s and N 1s core level spectra, appreciated from the contributions of different components to the deconvoluted peaks, shows that the protein concentration in SBF influences the building up of the BSA layer. Surface functionalisation with protein leads to a larger distribution of the oxygen sites and a slight deficiency in electron density around the oxygen atoms.

Due to the fact that hydroxyapatite is the main inorganic biological component of bones and teeth, an impressive number of studies are focussed on syntetic hydroxyapatite. In fact, the bone inorganic part consists in an amorphous phase of tricalcium phosphate and a crystalline phase of hydroxyapatite with nanometric

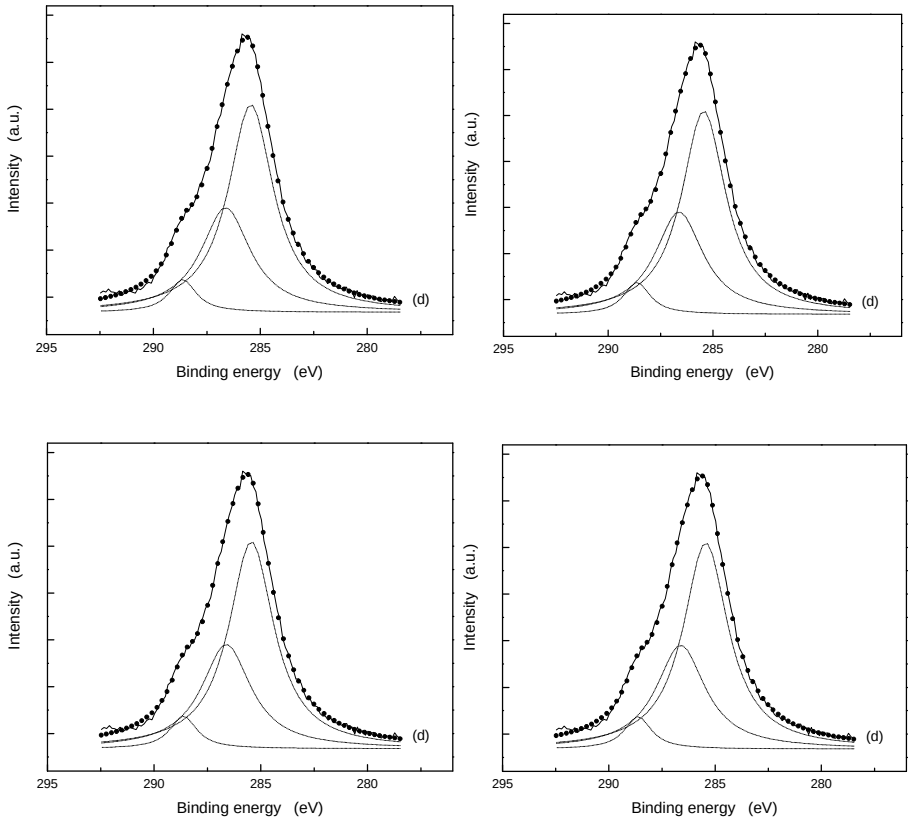

Fig. 4. Deconvoluted C 1s corelevel XPS spectra before immersion (a), and after one day immersion in SBF (b), SBF enriched with BSA (c) and SBF twice enriched with BSA (d).

Table II. Percental distribution of differently binded carbons to C 1s photoelectron peaks according to peak deconvolution.

BSA concentration in SBF (g/ℓ)	Binding energy (eV)		
	285.5	286.7	288.6
	Relative peak areas (%)		
3.33	82	13	7
6.67	51	42	5

crystal sizes, of needle shape, with a length of about 100 nm, 20–30 nm in width and thickness of 3–6nm [32]. In the enamel of teeth, containing about 95% of hydroxyapatite, the crystals are bigger but still with submicrometric sizes. We have investigated by XPS the atomic environment changes in sol–gel derived hydroxyapatite samples heat treated at high temperatures [31]. Beside structural effects of the increasing treatment temperature, the effects on the effective electronic charge density around calcium and phosphorus cations and on the structural units build around phosphorus atoms were evidenced.

An optimal scaffold for bone tissue should be osteoconductive and angiogenic and it should serve as a three-dimensional template to provide structural support to the newly formed bone through an interpenetrating network of pores to allow cell migration, tissue in-growth and vascularization [33, 34]. A wide range of three dimensional bioactive scaffolds has been developed which can be potentially used as delivery systems for therapeutic drugs relevant for bone repair processes. The new scaffold materials are composites that usually contain a glass or glass-ceramic component.

Our XPS investigation of titanium-hydroxyapatite sintered powders evidences the atomic environment changes induced by mechanical strain [25]. Hydroxyl species which increase the surface ability for self-assembly of nanoscale hydroxyapatite like structures on endosseous implants are evidenced on the surface of samples compressed at higher pressure.

CONCLUSIONS

The XPS results obtained from several biomaterials prove that XPS is a fundamental method for elemental analysis of their surface and for quantification of surface contamination. The investigation of iron containing biomaterials for hyperthermia therapy point out changes of iron concentration and valence state, as well as of Ca/P ratio on the sample surface, which can be controlled by heat treatment temeperature. The atomic environment on surface of titanium-hydroxyapatite composites is slightly affected by the sintering pressure, with influence on the attached hydroxyl functional group. Protein attachment on aluminosilicate samples was first evaluated by the relative concentrations of C, N and O. The results suggest that the surface is nearly saturated in taking up BSA functional groups regardless of BSA concentration in SBF. At the same time, the surface functionalisation with protein leads to a larger distribution of the oxygen sites and a slight deficiency in electron density around the oxygen atoms.

REFERENCES

i. **M. Coldea**, M. Neumann, St. Lutkehoff, S. Mahl, R. Coldea, J. Aloy Compd., 278, 72 (1998)

ii. V. Simon, R. Pop, M. Neumann, S.G. Chiuzbaian, S. Simon, **M. Coldea**, Rom. Reports in Physics, 53, 579 (2001)

iii. **M. Coldea**, M. Neumann, V. Pop, M. Demeter, J. Aloy Compd., 323-324, 431 (2001)

iv. V. Simon, R. Pop, M. Neumann, S.G. Chiuzbaian, **M. Coldea**, S. Simon, Mod. Phys. Lett. B., 16, 41 (2002)

v. V. Pop, **M. Coldea**, M. Neumann, S. Chiuzbaian, D. Todoran, J. Aloy Compd., 333, 1 (2002)

vi. V. Simon, R. Pop, S.G. Chiuzbaian, M. Neumann, **M. Coldea**, S. Simon, Mat. Lett., 57, 2044 (2003)

vii. V. Pop, **M. Coldea**, M. Neumann, O. Isnard, S.G. Chiuzbaian, J. Magn. Magn. Mater, 272-276, e613 (2004)

viii. **M. Coldea**, V. Pop, M. Neumann, O. Isnard, L.G. Pascut, J. Aloy Compd., 390, 16 (2005)

ix. **M. Coldea**, M. Neumann, S.G. Chiuzbaian, V. Pop, L.G. Pascut, O. Isnard, A.F. Takacs, R. Pacurariu, J. Aloy Compd., 417, 7 (2006)

x. R. Pacurariu, **M. Coldea**, M. Neumann, V. Pop, O. Isnard, M. Rakers, Phys. Status Solidi (b), 244, 3190 (2007)

xi. **M. Coldea**, R. Pacurariu, M. Neumann, L.G. Pascut, V. Rednic, AIP Conf. Proceed., 899, 636 (2007)

xii. L. Rednic, R. Pacurariu, V. Rednic, L.G. Pascut, V. Pop, M. Neumann, **M. Coldea**, J. Optoelectr. Adv. Mater., 9, 568 (2007)

xiii. V. Rednic, L. Rednic, **M. Coldea**, V. Pop, M. Neumann, R. Pacurariu, A.R.Tunyagi, Cent. Eur. J. Phys., 6, 434 (2008)

xiv. S. Khanra, **M. Coldea**, M. Neumann, P. Chaudhuri, K. Kuepper, T. Weyhermuller, M. Prinz, M. Raekers, S. Voget, A.V. Postnikov, F.M.F. De Groot, S.J. George, Inorg. Chem., 47, 4605 (2008)

xv. V. Rednic, **M. Coldea**, S.K. Mendiratta, M. Valente, V. Pop, M.Neumann, L. Rednic, J. Magn. Magn. Mater, 321, 3415 (2009)

xvi. R. Pacurariu, V. Rednic, **M. Coldea**, D. Benea, V. Pop, O. Isnard, M.Neumann, Phys. Status Solidi (b), 246, 50 (2009)

1. A.G. Cristina, Science, 237, 1588 (1988)
2. B.D. Ratner, Macromol. Chem. Macromol. Symp. 9, 163 (1988)
3. J.A. Gardella Jr., N.I.H. de Gatrica, J. Elecron Spectrosc. Relat. Phenom., 81, 227 (1996)
4. S.L. McArthur**,** Surf. Interface Anal. 2006; 38: 1380–1385
5. K.Ohura, M.Ikenaga, T.Nakamura, T.Yamamuro, Y.Ebisawa, T.Kokubo, Y.Kotoura, M.Oka, J. Appl. Biomaterials, 2, 153 (1991)
6. D. Eniu, D. Cacaina, M. Coldea, M. Valeanu, S. Simon, J. Magn. Magn. Mater., 293, 1, 310-313 (2005)
7. G.J. Ehrhardt, D.E. Day, Nucl. Med. Biol. 14, 233 (1987)
8. V. Simon, M. Spinu, R. Stefan, J. Mat. Sci.: Mater. Med., 18, 507 (2007)
9. K. Vijayanand, D.K. Pattanayak, T.R. Rama Mohan, R. Banerjee, Trends Biomater. Artif. Organs 18, 73 (2005)
10. F. Rossi, A. Valsesia, M. Manso, G. Ceccone, P. Colpo, Micro- and Nano-Structured Thin Films for Biological Interfaces, NATO Science Series, vol. 155, 2006, p. 285.
11. J. Figge, T.H. Rossing, V. Fencl, J. Lab. Clin. Med. 117, 453 (1991)
12. A. Rossi, B. Elsener, N.D. Spencer, Spectr. Eur. 6 (2004) 14.
13. S. Simon, R.V.F. Turcu, T. Radu, M. Moldovan, V. Simon, J. Optoelectr. Adv. Mater., 11, 1660 (2009)
14. V. Simon, D. Lazăr, R.V.F. Turcu, H. Mocuta, K. Magyari, M. Prinz, M. Neumann, S. Simon, Mat. Sci. Eng. B, 165, 247 (2009)
15. V. Simon, S. Cavalu, S. Simon, H. Mocuta, E. Vanea, M. Prinz, M. Neumann, Solid State Ionics, 180, 764 (2009)
16. V. Simon, S.G. Chiuzbaian, M. Neumann, D. Eniu, E. Indrea, A. Torok-Kiss, S. Simon, Mod. Phys. Lett. B., 14, 767 (2000)
17. V. Simon, H. Bako-Szilagyi, M. Neumann, S.G. Chiuzbaian, S. Simon, Mod. Phys. Lett. B, 17, 291 (2003)
18. V. Simon, L. Barză, S. Simon, S.G. Chiuzbăian, M. Neumann, Int. J. Mod. Phys. B, 18, 45 (2004)
19. V. Simon, D. Eniu, M. Neumann, S. Simon, Int. J. Mod. Phys. B, 18, 1, 45 (2004)
20. E. Culea, L. Pop, V. Simon, M. Neumann, I. Bratu, J. Non-Cryst. Solids, 337, 62 (2004)
21. V. Simon, D. Eniu, A. Takács, K. Magyari, M. Neumann, S. Simon, J. Optoelectr. Adv. Mater., 7, 2853 (2005)
22. V. Simon, D. Eniu, A. Takacs, K. Magyari, M. Neumann, S. Simon, J. Non-Cryst. Solids, 351, 2365 (2005)
23. V. Simon, D. Muresan, A.F. Takács, M. Neumann, S. Simon, Solid State Ionics, 178, 221 (2007)
24. V. Simon, M. Todea, A.F. Takács, M. Neumann, S. Simon, Solid State Commun., 141, 42 (2007)
25. V. Simon, D. Lazăr, C. Popa, A.F. Takács, M. Neumann, S. Simon, J. Optoelectr. Adv. Mater., 9, 587 (2007)
26. V. Simon, A. Colceriu, C. Prejmerean, M. Moldovan, M. Prinz, M. Neumann, J. Optoelectr. Adv. Mater., 9, 3350 (2007)

27. V. Simon, O. Ponta, S. Simon, D.A. Udvar, M. Neumann, Phys. Status Solidi (a), 205, 1139 (2008)
28. V. Simon, S .Cavalu, M. Prinz, E. Vanea, M. Neumann, S. Simon, European Cells & Materials, 16, S1, 55 (2008)
29. V. Simon, O. Ponta, S. Simon, M. Neumann, J. Optoelectr. Adv. Mater., 10, 2325 (2008)
30. V. Simon, S. Cavalu, S. Simon, H. Mocuta, E. Vanea, M. Prinz, M. Neumann, Solid State Ionics, 180, 764 (2009)
31. V. Simon, D. Lazăr, R.V.F. Turcu, H. Mocuta, K. Magyari, M. Prinz, M. Neumann, S. Simon, Materials Science and Engineering B, 165, 247 (2009)
32. N. Roveri, B. Palazzo, in: S.S.R. Kumar Challa (Ed.), Nanotechnologies for the Life Sciences, vol. 9, Wiley-VCH, 2006, pp. 283–307.
33. C. Popa, V. Simon, I. Vida-Simiti, G. Batin, V. Candea, S. Simon, J. Mat. Sci.: Mater. Med., 12, 1165 (2005)
34. G. Baciut, M. Baciut, V. Simon, S. Bran, R. Campian, H. Rotaru Int. J. Oral Max. Surg., 36, 1062 (2007)

STUDIA UNIVERSITATIS BABEŞ-BOLYAI, PHYSICA, LV, 1, 2010

PHYSICAL PROPERTIES OF MINERAL NANOSTRUCTURED CLAYS FOR MEDICAL APPLICATIONS

M. TĂMĂŞAN, A. VULPOI, V. SIMON[a]

ABSTRACT. Mineral clays attract renewed interest for medical applications. Important properties of clays which make them useful in pelotherapy are high surface area and fine grain size distribution, that imply enhanced absorption/adsorption capacity and high cationic exchange capacity. A pharmaceutically available clay recommended for a large range of medical applications was analyzed by X-ray diffraction, thermal analyses, specific surface area and particle size distribution analysis by UV laser diffraction method.

Keywords*: medical clay; XRD; DTA; specific surface area; particle size distribution.*

INTRODUCTION

Pelotherapy is the an old therapeutic treatment with clays or mud, which attracted renewed interest in the last decade [1-8]. The clays were primary used in treatment of disfunctions as well as for the detoxifying of the organism, and recently they are also considered for cancer treatment [9].

New drug delivery systems are investigated in order to formulate anticancer drugs without harmful adjuvant, to minimise the side effects and to achieve synergistic therapeutic effects [9,10]. Nanoparticles have been demonstrated to be able to preferentially deliver drugs to diseased tissues resulting in enhanced therapeutic efficacy. A suitable class of compounds for use as drug matrix or carrier is the class of medical clays. As potent detoxifiers, the medical clays can adsorb toxins and reduce side effects. Novel systems of chemoterapeutic agents loaded in montmorillonite clay nanoparticles for targeted drug delivery were developed [2, 3, 11].

A medical clay, pharmaceutically available, used for a large range of disfunctions as well as for the detoxifying of the organism was considered for a matrix material in a targeted delivery drug and investigated by X-ray diffraction analysis, thermal analyses DTA/TG and DSC, specific surface area using nitrogen adsorption/desorption method and particle size distribution analysis by UV laser diffraction method.

[a] *Babeş-Bolyai University, Faculty of Physics & Institute for Interdisciplinary Experimental Research, 400084 Cluj-Napoca, Romania*

EXPERIMENTAL

The investigated clay is available as Algo clay. According to the presentation data, it is 100 % natural clay from Tibet plateau and is recommended as a detoxifier for several afflictions. The therapeutic activity of these minerals is controlled by their physical and physico-chemical properties as well as their chemical composition, but for sure the main properties of clays which make them useful in pelotherapy are the structure, surface area and grain size distribution, that determine the absorption/ adsorption capacity and cationic exchange capacity.

The structure was investigated by X-ray diffraction (XRD) with a Shimadzu XRD-6000 diffractometer, using CuKα radiation (λ = 1.5418 Á), with Ni–filter. The XRD analysis was performed at a scan speed of 2°/min on a 2θ scan range of 10-80º and as calibrating material it was used quartz powder. Operating power of the X-ray source was 40 kV at 30 mA intensity.

Thermal analysis was conducted on Shimadzu type derivatograph DTG-60H (differential thermal and thermo gravimetric analyses) with a heating rate of 10ºC/min for a temperature range of 28-1400ºC. Alumina open crucibles were used and the measurement was made in a dynamic nitrogen and air atmosphere at a flow rate of 70ml/min each.

The surface area of the sample was determined by measuring nitrogen adsorption/desorption at 77K with surface area analyser Qsurf Series M1, on the basis of Brunauer, Emmet and Teller (B.E.T.) equation, $S_t = K\ (1 - P/P_o)\ V_a$, where S_t – total surface area; K = 4.35, a constant for nitrogen, assuming STP condition; $P/P_o = 0.294$ for gas mixture of 30% N_2 / 70% He; V_a – volume of gas (N_2) adsorbed. The measurements were performed using Three Point B.E.T. method with three gas mixtures.

Particle size distribution was achieved on a Shimadzu Nano Particle Size Distribution Analyzer SALD-7101 using a Laser diffraction method with a UV semiconductor laser (375 nm wavelength). The technique of laser diffraction is based on the principle that particles passing through a laser beam will scatter light at an angle that is directly related to their size: large particles scatter at low angles, whereas small particles scatter at high angles. The laser diffraction is accurately described by the Fraunhofer Approximation and the Mie theory, under the assumption of spherical particle morphology. The SALD-7101 analyzer principle is based on the Mie theory. The Mie model takes into account both diffraction and diffusion (absorption, refraction and reflection) of the light around the particle in its medium (Fig. 1).

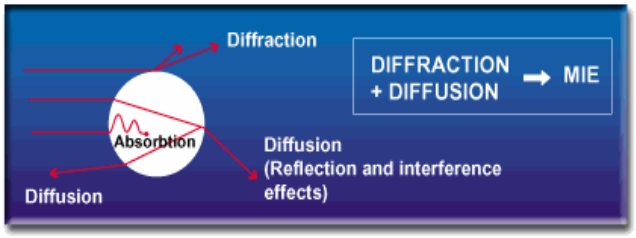

Fig. 1. Schematical depiction of processes considered in the Mie model.

The method relies on the fact that diffraction angle is inversely proportional to particle size. The intensity of the scattered light varies with the scattering angle and describes a spatial intensity distribution pattern. Particle size distribution measurement is not performed on individual particles, but rather on particle groups made up of large numbers of particles. Particle groups contain particles of different sizes, and the light intensity distribution pattern emitted by a group is composed of all the scattered light emitted from all the individual particles. The particle size distribution, in other words, what particle sizes are present in what proportions, can be obtained by detecting and analyzing this light intensity distribution pattern. This is the basic principle behind the laser diffraction method used in laser diffraction particle size analyzers [12].

RESULTS AND DISCUSSION

The X-ray diffraction pattern, presented in Fig. 2, emphasizes the presence of a major kaolinite crystalline phase [$Al_2Si_2O_5(OH)_4$, JCPDS 1:29-1488], as well as of a $Al_6Si_2O_{13}$ mullite crystalline phase, and gibbsite crystalls [13]. Kaolinite is a layered silicate mineral, with one tetrahedral sheet linked through oxygen atoms to one octahedral sheet of alumina octahedra. $Al_6Si_2O_{13}$ mullite, in fact $3Al_2O_3 \cdot 2SiO_2$, is the only stable binary compound existed under common pressure within the Al_2O_3-SiO_2 phase. Mullite structure mainly consists of chains of edge-sharing AlO_6 octahedra [14]. The complex real structure of mullite is able to incorporate big amounts of foreign atoms [15]. The size of the crystals estimated according to Scherrer's equation for the diffraction peaks is bellow 35 nm.

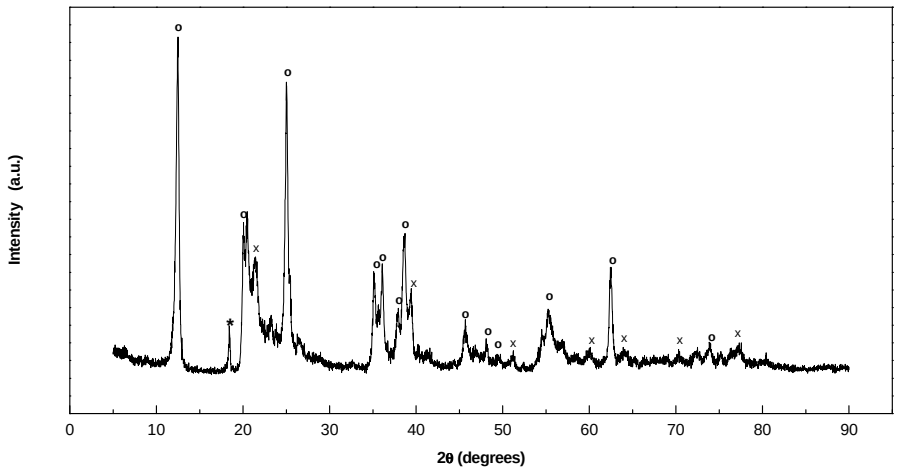

Fig. 2. XRD diffraction pattern of Algo medical clay.
○ - kaolinite; x - mulitte; ⋆ - gibbsite.

The DTA/TG runs of the mineral clay are represented in Fig. 3. The profile of the DTA curves presents first a very small endothermic peak at ~233 ºC with no decrease in mass. In the temperature range of 354ºC – 660ºC one can observe a typical endothermal dehydration by dehydroxylation with the maximum at 500 ºC, accompanied by a loss of mass, of ~14 % from the total mass of the sample [16]. FTIR studies on hydrated hydroxylated minerals [17] show that in such compounds occur both hydroxyl units and bonded water. Because any significant mass loss is evidenced about 100 ºC, it appears that Algo clay contains scarcely free water. Between 977 ºC – 1007 ºC appears an exothermal solid state transition with the maximum at 995.5 ºC and no loss of mass. These transformations are in good agreement with other results which show that endothermic dehydroxylation (or alternatively, dehydration) begins at 550-600 °C to produce disordered metakaolin, $Al_2Si_2O_7$, but continuous hydroxyl loss (-OH) is observed up to 900 °C and has been attributed to gradual deprotonation by oxolation of the metakaolin. The oxolation is a reaction of condensation between two coordinate metal complexes by a hydroxo (HO) ligand: M-OH+M-OH → M-HO-MOH → M-O-M +H_2O [18]. Further heating to 925-950 °C is assigned to a structural conversion of metakaolin in another of the aluminosilicates polymorphs.

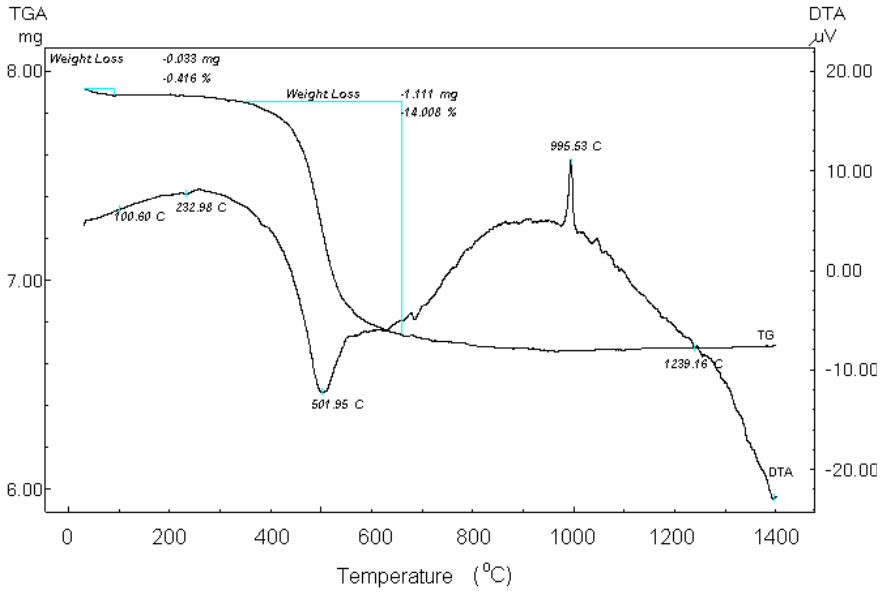

Fig. 3. TG and DTA curve of Algo medical clay.

The specific surface area of the sample, determined by nitrogen adsorption / desorption in three point method, is 21.74 m^2/g. This tehnique allowed also an analysis of pore size distribution and of total pore volume, which is presented in Fig. 4.

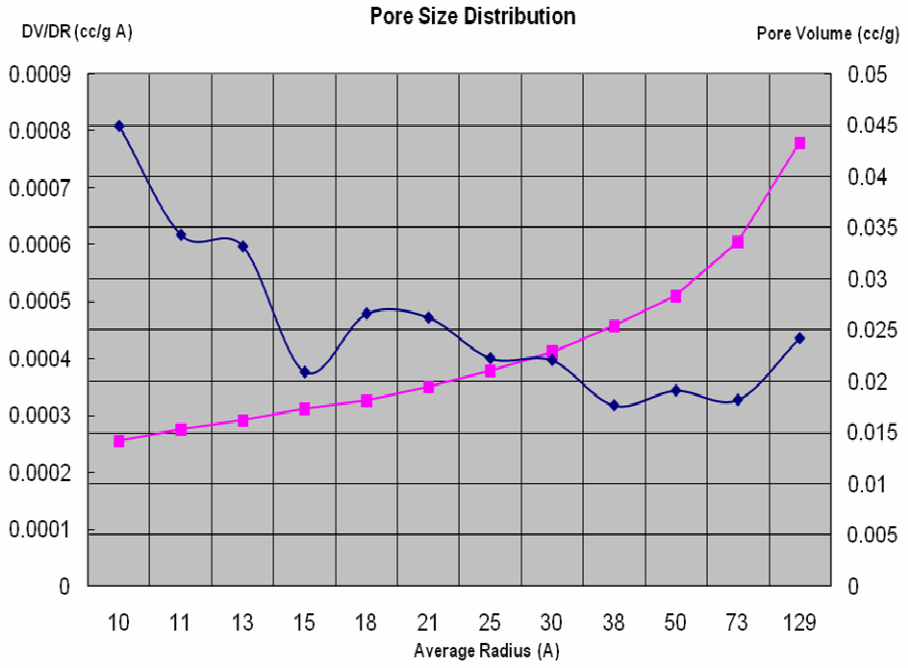

Fig. 4. Pore size distribution and pore volume by nitrogen adsorption/desorption method.

In the acceptation of International Union of Pure and Applied Chemistry (IUPAC), porous materials can be divided into three classes, depending on the pore size. Materials with pore diameter smaller than 2 nm are called *microporous*, materials with a pore diameter in between 2 and 50 nm are assigned as *mesoporous*, while materials with pore diameters larger than 50 nm are classified as *macroporous* [19, 20]. Therefore, the average radius of the pores of the clay mineral, acording to IUPAC clasifications, which varies in the range of 1 – 12.9 nm, indicate the presence of micro and meso types of pores. The total pore volume, obtained at maximum saturation (97 %) with N_2, is 0.079 cm^3/g.

The IUPAC classification is not unique. Although in recently published articles the materials with nanosized pores are denominated mesoporous [21, 22], other authors [23] consider that classes of pores are sorted in macroporosity (100–330 μm), mesoporosity (10–100 μm) and microporosity (30 Å to 10 μm), but in the most recent publications is largely used the term nanoporosity [24-26].

Particle size distribution measurements, performed on Shimadzu Nano Particle Size Distribution Analyzer SALD-7101, are presented in Fig. 5. The plot of particles diameter versus normalized particle amount indicate a range of 0.034 – 0.271 μm for the particle diameters (about 83% of the total amount) with the prevalence of the

0.1 µm (100 nm) diameters. Particles with larger diameters, in the ranges of 0.9 – 6 µm and 7 - 57 µm , are also evidenced on an detailed scale (Fig. 6). This differences in grain size distribution can match the proper exchange conditions for different cations. On the other hand, these grains will enable different degrees of water retention [27], with influence on the efficiency of pelotherapy.

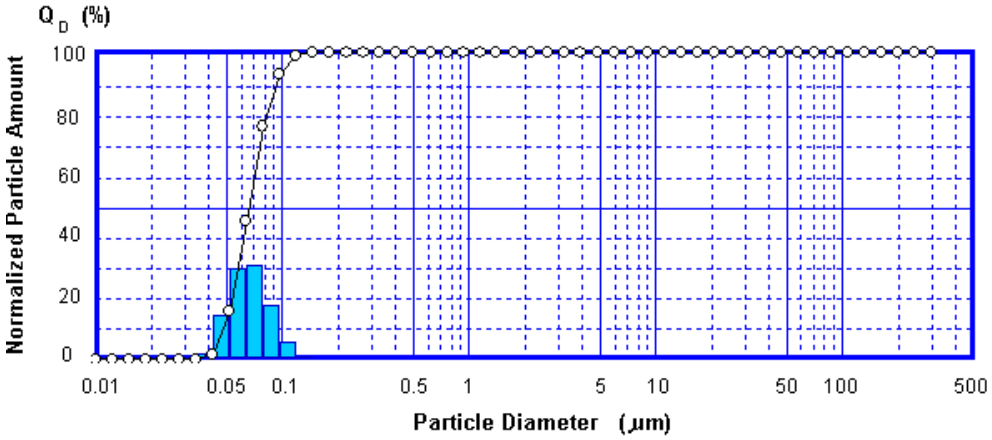

Fig. 5. Particle size distribution using laser diffraction method.

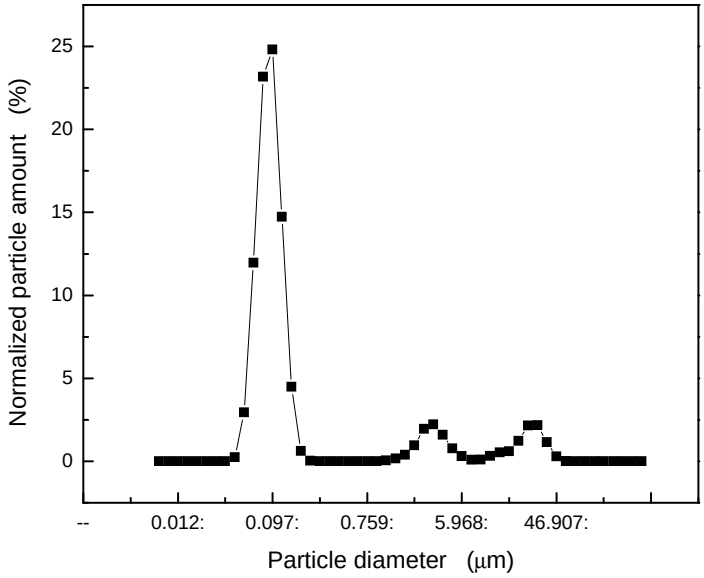

Fig. 6. Particle size distribution shown on detailed scale.

CONCLUSIONS

XRD analysis performed on mineral clay revealed the presence of two main crystalline phases, kaolinite and mullite. Gibbsite crystals are also evidenced. The crystal sizes are up to 35 nm. Thermal analysis evidences that the clay is hydrated hydroxylated. Specific surface area of 21.742 m^2/g, prevalent particle sizes in the range below 100 nm, as well as the nanopores of average radius in the range of 1 – 12.9 nm suggest that the investigated Algo medical clay can be considered not only for pelotherapy, but also in view of a suitable drug carrier and releaser.

ACKNOWLEDGEMENTS:

A.V. author wishes to thank for the financial support provided from programs co-financed by The Sectoral Operational Programme Human Resources Development, Contract **POSDRU 6/1.5/S/3 – „**DOCTORAL STUDIES: THROUGH SCIENCE TOWARDS SOCIETY".

REFERENCES

1. M. Bechtle, S. Chen, T. Efferth, Curr. Med. Chem., 17 (2010) 42.
2. M.I. Carretero , M. Pozo, Appl. Clay Sci., 47 (2010) 171.
3. M.I. Carretero , M. Pozo, Appl. Clay Sci., 46 (2009) 73.
4. E. Nieddu., L. Mazzucco, P. Gentile, T. Benko, V. Balbo, R. Mandrile, G. Ciardelli, React. Funct.Polym., 69 (2009) 371.
5. X. Wang, Y. Du, J. Yang, Y. Tang, J. Luo, J. Biomed. Mater. Res. A, 84 (2008) 384.
6. C. Aguzzi, P. Cerezo, C. Viseras, C. Caramella, Appl. Clay Sci., 36 (2007) 22.
7. Z.S. Yen, M.S. Lai, Emerg. Med. J., 23 (2006) 65.
8. M.I. Carretero, Appl. Clay Sci. 21 (2002) 155.
9. B. Sun, B. Ranganathan, S.-S. Feng, Biomaterials, 29 (2008) 475.
10. S.-S. Feng, L. Mei, P. Anitha, C.W. Gan, W. Zhou, Biomaterials, 30 (2009) 3297.
11. G. Carja, G.C. Chitanu, Y. Kameshima, H. Chiriac, K. Okada, Appl. Clay Sci., 41 (2008) 107.
12. R.M. Jones, Particle size analysis by laser diffraction: ISO 13320, standard operating procedures and Mie theory. American Laboratory, 2003.
13. D.B. Tilley, R.A. Eggleton, Clay Clay Miner., 44 (1996) 658.
14. R.X. Fischer, H. Schneider, Am. Mineral. 85 (2000) 1175.
15. H. Schneider, S. Komarneni (Eds.), *Mullite***,** Wiley, New York. 2006.
16. M. Bellotto, A. Gualtieri, G. Artioli, S.M. Clark, Phys. Chem. Miner., 22 (1995) 207.
17. R.L. Frost, Spectrochim. Acta A, 60 (2004) 1439. R.L. Frost, K.L. Eirickson, Spectrochim. Acta A, 61 (2005) 45.

18. S. Verdier, S. Delalande, N. Van Der Laak, J. Metson, F. Dalard, Surf. Interface Anal., 37 (2005) 509.
19. D. H. Everett, Pure Appl. Chem., 31 (1972) 577.
20. K.S.W. Sing, D.H. Everett, R.A.W. Haul, L. Moscou, R.A. Pierotti, J. Rouquerol, T. Siemieniewska, Pure Appl. Chem., 57 (1985) 603.
21. S. Tominaka, Y. Nakamura, T. Osaka, J. Power Sources 195 (2010) 1054.
22. Y.-P. Guo, T.-S. Lin, Y. Zhou, D.C. Ji, Y.-J. Guo, Micropor. Mesopor. Mater. 127 (2010) 245.
23. A.-M. Le Ray, H. Gautier, J.-M. Bouler, P. Weiss, C. Merle, Ceram. Int. 36 (2010) 93.
24. V. FitzGerald, R.A. Martin, J.R. Jones, D. Qiu, K.M. Wetherall, R.M. Moss, R.J. Newport, J. Biomed. Mater. Res. A, 91 (2009) 76.
25. K.-L. Ou, J. Wu, W.-F.T. Lai, C.-B. Yang, W.-C. Lo, L.-H. Chiu, J. Bowley, J. Biomed. Mater. Res. A, 92 (2010) 906.
26. S. Lin, C. Ionescu, E.M. Valliant, J.V. Hanna, M.E Smith, J.R. Jones, J. Mater. Chem., 20 (2010) 1489.
27. M.I. Carretero, M. Pozo, C. Sanchez, F.J. Garcia, J.A. Medina , J.M. Bernabe, Appl. Clay Sci., 36 (2007) 161.

STUDIA UNIVERSITATIS BABEŞ-BOLYAI, PHYSICA, LV, 1, 2010

HYDRATION-DRYING AND AGEING EFFECTS ON THE PEO- CLOTRIMAZOLE SYSTEM

M. TODICA[a]*, C. V. POP[a], LUCIANA UDRESCU[a], ELENA DINTE[b], MONICA POTARA[a]

ABSTRACT. The possibility to use the polyethylene oxide as polymeric matrix for the clotrimazole was analysed. The effects of hydration-drying and ageing processes on the properties of the polymeric matrix were observed by Raman spectroscopy. Similar observations were effectued on the clotrimazole. No modifications of the properties of the polymer and clotrimazole were observed after long time of conservation.

Keywords: *Polyethylene oxide, clotrimazole, hydration, ageing effect.*

Pacs Numbers: 78.30.Jw; 33.20.Fb

INTRODUCTION

The use of the polymeric matrix as support for the active substance represents a new direction of development of the pharmaceutical products with application on the treatment of the skin diseases[1,2,3]. The advantage is the possibility to focusse the action of the medical drug to a limited area of the skin, the long delivery time and the possibility to controlle the delivery rate of the active substance [4,5,6].

During the medical applications the pharmaceutical product is submitted to different situations, variation of the temperature and PH, UV and X rays exposure, hydration and draying process, long time conservation. The polymeric matrix and the active pharmaceutical substance are requested to have a high physical and chemical stability under the action of these aggressive factors.

One of the products of interest is the system polyethylene oxide-clotrimazole. The polyethylene oxide (PEO) is a very stable polymer in contact with the biological environment, and can be easy used to obtain hydro gels including active pharmaceutical substance[7]. The clotrimazole is a very efficient medical drug against many fungi, and it is suitable for direct application on the surface of the skin [8].

[a] *"Babes-Bolyai" University, Faculty of Physics, 400084 Cluj-Napoca, Romania.*
* corresponding author: email: *mihai.todica@phys.ubbcluj.ro*
[b] *University of Medicine and Pharmacy, Faculty of Pharmacy Cluj-Napoca, Romania*

In our work we observed the effect of repeated action of water and the effect of long time conservation on the physical properties of the polymer and of the active substance. The investigations were performed by specific method of physics, the Raman spectroscopy. Preliminary investigations concerning the pharmaceutical effects were already performed and published, and more detailed studies in this direction will be the subject of further works [9].

EXPERIMENTAL

The polymer used in our study is the polyethylene oxide PEO 750. In dried state, this polymer is solid powder heaving great affinity towards the water. The polymeric gels were prepared by mixing slowly the polymer and the pure water during 3-4 hours. The polymeric concentration of the samples was 6%. For the spectroscopic measurements, the gels were deposed on thin films on the microscope glass plates.

The dried gels were obtained by evaporation of water, at room temperature and atmospheric pressure, during 48 hours, respectively 7 days. The ageing effect was observed on samples conserved 12 months in closed recipients, in dark at room temperature and normal atmospheric pressure.

The clotrimazole, in powder state, was introduced in the PEO gel and mixed 4-5 hours, in order to obtain a homogeneous dispersion of the active substance in the polymeric matrix. The samples were investigated by Raman spectroscopy using a Raman microscope (Witec CRM 200), at the room temperature. All Raman spectra were excited with 100 mW of 633 nm light produced by a He-Ne laser and the spectra were recorded in backscattering geometry. A digital acquisition data is performed by the PC computer of the system.

RESULTS AND DISCUSSIONS

The polyethylene oxide has a repeat unit consisting on three linkages along the backbone, the O-C, C-C, and C-O bonds, and can adopt many conformations in function of the temperature or the presence of the solvents in its vicinity. The most probable structure of the monomer is the *trans* conformation, designed *ttt,* and corresponds to the minimum of the potential interaction energy between the atoms of the repeat unit. However, in the crystalline state the *gauche* conformation, designed *tgt,* appears with great probability [10,11]. These conformations are determined mainly by the electrostatic interactions between the neat positive and negative charges accumulate on the backbone [12-15]. The local structure of the polymer changes between these conformations, from *tgt* to *ttt*, when the polymer passes from the crystalline state to the aqueous state. Each modification of the local polymeric structure leads to modification of the vibration spectrum observed by Raman spectroscopy [16,17]. The vibration bands are determined by different molecular mechanisms, and can be correlated to the properties of the polymeric matrix in different circumstances.

In solid state, the fluctuations of the polymeric conformations are reduced, and the spectrum is characterized by well-defined and narrow vibration bands (Fig. 1, curve A). The most intense band at 853 cm^{-1} is assigned to the C-O stretching of the *tgt* conformer, and the band observed at 871 cm^{-1} is associated to the backbone stretching modes of the sequences *tgt - tgt - tgt* and *tgg – tgg – tgg*. Other vibration modes, associated to the sequences *ttt – tgt – tgt* or *tgt – tgt – tgt,* give bands in the domain 230 – 280 cm^{-1}, [18].

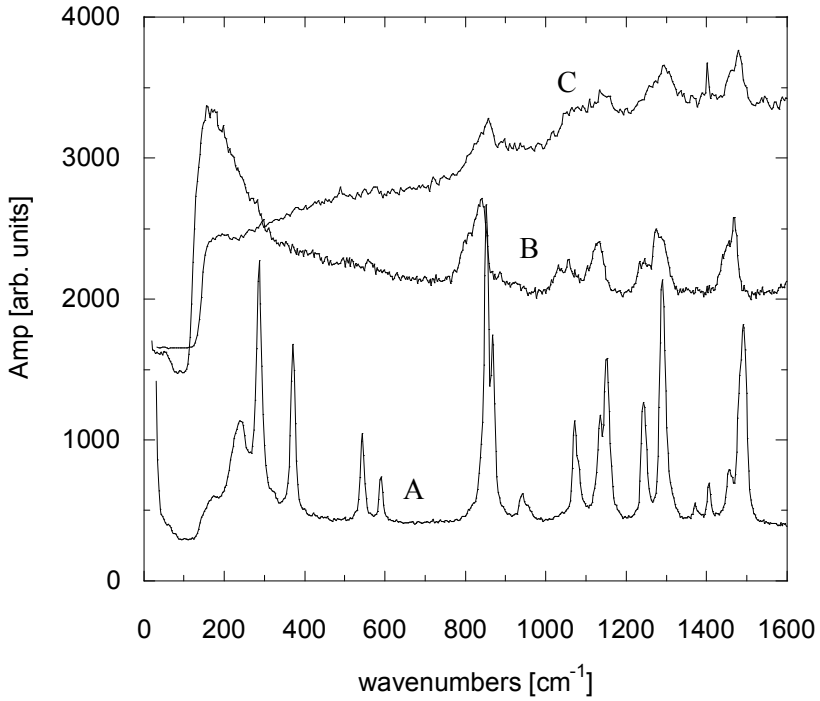

Fig. 1. The Raman spectra of the samples: the PEO in solid state, (curve A); the PEO gel, (curve B); and the PEO gel after 12 month of conservation, (curve C).

The aqueous state is characterized by a large distribution of the local conformations and important time fluctuations of these conformations. In this state the conformations distribution of PEO contains all possible conformer sequences *ttt, tgt. tgg, ttg* [10,18,19,20]. Each conformation gives rise to its characteristic spectrum and the recorded spectrum is a superposition of the individual spectra. The result is a broadening of the spectrum. This effect can be well observed in the domain 200-400cm^{-1}. There the spectrum is broad and some bands are missing in the spectrum of the aqueous state by rapport to the spectrum of solid PEO, (Fig. 1 curve B). We suppose that the vibration bands of PEO are masked by the broad spectrum of the

water. This supposition is confirmed by the fact that the intense band at 853 cm^{-1} of the solid PEO appears again in the spectrum of the aqueous state, but this band is broad and its intensity is strongly reduced. In the domain of 1000-1500 cm^{-1} we can also identify many bands characteristic of the solid PEO, but these bands are broad and without clear structure. The narrow bands of solid PEO observed at 1491 cm^{-1} and 1458 cm^{-1}, at 1288 cm^{-1} and 1244 cm^{-1}, at 1151 cm^{-1} and 1134 cm^{-1} respectively, merge in broad bands in the domain of 1420-1520 cm^{-1}, 1220-1320 cm^{-1}, and 1050-1150 cm^{-1} observed in the spectrum of the aqueous state. The apparition of the most important bands at the same wave numbers, in both the spectra, indicates the fact that the mains vibrations modes of the molecular bonds of the polymeric chain are weakly affected by the presence of the water [21]. Thus, the main properties of the polymer remain unchanged in the gel state. For the dried gel, we expect to find the characteristic vibration bands of the solid state at the same number wave. The spectrum of the dried gel depends on the time of drying process. The sample dried 48 hours is characterized by a broad spectrum without clear structure. However, some bands of the solid state can be identified in this spectrum, especially in the domain 1000-1500 cm^{-1}, but some differences can be observed (Fig. 2 curve A). In the spectrum of the solid state the vibration bands at 1491 cm^{-1} and 1458 cm^{-1}, at 1288 cm^{-1} and 1244 cm^{-1} at 1151 cm^{-1} and 1134 cm^{-1} are clearly separated and have high amplitude. In the spectrum of the dried gel the bands 1491 cm^{-1} and amplitude; the band 1151 cm^{-1} is very weak and the band 1134 cm^{-1} is missing from the spectrum.

In the domain (200-600 cm^{-1}) the spectrum is broad, like in the case of the aqueous state. The narrow bands of the solid state merge into a broad band centered at 455 cm^{-1}. This behavior indicates that the water was not completely removed from the sample, and some molecules of water were trapped on the polymeric matrix. For the sample dried 7 days, the spectrum is very similar to those of the solid state (Fig. 2 curve B). The water was completely removed from the gel and the polymer reaches its initial local conformation. The majority of the vibration bands of the crystalline state appear in the spectrum of the dried gel, indicating that the polymer was not affected by the removing process of the water.

Repeated hydration of the pharmaceutical products, accidentally or during the therapy, represents a frequent situation in the medical applications. Two series of samples were prepared by hydration of the gels already dried 48 hours, respectively 7 days. The spectra of both kinds of sample are large and without fine structure. The spectrum of the gel dried 48 hours contains the characteristic bands of the solid PEO at 853 cm^{-1} and 1491 cm^{-1}, but they are large and have very small amplitude (Fig. 3 curve C). In the spectrum of the second kind of samples, (obtained from the gel dried 7 days), these bands are very difficult to be observed, (Fig. 3 curve B). The spectrum is very broad. Taking into account the small concentration of the polymer, we can suppose that the adding process of water to the dried gel facilitate the dispersion of the polymer in the aqueous solution. In both cases the contribution of the polymer to the spectrum is masked by water [16,18].

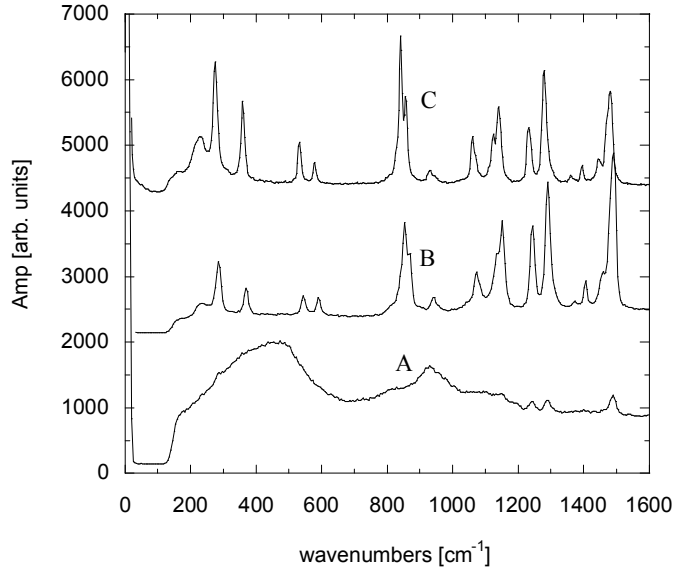

Fig. 2. The Raman spectra of the PEO gel dried 48 hours, (curve A); the PEO gel dried 7 days, (curve B); and PEO in solid state, (curve C).

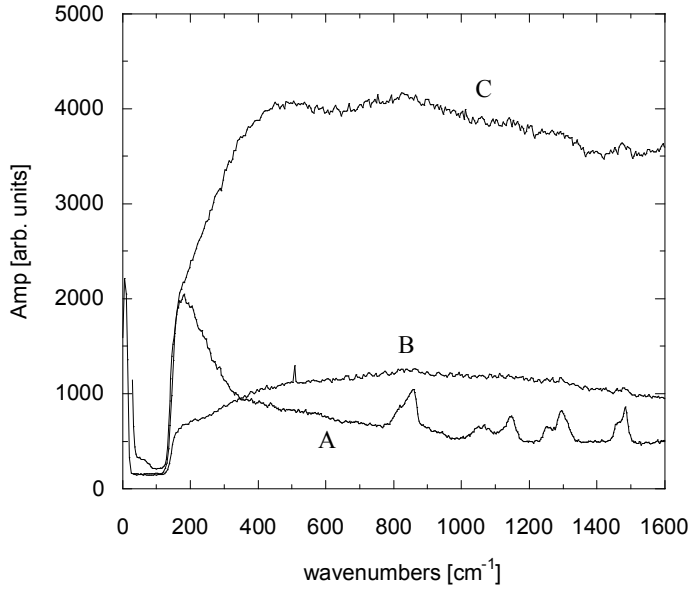

Fig. 3. The Raman spectra of the PEO gel, (curve A); PEO gel dried 48 hours and rehydrated, (curve C); and the PEO gel dried 7 days and rehydrated, (curve B).

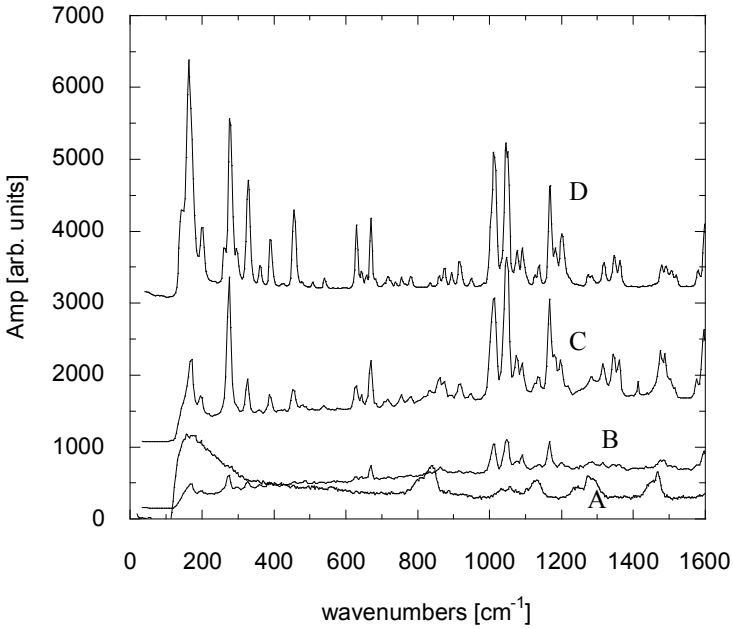

Fig. 4. The Raman spectrum of the initial PEO gel, (curve A); the spectrum of the clotrimazole recorded from the surface of the grains, (curve B); the spectrum of the clotrimazole recorded from the inner part of the grains, (curve C); and the spectrum of the clotrimazole in solid state, (curve D).

To observe the ageing effect of the polymeric matrix, the spectrum of the initial polymeric gel, (Fig. 1, curve B), was compared with the spectrum of the same sample which was kept 12 month in dark at room temperature and normal atmospheric pressure, (Fig. 1, curve C). The two spectra are very similar, except a little noisy, and demonstrates no structural modification of the polymer during the conservation.

Other interest of the study is the observation of the stability of the pharmaceutical product containing the active pharmaceutical substance. These samples were obtained by dispersion of the clotrimazole in the PEO gel. The analysis by optical microscopy shows a colloidal suspension of the clotrimazole in the polymeric matrix, on the appearance of small domains of the size of few micrometers. We called *grains* these domains. The Raman spectra were recorded from regions of the samples with different optical appearances, which represent only the polymeric matrix or only the grains of the clotrimazole. By modification of the focus of the laser, it is possible to record the spectrum from the surface of these domains or from theirs inner part. The spectra obtained from these regions are different, (Fig. 4). The spectrum of the clotrimazole in powder state and the spectrum of clotrimazole from the inner part of the grains, curves C and D, are very similar.

Only the amplitude of some bands is reduced in the spectrum C compared with the spectrum D, and the width of some bands is larger in this spectrum. The water doesn't penetrate the grains. The spectrum recorded from the surface of the grains, (curve B), became broad, and contains only few bands of the clotrimazole. Some molecules of water are attached to the surface of the grains and mask partially the spectrum of the clotrimazole. This fact explains the missing of some bands and the broadening of the spectrum B. The main properties of the clotrimazole are not affected by the polymeric matrix and water.

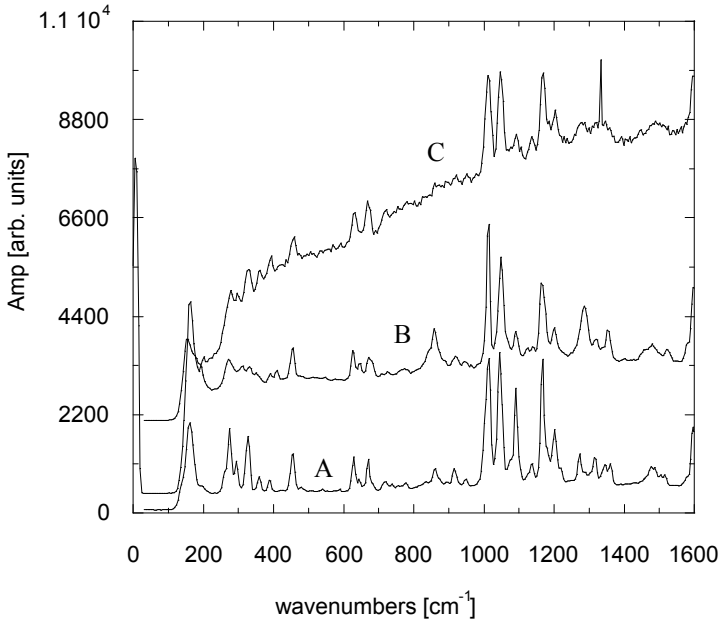

Fig. 5. The Raman spectrum of the clotrimazole in the initial PEO gel, (curve A); the spectrum of the clotrimazole in the PEO gel after 12 months of conservation, (curve B); and the spectrum of the clotrimazole recorded after the rehydration of the gel, (curve C)

As in the case of the polymeric matrix, the gel containing the clotrimazole was submitted to the rehydration process. The water was eliminated from the pharmaceutical product by evaporation and then it was added again. The most intense bands of the solid clotrimazole appear in this spectrum, but theirs amplitude are reduced, (Fig. 5, curve C). The intensity of the bands is determined by the local quantity of the substance under the incidence of the laser beam. The size of the grains of clotrimazole is reduced under the repeated action of water that explains the reduction of the intensity of the vibration bands. The adding-removing process of water contributes to a large dispersion of the active substance in the polymeric matrix, but do not modify its properties.

The stability of the active substance during long time of conservation is an important requirement imposed to the pharmaceutical products. We evaluated this stability by analyzing the Raman spectra of the clotrimazole in the initial PEO gel, (Fig. 5 curve A), and after 12 months of conservation, (Fig. 5 curve B). Except a little broadening of the spectrum B in the domain 270-400 cm^{-1}, both spectra are very similar. This behavior demonstrates no modification of the structure of clotrimazole included in the PEO matrix during long time conservation.

CONCLUSIONS

The repeated action of water and the ageing effects on the physical properties of the PEO matrix and clotrimazole, were observed by Raman spectroscopy.

The Raman spectra of the solid polymer and of the gel contain almost the same vibration bands in the domain 1000-1500 cm^{-1}, but they are different in the domain 200-400 cm^{-1}. This behavior indicates a broad dispersion of the local conformation of the polymer and important time fluctuation of these conformations in the aqueous solution.

The spectrum of the dried gel depends on the evaporation time of water. The water is completely removed from the gel after 7 days and the spectrum of the dried sample is practically similar to the spectrum of the polymer in the solid state. This behavior demonstrates a reversible interaction between the polymer and the water.

The hydration of dried samples leads to a large dispersion of the polymer in water and to a broadening of the recorded spectra. After 12 months of conservation the structure of the polymer remains unaffected.

A colloidal suspension is obtained by introducing the clotrimazole in the gel but the spectrum of the clotrimazole is not affected by the polymeric matrix. The properties of the clotimazole remain unchanged after 12 months conservation in the polymeric gel.

ACKNOWLEDGEMENT:

This work was supported for UBB TP 1 nr 20947 / 12. 07. 2007 grant.

REFERENCES

1. L. Maggi, L. Segale, M.L. Torre, E. Ochoa Machiste, U. Conte, *Biomaterials*, **23**, 1113, (2002).

2. Milen Dimitrov, Nikolai Lambov, *International Journal of Pharmaceutics* **189**, 105, (1999).

3. A.P. Munasur, V. Pillay, *Int. J. Pharm.*, **323**, 43, (2006).

4. Hoffman A.S., *Adv. Drug Del. Rev*. **43**, 3, (2002).

5. Jung Yun Chang, Yu-Kyoung Oh, Hak Soo Kong, Eun Jung Kim, Dong Deuk Jang, Ki Taek Nam, Chong-Kook Kim, *Journal of Controlled Release,* **82**, 39, (2002).
6. Sang-Wook Park, Byoung-Sik, Jae-Wook Lee, *Korea-Australia Rheology Journal*, **17**, 4, (2005).
7. Pankaj Dayal, Viness Pillay, R. Jayachandra Babu amd Mandip Singh, *AAPS Pharm. Sci. Tech.*, **6** (4), 573, (2005).
8. Gharima Sharma, S. Jain et al, *Acta Pharm*. **56**, 337, (2006).
9. Elena Dinte, R.I. Iovanov, S.E. Leucuta, *Farmacia*, **6**, 29, (2006)
10. P.J. Flory, *Statistical Mechanics of Chain Molecules*, (Interscience Publishers, New York, 1969).
11. P.G. de Gennes, *Scaling Concepts in Polymer Physics*, (Cornell University Press, Ithaca, London, 1979).
12. H.S. Lee, Y.K. Wang, S.L. Hsu, *Macromolecules*, **20**, 2089, (1987).
13. H.S. Lee, Y.K. Wang, W.J. MacKnight,. S.L. Hsu, *Macromolecules*, **21**, 270, (1988).
14. S. Yoon, K. Ichikawa, W. J. MacKnight, S. L. Hsu, *Macromolecules*, **28**, 5063, (1995).
15. S. Yoon, W.J. MacKnight, S.L. Hsu, *J. Appl. Polym. Sci.*, **21**, 197, (1997).
16. Barbara Stuart, *Polymer Analysis*, (John Willey and Sons, Chicester, 2002).
17. R.J. Young and P.A. Lovell, *Introduction to Polymers*, Second edition, (Chapman & Hall, London, 1991).
18. Xiaozhen Yang, Zhaohui Su, Dacheng Wu, Shaw Ling Hsu, and Howard D. Stidham, *Macromolecules*, **30**, 3796, (1997).
19. R.L. Jaffe, G.D. Smith, D.Y. Yoon, *J. Phys. Chem.*, **97**, 12745, (1993).
20. A. Abe, K. Tasaki, J.E. Mark, *Polym. J.* **17**, 883, (1985).
21. Monica Baia, S. Astilean, T. Iliescu, *Raman and SERS Investigations of Pharmaceuticals*, (Springer Verlag, Berlin, 2008)

STUDIA UNIVERSITATIS BABEŞ-BOLYAI, PHYSICA, LV, 1, 2010

SYNTHESIS AND ANALYSIS OF SOL-GEL DERIVED BIOGLASSES INCORPORATING SILVER

A. VULPOI, M. TĂMAŞAN, V. SIMON[a]

ABSTRACT. In this study are reported results obtained on a calcium phosphosilicate bioactive glass system containing silver, considered as potential biomaterial with antibacterial effect. The bioglasses were prepared via an acid-catalysed sol-gel route. The resulting samples were characterised by X-ray diffraction, differential thermal analysis and gravimetric thermal analysis, BET measurements for specific surface area determination, as well as by a UV laser particle size analysis.

Key words: *bioglass; silver incorporation; sol-gel.*

INTRODUCTION

Bioactive glasses were first introduced by Hench in the early 1970s [1]. These special glass systems are generally composed of SiO_2, CaO, P_2O_5 and Na_2O. They can be produced by melting process or by sol-gel process.

The sol-gel process, as the name implies, involves the evolution of inorganic networks through the formation of a colloidal suspension (sol) and gelation of the sol to form a network in a continuous liquid phase (gel) [2]. The most widely used precursors for silicate sol-gel derived systems are the alkoxysilanes, such as tetramethoxysilane and tetraethoxysilane. Many factors affect the resulting silica network, such as, pH, temperature and time of reaction, reagent concentrations, catalyst nature and concentration, H_2O/Si molar ratio, aging temperature and time [3].

Bioactive glasses have many applications but these are primarily in the areas of bone repair and bone regeneration via tissue engineering. All these applications are based on properties which are strongly dependent on the structure and surface features of bioglasses.

In the present work, the system under investigation consists of SiO_2, CaO, P_2O_5 and Ag_2O and it was prepared via an acid-catalyzed sol-gel route. The aim of introducing Ag_2O in the composition of the bioglass is to minimize the risk of microbial contamination [4-6].

[a] *Babeş-Bolyai University, Faculty of Physics & Institute for Interdisciplinary Experimental Research, Cluj-Napoca, Romania*

MATERIALS AND METHODS

The composition of the samples prepared via an acid-catalyzed sol-gel route is $56Si0_2 \cdot (40\text{-}x)CaO \cdot 4P_2O_5 \cdot xAg_2O$, where x = 0, 2 and 10 wt %. Tetraethoxysilan (TEOS) was used as precursor for $Si0_2$, calcium nitrate tetrahydrate as precursor for CaO, ammonium dibasic phosphate precursor for P_2O_5 and silver nitrate as precursor for Ag_2O. TEOS was mixed with ethanol and the other precursors with distillated water. Nitric acid was used as catalyst. After gelation the samples were dried at 110 ^oC and than they were finely ground with mortar and pestle.

The Specific Surface Area measurements were made with a Qsurf 9600 Series Surface Analyzer, working on the single point BET principle [7], using a dry mixture of helium and nitrogen [8].

The X-ray diffraction (XRD) analysis was carried out with a Shimadzu XRD-6000 diffractometer, using Cu K_α radiation (λ=1.5418 Å), with Ni-filter.

The differential thermal analysis (DTA) and gravimetric thermal analysis (GTA) were performed on Shimadzu analyser DTG-60H witch simultaneously measures TG and DTA, in air, using alumina crucibles, with hitting rate of 10 ^oC/min, from room temperature to 1000 ^oC.

Particle size distributions are calculated using the light intensity distribution data, with a SALD-7101 nano particle size analyzer.

RESULTS AND DISCUSSION

The XRD pattern (Fig. 1) show that the structure of 110 ^oC dried sol-gel derived samples is definitely dominated by the amorphous phase. However, for calcium phosphosilicate sample without silver the diffraction lines at 2θ = 26, 30 and 32.5^o denote the presence of some nanocrystals in this sample, but they are absent in the sample with 10 % Ag_2O. The size of the crystals is evaluated in the nanosize range according to the width of the diffraction peaks, based on Scherrer's equation [9].

In the DTA curves (Fig. 2) the first endothermic peak is due to water physisorbed on the samples. This is accompanied by a weight loss peak, as can be observed in the DTG curves. The next peaks which appear on the DTA curves of each sample between 200°C and 450°C are due to the residual nitrates decomposition and dehydroxylation, while the peaks recorded between 450°C and 550°C are due to decomposition of all remaining organic parts from the sample [10-12]. All these events are accompanied by a weight loss. The DTA curves of the samples without silver and 2 % Ag_2O also reveal a crystallization peak at 948°C, respectively at 932°C.

Particle size distributions were calculated using the light intensity distribution data. When a particle is irradiated with a laser beam, light is emitted from the particle in every direction. This is "scattered light". The intensity of the scattered light varies with the scattering angle and describes a spatial intensity distribution pattern. Particle size distribution measurement is not performed on individual particles, but rather on particle groups made up of large numbers of particles. Particle groups

contain particles of different sizes, and the light intensity distribution pattern emitted by a group is composed of all the scattered light emitted from all the individual particles. The particle size distribution, i.e. what particle sizes are present and in what proportions, can be obtained by detecting and analysing the light intensity distribution pattern. This is the basic principle behind the laser diffraction method used in laser diffraction particle size analyzers.

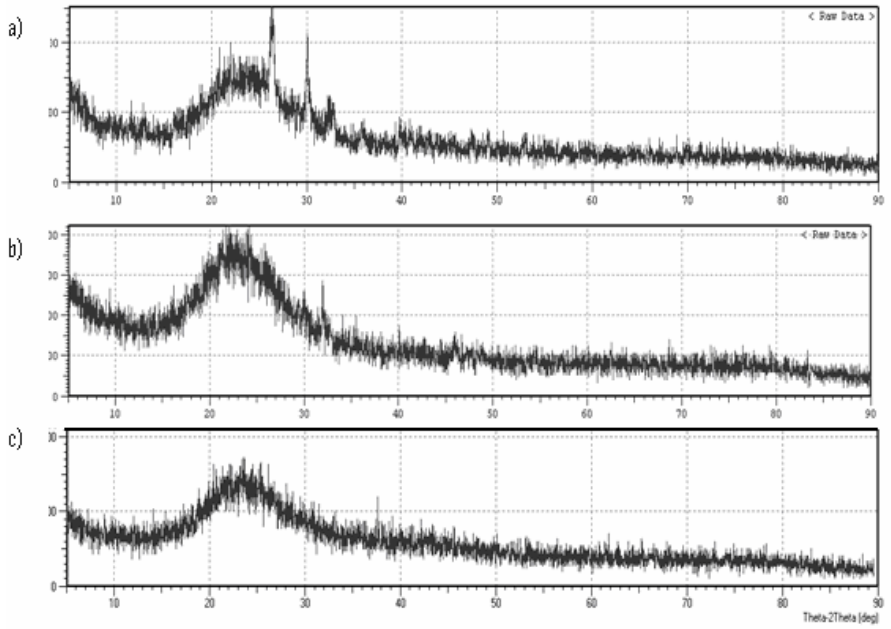

Fig. 1. XRD patterns of $56Si0_2 \cdot (40\text{-}x)CaO \cdot 4P_2O_5 \cdot xAg_2O$ bioglasses.
a) x = 0; b) x = 2; c) x = 10.

The particle size distribution diagram (Fig. 3) shows that particle sizes are ranged between 3-5 µm for the samples without silver and with low silver content, and a particle size distribution around 100 µm for the sample containing 10 % Ag_2O.

To follow the change of materials porosity with the addition of silver oxide, the specific surface area (SSA) was measured. The basic assumptions of the BET model are: (*i*) the surface is uniform, (*ii*) gas molecules can be physically adsorbed in an infinite number of layers, (*iii*) the heat energy values of adsorption for all layers except the first are equal to the heat of condensation of the adsorbate, (*iv*) formation of a new layer can start before the former layer is completely populated [13]. The porosity of sol–gel derived bioactive glasses provides high surface area and exposes a high concentration of surface hydroxyl groups, that enhance their potential as biomaterials [14].

a

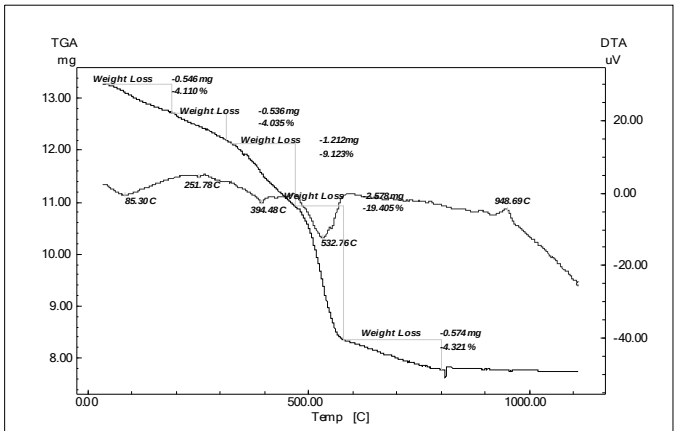

b

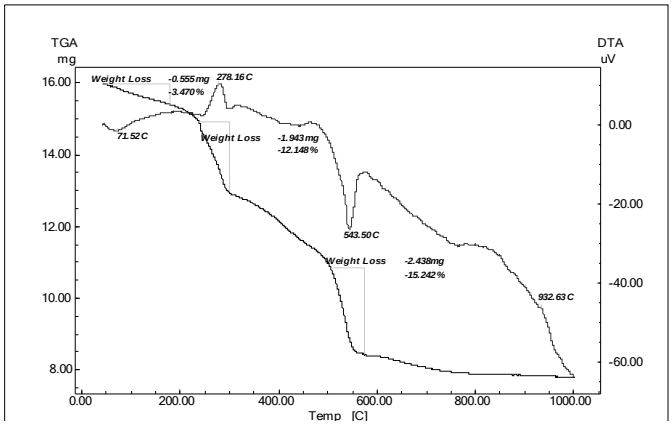

c

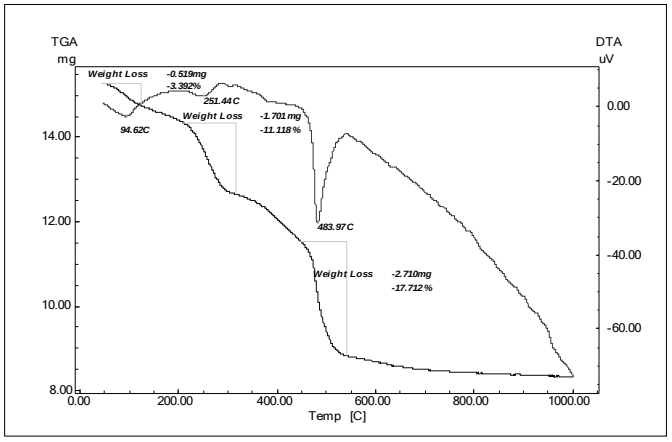

Fig. 2. DTA/DTG curves of $56Si0_2 \cdot (40\text{-}x)CaO \cdot 4P_2O_5 \cdot xAg_2O$ bioglasses.
a) x = 0; b) x = 2; c) x = 10.

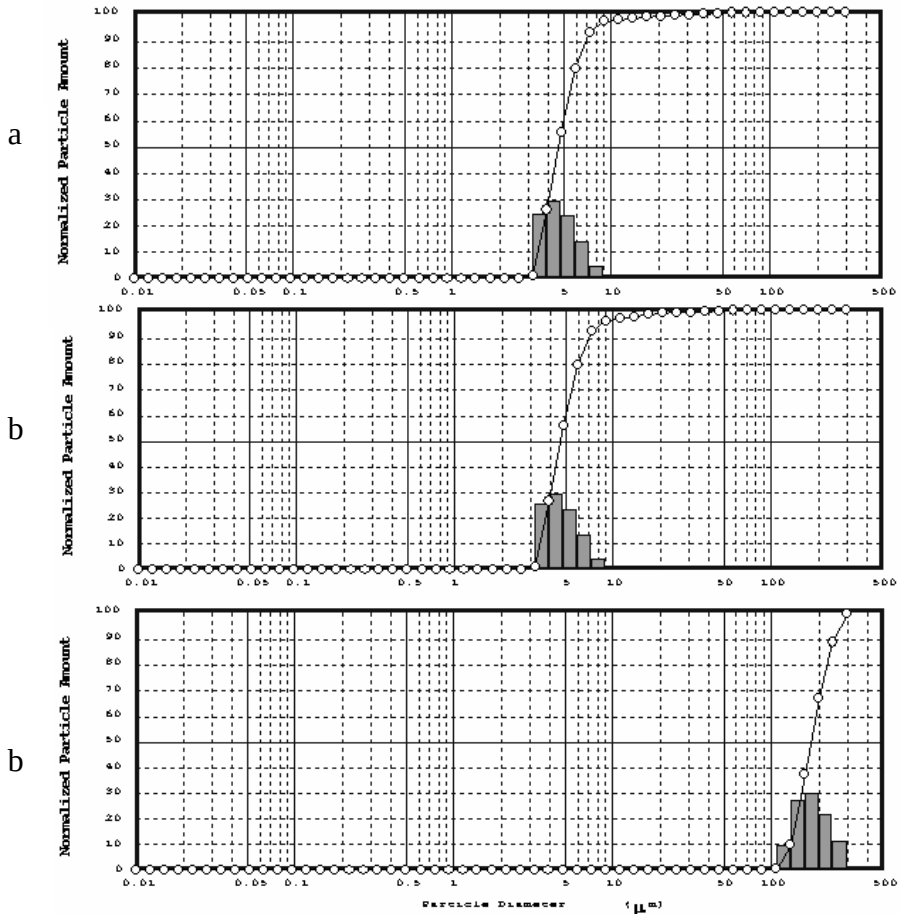

Fig. 3. Particle size distribution diagrams of $56Si0_2 \cdot (40\text{-}x)CaO \cdot 4P_2O_5 \cdot xAg_2O$ bioglasses. a) x = 0; b) x = 2; c) x = 10.

The SSA results for the investigated samples are given in Table 1. The highest value, 45.2 m^2/g, is measured for the bioaglass without silver. By addition of 2 % silver oxide to the composition of the bioactive glass the specific surface area decreases to 21 m^2/g at the second sample, and as Ag_2O content is increased to 10 % the specific surface recedes below 1 m^2/g. Size distribution and specific surface area results are congruent and points out that by increasing the Ag_2O content in calcium phosphosilicate bioglass, larger particle sizes and diminished specific surfaces are obtained.

Table 1. Specific surface area (SSA) of $56Si0_2 \cdot (40\text{-}x)CaO \cdot 4P_2O_5 \cdot xAg_2O$ bioglasses.

x (wt %)	0	2	10
SSA (m^2/g)	45.2	21.0	< 1

CONCLUSIONS

Bioactive glasses $56Si0_2 \cdot (40\text{-}x)CaO \cdot 4P_2O_5 \cdot xAg_2O$, with x = 0, 2 and 10 wt %, were prepared via an acid-catalysed sol-gel route. The samples obtained after 110 ^oC drying are definitely in amorphous state, but a residual nanocrystalline phase is evidenced in the sample without silver, and this disappears by addition of Ag_2O. The thermal analyses show the removal of physically adsorbed water, hydroxyl groups, nitrate and organic residues, up to 550°C. By increasing the content of silver oxide to 10 %, a growth of particle size from 3-5 µm to 100 µm, and a decrease of specific surface area from 45.2 m^2/g to less then 1 m^2/g is observed.

The silver addition as antibacterial agent in the calcium phosphosilicate host bioglass dried at 110 ^oC has to be considered in relation with the effect on specific surface area of samples.

ACKNOWLEDGEMENTS:

A.V. author wishes to thank for the financial support provided from programs co-financed by The Sectoral Operational Programme Human Resources Development, Contract POSDRU 6/1.5/S/3 – „DOCTORAL STUDIES: THROUGH SCIENCE TOWARDS SOCIETY".

REFERENCES

1. L.L. Hench, H.A. Paschall, J. Biomed. Mater. Res.7 (1973) 25.
2. C.J. Brinker and G.W. Scherer, Sol-Gel Science: The Physics and Chemistry of Sol-Gel Processing, Academic Press, Inc.: New York, 1990.
3. O. Lev, M. Tsionsky, L. Rabinovich, V. Glezer, S. Sampath, I. Pankratov, J. Gun, Anal. Chem., 67(1995) 22A.
4. M. Bellantone, Huw D. Williams, L L. Hench, Antimicrob. Agents Chemother., 46 (2002)1940.
5. S. P. Valappil, D. M. Pickup, D. L. Carroll, C. K. Hope, J. Pratten, R. J. Newport, M. E. Smith, M. Wilson, J.C. Knowles, Antimicrob. Agents Chemother., 51 (2007) 4453.
6. O. Lepparanta, M. Vaahtio, T. Peltola, D. Zhang, L. Hupa, M. Hupa, H. Ylanen, J. I. Salonen, M. K. Viljanen, E. Eerola, J. Mater. Sci. Mater. Med., 19 (2008) 547.

7. S. Brunauer, P.H. Emmett, E. Teller, J. Am. Chem. Soc., 60 (1938) 309.
8. A. Vulpoi, C. Ionescu, V. Simon, Studia Physica, LIV, 1 (2009) 10.
9. H.P. Klug, L.E. Alexander, X-ray Diffraction Procedures. John Wiley, New York 1954
10. M. Tamasan, T. Radu, S. Simon, I. Barbur, H. Mocuta, V. Simon, J. Optoelectr. Adv. Mat., 10 (2008) 948.
11. M. Cernea, E. Andronescu, R. Radu, F. Fochi, C. Galassi, J. Alloy Compd., 490 (2010) 690.
12. C. Ghitulica, E. Andronescu, O. Nicola, M. Birsan, Adv. Mater. Res., 47-50 / 2 (2008) 960.
13. Z.G. Djuric, I.M. Jokic, M.P. Frantlovic, K.T. Radulovic, Microelectron. Eng., 86 (2009) 1278.
14. S. Lin, C. Ionescu, E.M. Valliant, J.V. Hanna, M.E. Smith, J.R. Jones, J. Mater. Chem., 20 (2010) 1489.